ABSTRACT

Title of dissertation: DYNAMICS AND EXCITED STATES OF QUANTUM MANY-BODY SPIN CHAINS WITH TRAPPED IONS

Crystal Rosalie Senko,
Doctor of Philosophy, 2014

Dissertation directed by: Professor Christopher Monroe
Joint Quantum Institute,
University of Maryland Department of Physics
and
National Institute of Standards and Technology

Certain classes of quantum many-body systems, including those supporting phenomena like high-T_c superconductivity and spin liquids, are believed to be fundamentally intractable to classical modeling. Quantum simulations, in which synthetic materials are engineered by inducing well-controlled quantum systems like ultracold atoms to obey many-body Hamiltonians of interest, are a promising new approach to study this type of physics. However, current experiments have not yet simultaneously achieved the system sizes and the level of control necessary to observe and understand novel physics that cannot be classically modeled. In this work, I present several advances toward this ultimate goal of large-scale, highly controllable quantum simulations of many-body spin physics. We simulate long-range Ising and XY spin models in the presence of transverse and longitudinal magnetic fields using chains of up to 18 ultracold $^{171}Yb^{+}$ ions held in a linear Paul trap, where two hy-

perfine levels in each ion encode spin-1/2 states. The tunable spin-spin interactions and effective magnetic fields are engineered using laser fields, and the individual spin states are directly imaged with state-dependent fluorescence. The results in this thesis address several of the ongoing challenges in the development of synthetic quantum matter platforms. One such challenge is establishing more flexible capabilities in the sorts of Hamiltonians we can model. By observing suppression of the ground state spin ordering, we have demonstrated our ability to continuously tune the interaction range in a power-law interaction pattern, and hence the amount of frustration present in the spin system. We have additionally begun developing tools to study particles of higher spin, which could eventually be used to create and study topological phases of matter. Another challenge is the necessity of identifying problems that the next generation of experiments, with flexible (but not arbitrary) controls and classically intractable (but not infinitely large) system sizes, can feasibly shed new light on. We have made measurements of how the range of interaction affects dynamics of spin correlations propagating through the chain, and the excellent agreement between our observations and numerical simulations indicate that at larger sizes, our experiment can meaningfully contribute to the open question of the fundamental speed limit on the transfer of information through such a spin chain. Finally, for classically intractable system sizes, it will be crucial to have multiple techniques at our disposal for validating our understanding of the exact microscopic model being implemented. We have developed and demonstrated an MRI-like spectroscopic technique for probing the energies of the many-body Hamiltonian, which serves as a new method for validating quantum simulations of the transverse Ising

model. Our experiments can potentially be scaled up in the near future to study fully connected lattice spin models with several tens of spins, where classical computation begins to fail, and the results described in this thesis contribute to the effort to build experiments that can break new ground in the study of quantum many-body physics.

Table of Contents

List of Figures

Chapter 1: Introduction

In recent years, significant interest has been generated in the use of well-controlled quantum systems, particularly ultracold atoms, for the study of many-body physics [1, 2]. Experimental techniques for the control and manipulation of interacting quantum mechanical degrees of freedom have become sufficiently advanced that the field may soon be capable of accessing a regime of physics that has previously been inaccessible. In particular, the problems we are interested in (which may one day be more fruitfully studied in the context of quantum simulators than by other means) generally involve large numbers of interacting quantum systems that exhibit useful or otherwise interesting collective properties; some prototypical examples include spin liquids and high-T_c superconductors.

While such systems can be studied experimentally in solid-state materials, such as superconducting cuprates, or herbertsmithite (a material exhibiting characteristics of a spin liquid), these experiments have certain weaknesses. In particular, it is often of interest to obtain an understanding of the microscopic behavior of these systems, which can be difficult to do with the tools generally available in these 'bulk' experiments, such as measuring currents, studying the response to global applied magnetic fields, and so on.

One common method of attack in this situation, where microscopic degrees of freedom are difficult to access experimentally and the microscopic model is not analytically known, is to perform numerical simulations of various microscopic models that are guessed to have relevance to the problem in question. Such simulations can thus lend insight on what properties are key to obtaining the behavior of interest and what details are unimportant. Unfortunately, in the particular case of interacting quantum mechanical degrees of freedom, such simulations cannot be performed on a large scale.

The fundamental problem is the exponential scaling of the Hilbert space size: for example, in order to fully model the dynamics of N spin-1/2 particles, one must keep track of 2^N spin configurations. This is fine in cases where effective approximations are known to reproduce the behavior of interest, but this is not always true (and indeed, we don't necessarily have reason to believe there always will be ways to approximate the dynamics of a system without dealing with its entire Hilbert space, especially in cases where large-scale entanglement is present). In cases where no useful approximations are known, computational techniques break down for system sizes as small as 30 spin-1/2 particles.

These considerations help paint an outline of the niche that quantum simulation experiments are hoped to soon fill. Simulations done with inherently quantum mechanical particles, rather than the classical bits of a supercomputer, are hoped to have much better scaling properties: even if there is a superlinear increase of resources demanded to add more trapped atoms to an experiment, this increase is expected to be subexponential. At the same time, the level of control that we now

have over ultracold atomic systems gives us immediate access to tools that are challenging or even impossible to implement in more conventional material experiments. For example, atomic simulations feature control and readout of individual particles like spins, and a large degree of flexibility in the Hamiltonian implemented, even allowing us to study phenomena that do not occur in any other known system. As just one example, it is possible to create a system that effectively has no decoherence or disorder on the relevant timescales and energy scales, and then re-introduce such 'noise' effects in a controllable way. Thus, while I use the word 'simulation' as a shorthand for this class of experiments, it might be more accurate to call them something like 'experimental studies of quantum many-body physics', since there is more to the field than simply mimicking or simulating known materials.

General-purpose digital quantum simulators (also known as quantum computers) are still far from being practically achievable, but experiments which induce a system to obey the dynamics of a particular Hamiltonian of interest are being developed fairly rapidly. These experiments are sometimes referred to as emulations and sometimes as analog quantum simulations; here I use the terms interchangeably. There are a variety of platforms that can be used for this type of quantum simulation, which tend to have complementary strengths and weaknesses. For example, ultracold neutral alkali atoms are well suited for studies of transport, and when confined in an optical lattice allow the study of Hubbard-type models that are believed to have a connection to the phenomenon of high-T_c superconductivity. However, in these systems typically there are no long-range interactions. By contrast, the trapped ion system I will describe is well suited for studies of interacting

spins, and easily affords not only tunable long-range interactions but also might enable dynamic changes of the interaction pattern. However, physical transport (as opposed to transport of spin information) is typically absent. It is thus helpful to choose a suitable platform for the particular class of models that are of interest.

I will discuss only a specific platform in this thesis (after the introduction) - namely, the use of trapped ion chains to study spin systems with tunable long-range interactions. However, a brief survey of other atomic quantum simulation experiments serves to explicate the broad array of phenomena that can be studied with AMO techniques. This list is far from complete, and is intended only to convey the richness of these systems. And of course, even a comprehensive description of such atomic experiments neglects other promising quantum simulation platforms such as photons [3] and superconducting circuits [4].

A particularly large community has formed around the use of ultracold atoms to study many-body physics (for reviews of this field, see [1] and [2]). Quantum gas microscopes, in which neutral atoms are trapped in a lattice formed from laser light and imaged with single-site resolution, have enabled studies of fundamental statistical mechanics topics. Among many other applications, these experiments are being used to probe nearest-neighbor spin phenomena [5, 6] and microscopic studies of phase transitions like the superfluid to Mott insulator transition [7]. Emulations that are more closely related to real materials are also possible, such as systems obeying graphene-like physics with interactions that can be tuned to a degree not possible in the natural material [8]. Laser fields can be used to induce synthetic gauge fields that cause the atoms to obey the same physics as electrons in a magnetic [9] or

electric [10] field, opening a route to study quantum Hall physics in atomic systems. Strong interactions can be induced in ultracold fermions using a Feshbach resonance [11–14], which may allow atomic experiments to contribute to the understanding of such disparate phenomena as high-T_c superconductivity, the interaction of neutrons in neutron stars, or the quark-gluon plasma believed to have existed at the beginning of the universe. Another degree of freedom that many experimentalists are beginning to exploit is the use of long-range interactions, such as the dipolar interactions in polar molecules [15], or the van der Waals interactions in Rydberg atoms [16, 17]. With trapped ions specifically, a great deal of effort has been invested in developing the platform I will discuss in this thesis for studying spin systems with long-range interactions [18–26]. Other applications for using trapped ions to study many-body physics include simulations of polariton physics [27] and relativistic dynamics [28,29], with a variety of proposals also existing for the study of topics as varied as spin-boson models [30], microscopic models of friction [31], and even aspects of quantum field theories [32].

Currently, state-of-the-art atomic experiments are very close to reaching the goal of studying many-body physics in a regime inaccessible by other experimental or computational methods, though the field arguably has not simultaneously achieved both the system sizes and the level of control necessary to significantly expand the boundary of what types of physics can be observed. Still, the progress that has occurred in the past several years is suggestive that this goal can be attained in the not too distant future. For example, only six years have passed between the first proof-of-principle experiment demonstrating that trapped ions can be used to simu-

late spin physics and the current state-of-the-art in which we routinely manipulate 10 or more spins, with a good degree of control over as many as 18 spins so far, and have characterized many possible 'knobs' in our Hamiltonians.

1.1 Trapped ions as a spin emulator

The remainder of my thesis will specifically focus on the use of a chain of ions to simulate interacting spins. By isolating two hyperfine states in the ground electronic manifold of a trapped ion, we obtain a highly stable and controllable two-level system which may be considered as a quantum bit (qubit) for computation or a spin-1/2 particle for emulating many-body physics. (And as we will see in Chapter 7, we can replace the 'two's with 'three's to study spin-1 particles, or qutrits.) Laser beams imparting optical dipole forces can be used to engineer highly tunable interaction profiles: for example, we can create pairwise interactions which follow a power-law decay with the separation r between the pair of spins, $1/r^{\alpha}$, where we can continuously vary both the overall strength of the interactions and the parameter α, and it is also straightforward to apply effective magnetic fields along various directions. Additionally, the full spin configuration can be read out by collecting state-dependent fluorescence on a CCD.

At the time that I joined this quantum simulation effort, the then-current team had demonstrated the ability to map spin models onto trapped ions and thereby observe interesting many-body physics, and had already carried out several studies of this nature [18–21]. We are thus in a transitional period where we can no longer

meaningfully claim to be performing a proof-of-principle experiment. Because of this, and the fact that we are still at a system size small enough that the spin physics we see can be easily modeled on a computer, considering what extra value is added toward our long-term goals is a useful filter in selecting among the many directions we could explore with this flexible system. While the general principle we follow in planning the next experiment is usually to simply study the most interesting thing we can access with whatever capabilities we have at the time, we nevertheless have managed to make quite a bit of progress on some of the conceptual questions that arise as we make a serious effort to scale up our system. In particular, we have made contributions toward identifying useful problems to tackle with a larger simulator, in the form of measurements that might lead to improving bounds on the speed of transferring quantum information through systems with long-range interactions; toward developing validation and measurement techiques, in the form of spectroscopic protocols for measuring energies of the effective many-body Hamiltonian and extracting information about the individual interactions; and toward developing a less limited, more multipurpose device, in the form of demonstrating manipulation and entanglement of interacting spin-1 chains. As I leave the project, others are in the middle of technical upgrades that will soon enable even more exciting physics studies: the day that the first draft of this thesis was due, one of my colleagues hit our ion with a laser that will be used to rotate individual spins, and less than two weeks before that the cryogenic vacuum chamber that (hopefully) will be eventually used to push the system to 30, 50, or even more spins arrived. Thus, it has been an exciting time to work with this team.

1.2 Outline of the thesis

In this introduction, I've described why we are excited about quantum simulation in general, and given a brief high-level description of the project as a whole. Chapter 2 is devoted to the physics of our atom-laser interactions, which are at the heart of most manipulations we do. In this chapter, we will describe a typical experimental sequence (assuming that everything has been set up perfectly to this point), and then describe the physics underlying each step; discussion of experimental/hardware considerations will, for the most part, be left for the next chapter. The main focus will be the coherent operations, which involve pure spin rotations, spin-motion coupling, and the use of the spin-motion coupling to generate spin-spin interactions. The physics described in this chapter will hence serve as a background to understand both the experimental details and the studies of spin physics.

Chapter 3 discusses the apparatus, and experimental details that do not belong in any other chapter, at some length. The setup has been documented in other theses [33, 34], so I do not provide a comprehensive description of the hardware. I instead give an overview, highlighting some of the experimental requirements that may be unusually stringent, and discuss some aspects of the apparatus that have been developed or modified since the last thesis was written. Additionally, I document several experimental procedures that are essentially intended as answers to the question "I think we've measured this thing before, but how exactly did we do it?", and discuss a couple of otherwise-orphaned calculations and measurements that may have some bearing on future improvements to the current experimental

limitations.

Chapter 4 is a discussion of adiabatic preparation of ground states of the Ising model [23]. This technique was used in our studies of long-range antiferromagnetism, where we probed our ability to continuously tune the degree of frustration in our system [22] and in our studies of the addition of a longitudinal field to our Hamiltonian [24]. The latter two studies are, however, only briefly discussed, because they have been well documented not only in the publications but also in the theses of Rajibul Islam [33] and Simcha Korenblit [34].

Chapter 5 details the measurements we have made of how spin correlations build up as a function of time and distance after a global quench [25]. These measurements may have implications for the investigation of a fundamental question of how quickly information can propagate through an interacting spin system depending on the interaction pattern; our quantum simulator may be poised to immediately make a useful contribution toward understanding this question as soon as our system is large enough to measure dynamics that cant be classically simulated.

Chapter 6 covers the method we have developed for performing spectroscopy on the effective many-body spin system [26]. This technique, which is reasonably scalable, can be used to measure the individual spin-spin interactions directly, and also provides us with new ways to prepare interesting states without locally addressing individual spins.

Finally, Chapter 7 describes our recent and ongoing efforts to generate a spin-1 Hamiltonian. It may eventually be possible to use the techniques we are currently developing to create and study interesting topologically protected states; while such

techniques may not be necessary for the preservation of quantum information on our platform, it may be useful to have a clean system like trapped ions to test out these ideas before attempting to implement them on systems with more decoherence.

Chapter 2: Atom-laser interactions

This chapter discusses the physics of the various atom-laser interactions that are at the heart of our experiment. This material is placed ahead of the chapter detailing the experimental setup because its contents will be important for understanding the rationale behind some experimental choices and behind the various calibrations that will be described later.

Additionally, the concept of spin-motion coupling that forms the meat of this chapter is an idea that unifies many current experiments in quantum science, and it therefore merits a thorough discussion. I will point out the similarities between our Hamiltonians and those of other important quantum systems at appropriate points in the chapter, but list some examples here to highlight the diversity of topics that share this low-level connection to our experiments. The operation we refer to as a red sideband transition takes the form of a Jaynes-Cummings Hamiltonian [35], where the phonons or motional quanta in the trapped ion system map to photons in a cavity system. The Jaynes-Cummings model describes a two-level system interacting with a quantized mode of radiation [36], and underlies much work in cavity QED with atoms [37] or superconducting qubits [38]. The field of optomechanics also makes use of very similar ideas, where light is used to couple to and cool harmonic

modes of a massive object rather than of an ion in a potential well [39], to couple motion of a micromechanical oscillator to that of ultracold atoms, and to couple spin degrees of freedom (e.g., in a solid state qubit) to mechanical motion of a separate object [40]. The spin-dependent force that we generate by driving multiple motional sidebands resembles the spin-orbit coupling techniques used in ultracold gases to generate synthetic gauge fields [41], and for a single particle can be mapped exactly to the Dirac equation for relativistic electrons [28, 42]. And of course, for us the most relevant application of the spin-dependent force is the generation of spin-spin interactions mediated by phonons, which is an idea first proposed [43] and implemented [18, 44] for trapped ion systems, but could also be applied to other systems with long-range interactions such as polar molecules [45] or other dipolar particles (for example, atoms like Er or Dy with large magnetic dipole moments).

Before diving into details, I include a note on the rationale behind the organization of this chapter. I wanted to include full details on how the Hamiltonians are derived, what approximations are made, and so on. However, in an attempt to prevent the reader from being lost in the weeds, some of the detailed derivations have been banished to appendices. This allows me to use this chapter to highlight what I feel are the important equations and concepts to remember, and to attempt to provide a more high-level orientation.

2.1 Description of a typical experiment, providing a brief overview of the tools we need

The vast majority of the manipulations we do with our Yb^+ ions deal with some sort of laser-atom interaction. Consider the typical experiment setup during a data run (i.e., assuming that we have already loaded ions into the trap and performed the necessary calibrations), which consists of many repetitions of a very basic sequence:

1. State preparation
2. Application of a synthetic Hamiltonian
3. Measurement

I will often refer to a single repetition of this sequence as an experiment. It should hopefully be clear from context whether 'experiment' refers to 'an experiment' (as in a single sequence of preparation, time evolution, and measurement), 'the experiment'(as in the experimental apparatus), or to a collection of single-shot experiments resulting in some data plot.

During state preparation, we initialize both the motional and the spin states of the atoms. The motional preparation involves Doppler cooling the ions along all three principal axes of the trapping potential and sideband cooling the set of transverse motional modes that are used in generating the synthetic Hamiltonian. After the ions are cooled, the spin states are initialized to the $|\downarrow\downarrow\cdots\rangle_z$ state with optical pumping, and depending on the desired experiment, can be coherently rotated to (e.g.) $|\downarrow\downarrow\cdots\rangle_x$ or $|\downarrow\downarrow\cdots\rangle_y$.

To generate an artificial spin Hamiltonian, tunable spin-spin interactions and effective magnetic fields are applied using laser fields. In particular, the interactions arise from using spin-dependent optical dipole forces to couple spin states to motional degrees of freedom, allowing us to modulate the Coulomb interaction between the ions, while the effective fields arise from lasers coherently driving spin transitions without affecting the motional state.

After applying the spin Hamiltonian for the desired length of time, we read out the spin state in the σ_z basis by capturing spin-dependent fluorescence, generated by exposing the ions to a laser that resonantly scatters light from $|\uparrow\rangle_z$ but not from $|\downarrow\rangle_z$, on a CCD imager that affords spatial resolution of each separate ion. If we instead wish to measure the spins in a different basis, e.g. σ_x or σ_y, we perform a global rotation that maps (e.g.) $|\downarrow\rangle_x$ and $|\uparrow\rangle_x$ to $|\downarrow\rangle_z$ and $|\uparrow\rangle_z$ before exposing the ions to the readout light.

To gain a better understanding of these various operations, we will first briefly discuss the operations performed with near-resonant light, i.e. state preparation (Doppler cooling and optical pumping) and state measurement (spin-dependent fluorescence). We will then discuss in more detail the coherent operations, i.e. the rotations that may be performed as part of the initialization or the readout procedures and the generation of the effective spin Hamiltonian.

2.2 Resonant interactions, ytterbium level structure, and considerations regarding the Raman laser wavelength

We encode our spin states in the hyperfine energy levels of the ion $^{171}Yb^{+}$. This isotope has a nuclear spin of 1/2, which simplifies some of the manipulations that will be described below. For the spin-1/2 systems that I will discuss throughout most of the thesis, the spin states are defined within the ground $^2S_{1/2}$ manifold as $|\downarrow\rangle_z \equiv |F=0, m_F=0\rangle$ and $|\uparrow\rangle_z \equiv |F=1, m_F=0\rangle$, where F and m_F are quantum numbers associated with the total angular momentum of the atom and its projection along the z axis, respectively.

Doppler cooling, optical pumping, and detection all utilize the $^2S_{1/2} \leftrightarrow ^2P_{1/2}$ transition at 369.5 nm. A more complete description of these operations can be found in the paper [46] or in Steven Olmschenk's thesis [47]. A sketch of the relevant levels is shown in Figure 2.1. For these operations, we want to use a closed cycling transition, i.e. a transition where the atom always decays back to the energy manifold it started in. In Yb^{+}, 0.5% of spontaneous emission events result in the $^2P_{1/2}$ state decaying to $^2D_{3/2}$ [48]. While this D state will eventually decay to the S state, its lifetime is sufficiently long (roughly 53 ms) to disrupt all of these manipulations. We therefore apply another laser at 935 nm to repump the D state into the S state at a higher rate, using an intermediate state, $^3[3/2]_{1/2}$, whose lifetime is only 38 ns.

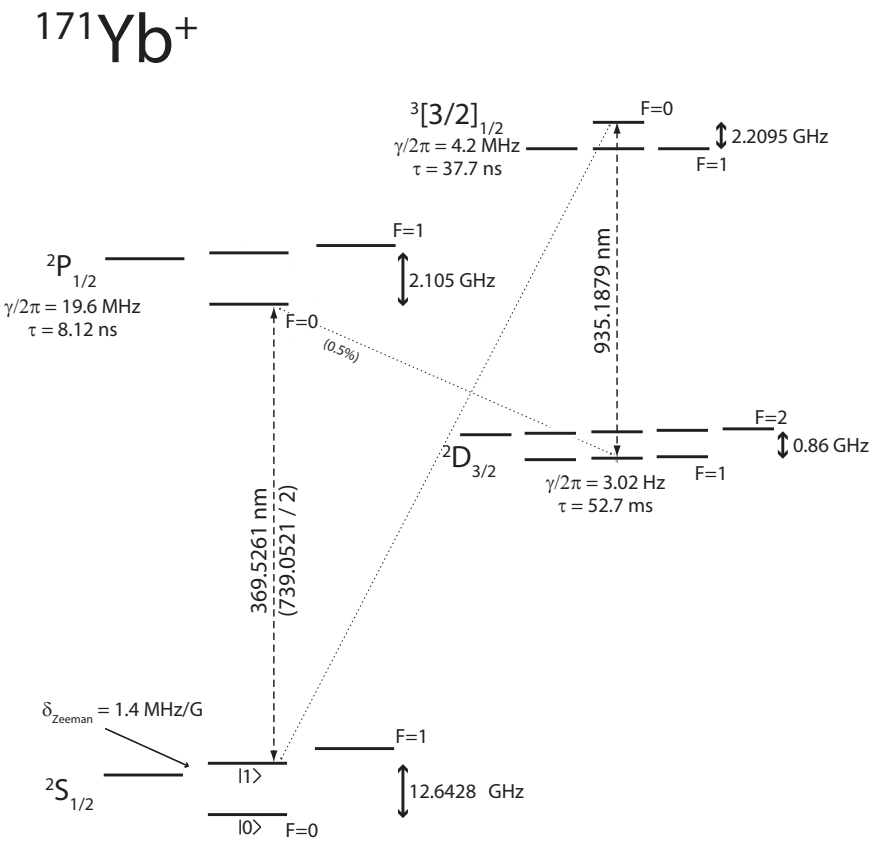

Figure 2.1: Diagram of the electronic energy levels of Yb^+ that participate in the cycling transition. The $^2D_{3/2}$ and $^3[3/2]_{1/2}$ levels need to be considered because the $^2P_{1/2}$ state decays to $^2D_{3/2}$ in 0.5% of spontaneous emission events, and $^3[3/2]_{1/2}$ is used for repumping population from $^2D_{3/2}$ to $^2S_{1/2}$. Dashed lines represent transitions that are driven with laser fields at the labeled wavelengths, and dotted lines represent spontaneous decay paths. The population decay rate γ and associated lifetime $\tau = 1/\gamma$, along with the hyperfine splittings of each level, are also shown.

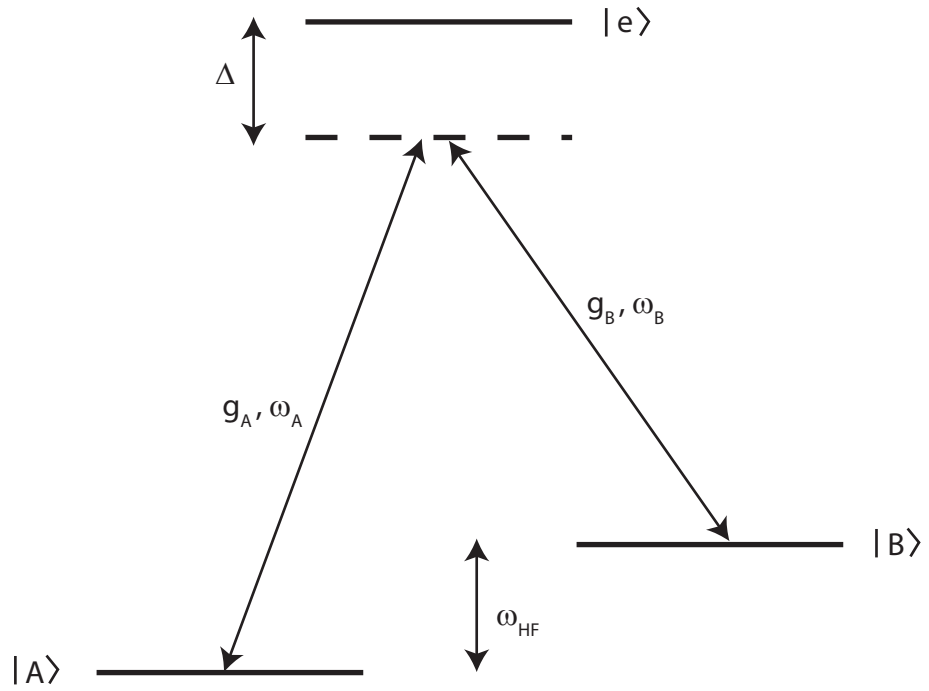

Figure 2.2: Example three level system, where each laser beam has its own frequency ω and single-photon Rabi frequency g; shown here is the case where the two laser beams have a beat frequency at exactly ω_{HF}, detuned by a large amount from the excited state $|e\rangle$.

2.2.1 Wavelength considerations for stimulated Raman transitions

As we will see below, the coherent operations on the spin states are all performed with stimulated Raman transitions. The idea here is to tune a pair of laser beams such that they are detuned from an excited state and their frequency difference is resonant with the hyperfine transition we wish to drive, as schematically depicted in Figure 2.2. In the limit of a large detuning from the excited state, this effectively drives transitions between the lower hyperfine states without significantly populating the excited state, with an effective Hamiltonian given by

$$\begin{aligned}\frac{H_{\text{eff}}}{\hbar} = & \frac{|g_A|^2}{\Delta}|A\rangle\langle A| + \frac{|g_B|^2}{\Delta}|B\rangle\langle B| \\ & + \left(\frac{g_A g_B^*}{\Delta}e^{i[(k_A-k_B)x+(\phi_A-\phi_B)]}|B\rangle\langle A| + \frac{g_B g_A^*}{\Delta}e^{i[(k_B-k_A)x+(\phi_B-\phi_A)]}|A\rangle\langle B|\right).\end{aligned} \tag{2.1}$$

Here, the lasers i have single-photon Rabi frequencies g_i, wavevectors k_i, and phases ϕ_i, and their frequencies are set such that $\omega_A - \omega_B = \omega_{HF}$, and $\hbar\omega_A - E_e \equiv \hbar\Delta$. The derivation of this result is presented in Appendix A. When dealing with the coherent operations between hyperfine states, we thus typically directly write down the Hamiltonian for a two-level system interacting with a single radiation field of frequency $\omega_A - \omega_B$, wavevector $\Delta k = k_A - k_B$, phase $\phi_A - \phi_B$, and Rabi frequency $\frac{g_A g_B^*}{\Delta}$.

Importantly, the two-photon Rabi frequency $\Omega \equiv \frac{g_A g_B^*}{\Delta}$ scales linearly with laser intensity I (assuming that the laser power is evenly distributed between the two frequencies), since each single-photon Rabi frequency g_i is proportional to the

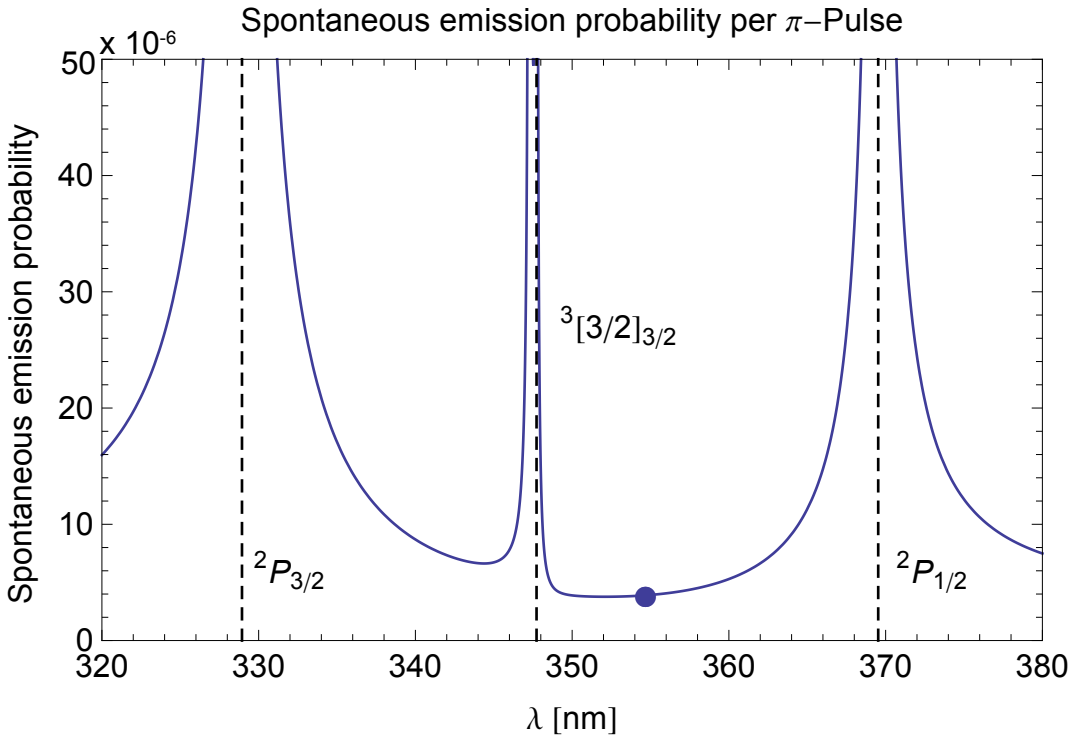

Figure 2.3: Plot of the probability of a spontaneous emission event during a resonant π pulse between the clock states, as a function of wavelength. In addition to the P states, there is a bracket state (discussed in the next section) theoretically predicted to lie between them. The marked point at 355 nm corresponds to the wavelength of a frequency-tripled vanadate laser, which is commercially available at high power; we see here that near this wavelength, the spontaneous emission rate is less than 10^{-5} during a π pulse.

electric field, and inversely linearly with the detuning from the excited state: $\Omega \sim I/\Delta$. By contrast, we found that the population in the excited state for $\Delta \gg g, \gamma$ is

$$|a_e|^2 = \left| \frac{g_A a_A + g_B a_B}{\Delta} \right|^2 \tag{2.2}$$

(see the appendix), so the probability of off-resonantly populating the excited state scales like I/Δ^2. Spontaneous emission from the off-resonantly populated excited state could therefore optically pump the atom to a dark state; however, our experiments take place on durations that are orders of magnitude shorter than the timescale for this optical pumping process.

Since the probability of a spontaneous emission from the excited state scales with the probability of populating it, we can improve the ratio of coherent interaction strength (Ω) to spontaneous emission rate by choosing a larger detuning. The picture gets slightly more complicated when considering multiple excited states, but this argument is generally true in the wavelength regions we consider, tuned inside the fine structure splitting. (However, for a detuning far outside the fine structure splitting, the contributions to the two-photon Rabi frequency from each excited state destructively interfere, so that there is not a net gain in suppressing spontaneous emission.) To visualize this dependence, the metric we plot is the probability of a spontaneous emission event occurring during the time it takes to perform a π rotation with the Raman beatnote tuned to the hyperfine resonance, which is independent of the intensity and hence the absolute Rabi frequency. Figure 2.3 shows the dependence on wavelength of this quantity.

By fortunate coincidence, frequency-tripled Nb:YVO_4 lasers that produce several watts at 355 nm are readily available commercially, and this wavelength is near an optimum for suppressing both spontaneous emission errors and differential AC Stark shifts [49].

2.2.2 Considerations regarding unusual 'bracket' states in Yb^+

Unlike most of the commonly used ion species, Yb^+ has some unusual extra electron energy levels, such as the ones labeled $^2F_{7/2}$ and $^3[3/2]_{1/2}$ in Figure 2.4. Most trapped ion quantum information experiments (including ours) use singly-ionized atoms whose electron shell structure consists of a single outer electron and a set of closed electron shells. In lighter atoms, the energy required to 'break' a closed shell is so high that the outer electron will be torn off the atom at a lower energy than what is required to promote an inner electron to a higher shell. By contrast, the 4f electrons in the outermost closed shell in the Yb^+ ground state can be promoted at a relatively low energy cost, resulting in these unusual energy levels.

(While I will be discussing the various coupling schemes and angular momentum states as though they exactly describe the behavior of the atom, in reality these are only approximate descriptions of the true eigenstates of the atom, especially for the complicated 69-electron configurations in Yb^+. For example, the $^3[3/2]_{1/2}$ state that I will discuss in some detail is actually a state that looks like a mixture of 77% of a $^3[3/2]_{1/2}$ configuration, 13% of a $^3[1/2]$ state, and 10% of some other set of eigenstates of J_c, K, and J, as defined below.)

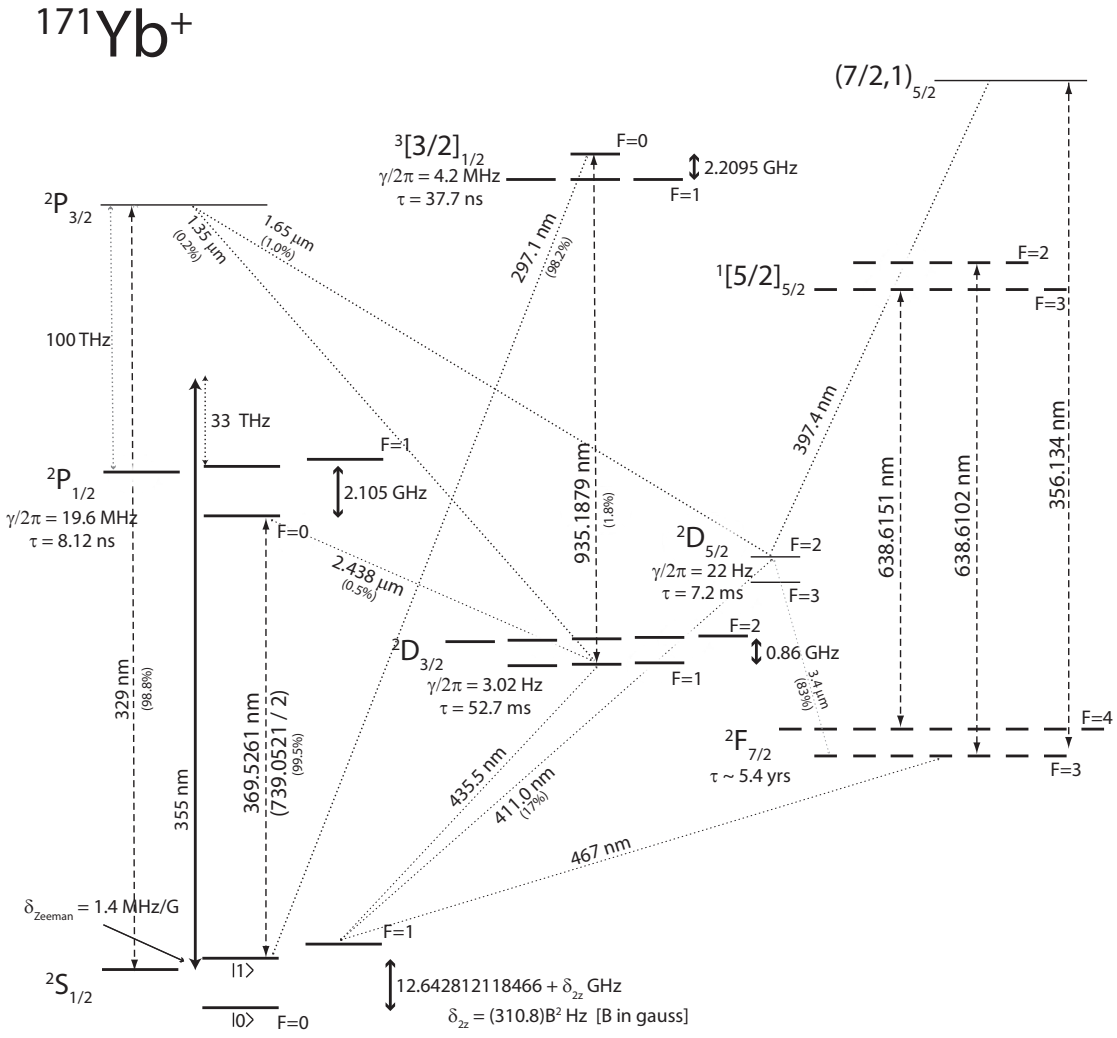

Figure 2.4: Diagram of the electronic energy levels of Yb^+ that are relevant for our experiments. The electronic states, wavelengths, lifetimes, and branching ratios are all indicated where known. For example, the transition between the $^2S_{1/2}$ and $^2P_{1/2}$ states occurs at 369.5261 nm; the lifetime of the $^2P_{1/2}$ state is 8.12 ns, and it decays to $^2S_{1/2}$ 99.5% of the time. Historically, the F state has been repumped on the 638 nm transition to $^1[5/2]_{5/2}$; however, we have now moved to using the 355 nm Raman laser for this task.

The states $^2S_{1/2}$, $^2P_{1/2}$, $^2P_{3/2}$, and $^2D_{3/2}$ all use the conventional LS coupling scheme. For LS coupling to hold, we require that L, the total orbital angular momentum of the outer electron(s), and S, the total spin of the electron(s), be good quantum numbers for the atom, meaning that the operators L^2 and S^2 approximately commute with the Hamiltonian of the atom, which is generally true for an atom with some number of closed shells and only one unpaired outer electron. The term symbols are then written as $^{2S+1}L_J$, where $J = L + S$ is the total angular momentum and L is conventionally notated with a letter. For these states, the electron configuration (of the outer shells) is simply given by $4f^{14}6s$, $4f^{14}6p$, or $4f^{14}5d$.

For the more exotic electronic states, different coupling schemes must be used to obtain the total angular momentum of the electrons. The core electrons now carry both spin and orbital angular momentum, so the total angular momentum J will result from coupling multiple angular momenta together in various ways. In the coupling schemes we will use, we assume that s_c and s_o (the total spin of the core and outer electrons, respectively) and l_c and l_o (the orbital angular momentum of the core and outer electrons) are all good quantum numbers. The total angular momentum J then results from coupling s_c, s_o, l_c, and l_o in various orders. In states where LS coupling holds, the total angular momentum of the electrons is obtained by coupling the total orbital angular momentum

$$L = l_c + l_o \tag{2.3}$$

to the total spin

$$S = s_c + s_o, \tag{2.4}$$

and finally coupling L to S as above,

$$J = L + S. \tag{2.5}$$

These relations are familiar from states like $^2S_{1/2}$, though they are simplified when the core electrons are in closed shells and carry no net angular momentum ($s_c = l_c = 0$).

In order to figure out what these quantum numbers are for a given level, at least for the states that use more unusual coupling schemes, it is usually necessary to dig into the electron configuration. For example, the electron configuration of the $^2F_{7/2}$ state is

$$4f^{13}(^2F)\ 6s^2. \tag{2.6}$$

This tells us that the core, consisting of 13 electrons in the $4f$ shell, has total spin $s_c = 1/2$ and orbital angular momentum $l_c = 3$, as indicated by the (^2F); the outer electrons consist of a closed $6s$ shell, which has $s_o = l_o = 0$. The F state is in fact another LS coupled state, and is unusual only insofar as an electron has been promoted from the $4f$ shell and the angular momenta arise from the core electrons rather than the outer electron(s).

The other levels that we commonly run into have a different set of good quan-

tum numbers J_c, K, and J, defined as

$$J_c = l_c + s_c, \tag{2.7}$$

$$K = J_c + l_o, \tag{2.8}$$

$$J = K + s_o. \tag{2.9}$$

In other words, the angular momenta of the core are coupled together first, after which the orbital angular momentum of the outer electrons is coupled in, and then the spin of the outer electrons. The term symbol in this coupling scheme is written as $^{2s_o+1}[K]_J$; based on this notation, we often informally refer to such states as bracket states.

We can again infer s_c, s_o, l_c, and l_o from the electron configuration: e.g., the configuration for the $^3[3/2]_{1/2}$ state is

$$4f^{13}(^2F_{7/2})\ 5d6s(^3D). \tag{2.10}$$

Here we see that the 13 electrons in the $4f$ shell have spin $s_c = 1/2$ and $l_c = 3$ and $J_c = 7/2 = l_c + s_c$, all inferred from the $(^2F_{7/2})$; the outer electrons (one in $5d$ and one in $6s$) together have spin $s_o = 1$ and $l_o = 2$, indicated by the (^3D). We could have ascertained $s_o = 1$ and $K = 3/2 = J_c + l_o$ just from the term symbol; however, picking out the values for s_c, l_c, and l_o allows us to make some determinations about which LS-type states have dipole-allowed transitions to and from the bracket state.

While some nasty math can be done to rewrite a state from the J_c, K, J eigenbasis in terms of states in the L, S, J eigenbasis, the math itself does not necessarily lend considerable insight into the nature of the bracket state. It is more helpful to keep in mind the following two rules of thumb: (A) any state of a given total angular momentum J will be a combination only of states with the same J, and (B) the possible values of L and S are constrained by the four base quantum numbers s_c, l_c, s_o, and l_o. For example, the ${}^3[3/2]_{1/2}$ bracket state can be written as a superposition of

$$\left|{}^3[3/2]_{1/2}\right\rangle = \frac{4}{\sqrt{21}}\left|{}^2P_{1/2}\right\rangle + \frac{1}{3}\sqrt{\frac{6}{7}}\left|{}^4P_{1/2}\right\rangle + \frac{1}{\sqrt{7}}\left|{}^4D_{1/2}\right\rangle, \tag{2.11}$$

and while we could not *a priori* guess these coefficients without resorting to combining lots and lots of Clebsch-Gordan coefficients, it is nevertheless clear why these are the only constituent LS-type states. Namely, we had $l_c = 3$ and $l_o = 2$, so the allowed values of $L = l_c + l_o$ are 1, 2, 3, 4, or 5, whereas we had $s_c = 1/2$ and $s_o = 1$, so $S = s_c + s_o$ can be $1/2$ or $3/2$. But in order to have $J = L + S = 1/2$, we are further restricted to $L = 1$ and $S = 1/2$ (i.e., the ${}^2P_{1/2}$ state), $L = 1$ and $S = 3/2$ (the ${}^4P_{1/2}$ state), or $L = 2$ and $S = 3/2$ (the ${}^4D_{1/2}$ state). In this case, the ${}^2P_{1/2}$ character makes this state a reasonable choice for repumping the ${}^2D_{3/2}$ state back down to the ${}^2S_{1/2}$ state, because transitions from ${}^2D_{3/2} \leftrightarrow^2 P_{1/2}$ and ${}^2P_{1/2} \leftrightarrow^2 S_{1/2}$ are both dipole-allowed.

There is another coupling scheme whose term symbol is written in a similar format to the one discussed above, ${}^{2s_o+1}[K]_J$, but where the quantum numbers are

coupled in a different order, given by $L = l_c + l_o$, $K = L + s_c$, $J = K + s_o$. In the case of our friend the $^3[3/2]_{1/2}$ state, we can see that the core electrons have a defined total angular momentum J_c, which was given in the subscript to the $(^2F_{7/2})$ in the electron configuration, clueing us in that the J_c, K, J scheme above is the appropriate one. In fact, all known states in Yb^+ that use this square bracket notation for the term symbol (at least, those listed in the NIST atomic levels database) use the J_c, K, J scheme.

For completeness, I will mention a fourth and final coupling scheme, where the good quantum numbers are $J_c = l_c + s_c$, $J_o = l_o + s_o$, and $J = J_c + J_o$. The term symbol for this scheme is $(J_c, J_o)_J$. For example, the 355 nm laser frequency is within a few THz of a transition from the $^2F_{7/2}$ state to the state $(7/2, 1)_{5/2}$. We can analyze the electron configuration of this state:

$$4f^{13}(^2F_{7/2})\ 6s6p(^3P_1), \tag{2.12}$$

telling us that $s_c = 1/2$ and $l_c = 3$, which are added to form $J_c = 7/2 = l_c + s_c$, and that $s_o = 1$ and $l_o = 1$, which are added to form $J_o = 1 = l_o + s_o$, and the term symbol tells us $J = 5/2$. This state is probably relevant to some of the cases that cause the ions to go completely 'dark' (in this context, meaning that they do not respond to light at any of the 369 nm transitions). There are several possible explanations for an ion not responding to resonant light: $^{171}Yb^+$ could be stuck in the long-lived F state; it could have become doubly ionized; a collision could have formed an ytterbium hydride (YbH^+) molecule; or it could be a different isotope,

e.g. $^{172}Yb^+$ or $^{174}Yb^+$. We observe that when the dark ions are singly charged, they can be brought back with the 355 nm light, except on rare occasions when a dark ion is captured during loading; thus, though we may occasionally load a different isotope, we don't seem to have any instances of ions being replaced with different isotopes from charge exchange.

We can see that excitation from the F state to the $(7/2, 1)_{5/2}$ state is a plausible pathway explaining why exposing 'dark,' singly-charged ions to 355 nm light brings them back to the S state. A similar analysis to the one above tells us this $(7/2, 1)_{5/2}$ state should have some $^2D_{5/2}$ character, which makes it plausible to drive a transition from $^2F_{7/2}$ to $(7/2, 1)_{5/2}$ and decay from there to $^2S_{1/2}$. Another possibility when 355 nm light resuscitates a dark ion is that it is dissociating the YbH^+ molecule. We have not performed a literature search to determine whether dissociation lines are known to exist near this wavelength, and it is unclear what fraction of dark singly-charged ions are molecular hydride and what fraction are atoms in the F state, so we do not know with certainty if either or both of these mechanisms explains our observations. However, we have good evidence that dark ions can sometimes be repumped with the 638 nm laser, indicating that we do sometimes populate the F state, so now that we no longer use the 638 nm laser and still see recovery of all our singly-charged dark ions, it is likely that the 355 nm light is at least repumping from the F state.

Incidentally, the 355 nm laser's useful side effect of seemingly repumping the F state to the ground state is probably not the only unexpected pathway for that laser to interact with the atom, and there is some evidence for other, more nefarious

side effects.

One side effect is that 355 nm light seems to not only effectively repump from the F state, but also to produce the F state more often than happens when the ion is in the dark. There is a somewhat plausible mechanism for this to occur, involving off-resonant excitation to the bracket state $^3[3/2]_{3/2}$ at roughly 348 nm above the S state, for which the 355 nm light is red detuned by ∼18 THz. This state has a large component of $^2P_{3/2}$ character, so the 355 nm light could conceivably couple to it (albeit at a very slow rate due to the large detuning), and it could plausibly decay to the $^2D_{5/2}$ state, which is known to decay to the $^2F_{7/2}$ state [50].

The other effect, more devastating to the experiments, is the seeming tendency of the 355 nm light to doubly ionize the atom. This effect is inferred from observations that an ion will sometimes go dark and simultaneously distort the chain, displacing the bright ions further from it than when it was bright. We even see that when the chain is on the verge of buckling into a zigzag configuration, such a dark ion can cause the zigzag transition to occur. Furthermore, when the trap frequency is lowered, the dark ion is usually kicked out of the trap entirely; this is also consistent with the ion being doubly charged, since the stability of the trap depends on the charge-to-mass ratio of the ion, so a trap optimized for singly-ionized Yb would be expected to be less stable for doubly charged Yb. When these dark ions are present, the only way to recover is to remove them from the trap entirely and reload the ion chain.

The most likely mechanism for this occurrence is photoionization due to the high intensity of the 355 nm light. While the second ionization energy is quite high,

it turns out to be only ∼6.04 eV above the $(7/2,1)_{5/2}$ state discussed above. The 355 nm photons have an energy of 3.5 eV, so once the ion is in the $^2F_{7/2}$ state, ionization could be achieved by absorption of three 355 nm photons, and would be resonantly enhanced to some degree by the presence of the $(7/2,1)_{5/2}$ state.

2.3 Coherent operations

The coherent operations that we perform on our cooled, spin-polarized, detectable ions are some of the most important aspects to understand about the physics underlying our experiment. Thus, for completeness and to ensure the reader is familiar with the notation used, I will discuss these operations from a fairly low level. The first part of the discussion follows a similar approach to that in Wineland et al. [51], which is an excellent reference on many of the fundamentals of manipulating trapped ions.

The Hamiltonian for a two-level atom in a harmonic potential interacting with a laser field may be written as [51]

$$H = \frac{\Omega}{2} |\uparrow\rangle\langle\downarrow| \exp\left(i\left[\eta\left(ae^{-i\omega_{tr}t} + a^\dagger e^{i\omega_{tr}t}\right) - \delta t + \phi\right]\right) + h.c. \tag{2.13}$$

Here, $h = 1$, Ω is the Rabi frequency, a and $a^\dagger$ are the lowering and raising operators of the harmonic oscillator with frequency ω_{tr}, $\eta = \Delta k x_0$ is the Lamb-Dicke parameter (where $x_0 \equiv \sqrt{\hbar/2m\omega_{tr}}$ is the characteristic length scale of the harmonic oscillator ground state), $\delta = \omega_{\mathrm{HF}} - \omega_L$ is the detuning of the laser frequency ω_L from the atomic transition frequency ω_{HF}, ϕ is the phase of the laser field, and h.c. de-

notes the Hermitian conjugate. Additionally, the interaction Hamiltonian has been written in a rotating frame with respect to the bare atomic and harmonic oscillator Hamiltonians.

(As mentioned above, we will be using stimulated Raman transitions rather than driving the 12.6 GHz transition directly, and so the laser parameters that enter are those of a pair of laser beams: ω_L is the difference frequency of the two lasers, ϕ is the difference of their optical phases, i.e. the phase of the beatnote, and Δk the difference wavevector. However, the formalism would be identical for a single laser driving a direct transition.)

Here I will point out the phase convention that we use for all of our pulses and Hamiltonian terms. We will be applying multiple frequencies for various tasks, as discussed in more detail below, and it is important to have a consistent definition. For us, this means we set all phases relative to the starting time of the initial Raman pulse in the experiment, which we take to be $t = 0$. Hence, if we set $\phi = 0$ for one frequency and $\phi = \pi$ for a different frequency, this means that the two frequency components of the laser fields have a relative phase of π *at* $t = 0$, i.e. at the start of the first pulse. This sets our convention for the phases of the Pauli matrices σ_x and σ_y: for example, if our first coherent operation in the experiment is taken to be a rotation about σ_x (e.g. to prepare a state with all spins along σ_y), then all other σ_x and σ_y operations are defined relative to this initial rotation. We therefore require the phases to be consistent throughout any single experiment, but are not sensitive to the fact that the optical phase at the ion *at the start of the experiment* may differ from experiment to experiment.

We can make the Lamb-Dicke approximation if the ion's motional wavepacket is confined to a region much smaller than the wavelength, or in this case the inverse wavevector, of the light, i.e., if $\eta(2\bar{n}+1) << 1$. In this limit, the $e^{i\eta(a+a^\dagger)}$ term can be approximated as $1 + i\eta(a + a^\dagger)$ and the above Hamiltonian can be written as

$$H \approx \frac{\Omega}{2} |\uparrow\rangle\langle\downarrow| \left(1 + i\eta \left(ae^{-i\omega_{tr}t} + a^\dagger e^{i\omega_{tr}t}\right)\right) e^{i[-\delta t+\phi]} + h.c. \tag{2.14}$$

If $\delta \approx 0$ (which requires $\delta \ll \omega_{tr}, \Omega$), then the phonon terms oscillating at $\pm\omega_{tr}$ can be neglected, leaving us with:

$$H_{carr} = \frac{\Omega}{2} \left(|\uparrow\rangle\langle\downarrow| e^{i\phi} + |\downarrow\rangle\langle\uparrow| e^{-i\phi}\right). \tag{2.15}$$

This is called a carrier transition, and allows us to drive pure spin transitions without affecting the motional state. We drive this carrier transition with an appropriate phase any time we wish to perform a coherent rotation of the spins, e.g. for initialization or for reading out in the σ_x or σ_y basis, and we additionally use the carrier to generate an effective magnetic field term in our simulated Hamiltonian: notice that the Hamiltonian above is simply a σ_x or σ_y operator, and hence maps exactly to a magnetic field term $B\sigma_\phi$.

If instead the detuning is set to $\delta \approx \pm\omega_{tr}$, we will keep only the term with an $a^\dagger |\uparrow\rangle\langle\downarrow|$ or an $a |\uparrow\rangle\langle\downarrow|$, respectively. The resulting interactions can be written as

$$H_{\text{rsb}} = \frac{i\eta\Omega}{2} |\uparrow\rangle\langle\downarrow| ae^{i\phi} - \frac{i\eta\Omega}{2} |\downarrow\rangle\langle\uparrow| a^\dagger e^{-i\phi}, \tag{2.16}$$

$$H_{\text{bsb}} = \frac{i\eta\Omega}{2} \left|\uparrow\right\rangle\!\left\langle\downarrow\right| a^\dagger e^{i\phi} - \frac{i\eta\Omega}{2} \left|\downarrow\right\rangle\!\left\langle\uparrow\right| a e^{-i\phi}. \tag{2.17}$$

These are referred to as red sideband and blue sideband interactions, respectively, where the nomenclature is usually to interpret the process involving a lower-frequency beatnote as red. As mentioned earlier, the red sideband interaction H_{rsb} is formally equivalent to the Jaynes-Cummings Hamiltonian [35], while the blue sideband interaction is sometimes referred to by analogy as an anti-Jaynes-Cummings Hamiltonian.

The red sideband operation, in conjunction with the optical pumping discussed earlier, can be used to cool the motion of the atom below the Doppler temperature. Sideband cooling involves many alternating pulses that optically pump the spin to $\left|\downarrow\right\rangle_z$ before driving the transition $\left|\downarrow\right\rangle_z \otimes \left|n\right\rangle \leftrightarrow \left|\uparrow\right\rangle_z \otimes \left|n-1\right\rangle$. In this manner, vibrational excitations are removed one quantum at a time until the ion reaches the lowest motional state $\left|n=0\right\rangle$, at which point the red sideband will have no effect and the ion will remain in the $\left|\downarrow\right\rangle_z \otimes \left|n=0\right\rangle$ state.

2.3.1 Spin-motion coupling and MS Hamiltonian

The simultaneous application of two beat frequencies, symmetrically detuned from the carrier (and typically tuned red of the red motional sidebands and blue of the blue motional sidebands), gives rise to the 'Mølmer-Sørensen' [52] Hamiltonian consisting of an oscillatory force whose direction is dependent on the spin state of the ion,

$$H_{MS} = \Omega \cos(\mu t + \phi_m) \left[\sigma_{\phi_s - \pi/2} + \eta\sigma_{\phi_s} \left(a e^{-i\omega_t t} + a^\dagger e^{i\omega_t t}\right)\right]. \tag{2.18}$$

Here, $\sigma_\phi \equiv \cos\phi\sigma_x + \sin\phi\sigma_y$. To obtain this Hamiltonian, we have applied frequencies $\omega_r = \omega_{HF} - \mu$ and $\omega_b = \omega_{HF} + \mu$, with associated beatnote phases ϕ_r and ϕ_b, respectively, which can be combined into the spin and motional phases ϕ_s and ϕ_m used in the Hamiltonian,

$$\phi_s = \frac{\phi_r + \phi_b + \pi}{2}, \tag{2.19}$$

$$\phi_m = \frac{\phi_r - \phi_b}{2}. \tag{2.20}$$

The derivation of this Hamiltonian from the fundamental laser-atom interaction Hamiltonian in 2.13 is shown in detail in Appendix B. We have assumed here that the experiment is configured in the 'phase-sensitive' geometry used in our current setup; it is possible to instead use a configuration where ϕ_s is sensitive to the difference of ϕ_r and ϕ_b rather than their sum. This could be advantageous in future experiments, since the interferometric optical phase that is present in both ϕ_r and ϕ_b would then cancel, such that optical phase drifts will no longer affect the spin phase [53]. (However, as discussed in the next chapter, this is not yet a limitation for us.)

In the experiments discussed in this thesis, we set the red sideband and blue sideband phases to $\phi_r = 0$, $\phi_b = \pi$, for which the spin phase becomes $\phi_s = \pi$ and the motional phase $\phi_m = -\pi/2$. As a result, $\sigma^{\phi_s} = -\sigma^x$ and $\sigma^{\phi_s - \pi/2} = \sigma^y$, and we can rewrite the Hamiltonian above as

$$H_{MS} = \Omega \sin(\mu t) \left[\sigma^y - \eta\sigma^x \left(a e^{-i\omega_{tr}t} + a^\dagger e^{i\omega_{tr}t}\right)\right]. \tag{2.21}$$

Usually we drop the off-resonant carrier term (the $\sin(\mu t)\sigma^y$), which is valid for

$\Omega \ll \mu$, to approximate the Hamiltonian as

$$H_{MS} = -\eta\Omega \sin(\mu t)\sigma^x \left(ae^{-i\omega_{tr}t} + a^\dagger e^{i\omega_{tr}t}\right). \tag{2.22}$$

This is the form I will use to show how we derive our usual formula for the spin-spin interactions. If the off-resonant carrier term may be neglected, the counter-rotating phonon terms that have factors of $e^{\pm i(\mu+\omega_{tr})t}$ could also be dropped, but since their effect is negligible it doesn't hurt anything to include them.

2.3.2 Spin-spin interactions arising from slow MS

The above Mølmer-Sørensen Hamiltonian considers only a single ion and a single mode of motion, but in general we have multiple ions with multiple modes of motion. The generalization to multiple ions and modes is simply

$$H_{MS} = -\sum_{i,m} \eta_{i,m}\Omega_i \sin(\mu t)\sigma_i^x \left(a_m e^{-i\omega_m t} + a_m^\dagger e^{i\omega_m t}\right), \tag{2.23}$$

where i indexes the ions and m the motional modes.

To show that the evolution under this Hamiltonian is roughly equivalent to that of a pure spin-spin interaction under certain conditions, we use the Magnus expansion for the evolution operator,

$$U(t) = T\left[e^{-i\int_0^t dt_1 H(t_1)}\right] = e^{\bar{\Omega}_1+\bar{\Omega}_2+\bar{\Omega}_3+\cdots}, \tag{2.24}$$

where T is the time-ordering operator and the first few orders of the expansion are given by

$$\bar{\Omega}_1 = -i \int_0^t dt_1 H(t_1), \tag{2.25}$$

$$\bar{\Omega}_2 = -\frac{1}{2!} \int_0^t dt_1 \int_0^{t_1} dt_2 \left[H(t_1), H(t_2)\right], \tag{2.26}$$

$$\bar{\Omega}_3 = \frac{i}{3!} \int_0^t dt_1 \int_0^{t_1} dt_2 \int_0^{t_2} dt_3 \left([H(t_1), [H(t_2), H(t_3)]] + [H(t_3), [H(t_2), H(t_1)]]\right). \tag{2.27}$$

When we go through the full derivation, shown in Appendix B, we find that the evolution operator is approximately given by

$$U \approx \exp\left(- \sum_{i,j,m} \sigma_i^x \sigma_j^x \frac{i \eta_{i,m} \eta_{j,m} \Omega_i \Omega_j}{2(\mu^2 - \omega_m^2)} \omega_m t \right), \tag{2.28}$$

where the only contribution considered comes from the second-order term $\bar{\Omega}_2$. The key points in the derivation are that the evolution operators will contain terms like $\sigma_x^i a_m$ and $\sigma_x^i a_m^\dagger$ coupling spin to motion from the first order, which can be neglected under the approximation $\eta_{i,m}\Omega_i \ll |\mu - \omega_m|$, and $\sigma_x^i \sigma_x^j$ spin-spin interaction terms from the second order, which arise from commuting $\sigma_x^i a_m$ with $\sigma_x^j a_m^\dagger$. With this Hamiltonian, there are no further commutators and the evolution operator in the appendix is exact.

The operator U is exactly the evolution operator of a set of static spin-spin interactions,

$$H_{\text{eff}} = \sum_{i,j} J_{i,j} \sigma_i^x \sigma_j^x, \tag{2.29}$$

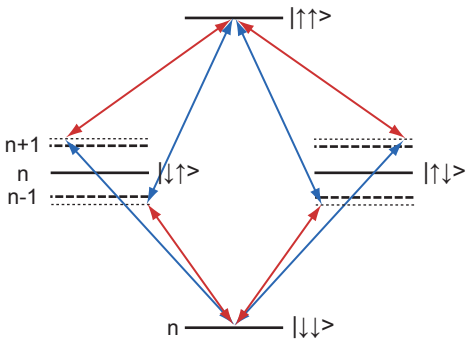

Figure 2.5: Two-body level diagram for MS interaction in a system of two ions, each with spin-1/2. There are four possible pathways where a red sideband and a blue sideband can resonantly couple $|\downarrow\downarrow\rangle$ to $|\uparrow\uparrow\rangle$ (Not drawn: there are similarly four pathways coupling $|\downarrow\uparrow\rangle$ to $|\uparrow\downarrow\rangle$.)

whose interaction strengths are given by

$$J_{i,j} = \sum_m \frac{b_{i,m} b_{j,m} \Omega_i \Omega_j \Omega_R}{2(\mu^2 - \omega_m^2)}, \tag{2.30}$$

where we have used $\eta_{i,m} = \Delta k \sqrt{\hbar/(2M\omega_m)} b_{i,m}$ to rewrite the effective couplings in terms of the recoil frequency $\Omega_R = \frac{\hbar(\Delta k)^2}{2M}$ and the normal mode matrix b that transforms local displacements of each individual ion into normal mode coordinates. The full derivation is shown in the second section of Appendix B, and includes the many small terms we have dropped to approximate the evolution operator as this static effective Hamiltonian.

2.3.3 Brief note on frequency combs

I discussed earlier the advantages of using a laser near 355 nm for the Raman transitions. The commercial lasers we use for this application actually have an additional advantage: they are mode-locked lasers with pulse repetition rates of

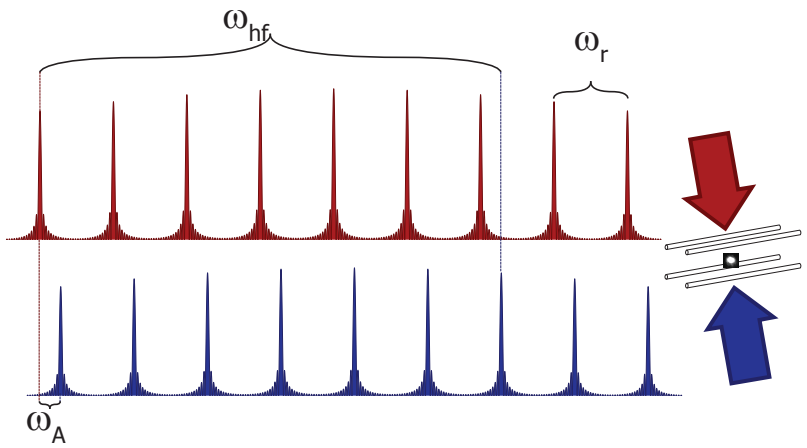

Figure 2.6: Sketch of two frequency combs, derived from the same laser with repetition rate ω_{rep} and offset from one another by a frequency ω_{offset}, such that the two combs combine to form a beat frequency at ω_{HF}.

80-120 MHz and pulse durations of about 10 ps. Hence, the pulse bandwidths are on the order of 100 GHz, meaning that the 12.6 GHz hyperfine splitting is readily spanned by this frequency comb. Hence, we can drive a Raman transition simply by splitting the laser beam and shifting one arm relative to the other with an acousto-optic modulator. As depicted in Figure 2.6, the condition for having two comb teeth on resonance with the hyperfine splitting is

$$\omega_{HF} = n\omega_{\text{rep}} \pm \omega_A, \tag{2.31}$$

where n is an integer, ω_{rep} the repetition rate, and ω_{offset} the relative shift from the modulators. Importantly, the laser itself can be left free-running in the sense that we do not need to stabilize either the repetition rate or the carrier-envelope phase (which is fortunate because we don't have the means to do either of these things). A shift in the carrier-envelope phase is equivalent to an offset in the absolute frequencies of

the comb teeth, and since we are using the laser for far-detuned Raman transitions, we are not sensitive to such shifts. The repetition rate affects the beat frequency, which does enter into the physics; however, since we only care about one particular beat frequency, we can stabilize the quantity $n\omega_{rep} + \omega_{\text{offset}}$ by using the modulator frequency, ω_{offset}, to compensate for changes in ω_{rep}, as will be discussed in the next chapter. For our purposes, we need not delve too far into the physics of using a pulsed laser, rather than continuous-wave lasers, to perform Raman transitions; there are, however, interesting subtleties relating to this technique, for which the interested reader is referred to [54, 55].

One detail that does matter is the selection of an appropriate repetition rate. As we saw, we want to be able to drive transitions off-resonantly. For this reason, we do not want the repetition rate to be a subharmonic of any of the transitions of interest, i.e. $n\omega_{\text{rep}} \neq \omega_{HF}$ (or $\omega_{HF} \pm \omega_{tr}$, etc), for any integer n. Furthermore, we also do not want these transitions to match any half-integer multiple of the repetition rate: $(n + 1/2)\omega_{\text{rep}} \neq \omega_{HF}$ for any n. The reason for this one is a bit more subtle; it turns out that under this condition, if we tried to drive (for example) a red sideband at $\omega_{HF} - \omega_{tr}$, we would then also have a beat frequency at $\omega_{HF} + \omega_{tr}$. This would cause multiple problems but most obviously would interfere with sideband cooling.

One final point which is worth noting about the physics of the Raman transitions is the presence of strong 4-photon differential AC Stark shifts. (Here, I refer to the more usual AC Stark shift caused by a single laser field as a two-photon Stark shift, because the shift results from absorption and emission of a pair of virtual photons; by a similar token, shifts resulting from the presence of both Raman laser fields

result from absorption and emission of two pairs of photons.) Because our Raman laser is at a wavelength where the lowest-order differential AC Stark shifts from the P states nearly cancel [49], the 2-photon light shift is almost negligible (typically a few hundred Hz from one arm of the two Raman beams, for our operating parameters). By contrast, the 4-photon differential shifts that (for our polarization setup) only occur in the presence of both beams can be many tens of kHz. These 4-photon shifts can be estimated as $\Omega^2/4\delta$, analogous to the usual formula for an AC Stark shift, where here Ω is the two-photon Rabi frequency for the Raman transition, and δ is the detuning of the Raman beatnote from the hyperfine splitting.

2.4 Definitions of common experimental protocols

Finally, because this chapter is intended to provide the background for understanding the next chapter on the apparatus, I define a few common terms that we frequently use in the lab referring to specific experimental protocols. The terms are mostly self-evident, and are included for completeness. These protocols are used for a variety of calibrations and initial set-up procedures that will be described in the next chapter.

2.4.1 Frequency scan

A laser or microwave pulse of fixed duration, amplitude, and frequency is applied to some initial state and its effect observed, resulting in one point on the frequency scan. The frequency of the pulse is incremented for each successive point.

(This is just to say that when I refer to a frequency scan I do not mean that the frequency is chirped during a single experiment.) Typically this is expected to result in a sinc^2 type Rabi lineshape.

2.4.2 Time scan/Rabi frequency measurement

The duration of a pulse of fixed frequency is incremented for each successive point on the scan. When the pulse is resonant with a transition between two energy levels, the populations will oscillate sinusoidally with duration and a function like $A\sin(2\pi\Omega t+\phi)+b$ can be fit to the resulting data set to obtain the Rabi frequency Ω.

2.4.3 Ramsey experiment

A pair of $\pi/2$ pulses are applied, separated by some amount of time. As pointed out by Norman Ramsey, this allows the frequency of a reference (e.g. the beat frequency of the Raman lasers) to be compared to that of an atomic transition (e.g. the hyperfine 'clock' transition in our ion) more precisely by extending the interrogation time without simultaneously making the measurement more susceptible to amplitude noise in the applied radiation. The picture that we have in mind here is of the first $\pi/2$ pulse preparing a superposition of the two relevant levels, e.g. $(|\downarrow\rangle_z+|\uparrow\rangle_z)/\sqrt{2}$. During the waiting time in the dark, the relative phase of the superposition evolves at the frequency of the hyperfine transition, and this phase is compared to that of the reference frequency by the second $\pi/2$ rotation. It is

common to vary the frequency of the applied $\pi/2$ pulses with a fixed waiting time, which allows a narrower resolution of the resonance, but for many of our calibrations we instead fix the frequency and vary the delay time. This turns out to have the effect that if the radiation is detuned by an amount δ from the atomic transition, the populations at the end of the Ramsey experiment will oscillate with a frequency δ.

Chapter 3: Experimental setup

This chapter discusses details of the experimental implementation of the simulations discussed in later chapters. Because most experimental considerations in the trapping and manipulation of $^{171}Yb^{+}$ have been documented in other group theses, and our apparatus in particular is well documented in Rajibul Islam's [33] and Simcha Korenblit's [34] theses, this chapter is not an exceedingly thorough record of the apparatus. I will first give a high-level overview, which serves to highlight some of the requirements that are unique or unusually stringent compared to other trapped ion quantum information experiments. I then document the apparatus in a piecemeal fashion, focusing on the upgrades that have occurred since the last thesis and the setup procedures that I am personally familiar with, and devote the rest of the chapter to the suite of diagnostics and calibration procedures that have been useful to us. A reader who is uninterested in delving into nuts-and-bolts discussions of details like how we set up the Raman laser beam path or distinguish between different sources of decoherence may wish to skip all but the overview.

3.1 Overview and unique requirements

The $^{171}Yb^{+}$ ions are held in a linear Paul trap - in our case, a hand-assembled three-layer trap, with RF voltage on the middle electrode providing the radial confinement and DC voltages on the segmented outer electrodes providing the axial confinement. Figure 3.1 sketches the trap electrodes. The geometry is such that the RF field has a node along a line at the center of the trap, and the trap voltages are configured such that the ions self-assemble into a chain along this so-called RF null. The electrodes are mounted inside an ultra-high vacuum (UHV) chamber. Despite the low pressure, which we estimate to be of order 10^{-11} Torr or less, we believe the background pressure to currently be a major limitation in holding on to long chains of ions.

The DC voltages for the trap electrodes are drawn from a computer-controlled power supply, and RF voltage at a frequency of 38 MHz is applied via a quarter-wave helical resonator attached to a feedthrough on the vacuum chamber. We (as well as other ion trapping groups) find empirically that in order to coax 2 or more ions to crystallize, i.e. localize in an ordered pattern along the RF null, it is necessary to lower both the radial confinement (RF voltage) as well as the axial confinement (DC voltages), a procedure we refer to as recrystallizing. This results in thermal changes to the helical resonator, or 'RF can', which form the other half of the current limitation to ion number: every time there is a collision with a background gas particle, the RF must be lowered to recapture the ions (i.e., to cool them to a localized phase before they are heated out of the trap), and once it is raised the

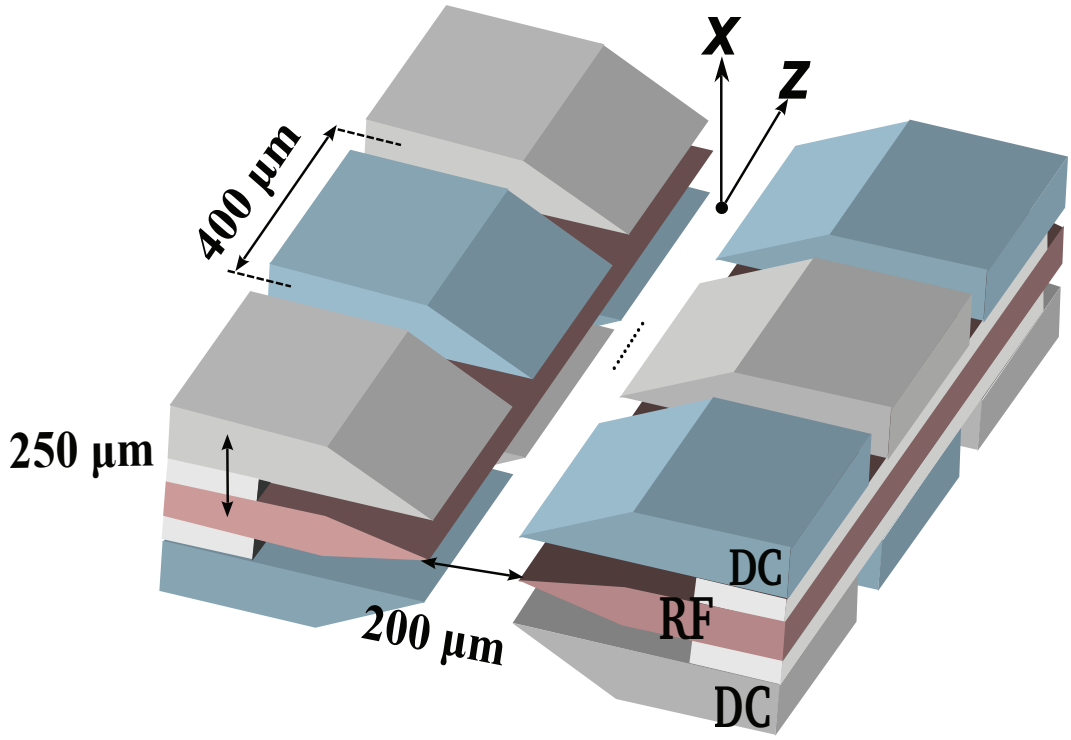

Figure 3.1: Sketch depicting the electrodes used to trap our ions. RF voltage is carried on the middle electrodes, highlighted in red, and the electrodes highlighted in blue carry DC voltages, while gray electrodes are held at ground. In this sketch, $+\hat{x}$ points in the direction of the imaging system, and small dots represent the ions, whose spacing is not to scale.

resonator takes several minutes to settle to a steady state.

The ions are cooled, initialized, and measured using 369.5 nm light resonant with the $^2S_{1/2}$-$^2P_{1/2}$ transition, along with 935 nm light that repumps population from the low-lying $^2D_{3/2}$ state. One crucial feature of our apparatus is the presence of beams detuned by roughly 400 and 800 MHz red of the $^2S_{1/2}$-$^2P_{1/2}$ transition, which irradiate a larger part of the trapping volume than the near-resonant 369 nm beams and, in the case of the 800 MHz detuned beam, with quite a bit more power. There is some evidence that the presence of these beams is important not only for crystallizing large numbers of ions, but even for keeping a moderate number of ions localized.

During the measurement process, we collect the state-dependent fluorescence with a high-numerical-aperture objective (NA = 0.23), discussed in more detail below, and focus it onto either a photomultiplier tube (PMT) for diagnostics or an intensified charge-coupled device (ICCD) camera for site-specific readout; this ability to image the entire spin configuration is critical for essentially all of the results later presented in this thesis.

We find that in case of a collision causing a long chain of ions to delocalize, it is necessary to immediately (within 1 second or so) turn on the Doppler cooling beams and begin lowering the trapping potentials, if we want to recapture all or most of the ions. This is because, despite the large (several eV) trap depths afforded by the Paul trap, once the ions are away from the RF null they can easily be heated out of the trap within a few seconds, due to driving from the RF field. (The mutual Coulomb interactions seem to also play a role in ejecting ions, since a single ion

can remain in the trap for hours, even if it is not localized at the RF null.) To automate the recapture process, roughly 10% of the light collected by the objective is siphoned off to a second PMT (the 'dropout PMT'). This signal is monitored during Doppler cooling, during which the ions consistently fluorescence at a certain rate regardless of what state they started in, and this allows the control program to pause data taking and switch to dropout recovery mode if the ions go dark for several experiments in a row.

To perform coherent operations, a microwave horn can be used to drive the hyperfine transitions at 12.6 GHz directly (which is sometimes useful for diagnostic purposes), but the vast majority of our experiments use a mode-locked 355 nm laser to perform stimulated Raman transitions. As discussed earlier, the bandwidth of the laser pulses offers a convenient way to bridge the 12.6 GHz hyperfine splitting without having to generate frequency shifts of more than 200 MHz, and the wavelength is near an optimum to suppress spontaneous emission errors. The stimulated Raman transitions are used to perform the carrier and sideband operations discussed in the previous chapter. This technique is used in many experiments utilizing $^{171}Yb^{+}$, but its importance is worth underscoring - with the long ion chains that we use, and the fact that we detune sidebands far from the motional modes to generate our interactions, we require a great deal of Raman laser power with good spontaneous emission properties to perform long coherent experiments. It is often easier to attain high optical power in the UV with mode-locked lasers, since frequency conversion (i.e. second and third harmonic generation) is usually required, and the efficiency of these processes depends on the instantaneous rather than the time-averaged power.

As we saw, the phase relationships among these various carrier and sideband operations, which correspond to effective magnetic fields and spin-spin interactions in the simulated Hamiltonian, or the basis in which the spins are prepared or measured, are crucial for orchestrating the desired simulation. In order to achieve this necessary phase control, we use an arbitrary waveform generator (AWG) to imprint the desired frequencies and phases onto the light with an acousto-optic modulator (AOM).

3.2 More detailed description of the apparatus

3.2.1 Trap and RF resonator

The trap electrodes are held in an ultra-high vacuum (UHV) chamber, to minimize unwanted interactions between the ultracold atoms and any stray background gases.

The application of appropriate RF and DC voltages to the electrodes sketched in Figure 3.1 leads to an effective pseudopotential that has the form of a 3-dimensional harmonic oscillator [51, 56]. When the aspect ratio of the trapping potential is set appropriately, the ions self-organize into a chain roughly at the RF null, where the time-varying electric fields cancel to zero.

The RF voltage is generated by applying roughly 250 mW at 38 MHz to a quarter-wave helical resonator, sometimes referred to simply as a can. This has the effect of increasing the voltage by a factor Q, where Q is the quality factor of the resonator. The loaded quality factor can be measured by monitoring the

reflected RF power as a function of frequency, using a directional coupler to pick off some of the reflection, and is given by $Q = \omega_{\text{center}}/\text{FWHM}$. Here, ω_{center} is the center frequency of the resonator, at which the reflected power is minimized, and FWHM is the full-width at half-maximum of the resonance, defined as the difference between the frequencies where the reflected power is half of its maximum value. This definition is chosen because our cans are nearly critically coupled, meaning that the reflection is nearly zero at the center of the resonance, so instead of comparing the reflected amplitude to zero we compare it to its value far away from the resonance. For these resonators, quality factors between 100 and 300 are typical.

As described above, the lowering of the RF potential to recapture delocalized atoms leads to changes in the secular trap frequency once the RF level is raised back to its normal operating point. This is probably due to thermal/mechanical changes in the resonator. Typically, the trap frequency changes by 1-5 kHz (out of 4.8 MHz) and (usually) settles back to its initial value within a few minutes. Our protocol for alleviating the effects of this change is to wait for a prescribed amount of time after lowering the RF to resume experiments. If the RF is lowered and raised back up immediately (e.g., because all the ions were recaptured right away), we wait 30 seconds for the system to re-equilibrate, and if it is left low for a few minutes (e.g., because we needed to reload one or more ions), we wait 2-3 minutes. Additionally, if we are experiencing frequent ion losses, we do not reload the trap more often than once every ten minutes.

We stabilize the frequency of the trap RF source to the point at which the reflection from the can is minimized, using a phase-sensitive Pound-Drever-Hall-like

technique (see figure). This has been helpful because the thermal changes in the can cause the center frequency to drift far enough to significantly impact the voltage delivered to the trap. This changing of the RF frequency contributes somewhat to the change in secular trap frequency, which scales like

$$\omega_{tr} \propto \frac{V_{RF}}{\Omega_{RF}}, \tag{3.1}$$

where V_{RF} is the amplitude of RF voltage applied to the trap and Ω_{RF} is its frequency. However, the change in secular frequency is too big to be fully explained by this - we see the RF frequency (at 38.8 MHz) change by roughly 1-2 kHz as it follows the can, which would result in changing the secular frequency by only a few hundred Hz out of 4.8 MHz. This indicates that the amplitude of the RF at the trap is also changing, since the changes we observe in the secular frequency are an order of magnitude larger than the frequency shift could explain. We hence speculate that the thermal effects in the can must change its coupling or quality factor (or both) in addition to changing its resonant frequency. In the near future, we plan to implement a capacitive pickoff monitoring the RF voltage at the trap, which will allow us to stabilize the amplitude directly and leave the RF frequency constant. This should stabilize the trap frequency much more effectively.

When a stray DC electric field displaces the ions from the RF null, they experience more micromotion, or driven motion at the frequency Ω_{RF} of the trap RF, than if they are perfectly aligned to the null. This is undesirable for a variety of reasons. Chief among them is the effect on the laser operations: due to the Doppler

effect, this motion will cause modulation of the frequency the atom 'sees' from a laser beam that has some wavevector component along the direction of the micromotion. Hence, less of the laser power is available at the desired laser frequency, and the atom perceives sidebands at $\pm\Omega_{RF}$ away from the actual laser frequency. In our current trap, we have never been able to fully compensate for micromotion while still aligning the principal axes in the direction we want them. This is evident when we lower the RF voltage, which leads to the ions dropping lower on the CCD image, indicating that the geometric imperfections are such that the ions are vertically displaced from the RF null. Fortunately, the geometry of the trap is such that a vertical displacement leads to micromotion in the vertical direction, which does not significantly affect the ions' interactions with the lasers that are more or less parallel to the table surface.

3.2.2 Resonant laser systems

The 369 nm light used for Doppler cooling, optical pumping, and readout is one of the workhorse systems in the apparatus. This laser system must deliver about 2.5 mW to the ions (split amongst various beams that may be frequency shifted with AOMs and EOMs), and its absolute frequency must be stable to roughly 1 MHz, since the atomic transition linewidth is about 20 MHz. As detailed below, this entails producing tens of mW of 369 nm light, which is attenuated significantly as it passes through AOMs, optical fibers, beamsplitters, and so on.

There are several possible solutions to these requirements. Right now, we

generate 739 nm light with a Ti:sapph laser (the Coherent MBR documented in Appendix C), which is stabilized to an absolute frequency reference using saturated absorption spectroscopy on the I_2 molecule, and frequency doubled with a commercial system (the Spectra Physics Wavetrain). We hope eventually to move to using diode lasers, which may prove to be a simpler and cheaper light source in the long run, since diodes that can be pulled to 369 nm have recently come on the market; however, it may be a few years before these systems reliably produce sufficient power for our needs. Another advantage of the system we use is the spectral purity: there is much less amplified spontaneous emission than is sometimes seen in diode lasers, and the cavity in the frequency doubler serves as a further frequency filter.

Roughly 50 mW of the 739 nm light is coupled into an optical fiber, sent through a fiber EOM from EOSpace to generate sidebands that are resonant with a transition in I_2, and piped to the iodine spectroscopy setup. The fiber EOM is driven with the output of an HP8672 frequency synthesizer A detailed description of such a setup can be found in Andrew Chew's undergraduate thesis [57]. The remainder of the light is sent through a polarization-maintaining single-mode optical fiber to the frequency doubler. As a result of the fiber coupling, the frequency doubler very rarely needs to be touched.

In the rare event that this cavity needs to be realigned, the manual provides a nice overview of the alignment procedure. Because the cavity geometry is very simple, it is generally not difficult to get light circulating once the waist of the input beam is mode-matched to the cavity. For coarse alignment, we usually look at the transmitted power on a photodiode as the cavity length is scanned, which will show

a signal of multiple peaks corresponding to multiple spatial modes of the cavity. This signal is used to optimize the alignment until most of the power is in the peak corresponding to the fundamental transverse mode (which is usually the rightmost peak on the oscilloscope trace) and the peaks corresponding to other transverse modes are suppressed to <10% of the height of the main peak. At this point, the signal should be good enough to stabilize the cavity, and final tweaks of the alignment can be done based on the output (doubled) power. Because the nonlinear LBO crystal is critically phase matched, meaning that the phase matching condition is met by tuning the angle of the crystal axis with respect to the polarization and wavevector of the cavity beam, it is usually necessary to iteratively walk the LBO angle in addition to the cavity mirrors to obtain the best doubling efficiency.

One trick that I have found for guessing whether there are further gains to be had by tweaking the alignment of the doubler cavity or input beam makes use of the setup locking the cavity length to be resonant with the input laser frequency. This simply involves briefly blocking the input beam while the doubler is locked and checking whether different lock points produce different output powers. The cavity is a triangular configuration with a prism forming one of the 'corners' (the other two of which are the mirrors that serve as the input and output couplers), and this prism is translated with a piezo to stabilize the length of the cavity. There are several positions within the throw of the piezo that match a resonance condition with the input wavelength, and the electronics are set up such that if the lock is lost, the piezo will be scanned to the next resonance. Thus, this trick depends on blocking the input beam for the right amount of time, allowing the electronics to

begin scanning when the signal is lost and 'catch' on the next lock point before the piezo returns to the beginning of its throw. If the cavity is well aligned, the output power should be insensitive to which lock point is chosen, and conversely if the output power is strongly dependent on the lock point, there are usually gains to be had with the alignment.

The 369 nm light emerging from the doubler is roughly 430 MHz red detuned from the $^2S_{1/2}, F = 1$ to $^2P_{1/2}, F = 0$ transition. AOMs are used to make up the frequency difference. The high AOM frequency is desirable because the resulting larger angular deflection makes it easier to separate 0th and 1st order beams, and ensures that any 0th order light making its way to the ions is far off resonant. Furthermore, we require a high-power, far-detuned cooling beam to deal with hot 'melted' ion chains, and this should be as far red of resonance as possible; using AOMs near 400 MHz allows us to generate a beam detuned by > 800 MHz. We use Brimrose QZF-420-40-370 AOMs unless otherwise noted. The AOMs are driven with an assortment of HP8640 and PTS-D310 or PTS-500 oscillators, each of which is amplified to a maximum RF power of 2 W.

A thick glass plate is used to pick off small portions of the 369 nm light for the Doppler cooling and optical pumping beam paths. The Doppler cooling light is sent through a resonant New Focus EOM at 7.37 GHz (half of 14.74 GHz, which is the sum of the hyperfine splittings in the $^2S_{1/2}$ and $^2P_{1/2}$ states), such that the second-order sideband from the EOM is 430 MHz red detuned from the $^2S_{1/2}, F = 0$ to $^2P_{1/2}, F = 1$ transition. This EOM is driven with a Vaunix Lab Brick signal generator, which is amplified to roughly 2 W, which is roughly the maximum RF

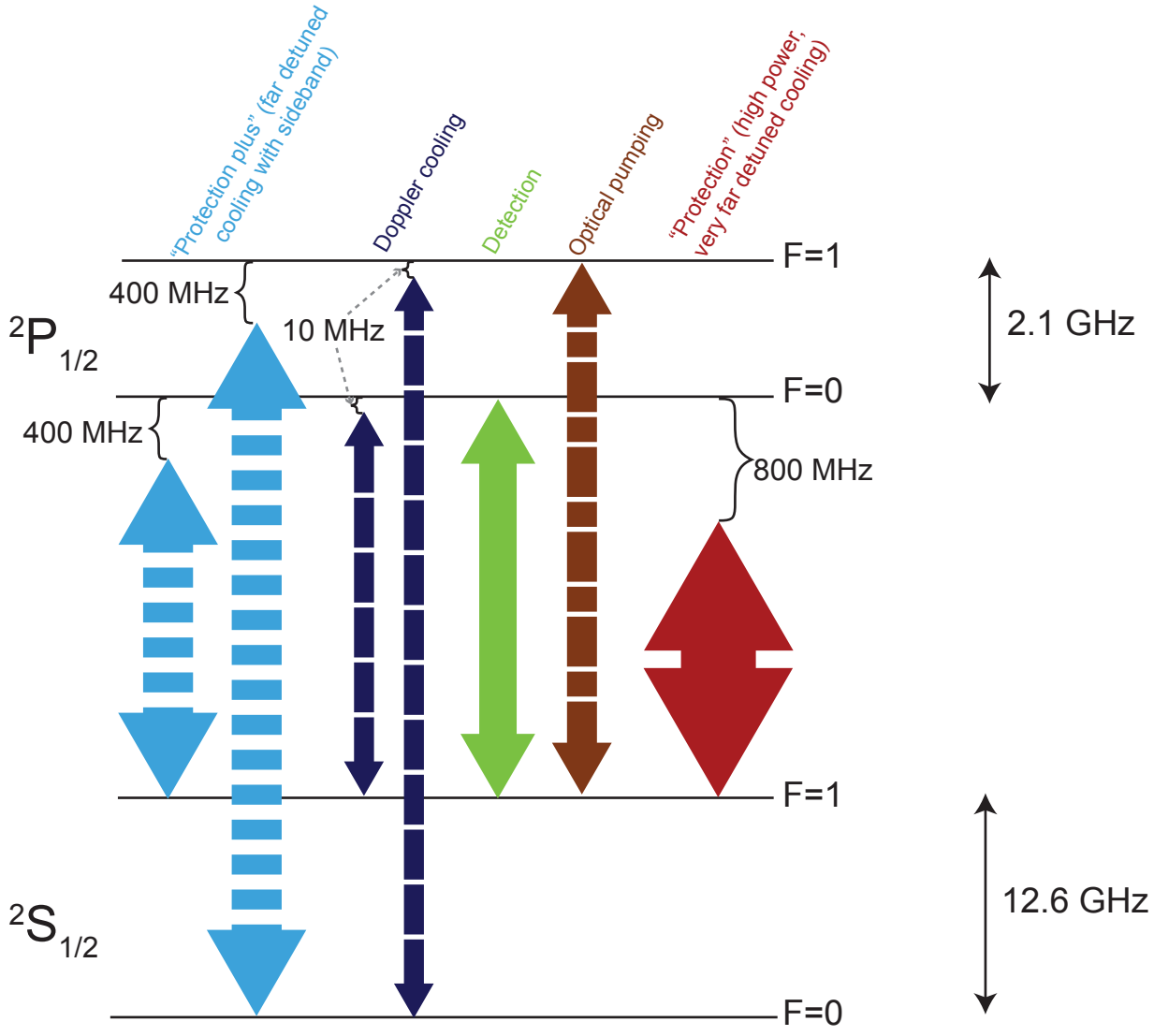

Figure 3.2: Diagram showing the various 369 nm frequencies used in our experiment relative to the hyperfine structure of the $^2S_{1/2}$ and $^2P_{1/2}$ states. Frequencies are not to scale. Not shown is the component of the optical pumping beam near the $F = 1$ to $F = 0$ transition (the EOM carrier), which is negligible (it does not cause fluorescence visible on the CCD in $^{174}Yb^+$).

power that is safe to apply to these EOMs without actively water cooling them. The Doppler cooling AOM shifts these frequencies to be roughly 10 MHz (half a linewidth) red-detuned from the transitions, in order to optimize the temperature of the Doppler cooled ions. A computer-controlled voltage-variable attenuator is used to lower the Doppler cooling power while experiments are running, for optimizing the temperature of the cooled ions, and raise the optical power when the experiments are not running, which helps in recapturing melted chains. The 0th order from the Doppler cooling AOM is fiber-coupled directly to the trap. This beam, which we call 'protection-plus', is necessary for recooling melted chains, because hot ions in the $F = 0$ state are otherwise not efficiently cooled. However, it is the only beam not used during a normal experimental cycle: it is blocked with a physical shutter during experimental runs, rather than being shuttered with an AOM, which saves some optical power. We believe this to be part of the reason it is so crucial to stop an experiment immediately after a dropout (melting event): namely, it is necessary to immediately open the shutter so that ions in $F = 0$ are cooled.

The optical pumping light is sent through a resonant New Focus EOM at 2.105 GHz EOM, such that the first-order sideband is $\sim$430 MHz red detuned from the ${}^2S_{1/2}, F = 1$ to ${}^2P_{1/2}, F = 1$ transition. The EOM frequency is derived from a PTS-3200 frequency synthesizer, whose amplified power is set such that the carrier is zeroed, which nearly maximizes the first-order sidebands. (This can be checked by redirecting the output of the EOM onto a scanning Fabry-Perot cavity and monitoring its transmission.) This beam is shifted by its AOM to be directly on resonance with the $F = 1$ to $F = 1$ transition.

A variable splitter consisting of a $\lambda/2$ waveplate and a thin-film polarizer is used to pick off some light for the detection beam. This beam is shifted to be on resonance with the $F = 1$ to $F = 0$ transition. The remaining transmitted light is the far-detuned 'protection' beam, which is shifted down in frequency by its AOM (Intraaction ASM-4001LA8.18) to be roughly 800 MHz red detuned from the $F = 1$ to $F = 0$ transition. A schematic of the various frequencies present is shown in Figure 3.2.

All of the beams are sent through optical fibers, which help somewhat to reduce unwanted resonant light scattering (discussed in a later section), and are eventually combined into a single beam path. The optical pumping and detection beams are combined on a nonpolarizing 50/50 beamsplitter before sending them through a single fiber. The other beams each get their own fiber. The near-resonant cooling beam is combined with optical pumping and detection on another 50/50 beamsplitter after the fibers. The protection and protection-plus beams are combined on a polarizing beam splitter, which allows the relative powers of the two to be varied. These are then combined with the 399 nm photoionization laser on a dichroic optic from Semrock. Finally, the cooling/optical pumping/detection beams are combined on yet another 50/50 beamsplitter with the 399/protection beams. Lenses in each beam path are set to attain beam waists ($1/e^2$ intensity radii) of roughly 100 μm horizontally by 10 μm vertically, for most of the 369 beams, and 250-300 μm horizontally by 50 μm vertically for the protection beams. This necessity of illuminating a larger volume with the protection beams is one reason why they require so much power.

Historically (meaning, when our MBR was running at full power, which it is not at the time I am writing this thesis - see Appendix C on this), a typical snapshot of laser powers coming out of the optical fibers might look like this:

Doppler cooling - 200 μW

Protection-plus - 400 μW

Protection - 3 mW

Optical pumping - 150 μW

Detection - 8 μW

Because the beamsplitters used to combine these beams are downstream from the optical fibers, the ions see roughly 1/4 of this power for the near-resonant beams, and roughly 1/2 of this power for the protection and protection-plus beams (which are ideally combined in a more or less lossless manner with the polarizing beamsplitter). The optical pumping (hopefully) would not suffer much from a reduction in power, but the Doppler cooling power is important for loading and recooling large chains.

(As a side note, when the protection beam is this powerful, we typically attenuate it to 1-1.5 mW before the beamsplitters. There has been some evidence that the ions are not cooled as efficiently and the detection count rates go down when this power is too high. The reason for this remains a mystery; we do not observe scatter from this beam when the ions are localized, so recoil heating is not likely to be a problem, and in any case the protection beam is nominally turned off during detection.)

We can work backward from the power measurements above to reason that

(with the assumption that we only require 1.5 mW of protection light out of the fiber) it is necessary to generate at least 16 mW out of the doubler. This calculation is conservative about what efficiencies can be readily maintained on a daily basis, using empirical values; for comparison, I also note values that should be achievable when the optics are new and more effort is expended. We assume transmission (including insertion loss) of 55% through the fibers (in principle, at least 70-80% should be achievable), of 50% through the resonant EOMs (meaning 50% of the total power is transmitted, not that 50% is put into the desired sidebands), and AOM diffraction efficiencies of 40% (55-60% or better should be achievable when the AOM is driven with $\sim$2 W of RF power). Additionally, there are something like 10-20 mostly-non-lossy optics (mirrors, lenses, waveplates) for each beam, so if the loss from each of these optics is around 1%, then we lose an additional 20% of our power from these elements. With these assumptions, we require the 369 nm source to provide something on the order of 2.3 mW for Doppler cooling, 3 mW for protection-plus, 1.7 mW for optical pumping, 45 μW for detection, and 8.5 mW for protection. Note that about half of the power is the off-resonant protection beam, whose frequency is less critical than the others; hence, it might make sense in the future to use two separate 369 nm lasers, one for the protection beam and one for everything else.

We can further calculate the laser power requirements for a longer chain, which will probably require us to expand the beams in the axial direction. I will assume for simplicity that the ion positions are dictated by a harmonic axial potential, which should be a conservative estimate, since in practice we are likely to start using

anharmonic potentials that allow us to space the ions more evenly. Our current record is a simulation with 18 $^{171}Yb^{+}$ ions in an axial potential with characteristic frequency 0.6 MHz, which corresponds to a chain length of 31 μm. For 50 ions, the chain length might be between 76 μm (for transverse confinement ν_x ~7 MHz and axial confinement $\nu_z \sim 0.35$ MHz - the transverse frequency is taken into account to ensure we are not picking an axial frequency that will cause the chain to buckle into a zig-zag configuration) and 96 μm ($\nu_x \sim 5$ MHz, ν_z ~0.35 MHz). We will hence probably want to expand the beam by a factor of 3 or so along the horizontal direction, so we are going to want at least 50 mW of 369 nm light for a chain this large. A similar calculation yields a 250 μm chain for 100 ions with $\nu_x \sim 7$ MHz and $\nu_z \sim 0.1$ MHz, in which case we might want to expand the beam by nearly a factor of 10, requiring perhaps 150 mW. It is unclear whether we will also need to expand the beam vertically (which would probably help recooling, but might not be strictly necessary), so the power budgets may be even more demanding than this.

We have historically produced >100 mW with the frequency-doubled MBR setup, and commercial systems like the intracavity-doubled M Squared laser can produce hundreds of mW of stable 369 nm light, so this is realistic for now, though it is out on the bleeding edge of what can be achieved with direct diode lasers. The next generation of experiments will probably also reconfigure the beam paths in some way, which will make the numbers more friendly. For example, there is nothing preventing us from sending the unused output of the final 50/50 beamsplitter onto the ions from a slightly different direction. Alternatively, sending detection and optical pumping light on a separate path along the axis of the ion chain would allow

us to focus these beams more tightly, and also free up a factor of 2 on the Doppler cooling power, since one of the 50/50 beamsplitters would no longer be required. (This will not be a feasible plan for the cooling beams, however, since these must have components along all three principal trap axes.)

3.2.2.1 Repump laser

As mentioned in the previous chapter, we need to clean up population falling into the long-lived $^2D_{3/2}$ state, and we do this by driving the transition at 935 nm from $^2D_{3/2}$ to $^3[3/2]_{1/2}$. This laser system is one of the simplest, consisting of a grating-tuned external cavity diode laser from Toptica (DL 100). Software is used to stabilize the frequency reading on a wavemeter that has a precision of 2 MHz (High Finesse WSU) by feeding back to the grating angle (controlled with a piezo). (The wavemeter, in turn, is calibrated with respect to the 739 nm light, after this is stabilized to the molecular iodine transition as an absolute frequency reference.) The laser is tuned to the $^2D_{3/2}, F = 1$ to $^3[3/2]_{1/2}, F = 0$ transition, and sidebands at 3.0695 GHz to drive the $^2D_{3/2}, F = 2$ to $^3[3/2]_{1/2}, F = 1$ transition are applied with a broadband fiber EOM from EOSpace. These sidebands are roughly 2% of the height of the carrier when measured using a Fabry-Perot cavity. The fiber outputs roughly 20 mW, which is combined with the 369 nm and 399 nm beams by sending it through the back of a dielectric UV mirror that is sufficiently transmissive at 935 nm.

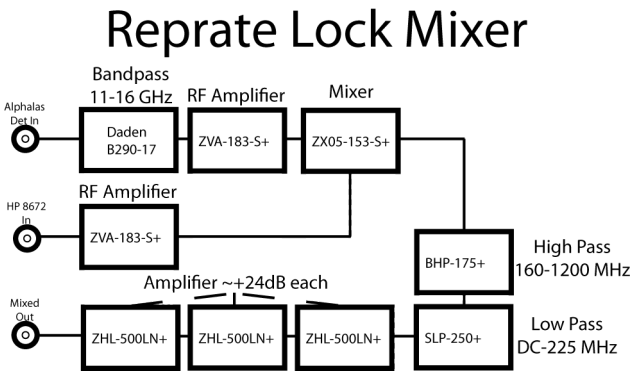

Figure 3.3: Schematic showing the electronic components used to generate the 195 MHz signal that will set the frequency f_{A1}. Except for the bandpass filter, all part numbers refer to Minicircuits components.

3.2.3 Raman laser

3.2.3.1 Beatnote stabilization electronics

As we discussed in the previous chapter, it is necessary to stabilize the beat frequency between the two Raman arms by feeding forward to an AOM frequency. This setup has been well described in [33] and [58], but here I give specifics of the current setup, which has changed since Rajibul wrote his thesis. We currently use a 4 W, water-cooled Paladin laser from Coherent, which has a repetition rate of $f_{rep} \sim$ 120.215 MHz. For this rep rate, the hyperfine splitting is given by $f_{HF} \approx 105 f_{rep} +$ 29.7 MHz. The two AOMs in the Raman arms will thus be driven at different frequencies f_{A1} and f_{A2} such that $f_{A2} - f_{A1} \approx 29.7$ MHz, or $f_{HF} \approx 105 f_{rep} + f_{A2} - f_{A1}$.

We choose f_{A2} to be the fixed frequency, which is about 225 MHz. Thus, we will adjust $f_{A1} \approx 195$ MHz such that

$$f_{HF} - f_{A2} = 105 f_{rep} - f_{A1} = const. \tag{3.2}$$

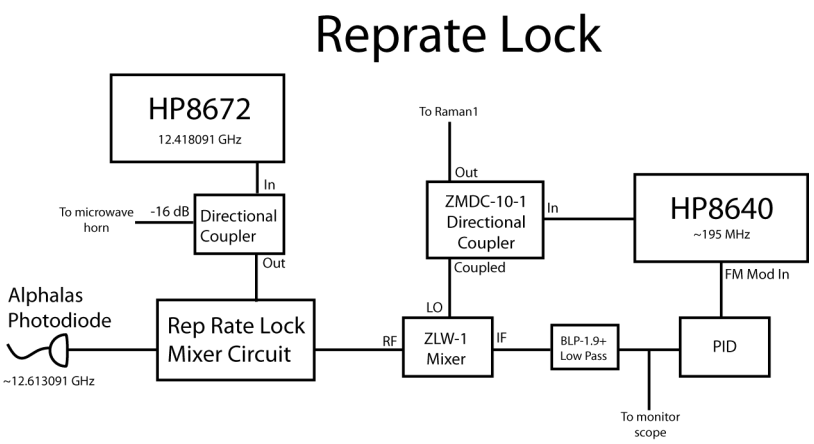

Figure 3.4: Schematic showing the electronic components used in the phase-locked loop stabilizing the AOM driver to the 195 MHz signal generated by the circuit in Figure 3.5.

This means that if f_{rep} decreases, we want f_{A1} to decrease with it. In order to accomplish this, we mix a signal at $105 f_{rep}$ (from a fast photodiode) with a microwave source (HP8672) which is set such that

$$105 f_{rep} - f_{8672} = f_{A1}. \tag{3.3}$$

This ensures that f_{A1} changes in the correct direction with the rep rate. The HP8672 is thus set to $105 f_{rep}$-195 MHz = 12418.091 MHz (for the exact rep rate measured in July 2013). A schematic of the electronics used for generating this 195 MHz signal that follows the fluctuations in the rep rate (i.e., the result of mixing the HP8672 signal with the 105th comb tooth) is shown in Figure 3.5.

In order to circumvent issues such as the possibility of a fluctuation in laser power causing fluctuations in the RF applied to the AOM, the 195 MHz signal thus generated is used as a frequency reference for a separate frequency source, an HP8640 that is phase-locked to the output of the mixer circuit described above. The

schematic for this part of the circuit is shown in Figure 3.4.

3.2.3.2 Optical layout

The first optic in our setup picks off a bit of light to monitor the repetition rate. This is sent onto a fast photodiode (Alphalas UPD-30-VSG-P), which is used for the beatnote lock discussed above.

Just after the pickoff we place a variable attenuator consisting of a $\lambda/2$ waveplate and a polarizing beam splitter (PBS). The waveplate can be rotated to set the polarization anywhere between (nearly) full transmission through the PBS to (nearly) full extinction (sending the light out of the other port of the PBS, where a beam dump captures the unused light). This is very useful for alignment purposes, as such lasers do not always have convenient power knobs, and the several watts of 355 nm light we work with is sufficient to burn hands and index cards, drill holes through chiller tubing, and cause sundry other acts of destruction. An AOM meant to noise-eat the power fluctuations is placed just before the variable attenuator, though this is not currently used. Then the beam is split with a 50/50 nonpolarizing beam splitter to form the two arms that will eventually impinge on the ion from different directions.

After the beam splitter, each beam is focused through an AOM with an $f =$ 100 mm lens. As with all lenses in this beam path, we aligned them by setting up a target downstream, setting their longitudinal (upstream/downstream) position, then translating them transverse to the propagation direction until they no longer

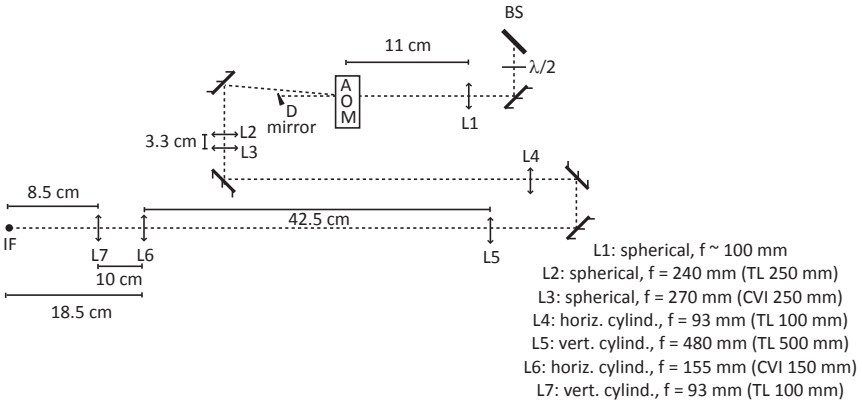

Figure 3.5: Partial sketch of the optics in the Raman 2 beam path, with distances as measured when the beam path was first set up. The Raman 1 beam path has identical optics, albeit with a different geometry. The distances not listed are 22 cm from the AOM to L2; 37 cm from L3 to L4; and 75 cm from L3 to L5 (not L4 to L5). The legend lists the actual focal lengths of each lens at 355 nm and the nominal focal lengths. All lenses shown here are plano-convex fused silica lenses from either Thorlabs (TL) with a UV coating or CVI with a 355 nm AR coating.

deflected the beam relative to the target position that is seen without the lens in place. The focal length was the shortest standard focal length that gave us a spot size we believed we could tolerate, as too high of an intensity can begin to damage the AOMs; with a roughly collimated input beam of waist ($1/e^2$ intensity radius) 500 μm, this means the diffraction limited waist is about 21 μm. (The diffraction limit can be calculated as 1.22 $\lambda f/R$, where λ is the wavelength of light, f is the focal length of the lens, and R is the diameter of the input beam. A slightly different, and (we hope) more accurate, result obtains for Gaussian optics; however, the difference is usually slight compared to the uncertainty of the measured input beam profile.)

The AOMs (Brimrose QZF-210-40-355) are chosen to be of the type that requires the laser to be focused through them with a relatively small waist (as opposed to the style manufactured by IntraAction, which operate better with a larger collimated beam) because this allows us to more easily image the front face of the AOM

directly onto the ions while also having the ions near the focus, or smallest beam size, so as to maximize the laser intensity. This imaging requirement is important because we will be applying multiple frequencies to one of these AOMs and we do not want the difference in angular deflection to be mapped onto a positional shift at the ions, which could lead to different ions seeing different relative powers of the frequencies. A $\lambda/2$ waveplate is placed in front of each AOM and its angle along with the AOM angle is used to optimize the diffraction efficiency, which should typically be at least 50% (often we see 70% or better) with an RF power of roughly 2 W (33 dBm). One of the AOMs is driven with a single frequency, and this is the one used for the feed-forward beatnote lock. The other is driven with multiple frequencies using an arbitrary waveform generator (discussed below).

A D mirror just before the recollimating lens ($f = 250$ mm) is used to pick off the unwanted 0th order light and send it into a beam dump. We have found that it is necessary to block stray 0th order light further downstream as well, since the orders are not sufficiently well separated at the recollimating lens to block all of the 0th order light without clipping the 1st order light. The downside of our scheme for imaging the AOMs is that 0th order light will hit the ions right on top of the 1st order light, causing unwanted Stark shifts and spontaneous emission.

Two telescopes comprising cylindrical lenses change the beam size to a waist ($1/e^2$ intensity radius) of roughly 100 μm horizontally and 10 μm vertically. This beam size is as tightly focused as we can make it vertically without seeing significant intensity noise at the ion due to pointing instability, and the horizontal waist is chosen such that the intensity variation is less than $\sim$3% across the entire ion chain

(estimated to be 31 μm long for a chain of 18 ions in a harmonic axial potential of frequency 600 kHz), assuming a perfect Gaussian intensity profile. (Note that this takes into account the factor of $\sqrt{2}$ from the angle of incidence of the Raman laser with respect to the ion axis.)

When the optics are set up, the beam size is profiled with a small portable web camera at the new image plane, which is referred to as the intermediate focus (IF). The longitudinal positions of the lenses were set such that the longitudinal position along the beam with the minimum vertical waist (at the intermediate focus) coincides with the position at which the AOM is well imaged (defined as the position where the beam shifts 2 μm or less when the AOM frequency is changed by 20 MHz). At the intermediate focus, we measure a waist of 90 μm horizontally and 9 μm vertically, slightly smaller than what we had intended. Note that we have seen that even when the imaging is done such that the center of the beam profile does not shift as the AOM frequency is changed, we do see a change in the waist at the intermediate focus, for example causing the spot size to go down to 80$\times$8.5 μm when the AOM frequency is shifted 20 MHz. Additionally, we have some evidence that the horizontal axis of the beam is tilted with respect to the ion chain axis, so the effective waist along the ions may be smaller than even 80 μm.

A $\sim$1:1 relay imaging system consisting of spherical lenses with $f \approx 100$ mm images the intermediate focus onto the ions. As the first lens in this relay system more or less recollimates the beams, the space between these lenses is a convenient location for the $\lambda/2$ and $\lambda/4$ waveplates that are installed for full polarization control at the ion, and for a delay stage in one of the arms. The polarization is set to be

horizontal (i.e., parallel to the surface of the table) by maximizing its transmission through a regular PBS (which is not normally part of the beam path, but is inserted only for the purpose of setting the polarization). We make finer adjustments using the ion for diagnostics once the beams are aligned, as described below.

Because we use a mode-locked laser with a pulse duration of roughly 10 ps, we must make the path lengths of the two beams equal to better than the pulse length of c*(10 ps) = 3 mm. This is the role of the 'delay stage' in one arm, which consists of a pair of mirrors that retroreflect the beam, mounted to a translation stage that allows fine adjustments of the path length in that arm. The path lengths can be coarsely estimated with a ruler (or piece of string, etc), after which a more sophisticated technique is generally necessary. To obtain a more precise estimate, we place fast (pulse-resolving) photodiodes in each beam path at the same distance from the ions, which can be accomplished to a precision on the order of 3 mm with a ruler when the photodiodes are close enough to the trap. We then pick off some light prior to the beam splitter, which is sent onto another photodiode, and use a time-to-digital converter (Picoharp 300) to measure the delay between a pulse hitting this first photodiode and hitting one of the photodiodes near the trap. This allows us to match the pulse arrival times to the measurement error of the Picoharp (4 ps) and to the precision of the placement of the photodiodes near the trap. Since the delay stage can be used to shift the relative path lengths by 100-200 ps, this procedure usually puts us in range of the stage, after which the ions will be used as the final signal to tweak the delay.

The final optic before the vacuum chamber in each Raman beam path is a

so-called bestform lens with effective focal length $f = 110$ mm at 355 nm. These lenses are used to help attain a small spot size (e.g. 10 μm in the vertical direction). A bestform lens has two radii of curvature, which are chosen to minimize coma and spherical aberration for a given focal length (given the constraint that both surfaces must be spherical), which helps to attain a spot size closer to the diffraction limit. In most cases, the beams can be roughly centered near the ions by indexing them against the trap electrodes (at very low power). After this, fine adjustments can be made by transverse translations of the lenses on 3-axis stages. This trick only works when the beam passes unobstructed through the chamber, such that a card can be used to observe the electrodes' shadow on the far side of the trap. Using the electrodes to index the beam also allows the focal position to be set close to its optimum, since we want the beam to be most tightly focused at the ions, which are positioned very close to the electrodes. The key idea for this is that the shadow appearing when a beam is occluded from one side appears on a different side of the image, depending on whether the obstruction or the focus of the beam is closer to the image, whereas when the focus of the beam is near the obstruction the shadow seemingly appears on both sides of the image. Figure 3.6 gives a cartoon illustration of this concept. In practice, when the beam is focused near the obstruction, the electrode shadow usually causes strange scattering when the beam is partially occluded, but by dithering the beam toward and away from the electrode as the longitudinal position of the lens is shifted it is possible to see at first the shadow coming in from one side, then a transition region where the shadow doesn't obviously come in from a particular direction, beyond which the

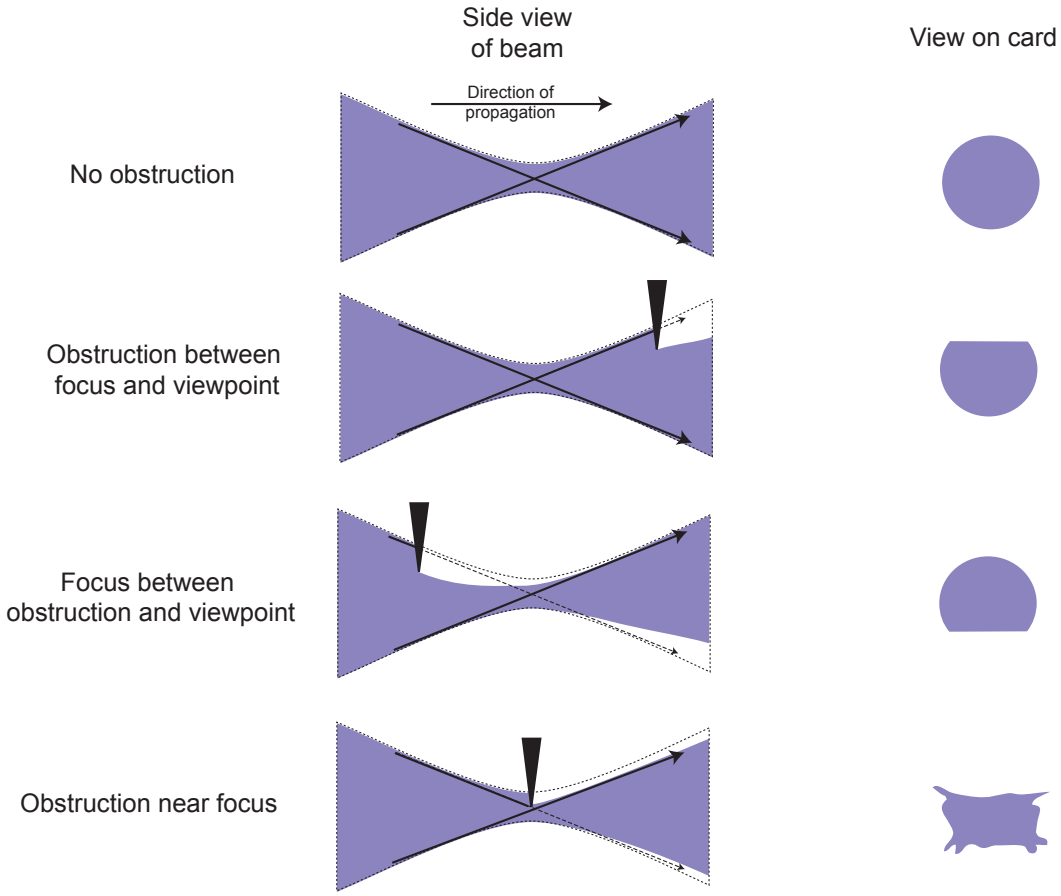

Figure 3.6: Qualitative illustration of the use of electrode shadows to roughly align the focus of the Raman beam. By longitudinally translating the final lens, it should be possible to observe different regions where the occlusion causes the shadows to appear from different directions.

shadow comes in from the other side, which gives a good starting point for the focal position of the beam.

Since the path lengths of the two arms may not be matched sufficiently well to drive Raman transitions with both arms, it is useful to have a technique for aligning each beam to the ion separately. This can mean driving the AOM in the beam with two frequencies that are chosen to drive copropagating Raman transitions, or using a Ramsey experiment (with microwaves providing the $\pi/2$ pulses) to detect

the Stark shift of the beam. For either of these procedures, it is important that the beam we are attempting to align have an excess of σ^+ polarization over σ^- polarization, or vice versa; with our current geometry, this is most easily accomplished by (A) using the $\lambda/4$ waveplate to make the light circularly polarized, and (B) temporarily swapping the currents to the magnetic field coils, such that the field is along the laser's direction of propagation. Once both beams are transversely aligned to the ion, reconfiguring the polarizations, frequencies, and magnetic field to drive non-copropagating Raman transitions and scanning the delay (while rechecking the transverse alignment of the beam going through the delay stage at each point, if necessary) should be sufficient to find a signal of Raman transitions.

When a Raman beam path becomes completely misaligned for whatever reason, it is usually easiest to trace back to the point furthest downstream where the beam path is still functioning acceptably, and work forward from there to realign the optics. In anticipation of this happening on occasion, and changes being made to the beam path, there are several practices we consider in designing the beam path to start with. Many alignment issues are greatly simplified if all the spherical lenses are mounted in such a way that they are easily removed and repeatably replaced, even if this is not necessary for the initial setup. For example, the bestform lenses are mounted in short lens tubes that screw onto longer lens tubes, and other lenses use a nested mount wherein the lens is mounted in an inner ring that can be secured within an outer ring using a set screw. (It would also be nice to do this with the cylindrical lenses, but it isn't feasible with the mounts we use.) Likewise, the final focusing lenses before the trap, as well as any lenses whose position may be used to

fine-tune the alignment at the ion, are mounted on 3-axis translation stages when feasible. Finally, alignment is much simpler if there are at least two independent mirrors (for full position and angle control) steering the beam into any important region (e.g., aligning the beam through an AOM or delay stage, or onto the ions). While beam splitters can be used in place of an additional mirror for aligning the reflected port, and their presence is better than no additional knobs, this is not ideal because a beam splitter's angle is generally not completely decoupled from the alignment of the transmitted beam. Some of these ideas, especially the two-independent-mirror criterion, could add to the pointing instability, but in practice adding an extraneous mirror or three does not seem to appreciably change the coherence time, so in these setups it is an overall gain to have independent mirrors.

3.2.4 Fluorescence collection and state diagnosis

We discussed in the previous chapter that the spin states can be measured by exposing the ion to light that is only resonant with one of the spin states, and collecting the resulting fluorescence. In our experiment, the collection optic is a commercial objective from CVI with a working distance of 13 mm, effective focal length of 20 mm, and numerical aperture 0.23. The light is focused through a 400 μm pinhole and imaged with a doublet onto either an ICCD [59] or a PMT. Interference filters in the imaging path block 355 nm and 935 nm light, as well as most of the visible spectrum. As mentioned previously, 90% of the collected light is imaged for state detection, while 10% is sent to a separate PMT that allows us to

monitor the Doppler cooling fluorescence to detect melting events.

When the imaging is already set up to be focused on the ICCD, the objective can be aligned to the center of the trap by indexing it against scatter from the trap electrodes. The procedure that we use is as follows. The protection, protection-plus, and photoionization beams are blocked from the trap, and the remaining 369 nm beams are translated upward (using a lens on a stage) until they scatter off the electrodes. The objective is then moved to a position where the edge of the electrode is in focus. The corners of the center electrode are found by translating both the objective and the 369 nm light, and their coordinates with respect to the objective position are noted. We then center the objective horizontally at the average of these coordinates, translate the objective and lasers vertically to find the coordinates of the top and bottom electrodes, and use the average of these to position the objective vertically. For positioning the focal direction, we have found empirically that the objective needs to be moved roughly 0.009 inches ($\sim$230 μm) closer to the trap than the position where the electrodes were in focus.

The detection cycle for each experiment consists of exposing the ions to 'detection' light, resonant with the $|\uparrow\rangle_z$ ('bright') state but not the $|\downarrow\rangle_z$ ('dark') state, for 3 ms. To calibrate the readout, we perform 1000 cycles of preparing and measuring an all-dark state, $|\downarrow\downarrow\downarrow\cdots\rangle_z$, and 1000 cycles of an all-bright state, $|\uparrow\uparrow\uparrow\cdots\rangle_z$. Single-shot discrimination is performed by summing the columns of the resulting image into a 1-dimensional row, since the vertical direction yields no additional information in a linear chain, and fitting the resulting profile to a sum of Gaussians whose positions and widths are determined from the calibration images. The individual ion states

are then discriminated by comparing the fit amplitudes to calibrated thresholds (see below).

The calibration also allows us to determine the detection errors for each ion, i.e. the probability of misidentifying a dark state as bright or vice versa for a given threshold. These known errors are used to correct the probability distributions for detection errors, while also considering standard errors from shot noise [60].

The optimal thresholds are determined by performing a Monte Carlo simulation in which certain target states are 'prepared' by randomly choosing an amplitude from the appropriate calibration ensemble (e.g., for the target state $|1010\cdots\rangle$ the amplitude of the first ion is chosen from the pool of amplitudes which were fit to the first ion in the bright calibration), discriminated with a given threshold, and corrected for the detection error given the chosen threshold. A threshold is then chosen that is insensitive to statistical fluctuations and gives corrected probability distributions that match the known input ensemble well; the recovered probability distributions are nearly identical for a wide range of threshold choices.

3.2.5 Arbitrary waveform generation

The amplitudes, frequencies, and phases needed to apply the Ising Hamiltonian are imprinted on the 355 nm laser beams by driving the AOM in the Raman 2 beam path with an arbitrary waveform generator (AWG). The AWG (Agilent M9502A)

is programmed to output a voltage of form

$$\begin{aligned} V(t) = \quad & V_1 \sin[2\pi(f_{HF} - \mu - f_{\text{offset}})t] + V_2 \sin[2\pi(f_{HF} + \mu - f_{\text{offset}})t + \varphi] \\ & + V_3(t) \sin[2\pi(f_{HF} - f_{\text{offset}})t + \varphi/2] \end{aligned} \tag{3.4}$$

where V_1 and V_2 are the amplitudes of the components that generate the $J_{i,j}$ couplings, $f_{\text{offset}} = 105 f_{\text{rep}} - f_{A1}$ takes into account the repetition rate of the laser and the frequency shift f_{A1} of the Raman 1 beam path, and by our convention φ is set to π to give a spin-spin interaction $\sigma_x \sigma_x$. The time-dependent voltage $V_3(t)$ sets the time-dependent amplitude of the transverse field $B(t)$. The AWG output signal (Eqn. 3.4) is amplified to a peak power of 1.8 W before being applied to the AOM, generating frequency components relative to the other beam path at $f_{HF} - \mu$, $\omega_{HF} + \mu$, and ω_{HF}, with corresponding amplitudes set by V_1, V_2, and $V_3(t)$.

Importantly, the laser power required to generate $B(t)$ is on the order of $100\times$ smaller than that for the interactions, so that the voltage V_3 only needs to be modulated over a small range, allowing us to make the approximation $B \propto V_3$. If we were to additionally use time-dependent profiles for V_1 and V_2, it would probably be necessary to take the nonlinearities of the system into account. (For example, the two-photon Rabi frequency scales as the product of the electric fields of the two laser beams, so we have $\Omega \propto E_1 E_2$; the power diffracted by the AOM, proportional to E_2^2, can be approximated as $E_2^2 \propto \sin^2 V_{RF}$, so $\Omega \propto E_1 \sin(\pi V_{RF}/V_0)$, where V_0 is the voltage at which the diffraction efficiency turns over; and the interaction strengths $J_{i,j}$ scale as $\Omega_i \Omega_j \propto \sin^2(\pi V_{RF}/V_0)$.

3.3 Diagnostics, calibrations, other procedures for getting the system ready

3.3.1 Loading, and troubleshooting when loading isn't working

When loading ions, we first lock the 739 nm and 935 nm lasers to the correct wavelength and set the 399 nm laser wavelength before turning on the oven, where we run roughly 2.5 A of current through the needle holding the solid ytterbium in order to resistively heat it and create an atomic beam. Usually, it takes roughly 2 minutes for the oven to heat to the point of delivering a steady flux of neutral atoms. During loading, we continuously send the photoionization, Doppler cooling, and 935 repumping beams to the trap: once the 399 nm laser excites a neutral atom to the P state, the 369 nm photons have sufficient energy to ionize the atom. We additionally send in long pulses (of order 200 ms) of a 355 nm beam; since these photons are also sufficiently energetic to ionize an atom, the higher intensity of the 355 nm light leads to a faster loading rate, suggesting that the second photon is the limiting reagent in loading ions into the trap.

If this procedure fails to produce a trapped atom, the usual culprits are the lasers and voltages. On occasion, the DC voltages are set incorrectly by the recrystallization program, which can be seen by checking the sensed voltages. When the DC voltages and laser frequencies are set correctly, the next step is usually to switch the lasers to the wavelengths used for $^{174}Yb^{+}$ and load from the oven containing Yb in its natural abundance. The even isotopes like $^{174}Yb^{+}$ have no nuclear spin and

hence no hyperfine structure; this drastically simplifies the number of parameters that must be set correctly to load and detect an ion, because the ions will be much less sensitive to magnetic fields and laser polarizations, and neither the 7.37 GHz sidebands on the 369 nm light nor the 3.07 GHz sidebands on the 935 nm light are necessary to repump to the cycling transition. If loading is still difficult, a common problem is misalignment of either the 399 nm photoionization beam or one of the 369 nm cooling beams. The 935 nm beam is less sensitive because it illuminates a larger volume of the trapping region, but its alignment is also a possible suspect. If loading proceeds normally with $^{174}Yb^{+}$, the magnetic field coils and the sidebands on, and polarizations of, the Doppler cooling light and 935 nm repump light are the likely culprits.

3.3.2 Daily calibration routine for spin-1/2 Ising experiments

We have developed a standardized routine for a daily tuneup and calibration of the system when we are taking data for spin-1/2 experiments. After loading a single ion, we direct the fluorescence to the PMT and check the count rates from the detection and Doppler cooling beams. Because there is a slight amount of background scatter from the 369 nm lasers into the detectors, we compare the count rates with and without the presence of the 935 nm repump beam. We find that detection is optimized when there are on average 12 counts in a 0.8 ms window, which is slightly below the saturation count rate; the counts from the Doppler cooling beam should be roughly half the saturation count rate, so we aim for 7-8

counts in a 0.8 ms window. We additionally check that optical pumping prepares the $|\downarrow\rangle_z$ state with fidelity ∼99-99.5% by exposing an optically pumped ion to the detection light and measuring the probability of the ion scattering more photons than would be expected from the $|\downarrow\rangle_z$ state. We choose our optical pumping fidelity goal of $99 - 99.5\%$ somewhat arbitrarily as the best we can typically achieve; in principle this number can be made arbitrarily good. Right now, our best guess for the limiting factor on the optical pumping is that repumping of the ${}^3D_{3/2}, F = 2$ manifold is limited by the power and/or frequency of the sidebands on the 935 nm light, which affect optical pumping most strongly because detection light should never couple to the ${}^3D_{3/2}, F = 2$ manifold, and because we typically Doppler cool for 3 ms but only optically pump for 10-20 μs (which is already longer than we should need). Furthermore, exposing the ion to optical pumping light for longer durations often results in a gradual improvement of the fidelity over several ms, which is also suggestive of the fidelity being limited by population getting temporarily trapped in the ${}^3D_{3/2}$ state.

We set the Raman AOM frequencies to drive a resonant carrier transition and check the Rabi frequency of this transition. We usually tweak the alignment of the Raman beams daily to maximize the Rabi frequency before recording it and the pulse durations corresponding to $\pi/2$ and π rotations. We perform a broad frequency scan, with a pulse duration roughly equivalent to a π rotation on the 'Zeeman transitions' to the $m_F = \pm 1$ states, as a diagnostic; this scan will display the locations of the Zeeman transitions and of the motional sidebands, so acts as a quick check that the magnetic field and trap potential are not drastically different

than expected and that no unexpected spectral features have appeared. After this scan, the rest of the calibrations are all performed after sideband cooling to the ground state of the relevant transverse mode. We next do a time scan looking at Rabi flopping of a ion out to long durations corresponding to perhaps a 50π rotation; if there are any significant errors (meaning a deviation from the expected sinusoidal curve that is larger than the quantum projection noise could explain) before roughly a 20π rotation, this usually indicates either a cooling problem (which causes the ion to sample multiple Rabi frequencies based on the motional state, as discussed further below in the section on Debye-Waller factors) or a problem with intensity noise, which usually means the Raman beams are not well centered (this amplifies the effect of any pointing instability on the Rabi frequency, since the slope of the beam intensity versus position is only zero at the center of the beam).

The motional sidebands drift around day to day, which we believe to be caused by variations in the helical resonator. Our next calibration is therefore to measure the exact AOM frequencies at which the sidebands are excited. This is done with a low AWG voltage, corresponding to a low power in that beam only, in order to ensure we are not significantly shifting the resonance with a 4-photon Stark shift. Because we do this with a sideband-cooled ion, it is necessary to add a π pulse preparing the ion in the $|\uparrow\rangle_z$ state before probing the red sideband. (This is because the $|\downarrow_z, n=0\rangle$ state is unaffected by the red sideband: we can drive $|\uparrow_z, n=0\rangle$ to $|\downarrow_z, n=1\rangle$, but there is no $|\uparrow_z, n=-1\rangle$ state to which $|\downarrow_z, n=0\rangle$ can be driven.)

We should know ahead of time how far we will be detuning the Mølmer-Sørensen interaction from the center-of-mass mode and how high of a sideband

Rabi frequency we want, based on the interaction profile we want (i.e., what J_0 and α in the $J_{i,j} \sim J_0/|i-j|^\alpha$ approximation). So next we detune the sidebands by this amount (typically of order 100 kHz from the center of mass mode) and perform a Ramsey experiment on the $|\downarrow\rangle_z$ to $|\uparrow\rangle_z$ transition, with both beams and two sidebands turned on between the $\pi/2$ pulses, in order to characterize the Stark shift induced by the sidebands. (This assumes that we already know the frequency of this transition very precisely; we characterize this parameter by performing a Ramsey experiment in which the ion is not exposed to any light between the $\pi/2$ pulses. This rarely changes day to day, so it is not typically part of the calibration routine). The relative power of the two sideband frequencies is then adjusted so that the 4-photon Stark shifts roughly cancel, such that the hyperfine frequency is shifted less than a few hundred Hz by the presence of the light.

We characterize the sideband Rabi frequencies by driving Rabi flopping on each sideband, so that we can calculate the exact interaction profile we will be generating. Importantly, this measurement is done by applying both sidebands, leaving one detuned (by 100 kHz or whatever) while the other is on resonance driving Rabi flopping. This is necessary because the Rabi frequency is not linear in the AWG signal for a variety of reasons, as discussed in the section on the AWG above, so we apply the off-resonant sideband to ensure a more accurate measurement.

Next we load a second ion and drive the Mølmer-Sørensen interaction. This gives us the best signal to fine-tune the detunings: we scan the frequency of the red sideband until the $|\downarrow\downarrow\rangle_z$ to $|\uparrow\uparrow\rangle_z$ transition probability is maximized. Ideally this should occur when the sidebands are detuned by an equal amount from the

carrier transition; the fact that we often have to shift the red sideband frequency by of order a few hundred Hz is likely an indication of residual Stark shifts on that scale. This interpretation is most easily understood by looking at the cartoon in Figure 2.5, where we can see that Stark shifts will change the energy difference between $|\downarrow\downarrow\rangle_z$ and $|\uparrow\uparrow\rangle_z$, and hence the two-sideband resonance, such that one of the sideband frequencies must be shifted to tweak the interaction back onto resonance. We then take a trace of 'brightness' versus duration to characterize the coherence time of the interaction. We typically do this calibration with the PMT, which yields sufficient information to check that the dynamics mostly involves $|\downarrow\downarrow\rangle_z$ and $|\uparrow\uparrow\rangle_z$ (the histogram of PMT counts will then be bimodal when there is an 'average brightness' of 1 ion).

Then we calibrate the effective B field with the new frequency: We take the average of the two AOM frequencies found with the Mølmer-Sørensen resonance and set this to be our new carrier frequency, on the assumption that the required shift in the sideband frequency was due to residual Stark shifts. We then detune the sidebands by roughly 800 kHz from the center-of-mass mode and calibrate the Rabi frequency of a simultaneously applied carrier (corresponding to an effective B field) versus the AWG amplitude used to drive it. It is necessary to calibrate this with the sidebands on because of nonlinearities in the AOM and in one of the RF amplifiers, and the larger detuning is used to suppress the spin-motion coupling during this measurement. Also, we note that the Rabi frequency is dependent on the carrier phase relative to the Mølmer-Sørensen spin phase, seemingly due to some weird interference effect. Hence, if we will be using both a transverse and a longitudinal

effective B field, we need to calibrate these separately.

Finally, we load the number of ions we will be doing experiments with, and calibrate detection with the CCD by taking 1000 images of the $|\downarrow\downarrow\cdots\rangle_z$ state (prepared by optical pumping) and 1000 images of the $|\uparrow\uparrow\cdots\rangle_z$ state (prepared by optical pumping and a global rotation by π on the carrier).

3.3.3 Less frequent calibrations and measurements

As mentioned above, we do not typically need to calibrate the hyperfine frequency of the $|F=0, m_F=0\rangle$ to $|F=1, m_F=0\rangle$ transition on a daily basis, because it is quite stable over a period of weeks or months, but we nevertheless need to have measured this number at some point. Similarly, there are several other important checks and calibrations that we typically do not look at frequently, which I will now list here.

3.3.3.1 Thermometry for checking Doppler and sideband cooling

When we change any of the Doppler cooling parameters (e.g. the amplitude of the RF driving the AOM), we may want to check that the ion is still being efficiently cooled. The traditional way this is done is by comparing the heights of the red sideband and blue sideband transitions, which should show an asymmetry of $\bar{n}/(\bar{n}+1)$, where $\bar{n}$ is the mean phonon occupation number [61]. This, however, requires that the power is identical at the red sideband and blue sideband frequencies, which is not automatically the case in our setup (e.g. due to the frequency dependence

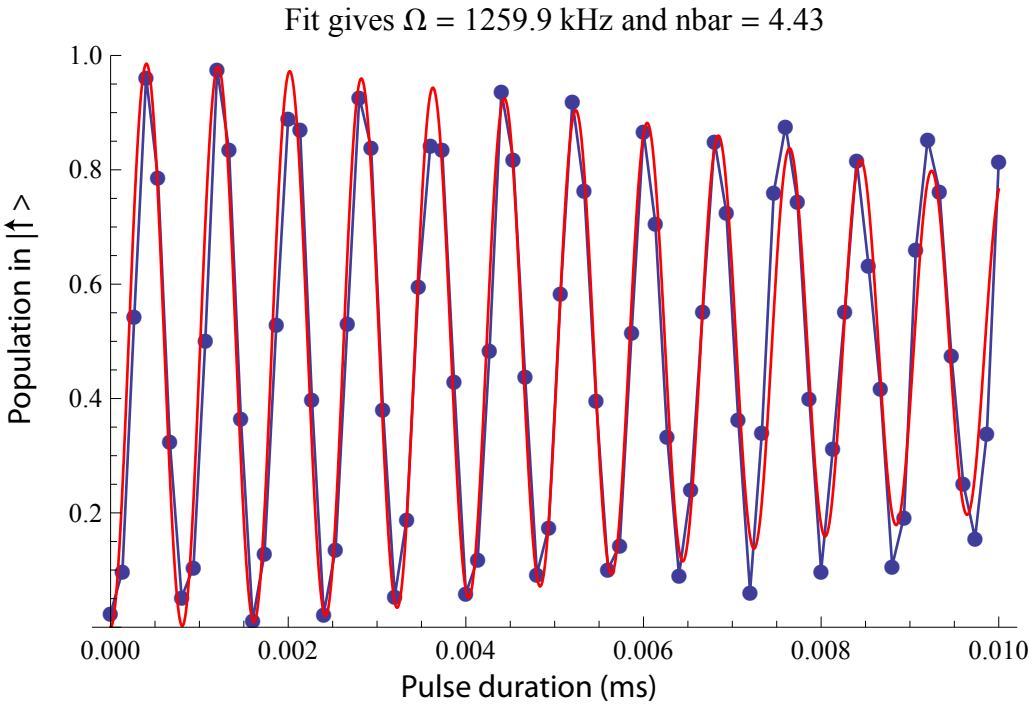

Figure 3.7: Use of the carrier Rabi flopping envelope to estimate the temperature of a Doppler cooled ion (here, with unoptimized cooling parameters); the effect of the temperature is to cause damping of the Rabi flopping.

of the AWG amplitude and of the AOM diffraction efficiency). Additionally, for sufficiently large $\bar{n}$, this requires us to precisely resolve a fairly small asymmetry. We have been using slight variations on this idea to do our thermometry without comparing the two motional sidebands.

To measure the temperature of a Doppler cooled ion, we take advantage of the long coherence time of our Rabi flopping on the carrier, and measure the effect of the so-called Debye-Waller factors. The idea here is to make use of the corrections to the Lamb-Dicke approximation that come in as the ion heats up, where the carrier Rabi frequency has a factor [51]

$$\langle n|e^{ikx}|n\rangle = e^{-\eta^2/2} L_n^0(\eta^2), \tag{3.5}$$

where $L_n^\alpha(x)$ is a generalized Laguerre polynomial. We assume that the ion is in a thermal state, in which case the occupation of a given level n is given by

$$P(n, \bar{n}) = \frac{\bar{n}^n}{(\bar{n}+1)^{n+1}}. \tag{3.6}$$

We can then fit a Rabi flopping trace (i.e., transition probability versus carrier duration) to the weighted sum over the different Rabi frequencies:

$$P(\uparrow) = \sum_n P(n, \bar{n}) \sin^2(\pi e^{-\eta^2/2} L_n(\eta^2) \Omega t) \tag{3.7}$$

to extract the average occupation number $\bar{n}$. An example trace with its fit is shown in Figure 3.7. As can be seen in both the data and the fit, the decay due to nonzero

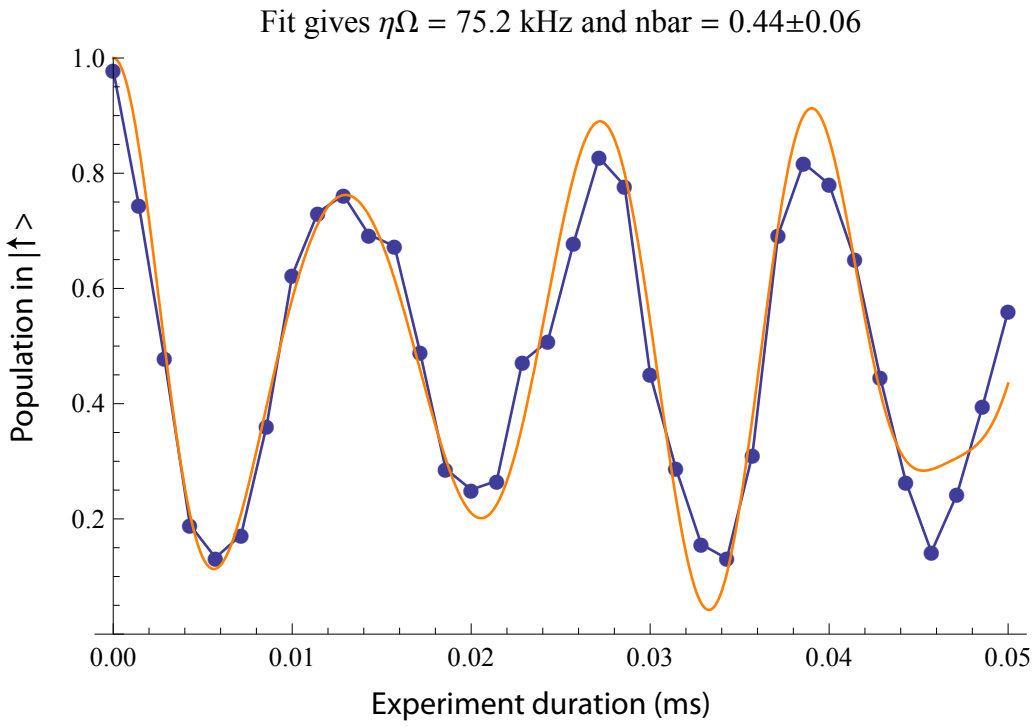

Figure 3.8: Use of the sideband Rabi flopping envelope to estimate the temperature of a sideband-cooled ion (again, with unoptimized cooling parameters). The stronger dependence on n of the sideband Rabi frequency leads to a more distinctive signature of the phonon occupation than we saw with the carrier Rabi flopping.

ion temperature bears a very strong resemblance to any other kind of decoherence (for example, due to intensity noise), so this is only a reliable estimate of the temperature when we can already check that a sideband-cooled ion displays a much longer coherence time, and hence that the decay in contrast is primarily an indication of the ion temperature (which is typically the case for our experiment).

A more sensitive probe at low temperature (e.g. $\bar{n} < 3-4$) takes advantage of the stronger dependence on n of the *sideband* Rabi frequency. Instead of measuring the asymmetry between the sidebands, we simply drive red-sideband Rabi flopping

on a single ion, and fit the resulting trace (as seen in Figure 3.8) to

$$P(\uparrow) = \sum_n P(n, \bar{n}) \cos^2(\eta\sqrt{n}\Omega t), \tag{3.8}$$

using the fact that the red-sideband Rabi frequency depends on n as $\eta\sqrt{n}\Omega$ for an ion in the Lamb-Dicke regime [51]. These two methods tend to agree reasonably well when $\bar{n}$ is between perhaps 1 and 4. For lower temperature, the washing out of the carrier Rabi flopping is so minute as to be difficult to distinguish from other sources of decoherence in the Rabi flopping, and for higher temperature, the sideband Rabi flopping is too washed out to get a precise estimate of $\bar{n}$ (and additionally, higher-order corrections like the Debye-Waller factors above may start to become relevant).

We also characterize the motional heating rate by measuring the temperature of a sideband-cooled ion as a function of the time after sideband cooling. This should be relatively constant, but we've seen it change over time for unknown reasons, perhaps because of stray Yb or some other contaminant settling on the electrodes. In July 2012, the heating rate was roughly 20 quanta per second, but in November 2013, it was roughly 130 quanta per second. In the November 2013 measurement, we additionally checked whether the heating rate increased when the Raman lasers were turned on during the waiting time, and found no difference (i.e., the 355 nm light did not seem to cause any additional heating).

3.3.3.2 Sideband parameters for different axial confinements

We change the DC endcap voltages, and hence the axial trap frequency, as one way of varying the power law with which our interactions decay. When we do so, there are some other changes that need to be made or calibrated.

Firstly, the axial trap frequency must be characterized. Because we deliberately set the geometry of the Raman lasers to be minimally coupled to this direction of motion, we must infer this indirectly from the transverse mode spectrum. The center-of-mass frequencies of the transverse and axial directions and the frequency of the transverse 'tilt' mode are related by $\nu_{COM,z}^2 = \nu_{COM,x}^2 - \nu_{tilt,x}^2$. Because increasing the axial confinement in this manner also decreases the transverse confinement, we additionally need to reset the frequency used for sideband cooling, which we otherwise leave fixed.

Secondly, we often need to optimize the voltages to minimize micromotion, as well as to rotate the angle of the principal trap axes to optimize their alignment with respect to the Δk of the Raman beams. In practice, we use the same signal for both of these, and simply adjust the voltages to maximize the carrier Rabi frequency with the Raman lasers. As detailed above, the Rabi frequency will be suppressed by any coupling to hot modes of motion, and since we only sideband cool one set of transverse modes, the modes along other axes (especially the axial modes) will be hot enough to see a slight effect when Δk couples to them, so optimizing the alignment of the trap axes should maximize the Rabi frequency. At the same time, any excess micromotion along Δk will also reduce the Rabi frequency because the oscillatory

Doppler shifts will modulate the frequencies seen by the ion, so maximizing the Rabi frequency also ensures that we have minimized the micromotion in this direction.

3.3.3.3 Coupling to unwanted Zeeman levels

Because our Raman beams nominally have horizontal polarization, and the magnetic field is nominally vertical, the Raman lasers should have no π polarization and hence should not be able to drive transitions from $|F = 0, m_F = 0\rangle$ to $|F = 1, m_F = \pm 1\rangle$. We periodically make small adjustments of the currents to the magnetic field coils and of the polarizations of the Raman beams to minimize the coupling to these unwanted transitions. We tend to be able to extinguish one of these transitions very well at the expense of coupling more strongly to the other, so typically we choose to operate under conditions where the two transition strengths are roughly equal, with Rabi frequencies of 10-20 kHz (for a power corresponding to a $\sim$1 MHz Rabi frequency on the clock transition). We do this mostly to reduce unwanted off-resonant coupling to these transitions, since the small tweaks that we make do not generally increase the Rabi frequency of the clock transition appreciably.

3.3.3.4 Coherence time of the atom

We perform a variety of checks on the coherence time, in order to distinguish among the effects of different sources of decoherence. The most basic check is to perform a simple Ramsey coherence experiment, in which the delay between a pair

of slightly-detuned $\pi/2$ microwave pulses is varied, and the ion is nominally in the dark between the pulses. An exponential can then be fit to the fringe contrast of this experiment to extract a quantitative estimate of the coherence time. Generally speaking, if Rabi oscillations are clean and coherent well past a π rotation, amplitude noise will not play a role in the dynamics of the Ramsey fringes, and the dominant contribution to their decay is frequency/phase noise between the qubit and the oscillator. We should see that the decay is consistent with a 1/e coherence time of 1 second or better (at some point, we measured this to be 1.2 seconds), though we usually only check out to a delay of a few hundred ms and extrapolate from there, since this is far longer than what we need for our experiments. If this is not the case, it is indicative of some problem with magnetic field noise or optical pumping from residual resonant light, as discussed further below.

We additionally check that when the microwave pulses are replaced by carrier Raman pulses, the Ramsey coherence time does not suffer, which should be the case when the beatnote lock is functioning well. (It is not clear *a priori* that these coherence times should be the same, since the phase of the carrier rotations is dependent on an interferometric optical phase, and it is a bit surprising that this phase is as stable as it seems to be. In practice, though, we are able to attain nice Ramsey fringes with the laser for delays of several hundred ms, whose contrast is consistent with a $\sim$1 second coherence time, so it seems that this optical phase is actually quite stable over timescales of 100 ms or more.) In the past, we used this metric (i.e., different coherence times using microwaves versus lasers to perform the $\pi/2$ rotations) to diagnose a noise source in the beatnote lock circuit that was

affecting the phase stability of the Raman operations.

There are two main sources of decoherence remaining when the ion is nominally in the dark: magnetic field noise, and spontaneous scattering from residual 369 nm light. There are a few ways for us to characterize these separately. Magnetic field noise can be checked by measuring the coherence time of the ± 1 magnetic sublevels. These are typically around half a ms for us, which is much shorter than the timescales over which we see unwanted spontaneous scattering, so they are limited mainly by magnetic field noise. The Zeeman shifts of the different transitions are known: $\sim$1.4 MHz/G for the ± 1 sublevels, and 310 Hz/G^2 or, at 5 G, $\sim$3 kHz/G for the clock transition. Since the ± 1 transitions are roughly 500 times more sensitive to field fluctuations than the clock transition, its coherence time should correspondingly be roughly 500 times longer, if field noise is its main limitation.

We also characterize the spontaneous scattering directly. Scattering from the $|\downarrow\rangle_z$ state is easy to measure by leaving an optically pumped ion in the dark for varying amounts of time and characterizing the rate at which it is pumped to a bright state in the $F = 1$ manifold. However, we find that there is much more scattering from $|\uparrow\rangle_z$ than from $|\downarrow\rangle_z$. This is measured by preparing $|\uparrow\rangle_z$ with a π pulse, leaving this state in the dark for varying amounts of time, and rotating $|\uparrow\rangle_z$ back to $|\downarrow\rangle_z$ with another π pulse. The final rotation is important because most of the 369 nm light is closest in frequency to the $^2S_{1/2}, F = 1$ to $^2P_{1/2}, F' = 0$ transition, which, when causing an excitation and spontaneous emission, will still leave the atom in the $F = 1$ manifold; however, 2/3 of these scattering events will swap the population to one of the $m_F = \pm 1$ states, which is not resonant with the

π rotation back to $|\downarrow\rangle_z$.

The spontaneous scattering caused by resonant light leakage is fairly variable, especially since it seems to depend fairly sensitively on the alignment of the AOMs in the 369 nm beam paths (presumably, this has something to do with certain spots in the AOM crystals scattering more light than other spots). To give a rough estimate of what is typical, the last time the AOMs were tweaked to minimize scattering, there was roughly a 10% probability of the $|\uparrow\rangle_z$ to be scattered into one of the $m_F = \pm 1$ states after 600 ms nominally in the dark.

Currently, a lot of these coherence issues are arguably moot, since our coherence time is very drastically reduced in the presence of the Raman lasers (e.g., during a simulation). However, when we attempt to improve the coherence of our system, having narrowed down the possible sources of decoherence may be helpful. Additionally, as I will discuss a bit later in the chapter, our simulations are beginning to reach a number of spins where we care more about small effects, like the introduction of spontaneous scattering errors from the 369 nm light leakage.

We quantify the dephasing caused by the Raman lasers by performing yet another Ramsey experiment, but with the Raman lasers turned on (with far-off-resonant beatnotes) during the delay between the Raman $\pi/2$ pulses. The coherence time is then reduced to 2-3 ms. This is consistent with other diagnostics we have done; for example, the contrast of Mølmer-Sørensen Rabi flopping between $|\downarrow\downarrow\rangle_z$ and $|\uparrow\uparrow\rangle_z$ decays on a similar timescale. Similarly, increasing the length (and hence decreasing the rate of change) of an adiabatic ramp (like those discussed in the next chapter) results in higher ground state population up until the length of the

experiment exceeds ∼3 ms, after which the population prepared in the ground state again decreases.

There are several indications that the decoherence caused by the Raman lasers is due to intensity fluctuations, and moreover, we believe that these are currently limited by power fluctuations rather than pointing instability. One piece of evidence for this is a measure of the fractional change of the Rabi frequency vs that of a Stark shift. If the main source of decay in a Rabi flopping fringe (or Ramsey fringe) is due to noise in the Rabi frequency (or detuning), the shape of the decay envelope can be estimated with some assumptions about the distribution of the noise. In particular, we assume that the Rabi frequency is given by $\Omega = \Omega_0 + \delta\Omega$, where $\delta\Omega$ is normally distributed with width σ,

$$P(\delta\Omega) = \frac{1}{\sqrt{2\pi}\sigma} e^{-\delta\Omega^2/2\sigma^2}. \tag{3.9}$$

When performing an average over the entire distribution, the Rabi fringes will have a Gaussian envelope:

$$P_\uparrow(t) = \frac{1}{2}\left(1 - e^{2\sigma^2 t^2}\cos(2\Omega_0 t)\right). \tag{3.10}$$

We fit this function with free parameters Ω_0 and σ to both a long Rabi flopping scan (on a sideband-cooled ion) and a Ramsey fringe where the detuning was given by the Stark shift from a detuned red sideband (250 kHz from the center of mass mode with a strength $\eta\Omega$ =75 kHz). In the first case, the Rabi frequency was 1085 ± 35

kHz (i.e., the fit resulted in $\Omega_0 = 1085$ kHz and $\sigma = 35$ kHz), indicating fluctuations of 3% in the laser intensity, which is consistent with photodiode measurements of the Raman laser power noise. In the second case, the Stark shift was 38.4 ± 2.3 kHz, for a fractional change of 6%; because the measured shift is the 4-photon Stark shift mentioned earlier, which scales as the square of the intensity, this is also consistent with the fluctuations being caused by intensity noise on the level of 3%.

We have also made comparisons of the coherence time with the Raman lasers on as a function of the final lens positions, i.e., the beam waist at the ion. The assumption made here is that a smaller beam waist is more sensitive to pointing instability. These measurements were done with beam waists corresponding to peak Rabi frequencies of $\sim$2000 kHz, $\sim$1000 kHz, and $\sim$500 kHz. We found that at the tightest focus (Ω_{max} $\sim$2000 kHz) with the Raman 2 power set for $\Omega \sim 1000$ kHz, the coherence time was shorter than at the lens positions where Ω_{max} $\sim$1000 kHz. On the other hand, a similar comparison between the Ω_{max} $\sim$1000 kHz and Ω_{max} $\sim$500 kHz lens positions did not show a significant decrease in the coherence time. We therefore have been operating with the lenses at the Ω_{max} $\sim$1000 kHz positions, and interpret these results as evidence that we are in a regime where the dominant contribution to intensity noise is laser power noise. (Making the focus as tight as possible, though, clearly increased the pointing instability.)

3.4 Fidelity considerations for scaling to larger chains

One consideration that has so far not been a big concern for us is the exponential compounding of errors with system size. By this I mean the fact that if the error rate (due to spontaneous emission, imperfect initialization, etc.) is x for a single ion, the fidelity for an N ion simulation will scale like $(1-x)^N$. This has not been so big of an issue thus far, both because we tend to work with shortish chains (most of the experiments in this thesis were performed with 11 or fewer spins) and because the ion system is inherently fairly clean. For example, in spectroscopy data displayed in Chapter 6, we see that there is an 80% probability of measuring the $|\uparrow\uparrow\uparrow\uparrow\uparrow\uparrow\uparrow\uparrow\rangle_x$ state that we expect to be making with good fidelity, and working backwards from $0.8^{1/8} = 0.97$, we can infer that the probability of errors is 3% for a single spin, which we might not consider unreasonable. But for a 30 spin system with this level of fidelity, the chances of performing the experiment without an error go down to 43%, even without taking into account the fact that the average error per ion may be higher with so many ions. It will thus become important to optimize all our parameters more carefully as we work toward larger systems; while errors on the order of 1% in (e.g.) optical pumping, π rotations, etc, make very little difference with a few ions,

However, there will be sources of error that may be less amenable to improvement with not-too-major technical upgrades. With the current setup, I believe the next hard limitation we will run into, where we might be unable to improve the error without a major reconfiguration of the experiment, may be spontaneous emission

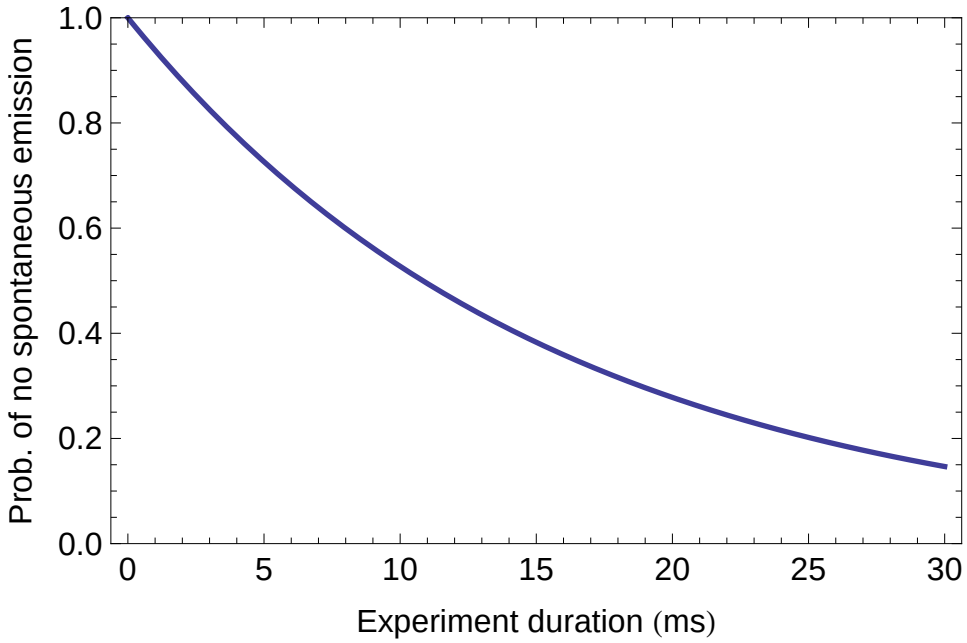

Figure 3.9: Probability that there are NO spontaneous emission events from the Raman lasers vs. experiment duration, assuming a laser power corresponding to a carrier Rabi frequency of 1 MHz.

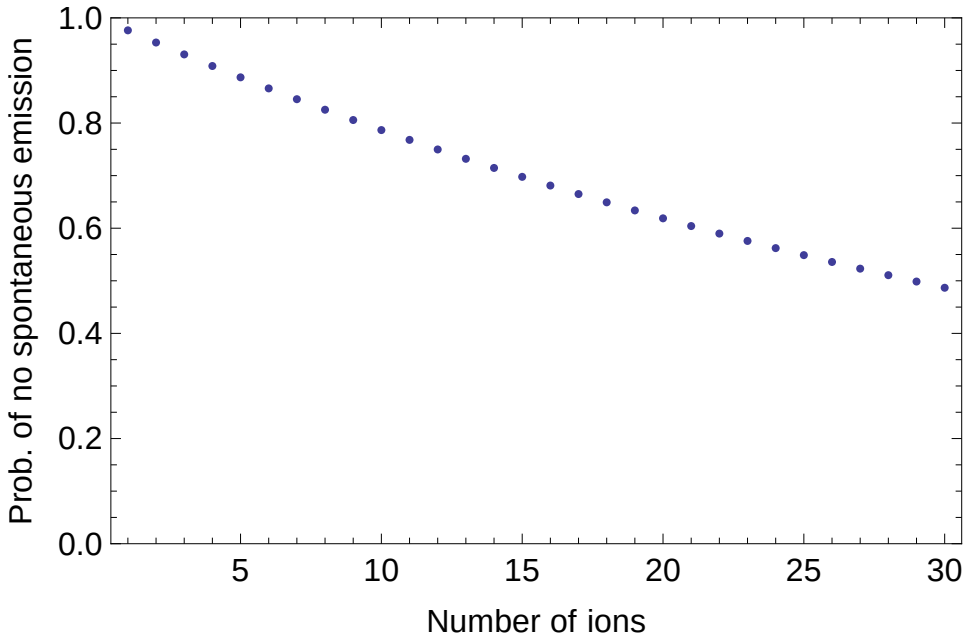

Figure 3.10: Probability that there are NO spontaneous emission events from the Raman lasers vs. ion number, assuming a laser power corresponding to a carrier Rabi frequency of 1 MHz and an experiment duration of 3 ms.

due to the Raman lasers. Earlier, we calculated that the spontaneous emission rate is roughly 4 $\times 10^{-6}$ of the Rabi frequency. With a laser power corresponding to a carrier Rabi frequency of 1 MHz, this means that if we model the probability of NOT having a spontaneous emission event from the Raman beams as $e^{-t/\tau}$, we can estimate the time constant to be $\tau = 125$ ms. This sounds long compared to our experiment durations, but it means the fidelity of a 3 ms experiment can at best be $\sim$98%. Some plots of the dependence on experiment duration and ion number are shown in Figures 3.9 and 3.10. This issue could potentially be circumvented to some degree by increasing the laser intensity, since the interaction strengths $J_{i,j}$ scale as the square of the intensity and the spontaneous emission rate scales linearly with intensity, but this solution may be technically and/or fiscally challenging. In the long run, the solution to the more general fidelity problem will probably be to circumvent it by choosing robust observables - for example, measuring correlations between pairs of spins will (ideally) be no more prone to errors in large spin chains than in smaller ones.

Chapter 4: Ground state studies in the transverse-field Ising model

For a variety of reasons, most of the first trapped ion quantum simulations of interacting spins were focused on the study of ground states of the transverse field Ising model [19–24, 44]. A transverse-field Ising model (one of the easiest spin systems to create using trapped ions) is one of the simplest models to admit a quantum phase transition [62], and hence the ability to study the ground states of this model enables various investigations regarding the physics of quantum phase transitions. Indeed, one of the explicit goals of quantum simulation experiments early on was the mapping of phase diagrams of various interesting quantum systems, although in recent years more emphasis has been placed on studying dynamics. Furthermore, the ability to prepare nontrivial ground states of the Ising model could be useful as a starting point for other studies. We will also return to ground states at the end of the thesis when I discuss our recent experiments in a spin-1 system.

Ground state preparation has been a valuable tool, allowing us to probe the effects of new 'knobs' in the experiment like the ability to continuously tune the interaction range (and hence level of frustration), as discussed further toward the end of the chapter, or the ability to add a more general effective magnetic field. These results have been published in [22] (focused on the creation of antiferromagnetic

ground states and the detection of variable frustration via the fidelity of the ground state preparation), [23] (investigating the effects of different ramping schemes on the errors introduced from non-adiabaticity), and [24] (introducing a global longitudinal field in addition to the transverse field, and observing the phases resulting from the dependence of the ground state on the relative strength of the longitudinal field). Additionally, the studies of antiferromagnetism in [22] are discussed in Rajibul Islam's thesis, and the studies of the longitudinal field in [24] are discussed in Simcha Korenblit's thesis. Here, I very briefly discuss the experiments on frustrated antiferromagnetism to give a flavor of the motivation for pursuing these ground state studies.

4.1 Brief sketch of the general adiabatic protocol

As discussed previously, the spin model we implement for these studies is given by

$$H = \sum_{i<j} J_{i,j}\sigma_i^x\sigma_j^x + B_y(t)\sum_i \sigma_i^y = H_J + H_B, \tag{4.1}$$

where σ_i's are the spin-1/2 Pauli matrices for the ith spin; sums run from 1 to N, the number of ions; $B_y(t)$ is the time-dependent strength of an effective transverse magnetic field, and $J_{i,j}$'s are the strengths of the spin-spin coupling, which are in general long-range for a trapped ion experiment and roughly follow a power law decay with distance, $J_{i,j} \sim J_0/|i-j|^\alpha$, for the experiments in this thesis.

The protocol for preparing the ground state of the pure Ising model, at $B_y = 0$, exploits the fact that we have access to a trivial Hamiltonian whose ground state

is known and easily prepared: when the couplings are turned off, $J_{i,j} = 0$, we have merely

$$H_B = B_y \sum_i \sigma_i^y. \tag{4.2}$$

The ground state of this Hamiltonian is clearly a polarized state with all spins pointing along y on the Bloch sphere, $|\psi_0\rangle = |\rightarrow\rightarrow\cdots\rightarrow\rangle_y$. Conveniently, this is one of the few states that is easy for us to prepare, by optically pumping the spins to $|\downarrow\downarrow\cdots\downarrow\rangle_z$, then performing a coherent global rotation with the Raman lasers.

Having prepared the known ground state of a trivial Hamiltonian, we can now slowly turn off the transverse field Hamiltonian and turn on the Ising couplings, as illustrated in Figure 4.1; if done properly, the spins will adiabatically follow the instantaneous ground state, and end in the Ising ground state that we were interested in, i.e. the ground state of

$$H_J = \sum_{i<j} J_{i,j} \sigma_i^x \sigma_j^x. \tag{4.3}$$

Alternatively, the ramp can be stopped at any value of B_y/J_0, for example, to probe the region near the phase transition.

For historical reasons, we modify this protocol slightly to leave the Ising couplings continuously on, while ramping only the effective magnetic field (Figure 4.1(b)). We thus start with a large magnetic field, $B_y \gg J_0$, such that the polarized state we prepare has nearly a 100% overlap with the true ground state. The initial value of the transverse field is typically chosen to be around 5-10J_0, which for most of the experiments described here corresponds to roughly a 99% overlap between the polarized state and the true initial ground state. This is chosen as a

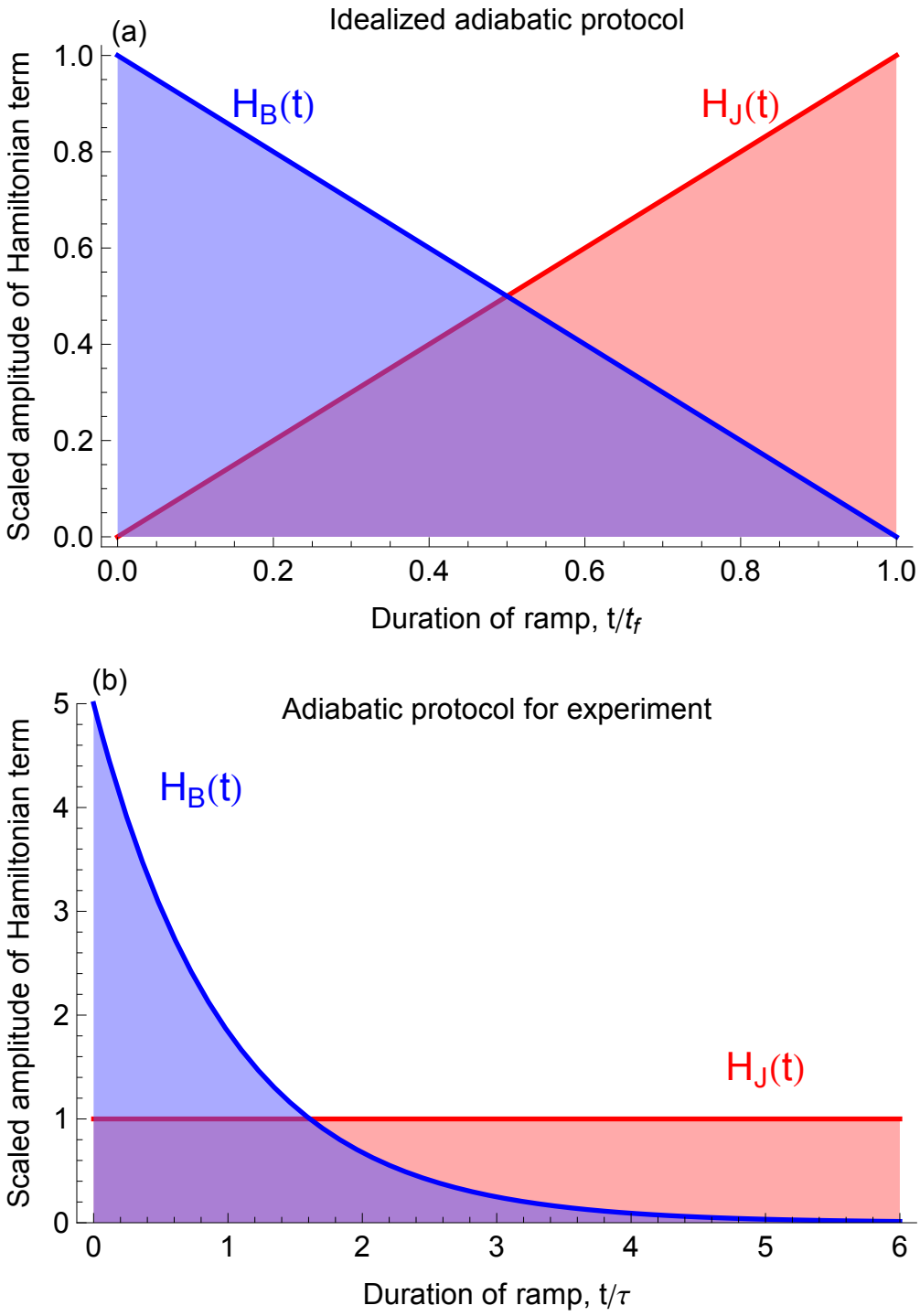

Figure 4.1: Illustrations of two different adiabatic protocols. In (a), the ground state of H_B is prepared, and H_B is linearly ramped from full strength to 0 while H_J is simultaneously ramped from 0 to full strength. In (b), H_J is held fixed, and H_B is started at a value sufficiently large that the ground state of H_B that is prepared has a good overlap with the true ground state, then ramped with an exponential time dependence.

reasonable tradeoff among the various sources of error; a larger initial field would improve the fidelity of the initial ground state at the expense of requiring either a faster ramp rate (causing diabatic excitations) or a longer ramp (which makes the experiment more susceptible to decoherence).

The decision to hold H_J static was made because generating the Hamiltonian in 4.1 requires of order $100\times$ more laser power for the J term than for the B_y term, even for $B_y \sim 10J_0$. Since uncontrolled Stark shifts, which scale linearly or quadratically with intensity, can cause dephasing errors, we have historically preferred to hold $J_{i,j}$ constant for purposes of minimizing the *change* in Stark shift, which unlike a static shift cannot be calibrated for as was described in the previous chapter. This was a bigger issue before we switched to using a mode-locked 355 nm Raman laser; in the old setup, the Raman detuning from the $^2\mathrm{P}_{1/2}$ state was only 3 THz (as compared to 33 THz now), and the Stark shifts were much larger.

4.1.1 Different ramp profiles

In theoretical treatments, the Hamiltonian terms are often taken to be linearly dependent on time, since a constant rate of change simplifies many calculations dramatically. However, ramping B_y linearly in our experiments would either introduce large diabatic errors or require an experiment duration that far exceeds the coherence time, as will be discussed more quantitatively below. We therefore take advantage of the fact that the excitation probability depends not only on the rate of change of B_y, but also on the instantaneous energy gap between the ground and first cou-

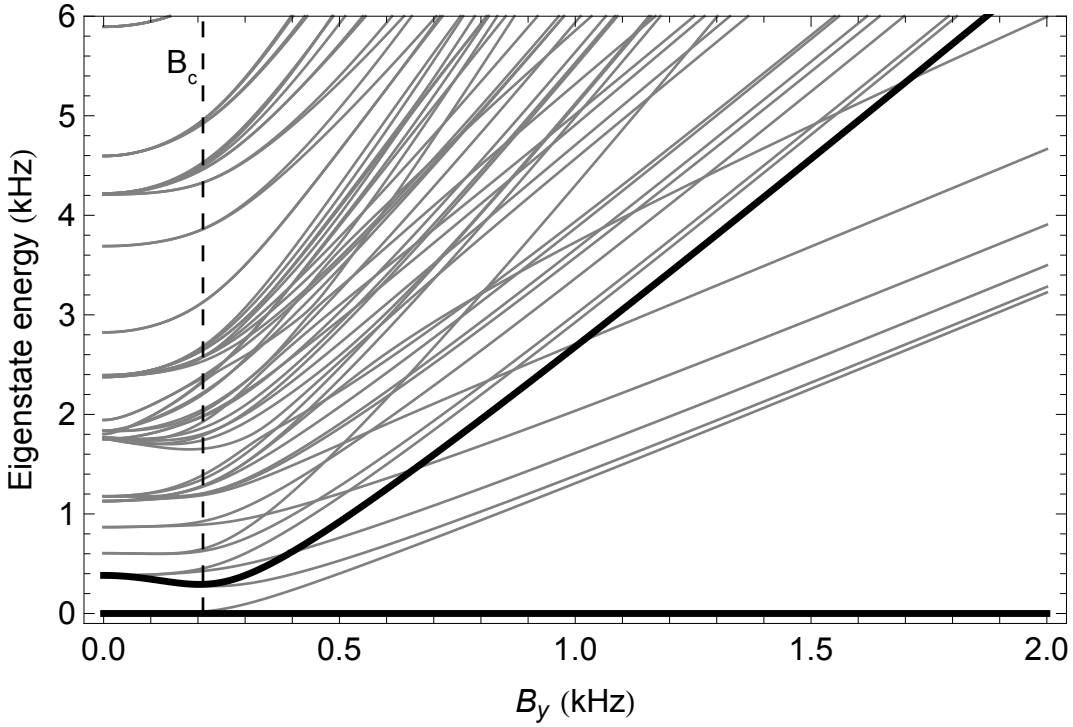

Figure 4.2: Low-lying energies for a system of 6 ions, with Ising coupling profile determined from experimentally measured parameters: center-of-mass trap frequencies of $\nu_z = 0.7$ MHz and $\nu_x = 4.8$ MHz, $\eta\Omega = 27.5$ kHz, and with a detuning of 90 kHz from the center-of-mass mode. Bold lines indicate the ground and first coupled excited states, and the vertical dashed line indicates the critical field value B_c.

pled excited states, to tailor a time profile for $B_y(t)$ that decreases the experiment duration without deviating as far from adiabaticity.

Figure 4.2 shows a typical energy landscape vs. transverse field strength for a system of 6 spins, with antiferromagnetic Ising couplings whose interaction range is given by $\alpha \sim 1$. At large B_y, far from the critical (minimum) energy gap Δ_c, the excess energy of the first coupled excited state is roughly linear with B_y, and then undergoes an avoided level crossing when the B_y and $J_{i,j}$ terms contribute similar energies. Notably, the first *coupled* excited state is not equivalent to the state with the second-lowest energy, as the system can only be excited to a state $|e\rangle$ if the

changing Hamiltonian has a matrix element between $|e\rangle$ and $|g\rangle$, $\langle e|H_B|g\rangle \neq 0$.

To quantify the adiabaticity of a particular ramp schedule, we introduce a parameter

$$\gamma = \left| \frac{\Delta^2(B_y)}{\dot{B}_y(t)} \right|, \tag{4.4}$$

where $\Delta(B_y)$ is the instantaneous energy gap between the ground and first excited states. A larger value of γ means the ramp is more adiabatic at that value of B_y, and hence adiabaticity requires $\gamma \gg 1$. This parameter can be seen to be an appropriate choice in light of the usual adiabaticity criterion [63],

$$\left| \frac{\dot{B}_y(t)\epsilon}{\Delta_c^2} \right| \ll 1, \tag{4.5}$$

where ϵ is a number of order 1 parametrizing the coupling between the ground and excited states, $\epsilon = \text{Max}[\langle e|dH/dB|g\rangle]$. From either of these, we can see that a ramp deviates further from adiabaticity both as the energy gap shrinks and as the ramp rate $\dot{B}_y(t)$ increases.

From these considerations, if we look again at Figure 4.2 it is clear that the field need not be ramped as slowly at large B_y, where there is a large energy gap, as at smaller B_y, near the critical gap. Thus, ramping the field more quickly first and more slowly as we approach the critical gap allows us to decrease the experiment duration without sacrificing adiabaticity. This is fortunate in light of experimentally achievable critical gaps and coherence times. For example, in order to satisfy the criterion $\gamma \gg 1$ for the parameters shown in Figure 4.2 (for which the largest nearest-

neighbor coupling is $J_{\max} = 0.78$ kHz and $\Delta_c = 0.29$ kHz), we would require a linear ramp,

$$B_y(t) = 5J_{max}(1 - \frac{t}{t_f}), \tag{4.6}$$

, to have a duration $t_f \gg 46$ ms, far exceeding the coherence time of the interactions, which is roughly 2.4 ms. Alternatively, a nearly adiabatic ramp ($\gamma = 1$) could be performed in 2.4 ms if the initial field is $B_y(0) = 0.2$ kHz, or roughly $0.25J_{max}$, but in this case the true ground state would have less than a 25% overlap with the prepared ground state of H_B - clearly not a good option either.

It follows that we want $B_y(t)$ to be some decreasing concave-up function of time. We typically choose a decaying exponential with initial value B_0 and time constant τ,

$$B_y(t) = B_0 e^{-t/\tau}, \tag{4.7}$$

chosen because of the simple functional form that displays the desired qualitative criteria. We thus do not ramp the field all the way to zero, but typically choose ramp durations on the order of 6τ, such that the field is decreased to e^{-6} of its initial value. For $B_0 \sim 5J_0$ to $10J_0$, this results in a final field value of $B \sim 0.01J_0$ to $0.02J_0$, deep within the ordered phase where the true eigenstates are well approximated by the H_J eigenstates.

At the critical point of the Hamiltonian shown in Figure 4.2, the rate of change of the exponential ramp is $|\dot{B}_y(t)| = 0.3B_0/t_f$. Adiabaticity then requires $t_f \gg 14.5$ ms, a factor of 3 less time than the requirement found for linear evolution. Note that the adiabaticity gains of exponential ramps can be realized whenever the critical gap

occurs towards the end of a linear ramp ($B_c/B_0 < \tau/t_f$), which is generally the case for the Ising Hamiltonian (Eq. 4.1).

It is possible to further optimize the adiabaticity of a ramp using knowledge of the energy structure of the Hamiltonian. Such local adiabatic ramps keep the adiabaticity γ fixed at all points along the evolution by adjusting $\dot{B}(t)$ based on the instantaneous gap $\Delta(B(t))$ [64,65]. Specifically, a local adiabatic ramp would follow the profile $B(t)$ that solves the differential equation 4.4 with γ fixed.

To solve Eqn. 4.4, it is necessary to know $\Delta(B)$ everywhere along the evolution. This requires knowledge of the first *coupled* excited state of the N-spin Hamiltonian (Eq. 4.1), which, for the system sizes we have checked, is always the 3^{rd} excited state at small B and the $(N+1)$th excited state at large B. Determining the local adiabatic evolution profile therefore relies on calculation of only the lowest $\sim N$ eigenvalues, which is much more computationally approachable than direct diagonalization of a $2^N \times 2^N$ matrix [66].

For a local adiabatic ramp, the critical time t_c may be calculated by integrating Eq. 4.4. Since $\dot{B}(t)$ is negative throughout the evolution, we find

$$t_c = \gamma \int_{B_c}^{B_0} \frac{dB}{\Delta^2(B)} \tag{4.8}$$

Similarly, we may calculate the total evolution time

$$t_f = \gamma \int_{0}^{B_0} \frac{dB}{\Delta^2(B)} \tag{4.9}$$

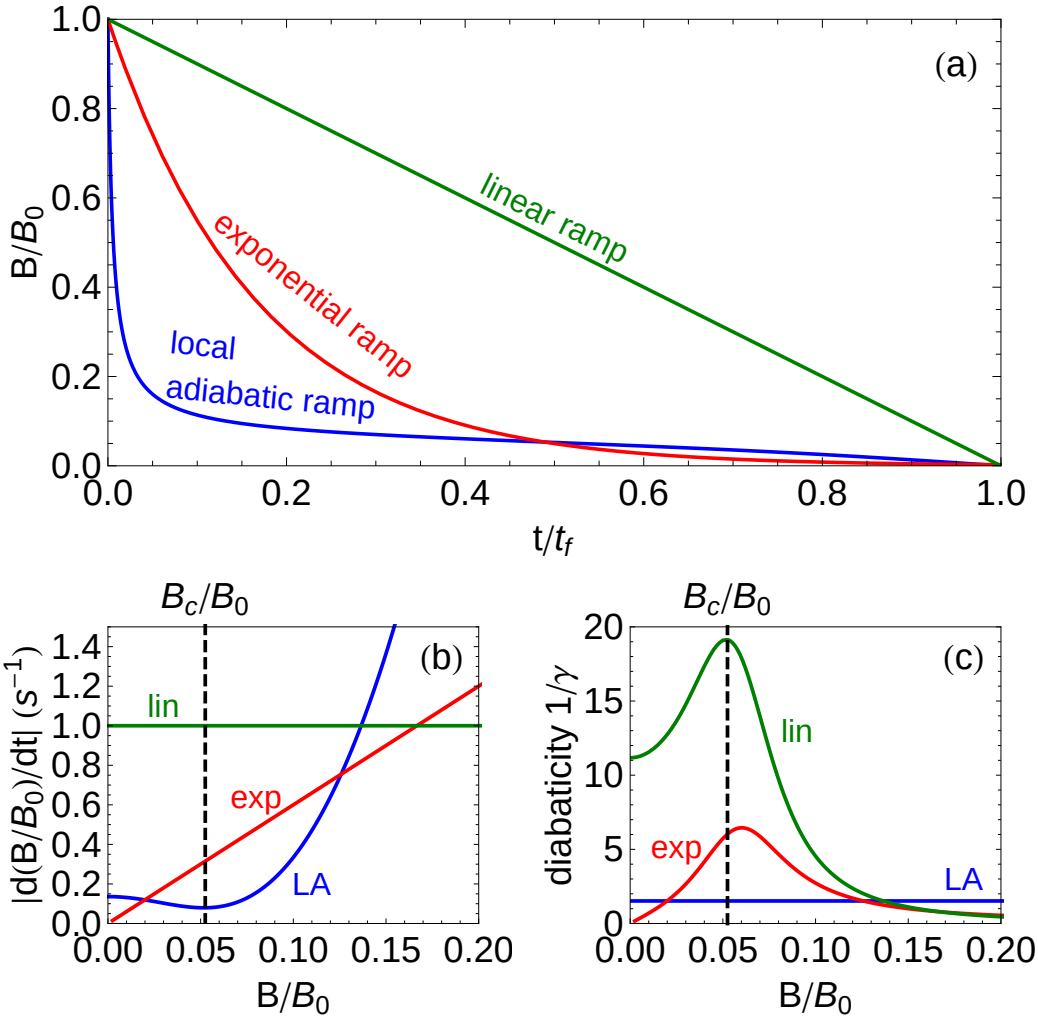

Figure 4.3: (a) Local adiabatic ramp profile calculated for the energy levels in Figure 4.2, along with a linear ramp and an exponential ramp with decay constant $\tau = t_f/6$. (b) The slope of the local adiabatic (LA) ramp is minimized at the critical field value B_c, and is smaller than the slopes of the exponential and linear ramps at the critical point. (c) The inverse of the adiabaticity parameter γ (see text) is peaked near the critical point for exponential and linear ramps but constant for the local adiabatic profile.

which shows a linear relationship between the total time t_f and the adiabaticity parameter γ. Satisfying the adiabaticity condition $\gamma \gg 1$ for the Hamiltonian in Figure 4.2 implies $t_f \gg 3.6$ ms (for these ramps we assume that the field is taken all the way to zero), a factor of 4 and 12 less time than exponential and linear ramps, respectively. The fact that local adiabatic evolution can lead to faster ramps while satisfying adiabaticity has been well-explored in Ref. [64], where it was shown that local adiabatic ramps could recover the quadratic speedup of Grover's quantum search algorithm. In contrast, it was found that linear ramps offer no improvement over classical search [67].

Figure 4.3(a) compares a linear, exponential, and local adiabatic ramp profile for the Hamiltonian shown in Figure 4.2. The local adiabatic ramp spends much of its time evolution in the vicinity of the critical point, since the transverse field changes slowly on account of the small instantaneous gap. This is further illustrated in Figure 4.3(b), which shows that at the critical point, the slope of the local adiabatic ramp is minimized and smaller than slopes of the exponential or linear ramps. As a result, the inverse of the adiabaticity parameter, $1/\gamma$, is peaked near the critical point for exponential and linear ramps, greatly increasing the probability of non-adiabatic transitions away from the ground state (see Figure 4.3(d)). By design, the local adiabatic ramp maintains constant adiabaticity for all values of B and does not suffer from large non-adiabaticities near B_c.

We theoretically calculate and experimentally measure the ability for each of the ramp profiles described above to prepare our spin system into the ground state of Eqn. 4.1 at $B = 0$. For this measurement, we use $N = 6$ ions and create antifer-

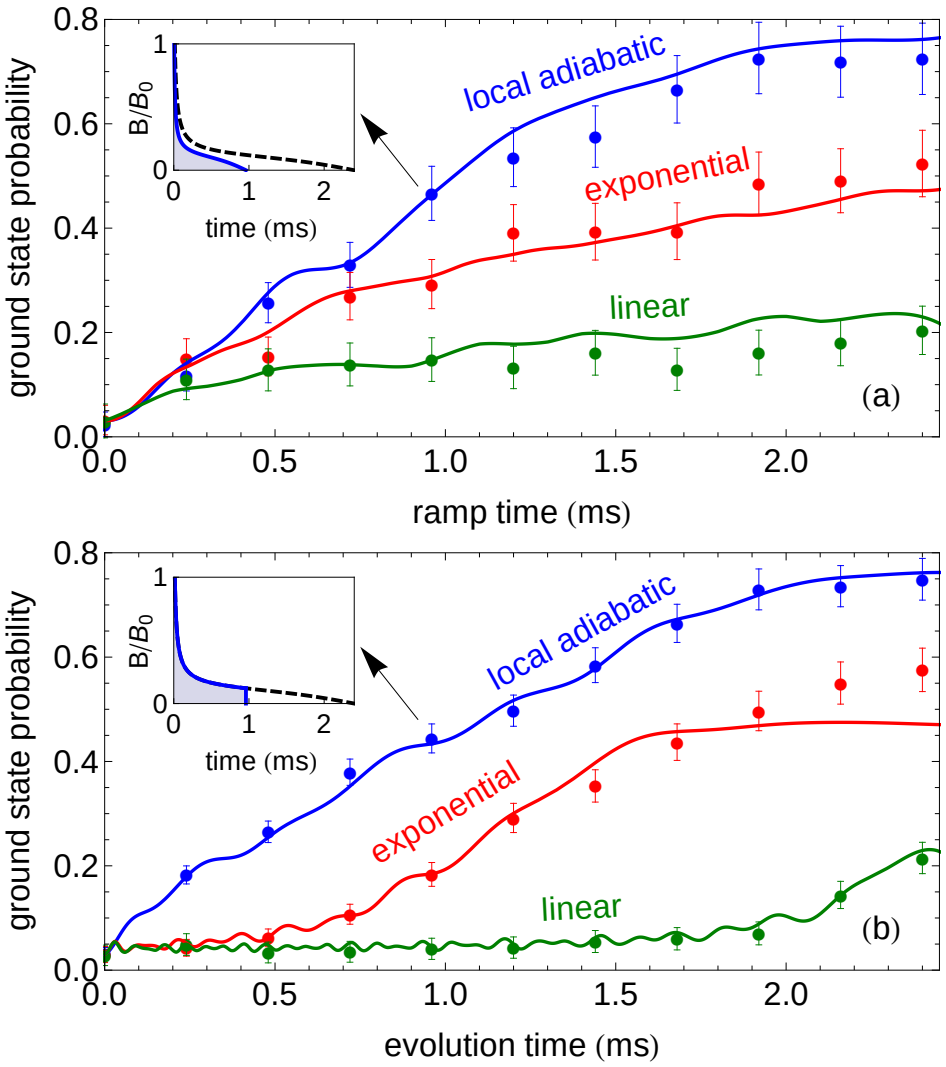

Figure 4.4: (a) Probability of preparing the AFM ground state (i.e., either of the $|010101\rangle$ or $|101010\rangle$ configurations) after local adiabatic, exponential, and linear ramps with t_f varied from 0 to 2.4 ms. The local adiabatic ramp gives the ground state with highest probability. Solid lines indicate the theoretical prediction. Inset: 0.96 ms local adiabatic ramp profile compared to the 2.4 ms profile (dotted). (b) Probability of preparing the AFM ground state for various times during $t_f = 2.4$ ms simulations with three different ramp profiles. The linear ramp takes ∼2.3 ms to reach the critical point, while the local adiabatic and exponential ramps need only 1.2 ms. The inset shows the 2.4 ms local adiabatic profile evolved for 0.96 ms. The end points of parts (a) and (b) differ slightly in the experiment because these are two separate data sets.

romagnetic spin-spin interactions of the form $J_{i,j} = (0.77 \text{ kHz})/|i-j|$. These long-range antiferromagnetic interactions lead to a fully-connected, frustrated system as all pairwise coupling energies cannot be simultaneously minimized. Nevertheless, the ground state of the system is easily calculable for 6 spins and is found to be a superposition of the two Néel-ordered AFM states, $(|010101\rangle + |101010\rangle)/\sqrt{2}$, as would be the case for nearest-neighbor interactions.

Figure 4.4(a) shows the probability of creating the AFM ground state when the transverse field $B(t)$ is ramped using linear, exponential, and local adiabatic profiles. The total ramp time t_f is varied from 0 to 2.4 ms, with a new ramp profile calculated for each t_f. Each data point is the result of 4000 repetitions of the same experiment. In agreement with the predictions above, the data show that local adiabatic ramps prepare the ground state with higher fidelity than exponential or linear ramps.

The solid lines in Figure 4.4 plot the theoretical prediction of the ground state probability with no free parameters. In each case we begin by numerically integrating the Schrödinger equation using Hamiltonian 4.1 with the desired $B(t)$ and the initial state $|\psi(0)\rangle = |000\ldots\rangle_y$. At the end of the ramp we calculate $|\langle\psi(t_f)|\psi(t_f)\rangle|^2$ and extract the probability of the ground state spin configuration. We account for decoherence-induced decay of the ground state probability by multiplying the calculated probability at time t by $\exp[-t/t_d]$, where t_d is the measured $1/e$ coherence time of our spin-spin interactions.

The fact that local adiabatic ramps do not yield 100% ground state probability at $t_f = 2.4$ ms is not surprising, given that the adiabatic condition is $t_f \gg 3.6$ ms for

our experimental parameters. For comparison, the $\sim 80\%$ ground state population found with a 2.4 ms local adiabatic ramp would take an exponential (linear) ramp 9.7 ms (29 ms) to achieve – a factor of 4 (12) longer. However, these significantly longer ramps do not yield high-fidelity ground state preparation in practice, since significant spin decoherence effects arise in our experiment after about 2.4 ms. Local adiabatic ramps therefore offer the best way to prepare the ground state with high probability.

The data in Figure 4.4(b) show how the ground state probability grows during a single 2.4 ms linear, exponential, or local adiabatic ramp. The ground state population grows quickly under local adiabatic evolution since the transverse field $B(t)$ is reduced quickly at first. In contrast, the linear ramp does not approach the paramagnetic to AFM phase transition until ~ 2 ms, and the AFM probability is suppressed until this time. Once again, local adiabatic ramps show the largest ground state probability at each time.

4.1.2 Prevalence of the ground state

In our experiments, there is typically some diabatic error resulting from the inability to ramp the Hamiltonian slowly enough to prevent excitations, even when we use optimized local adiabatic ramps. (The ultimate limiting factor from a technical perspective is the coherence time of the interactions, which prevent us from making the ramp infinitely long.) This may hinder the identification of unknown ground states in many cases. However, in the protocol described above, the ground state

will always be the most prevalent state, subject to certain conditions (in particular, including that the ramp is not truly instantaneous).

The reasoning behind this claim can be laid out in a qualitative argument. In the protocol described above, we begin in the state $|{\rightarrow}{\rightarrow}\cdots{\rightarrow}\rangle_y$. This is an equal superposition of all of the σ^x eigenstates, which are clearly eigenstates of the Ising Hamiltonian H_J above. Hence, in a perfectly instantaneous ramp, i.e. suddenly turning on H_J with $B_y = 0$, every eigenstate is equally probable (and in particular, measuring the ground state is exactly as likely as measuring any other state). At the other extreme, if the ramp is perfectly adiabatic, the ground state will be fully populated. In an intermediate case where the field $B_y(t)$ is ramped at a fast but finite rate, the quantum simulation is more adiabatic than in the instantaneous case, and the ground state is slightly more prevalent than any other state. Thus, our ability to measure the probability of creating each of the 2^N spin configurations along σ^x allows us to identify a ground state.

We test this experimentally by measuring the probability for all of the 64 spin states at each local adiabatic ramp data point in Figure 4.4(a). These probabilities are shown in Figure 4.5. When the total ramp time is 0.00 ms (i.e. instantaneous), we measure a distribution with nearly equal probability in each of the possible states, as expected. As the total ramp time is made longer (up to 2.4 ms), the populations in the two degenerate AFM ground states emerge as the most probable compared to any other spin configuration.

A more formal argument for why the ground state should be most prevalent can be made by way of analogy to a Landau-Zener process [68] in a two-level system

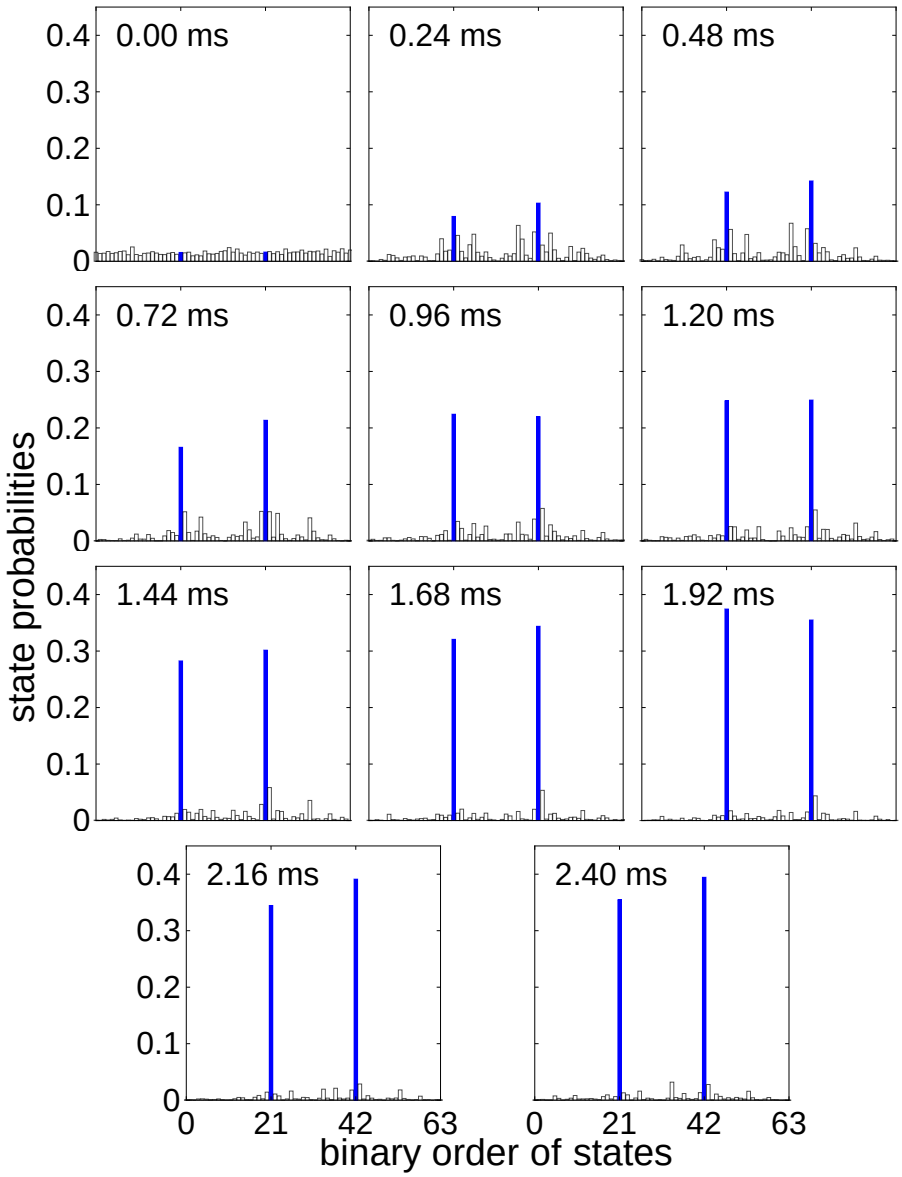

Figure 4.5: State probabilities of all $2^6 = 64$ spin configurations for each local adiabatic data point in Figure 4.4(a), ordered in binary notation (e.g., $|010101\rangle = 21$ and $|101010\rangle = 42$). The two degenerate AFM states (solid blue) are the most prevalent for all times.

comprised of the ground and first coupled excited states. In the Landau-Zener framework, a system that starts in the state $|{\rightarrow}{\rightarrow}\cdots{\rightarrow}\rangle_y$, the ground state of the Hamiltonian in Eq. 4.1 when $B_y/J_0 \gg 1$, will be transformed into the new ground state $|{\leftarrow}{\leftarrow}\cdots{\leftarrow}\rangle_y$ at $B_y/J_0 \ll -1$ if $B_y(t)$ is ramped adiabatically. Likewise, an instantaneous switch from $B/J \gg 1$ to $B/J \ll -1$ will leave the system in an excited state with 100% probability.

Our experiment most closely resembles half of a Landau-Zener process, in which $B_y(t)$ starts with $B_y \gg J_0$ and ends at $B_y = 0$. One can write an analytic expression to calculate the transition probability for this half-Landau-Zener evolution [69], which has a maximum value of 0.5 for an instantaneous ramp. Any fast but finite ramp will give a transition probability < 0.5, and the ground state will always be more prevalent than the excited state.

The technique of identifying the most prevalent state as the ground state is subject to some limitations. First, the initial state (before the ramp) should be a uniform superposition of all spin states in the measurement basis – a condition satisfied by preparing the state $|{\rightarrow}{\rightarrow}\cdots{\rightarrow}\rangle_y$ and measuring along $\hat{x}$. If some spin states are more prevalent than the ground state initially, then some non-zero ramp time will be necessary before the ground state probabilities "catch up" and surpass these initially prevalent states. Second, the ramp must not pass through any real energy crossings (as distinct from the avoided level crossing of the Landau-Zener problem), or first-order phase transitions. Third, the ground state must not contain a higher number of spin configurations (due to degeneracy or because it is a nondegenerate superposition of many configurations) than the first coupled excited state, as this

also places some non-zero limitation on the ramp time.

Another consideration in determining the ground state is that the difference between the measured ground state probability P_g and next excited state probability P_e must be large compared with the experimental uncertainty, which is fundamentally limited by quantum projection noise $\sim 1/\sqrt{n}$ after n repetitions of the experiment [70]. That is, we require

$$P_g - P_e > \sqrt{\Delta P_g^2 + \Delta P_e^2}, \tag{4.10}$$

where $\Delta P_i^2 = P_i(1 - P_i)/n$ is the variance in the estimate of P_i from quantum projection noise. Manipulating the expression

$$P_g - P_e > \sqrt{\frac{P_g(1 - P_g)}{n} + \frac{P_e(1 - P_e)}{n}}, \tag{4.11}$$

we find the required number of experiments is given by

$$n > \frac{P_g(1 - P_g) + P_e(1 - P_e}{(P_g - P_e)^2}. \tag{4.12}$$

In a large system undergoing a diabatic ramp, the probability of creating the ground state will be small ($P_g \ll 1$, implying that also $P_e \ll 1$), allowing us to simplify this expression to

$$n > \frac{P_g + P_e}{(P_g - P_e)^2}. \tag{4.13}$$

Assuming an exponential distribution of populated states during the ramp (as

may be expected from Landau-Zener-like transitions), the number of required runs should then scale as $n \sim (\bar{E}/\Delta)^2$ in the limit $\bar{E} \gg \Delta$, where $\bar{E}$ is the mean energy imparted to the spins during the ramp, and Δ is the energy splitting between the ground and first coupled excited state.

As the system size N grows larger, two effects contribute to a shrinking critical gap Δ_c, further reducing the adiabaticity of transverse-field ramps in the context of our frustrated AFM system. The first is the well-known result for transverse-field Ising models that $\Delta_c \to 0$ as the system size approaches the thermodynamic limit $N \to \infty$ [62]. The second effect arises from the fact that identical laser and trap parameters produce longer-range interactions at larger N, which lead to more frustration and smaller energy gaps in the system [22], as we will discuss further below.

To show the potential scaling power of local adiabatic evolution, we perform quantum simulations with up to 14 ions. In this regime, we are unable to directly calculate the local adiabatic ramp profile using a standard desktop computer due to the exponential growth of the computation time (just building a $2^{14} \times 2^{14}$ matrix of machine-sized 64-bit numbers requires 2 GB of RAM). Instead, we approximate the gap $\Delta(B)$ by the piecewise function

$$\Delta(B) = \begin{cases} \Delta_c & \text{if } B \leq B_c \\ \Delta_c + 4(B - B_c) & \text{if } B > B_c \end{cases} \tag{4.14}$$

with B_c and Δ_c extrapolated from calculations for 3-10 ions. This $\Delta(B)$ is then used

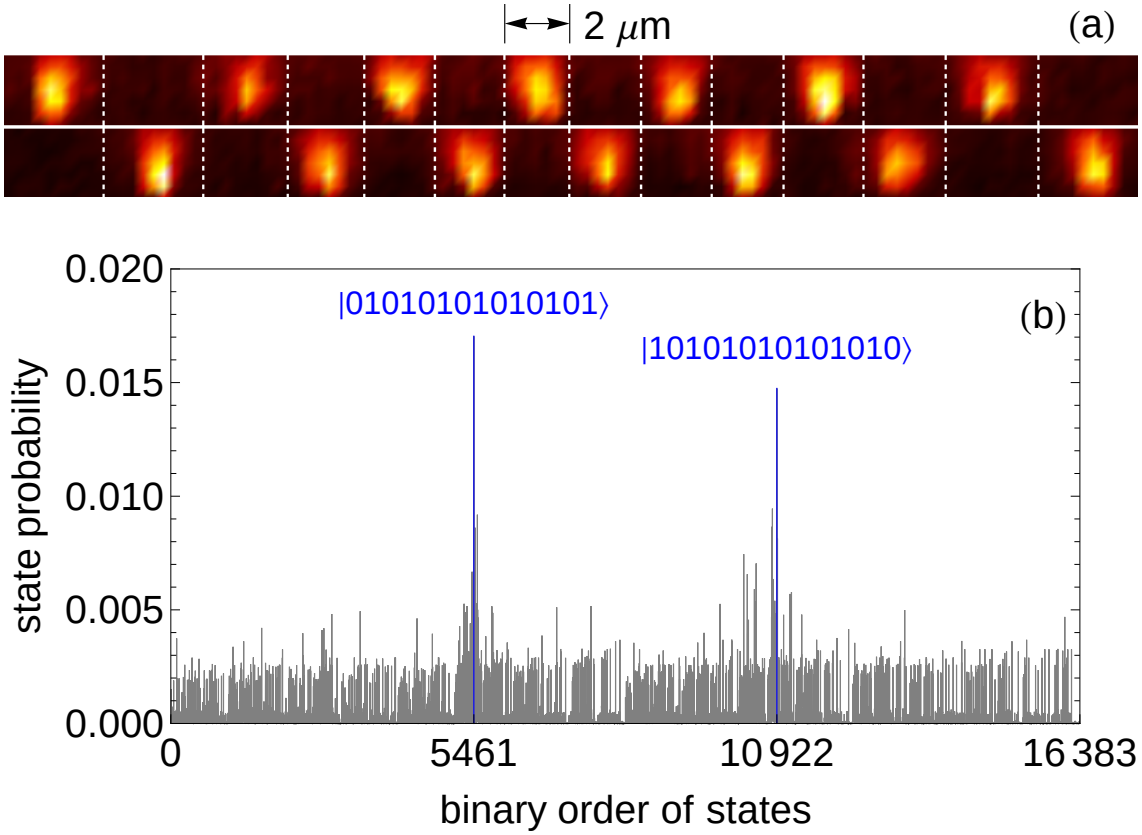

Figure 4.6: (a) Camera images of experimentally prepared AFM ground states for $N = 14$. (b) State probabilities of all $2^{14} = 16384$ spin configurations for the 14-ion local adiabatic ramp described in the text. The Néel-ordered ground states are unambiguously the most prevalent, despite a total probability of only 3%.

to solve the differential equation 4.4. For $N > 10$ the ramp thus found continues to outperform exponential and linear ramps, as seen in Figure 4.6.

4.2 Studies of variable frustration

The ideas discussed above were used in our experiments demonstrating control over the amount of frustration in a long-range antiferromagnetic spin chain [22], though chronologically the frustration studies were performed earlier. In these experiments, we exploited the fact that for a more long-range interaction profile

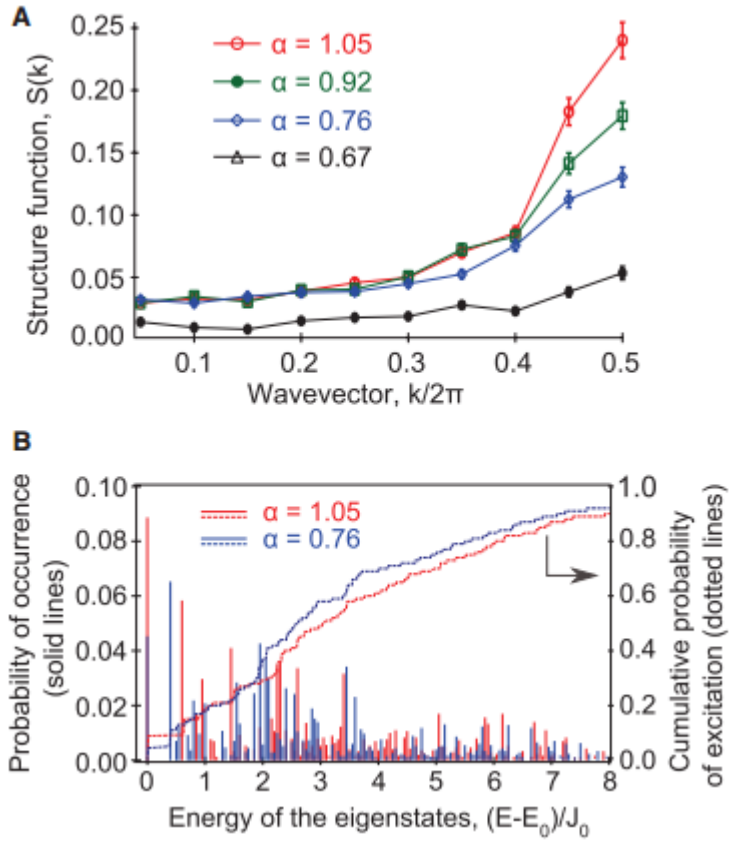

Figure 4.7: (a) Structure function $S(k)$ versus wave vector k for various ranges of interactions, corresponding to different degrees of frustration, in a system of 10 spins. The increased level of frustration for the longer-range interactions reduces the antiferromagnetic spin order, here signified by a peak at $k = \pi$. The detection errors may be larger than shown here for the longest range of interactions, for which the decreased ion spacing may have increased spatial crosstalk. (b) Distribution of observed states for two different ranges of interaction, sorted according to their energy, which for 10 spins can be exactly calculated from Eq. 4.1 with $B = 0$. The dashed lines indicate the cumulative distribution functions for these two interaction ranges.

(smaller α), corresponding to a greater degree of frustration, the critical gap for antiferromagnetic interactions decreases. From the arguments we have already seen, it is clear that applying ramps with a fixed profile (here, an exponential with initial value $B_0/J_0 = 5$ and time constant $\tau = 400$ μs) will thus result in increased diabaticity and hence lower ground state fidelity for a more frustrated system.

Figure 4.7(a) shows this effect by plotting the structure function $S(k)$ for various interaction ranges. The structure function is essentially the spatial Fourier transform of the averaged two-point correlation functions; it is defined as

$$S(k) = \frac{1}{N-1}\left|\sum_{r=1}^{N-1} C(r)e^{ikr}\right|, \tag{4.15}$$

where $C(r) = \frac{1}{N-r}\sum_{m=1} N - rC_{m,m+r}$ is the average correlation between spins r sites apart, and the connected correlation function is

$$C_{i,j} = \left\langle \sigma_i^x \sigma_j^x \right\rangle - \left\langle \sigma_i^x \right\rangle \left\langle \sigma_j^x \right\rangle. \tag{4.16}$$

Hence, a peak in the structure function at $k = \pi$, corresponding to a periodicity of 2 lattice sites, is indicative of the antiferromagnetic order expected in the ground state. In the data, it is clear that the antiferromagnetic ordering is suppressed as the interactions are made longer range. Other metrics besides the structure function can be used, including directly measuring the population in the Néel ordered ground states, which similarly decreases with interaction range. However, the structure function is a useful metric in that it could more easily be compared to measurements with

solid-state systems, for example those made by neutron scattering, and because it is more robust to errors than the N-point correlation function involved in measuring the population of the ground state directly.

We can additionally order the states by their energy, which is directly calculable from Eq. 4.1. As seen in Figure 4.7(b), the result is suggestively similar to the exponential profile that might be expected from a finite-temperature ensemble. However, there are distinct differences between the state we believe we make and a thermal state, including the existence of coherences between the different eigenstates and the fact that states of certain symmetries are not populated at all.

Chapter 5: Dynamics of spin correlations after a global quench

In the quest to build a quantum simulator that can address questions inaccessible to other techniques, it is important that in addition to pushing the envelope of our technical capabilities and system size, we also search for questions that might fruitfully be addressed with the next generation of experiments. For example, while we may have access to several tens of spins within a couple of years, we probably won't have access to thousands, and while we may substantially improve the flexibility of the types of operations we can do, we probably won't have completely arbitrary control of the Hamiltonian. We therefore want to identify problems that are well-suited to these parameters that nevertheless may offer us a chance to study physics that would otherwise be inaccessible.

In this chapter, I describe a global quench experiment with long-range Ising and XY interactions, which is straightforward to perform, works exceedingly well in a system of 11 spins, and offers the potential to shed new light on a fundamental question of how the interaction profile bears on the maximum speed with which distant spins can become correlated. Since the significance of these results is paritally in the fact that we have identified a promising *open* problem to tackle with a larger system, the story doesn't neatly tie off all the loose ends. I will discuss the motivation

for studying these sorts of dynamics, but we cannot yet offer a complete picture with intuitive cartoons explaining why we should see the exact behavior we do. The results in this chapter have been published in [25].

5.1 Motivation: Lieb-Robinson bound and its implications

The maximum speed with which information can propagate in a quantum many-body system directly affects how quickly disparate parts of the system can become correlated [71–74] and how difficult the system will be to describe numerically [75]. For systems with only short-range interactions, Lieb and Robinson derived a constant-velocity bound that limits correlations to within a linear effective light cone [76], analogous to causal light cones that arise in relativistic theories. Lieb-Robinson bounds have strongly influenced our understanding of locally-interacting quantum many-body systems. These bounds restrict the many-body dynamics to a well-defined causal region outside of which correlations are exponentially suppressed [77]. Their existence has enabled proofs linking the decay of correlations in ground states to the presence of a spectral gap [78, 79], as well as the area law for entanglement entropy [75, 80, 81], which can indicate the computational complexity of classically simulating a quantum system. Furthermore, Lieb-Robinson bounds constrain the timescales on which quantum systems might thermalize [82–84] and the maximum speed with which information can be sent through a quantum channel [85]. Recent experimental work has observed an effective Lieb-Robinson (i.e. linear) light cone in a 1D quantum gas [6].

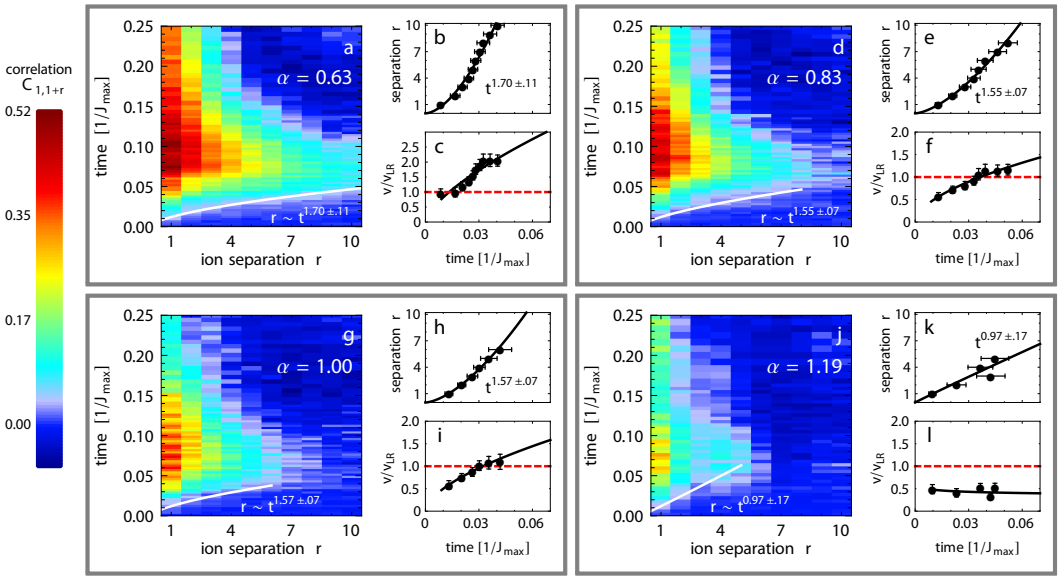

Figure 5.1: (a-c): Dependence of correlations on separation and time (a), extracted light-cone boundary (b), and correlation propagation velocity (c) following a global quench of a long-range Ising model with $\alpha = 0.63$. The curvature of the boundary shows an increasing propagation velocity (b), quickly exceeding the short-range Lieb-Robinson velocity bound, v_{LR} (c). Solid lines give a power-law fit to the data. Complementary plots are shown for $\alpha = 0.83$ (d-f), $\alpha = 1.00$ (g-i), and $\alpha = 1.19$ (j-l). As the system becomes shorter-range, correlations do not propagate as far or as quickly through the chain; the short-range velocity bound v_{LR} is not exceeded for our shortest-range interaction.

When interactions in a quantum system are long-range, the speed with which correlations build up between distant particles is no longer guaranteed to obey the Lieb-Robinson prediction. Indeed, for sufficiently long-ranged interactions, the notion of locality is expected to break down completely [86]. Violation of the Lieb-Robinson bound means that comparatively little can be predicted about the growth and propagation of correlations in long-range interacting systems, though there have been several recent theoretical and numerical advances [72, 73, 78, 86–88].

In this experiment, we have directly measured the shape of the causal region

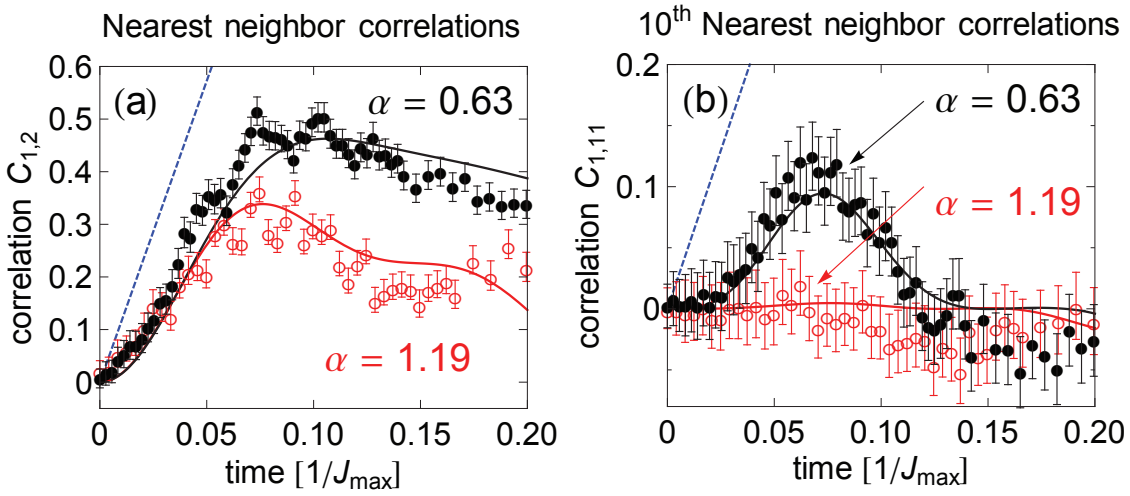

Figure 5.2: (a) Nearest- and (b) 10th-nearest-neighbor-correlations in the Ising model for our shortest- and longest-range interaction compared to the exact solution (i.e. no free parameters) from Eq. 5.3 (solid). The dashed blue curves show a long-range bound for any commuting Hamiltonian.

and the speed at which correlations propagate within Ising and XY spin chains. To induce the spread of correlations, we perform a global quench by suddenly switching on the spin-spin couplings across the entire chain and allowing the system to coherently evolve. The dynamics following a global quench can be highly non-intuitive; one picture is that entangled quasi-particles at each site propagate outwards, correlating distant parts of the system through multiple interference pathways. This process differs substantially from local quenches, where a single site emits quasi-particles that may travel ballistically [73, 83], resulting in a different causal region and propagation speed than in a global quench (even for the same spin model). An experimental study of local quenches appears in [89].

We initialize a chain of 11 ions by optically pumping to the product state $|\downarrow\downarrow\downarrow\ldots\rangle_z$. At $t = 0$, we quench the system by abruptly turning on a Hamiltonian,

representing either an Ising model

$$H_{Ising} = \sum_{i,j} J_{i,j} \sigma_i^x \sigma_j^x \tag{5.1}$$

or an XY-type model (with $\sigma_z \sigma_z$ terms rather than $\sigma_y \sigma_y$ terms)

$$H_{XY} = \frac{1}{2} \sum_{i,j} J_{i,j} \left(\sigma_i^x \sigma_j^x + \sigma_i^z \sigma_j^z \right), \tag{5.2}$$

where as before, the interactions roughly follow a power-law profile, $J_{i,j} \sim J_0/|i-j|^\alpha$. The final section in this chapter provides a discussion of how we can extract the effective dynamics of the XY Hamiltonian H_{XY} above using the transverse-field Ising model that we are proficient at generating. We choose values of $\alpha = \{0.63, 0.83, 1.00, 1.19\}$ for these experiments. For values $\alpha < 1$, the system is strongly long-range, since in the thermodynamic limit the interaction energy per site diverges, and so the generalized Lieb-Robinson-type bound for systems with power-law interactions in Ref. [78] breaks down.

After quenching to the Ising or XY model with our chosen value of α, we allow coherent evolution for various lengths of time before resolving the spin state of each ion using a CCD camera. The experiments at each time step are repeated 4000 times to collect statistics. To observe the buildup of correlations, we use the measured spin states to construct the connected correlation function

$$C_{i,j}(t) = \langle \sigma_i^z(t) \sigma_j^z(t) \rangle - \langle \sigma_i^z(t) \rangle \langle \sigma_j^z(t) \rangle \tag{5.3}$$

between any pair of ions at any time. This allows us to distinguish between the trivial, classical correlations in a product state and correlations that could result from entanglement: for example, the states $|\uparrow\uparrow\rangle_z$, $|\downarrow\downarrow\rangle_z$, and $(|\uparrow\uparrow\rangle_z + |\downarrow\downarrow\rangle_z)/\sqrt{2}$ all result in $\langle\sigma_i^z(t)\sigma_j^z(t)\rangle = 1$, whereas the connected correlation $C_{i,j}(t)$ is nonzero only for $(|\uparrow\uparrow\rangle_z + |\downarrow\downarrow\rangle_z)/\sqrt{2}$. Since the system is initially in a product state, $C_{i,j}(0) = 0$ everywhere. As the system evolves away from a product state, evaluating Eqn. 5.3 at all points in space and time provides the shape of the light-cone boundary and the correlation propagation velocity for our long-range spin models.

5.1.1 Ising model results

Figures 5.1 and 5.2 show the results of globally quenching the system to a long-range Ising model for several different interaction ranges. In each case, we extract the light-cone boundary by observing the time it takes a correlation of fixed amplitude (here, $C_{i,j} = 0.04 \approx 0.1C_{i,j}^{\max}$) to travel an ion-ion separation distance r. For strongly long-range interactions ($\alpha < 1$), the region within the light-cone grows faster than linearly, which violates the Lieb-Robinson prediction. This fast propagation of correlations is not surprising, because even the direct long-range coupling between distant spins produces correlations in a time $t \propto 1/J_{i,j} \sim r^{\alpha}$. Thus, faster-than-linear light-cone shapes are expected to be a general feature of any 1D long-range interacting Hamiltonian with $\alpha < 1$.

Increasing propagation velocities quickly surpass the Lieb-Robinson velocity for a system with nearest-neighbor interactions, $v_{LR} = 12eJ_0$ [see Figure 5.1(c,f,i)].

Such violations indicate that predictions based on the Lieb-Robinson result – including those that bound the growth of entanglement or correlation lengths in the system – can no longer be trusted.

For the specific case of the pure Ising model, the correlations at any time can be predicted by an exact analytic solution [87, 90]:

$$\begin{aligned} C_{i,j}(t) &= \frac{1}{2}\prod_{k\neq i,j}\cos[2(J_{i,k}+J_{j,k})t] \\ &+ \frac{1}{2}\prod_{k\neq i,j}\cos[2(J_{i,k}-J_{j,k})t] \\ &- \prod_{k\neq i}\cos[2J_{i,k}t]\prod_{k\neq j}\cos[2J_{j,k}t]. \end{aligned} \tag{5.4}$$

In Eq. 5.4, correlations can only build up between sites i and j that are coupled either directly or through a single intermediate spin k; processes which couple through more than one intermediate site are prohibited. For instance, if the $J_{i,j}$ couplings are nearest-neighbor-only, $C_{i,j}(t) = 0$ for all $|i-j| > 2$. This property holds for any Hamiltonian whose terms all commute with each other, as shown in a later section, and explains why the spatial correlations shown in Figure 5.1 become weaker for shorter-range systems.

The products of cosines in Eq. 5.4 with many different oscillation frequencies result in the observed decay of correlations when $t \gtrsim 0.1/J_{\max}$. At later times, rephasing of these oscillations creates revivals in the spin-spin correlation. One such partial revival occurs at $t = 2.44/J_{\max}$ for the $\alpha = 0.63$ case; we observe the revival for this α (Figure 5.3) as verification that our system remains coherent for a

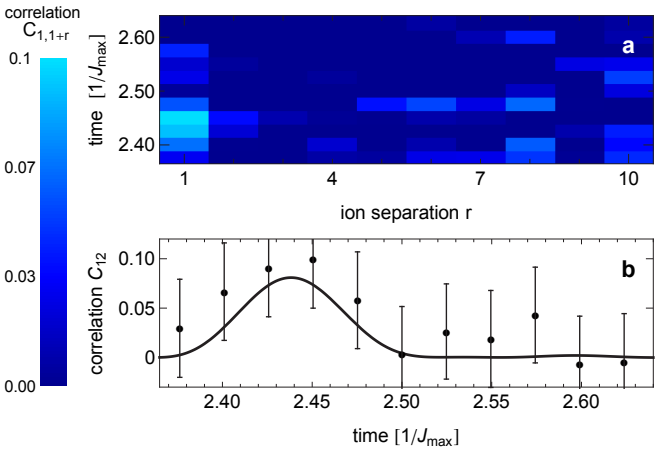

Figure 5.3: (a), Spatial correlations measured at long times after a global quench of an Ising model with $\alpha = 0.63$. (b), A small partial revival in correlation between sites 1 and 2 is evident, showing quantum coherence at long times. The black line shows the exact solution predicted from equation 5.4. Error bars, 1 s.d.

timescale much longer than that which determines the light-cone boundary.

5.1.2 XY model results

We repeat the quench experiments for an XY-model Hamiltonian using the same set of interaction ranges α, as shown in Figures 5.4 and 5.5. Dynamical evolution and the spread of correlations in long-range interacting XY models are much more complex than in the Ising case because the Hamiltonian contains non-commuting terms. As a result, no exact analytic solution comparable to Eq. 5.4 exists.

Compared with the correlations observed for the Ising Hamiltonian, correlations in the XY model are much stronger at longer distances – particularly for short-range interactions. Processes coupling through multiple intermediate sites (which were disallowed in the commuting Ising Hamiltonian) now play a critical role in

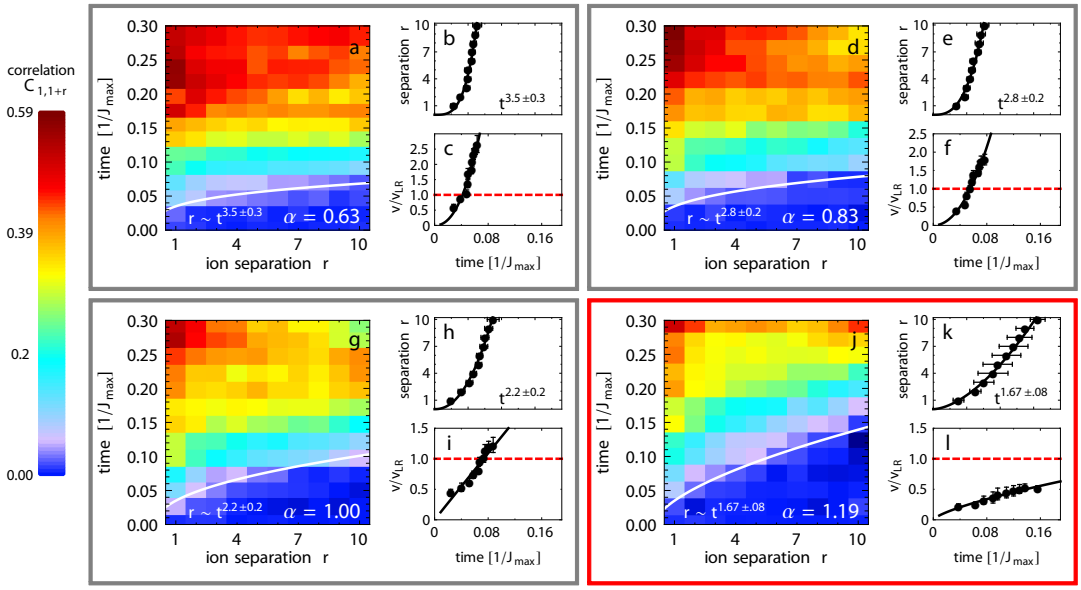

Figure 5.4: Global quench of a long-range XY model with four different interaction ranges. (a-l): Panel descriptions match those in Figure 5.1. In each case, when compared with the Ising model, correlations between distant sites in the XY model are stronger and build up more quickly. For the shortest-range interaction [red box, (j-l)], we observe a faster-than-linear growth of the light-cone boundary, despite $\alpha > 1$; no known analytic theory predicts this effect.

building correlations between distant spins. These processes may also explain our observation of a steeper power-law scaling of the light-cone boundary in the XY model. However, we note that without an exact solution, there is no *a priori* reason to assume a power-law light-cone edge (used for the fits in Figures 5.4 and 5.5), and deviations from power-law behavior might reveal themselves for larger system sizes.

An important observation in Figure 5.4(j-l) is that of faster-than-linear light-cone growth for the relatively short-range interaction $\alpha = 1.19$. Although faster-than-linear growth is expected for $\alpha < 1$ (see previous section) and forbidden in local quenches for $\alpha > 2$ [73, 88], no theoretical description of the light-cone shape exists in the intermediate regime $1 < \alpha < 2$. Our experimental observation has

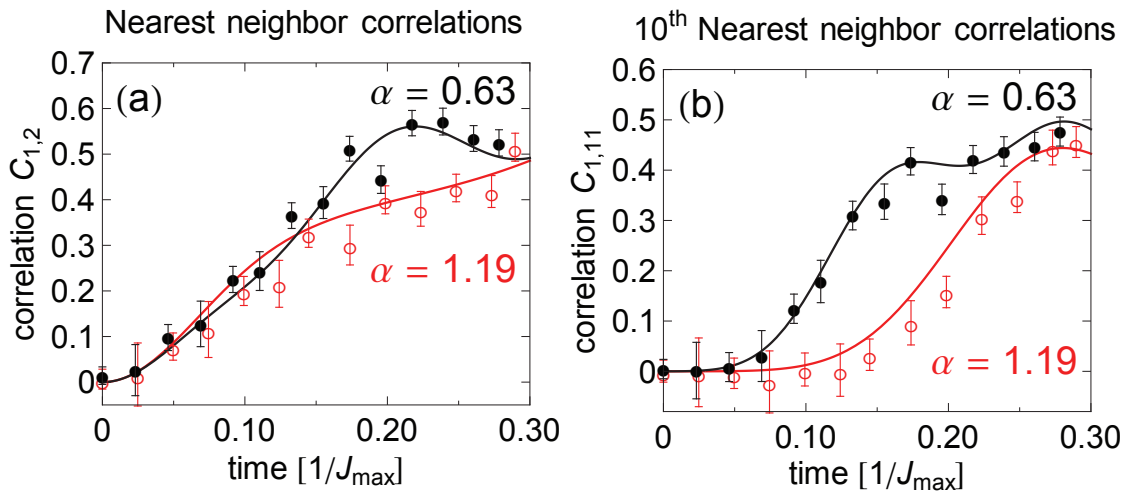

Figure 5.5: (a) Nearest- and (b) 10th-nearest neighbor correlations compared to a solution found by numerically evolving the Schrödinger equation of an XY model with experimental spin-spin couplings.

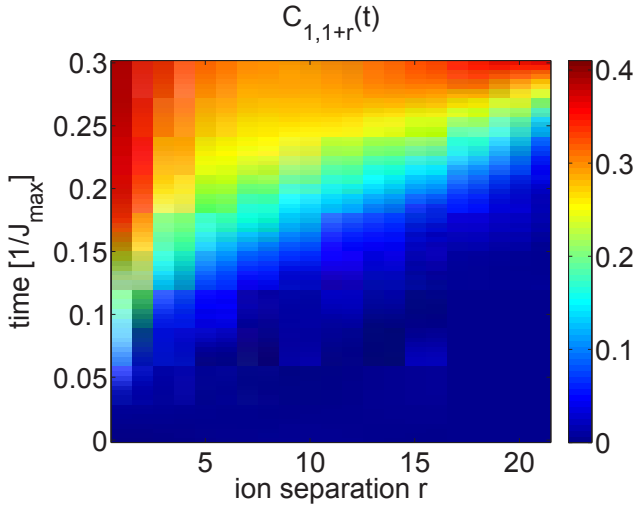

Figure 5.6: Calculated spatial and time-dependent correlations for an $N = 22$-spin XY model with spinspin couplings $J_{ij} \approx J_0/|i-j|^{1.19}$, found by numerically evolving the Schrödinger equation.

prompted us to numerically check the light-cone shape for $\alpha = 1.19$; we find that faster-than-linear scaling persists in systems of up to 22 spins before our calculations break down, as displayed in Figure 5.6.

Whether such scaling continues beyond ∼30 spins is a question that, at present, quantum simulators are best positioned to answer. In Figures 5.2 and 5.5, the excellent agreement between data and theory demonstrates that experiments produce the correct results in a regime still solvable by classical computers. For larger systems, where numerical evolution of the Schrödinger equation fails, the quality of quantum simulations could still be benchmarked against the exact Ising solution of equation 5.4. Finding close agreement in the Ising case would then build confidence in an XY model simulation, which cannot be validated by any other known method.

For the XY model, we additionally study the spatial decay of correlations outside the light-cone boundary. The data is shown in Figure 5.7 and is well-described by fits to exponentially decaying functions. Recent theoretical work [88] predicts an initial decay of spatial correlations bounded by an exponential, followed by a power-law decay; we speculate that much larger system sizes and several hundred-thousand repetitions of each data point (to sufficiently reduce the shot-noise uncertainty) would be necessary to see this effect.

A perturbative treatment of time evolution under the XY Hamiltonian yields the short-time approximation for the correlation function $C_{i,j}(t) \approx (J_{i,j}t)^2$. These values are plotted as dashed lines along with the data in Figure 5.7. While the perturbative result matches the data early on, it clearly fails to describe the dynamics at longer evolution times. The discrepancies indicate that the light-cone shapes

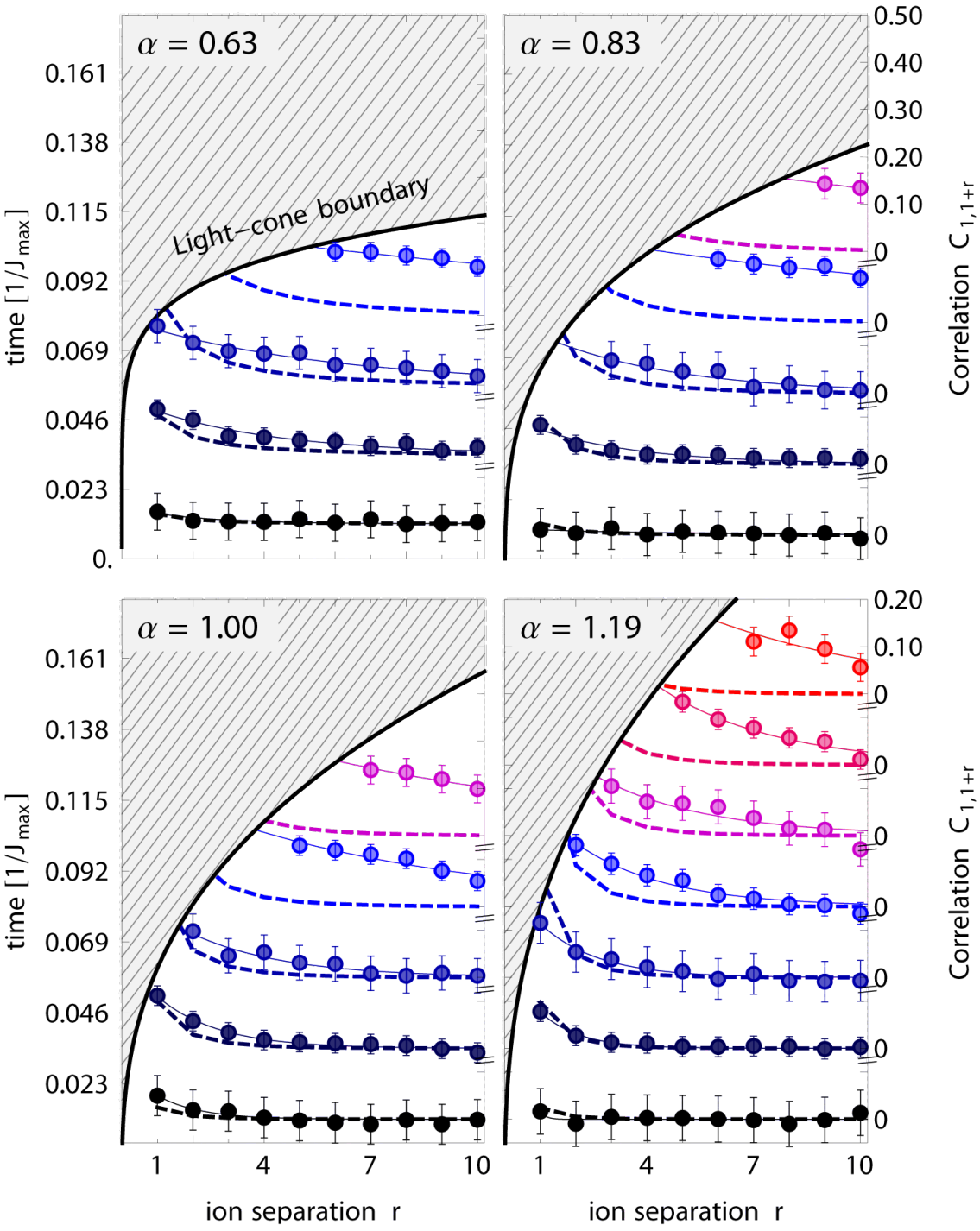

Figure 5.7: Decay of spatial correlations outside the light-cone boundaries for a long-range XY model with $\alpha = \{0.63, 0.83, 1.00, 1.19\}$. The hatched region indicates the area inside the light-cone boundary $C_{i,j} = 0.15$. Solid lines give an exponential fit to the data while dashed lines show the predictions from a perturbative calculation. Perturbation theory does not accurately describe the dynamics at later times.

observed in the XY model are fundamentally non-perturbative; rather, they result from the build-up of correlations through multiple intermediate sites and cannot be understood by any known analytical method.

In conclusion, we have made experimental observations of the causal region and propagation velocities for correlations following global quenches in Ising and XY spin models. The long-range interactions in our system lead to a breakdown of the locality associated with Lieb-Robinson bounds, while dynamical evolution in the XY model leads to results that cannot be described by existing analytic or perturbative theory. Our work demonstrates that even modestly-sized quantum simulators can be an important tool for investigating and enriching our understanding of dynamics in complicated many-body systems.

5.1.2.1 Multi-hop processes are forbidden for commuting Hamiltonians

Here we prove the claim that for commuting Hamiltonians, distant spins can only become correlated if they are directly coupled or if they share an intermediate spin to which they both couple; multi-hop processes (e.g. site A coupling to site D through sites B and C) are disallowed.

We consider the time evolution of the operator σ_i^z, the Pauli matrix in the z direction at site i. We can expand the time evolution operator using the Baker-

Campbell-Hausdorff lemma:

$$\begin{aligned}\sigma_i^z(t) &= e^{iHt}\sigma_i^z e^{-iHt} \\ &\approx \sigma_i^z + it[H,\sigma_i^z] - \frac{t^2}{2}[H,[H,\sigma_i^z]] + \ldots \end{aligned} \tag{5.5}$$

where H is a general commuting spin-spin Hamiltonian that we may write as $H = \frac{1}{2}\sum_{p<q} h_{p,q}$, with terms $h_{p,q}$ acting only on sites p and q. It is immediately clear that unless p or q is equal to i, these terms in the Hamiltonian cannot contribute to the time evolution since they commute with the Pauli operator at site i. We can use this fact to rewrite Eq. 5.5,

$$\sigma_i^z(t) \approx \sigma_i^z + it\left[\sum_{i<p} h_{i,p}, \sigma_i^z\right] + \ldots \tag{5.6}$$

It is clear from Eq. 5.6 that the only terms which influence the time evolution of σ_i^z are those which are directly connected to site i. Similarly, the time evolution of the Pauli z operator at site j is given by

$$\sigma_j^z(t) \approx \sigma_j^z + it\left[\sum_{j<q} h_{j,q}, \sigma_j^z\right] + \ldots \tag{5.7}$$

Therefore, the only way for sites i and j to become correlated is either $j \in p$ (direct hops) or $p = q$ (single intermediate point). No multi-hop processs beyond these may contribute to the buildup of correlations.

5.2 Technique for doing dynamics of XY without a field

In order to simulate an XY model, we can use our old friend the transverse-field Ising model with a large field term. In order to show this, I will write our Hamiltonian in a slightly different basis than what we use in the lab to simplify the formalism; of course, this is exactly the same physics we expect to see in the lab, and we will simply need to redefine what we mean by operators like σ_+. The Hamiltonian for this is

$$H = \sum_{i,j} J_{i,j} \sigma_x^i \sigma_x^j + B \sum_i \sigma_z^i, \tag{5.8}$$

and we will take $B \gg J_{max}$. In order to see the effect of the B term, we can break up the interaction term into four parts:

$$\sigma_x^i \sigma_x^j = \sigma_+^i \sigma_+^j + \sigma_+^i \sigma_-^j + \sigma_-^i \sigma_+^j + \sigma_-^i \sigma_-^j. \tag{5.9}$$

But because the $\sigma_+\sigma_+$ and $\sigma_-\sigma_-$ terms involve flipping a pair of spins along the strong field, these processes will be energetically disallowed, so

$$\sigma_x^i \sigma_x^j \approx \sigma_+^i \sigma_-^j + \sigma_-^i \sigma_+^j. \tag{5.10}$$

A line or two of algebra can be used to show that

$$\sigma_+^i \sigma_-^j + \sigma_-^i \sigma_+^j = \left(\sigma_x^i \sigma_x^j + \sigma_y^i \sigma_y^j\right)/2, \tag{5.11}$$

which is the XY interaction we were interested in.

The intuition we have for what is going on here is as follows. In the high B limit, the eigenstates are roughly the σ_z eigenstates of the field. The eigenstates are broken up into different energy manifolds depending on how many spins are pointing up along the field: for instance, the lowest energy state is (roughly) $|\downarrow\downarrow\cdots\rangle_z$, and the next manifold (an energy $2B$ away) contains the N states with a single spin in $|\uparrow\rangle_z$, etc. Since the Ising interaction term is only a small perturbation, it does not drive transitions between the different manifolds, but can drive dynamics within a single manifold. This has the effect of a flip-flop interaction, since J can only couple (e.g.) $|\uparrow\downarrow\cdots\rangle_z$ to $|\downarrow\uparrow\cdots\rangle_z$, without leaving the manifold via a $\sigma_+\sigma_+$ or $\sigma_-\sigma_-$ effect.

This line of argument makes it clear that if the system remains within a single energy manifold (e.g., with a single spin pointing up), the dynamics will be well approximated by the XY interaction at all times, since the only effect of the transverse field will be to impart a global phase (e.g., e^{-2iBt} relative to the ground state, in the manifold with only one spin pointing up).

However, if multiple manifolds are populated, then the presence of the transverse field will cause nontrivial modifications to the XY dynamics, because the different manifolds will pick up different relative phases. The transverse field can hence only be neglected under special conditions: namely, at times $t = 2\pi n/B$, where n is an integer, all of the manifolds will 'rephase' and the resulting state will be the same state that would have resulted from evolution under a pure XY interaction. This argument can be made more formal by looking at the evolution

operator of the effective Hamiltonian,

$$U = \exp\left[-i\left(\sum_{i,j} J_{i,j}\left(\sigma_+^i\sigma_-^j + \sigma_-^i\sigma_+^j\right) + B\sum_i \sigma_z^i\right)t\right]. \tag{5.12}$$

(Since this Hamiltonian is constant, we do not need to resort to the Magnus expansion as we did in deriving the effective spin Hamiltonian.) The $J_{i,j}$ terms wind up commuting with the σ_z terms, as shown below, and we can therefore rewrite the evolution operator into a product of terms,

$$U = \exp\left[-i\sum_{i,j} J_{i,j}\left(\sigma_+^i\sigma_-^j + \sigma_-^i\sigma_+^j\right)t\right]\exp\left[-iB\sum_i \sigma_z^i t\right]. \tag{5.13}$$

We can easily recognize that the rightmost term will be reduced to the identity operator (modulo perhaps a global phase) at times $t = 2\pi n/B$, so at those times the evolution operator will be exactly that of a pure XY interaction with no fields present.

In order to gain a bit of understanding into how the approximations we have made may start to break down, we can go through the formalism of splitting up the evolution operator using the Zassenhaus formula [91], which is an analog to the more familiar Baker-Campbell-Hausdorff formula. The Zassenhaus formula gives an expansion of the exponential of the sum of noncommuting terms,

$$e^{X+Y} = e^X e^Y e^{-\frac{1}{2}[X,Y]} e^{\frac{1}{3}[Y,[X,Y]]+\frac{1}{6}[X,[X,Y]]}\ldots \tag{5.14}$$

Here, we have

$$X = -i \sum_{i,j} J_{i,j} t \left(\sigma_+^i \sigma_-^j + \sigma_-^i \sigma_+^j \right), \tag{5.15}$$

$$Y = -iBt \sum i \sigma_z^i. \tag{5.16}$$

To calculate their commutator, we will need the commutators

$$[\sigma_+, \sigma_z] = [|\uparrow\rangle \langle\downarrow|, |\uparrow\rangle \langle\uparrow| - |\downarrow\rangle \langle\downarrow|] = -2\sigma_+, \tag{5.17}$$

$$[\sigma_-, \sigma_z] = [|\downarrow\rangle \langle\uparrow|, |\uparrow\rangle \langle\uparrow| - |\downarrow\rangle \langle\downarrow|] = 2\sigma_-. \tag{5.18}$$

So we get

$$\begin{aligned} [X, Y] = & \quad - \textstyle\sum_{i,j,k} J_{i,j} B t^2 \left[\sigma_+^i \sigma_-^j + \sigma_-^i \sigma_+^j, \sigma_z^k \right] \\ = & \quad - \textstyle\sum_{i,j,k} 2 J_{i,j} B t^2 \left(\delta_{ik} \left(-\sigma_+^i \sigma_-^j + \sigma_-^i \sigma_+^j \right) + \delta_{jk} \left(\sigma_+^i \sigma_-^j - \sigma_-^i \sigma_+^j \right) \right) \\ = & \quad 0. \end{aligned} \tag{5.19}$$

So all of the commutators are zero, and we can factorize the evolution operator without worrying about Zassenhaus formulas and whatnot. However, this makes it clear that handwaving away the B field relies heavily upon having already approximated away the $\sigma_+\sigma_+$ and $\sigma_-\sigma_-$ terms; if they still remained, we would have a nonzero commutator

$$[X, Y] = \sum_{i,j} 4 J_{i,j} B t^2 \left(\sigma_+^i \sigma_+^j - \sigma_-^i \sigma_-^j \right). \tag{5.20}$$

The exponential of this operator will not reduce to the identity at times $t = 2\pi n / B$,

due to the presence of the $J_{i,j}$ (and of course there are yet further terms to consider); thus, to the extent that the $\sigma_+\sigma_+$ and $\sigma_-\sigma_-$ terms contribute to the dynamics, so too will the effect of the transverse field be non-negligible.

Chapter 6: Spectroscopy of a quantum many-body spin system

In all of the results presented so far in this thesis, we have been comparing our dynamics - which can mean hopefully-adiabatic preparation of ground states or the quench experiments in the previous chapter - to a theoretical model. This has served as a much-needed validation of our understanding of our experiments. Indeed, our foreknowledge of the results we expect to obtain has often helped us diagnose subtle complications, allowing us to work backwards to notice when (for example) the spin-state readout is mis-calibrated or when the transverse motional modes jump in frequency due to thermal changes in the helical RF resonator. However, as we scale our system toward classically-intractable sizes, comparison to exact numerical results will become impossible by design. We will therefore require as many validation and verification techniques as possible, such that once we are in a position to attempt to study new and poorly-understood physics, we have the means to check whether various aspects of our simulator are working as desired.

Many single-particle diagnostics will remain useful in larger experiments; for example, it is easy to imagine future generations of the experiment automating periodic measurements such as checking the Rabi frequencies on each spin, the frequencies of each normal mode, and the image calibrations. However, it may

also be useful to have ways of peering more directly into the many-body effects in our system. This chapter introduces a first step toward validating the many-body dynamics of the interacting spins, namely, a technique for performing coherent spectroscopy on the simulated Hamiltonian. By making use of our ability to read out entire spin configurations, we can implement a protocol for inferring the entire spin-spin interaction matrix in an Ising Hamiltonian from measurements of energy splittings. The number of measurements required for this protocol scales linearly with the number of spins, so this could even be useful for much larger system sizes. I also discuss some preliminary efforts to measure energy spectra for a fully quantum Hamiltonian, namely an Ising model with nonzero transverse field, and demonstrate that we have directly measured the critical energy gap near a quantum phase transition.

6.1 Description of the general technique, and demonstration of single-spin-flip spectroscopy

As before, we consider a long-range transverse Ising Hamiltonian,

$$H_{\text{eff}} = \sum_{i<j} J_{i,j}\sigma_i^x\sigma_j^x + B(t)\sum_i \sigma_i^y, \tag{6.1}$$

where $h = 1$, σ_i^γ ($\gamma = x, y, z$) is the Pauli matrix for spin i along direction γ; $J_{i,j} \sim J_0|i-j|^{-\alpha}$ is a long-range coupling strength between spins i and j with α tunable between 0 and 3 [43]; and $B(t)$ is the energy associated with a time-

dependent transverse magnetic field. (For consistency with prior publications and with language typically used in the lab, energies, like $J_{i,j}$ and $B(t)$, and frequencies are referred to interchangeably. Additionally, we refer to the transverse field term $B(t)$ only in terms of its effective energy. We believe this convention is simpler than assigning a fictitious magnetic moment to our fictitious simulated spins.) The σ_x eigenstates are denoted by $|1\rangle$ and $|0\rangle$, where $|1\rangle$ ($|0\rangle$) represents the state $|\uparrow\rangle_x$ ($|\downarrow\rangle_x$), respectively.

As mentioned previously, the ability to generate antiferromagnetic $J_{i,j}$ couplings of varying interaction range [22, 43, 92] has recently attracted much interest in a variety of contexts such as studying the spread of correlations after a quench [72, 73], observing prethermalization of a quantum system [84, 93], and directly measuring response functions [94]. Developing a general protocol to measure the spin-spin couplings will be an important validation goal. Previous experiments have fully characterized the interactions in small systems using techniques which may be difficult to scale up, such as Fourier decomposition of multi-spin dynamics [18] or manipulating each of the $\sim N^2/2$ pairs of spins separately using electromagnetic field gradients for frequency [95] or spatial addressing [89]. By contrast, the protocol we introduce below allows the couplings to be measured by taking $\sim N$ frequency spectra, with the entire measurement taking a time which has the same scaling with system size and interaction range α as the gradient techniques in [95] and [89], and requires only global interactions and site-resolved measurements.

We measure the energy splittings in our spin system using a weakly modulated

transverse field as a probe,

$$B(t) = B_0 + B_p \sin(2\pi\nu_p t), \tag{6.2}$$

where $B_p \ll J_0$ is small compared to the nearest-neighbor interactions. When the probe frequency ν_p is matched to the energy difference $|E_a - E_b|$ between two eigenstates $|a\rangle$ and $|b\rangle$, the field will drive transitions between the two states if there is a nonzero matrix element $\langle b| B(t) \sum_i \sigma_i^y |a\rangle \neq 0$ [96]. For example, in the weak-field regime $B(t) \ll J_0$, the Hamiltonian eigenstates are well approximated by symmetric combinations of the σ^x eigenstates: e.g., $|0101\cdots\rangle$ and $|1010\cdots\rangle$ are degenerate eigenstates at $B = 0$, but for very weak, nonzero transverse field, the eigenstates are roughly given by $(|0101\cdots\rangle + |1010\cdots\rangle)/\sqrt{2}$ and $(|0101\cdots\rangle - |1010\cdots\rangle)/\sqrt{2}$. In this regime, the matrix element $\langle b| B(t) \sum_i \sigma_i^y |a\rangle$ is nonzero only when $|a\rangle$ and $|b\rangle$ differ by the orientation of exactly one spin.

Although we cannot directly measure absorption (or emission) of energy from (or into) the transverse field, the spatial information afforded by detecting individual spin states allows us to observe the multiple transitions away from a given initial state. In the weak-field regime, a transition at a single frequency can easily be monitored, and the stability of the transition frequency can provide a good proxy for that of the entire Hamiltonian. Each splitting depends on multiple spin-spin couplings – for example, a transition from $|1111\cdots\rangle$ to $|0111\cdots\rangle$ requires energy

$$\Delta E = 2(J_{1,2} + J_{1,3} + \cdots + J_{1,N}) \tag{6.3}$$

As we have seen before, any given interaction $J_{i,j}$ is sensitive to the laser intensities at ions i and j, as well as all of the motional mode frequencies:

$$J_{i,j} = \Omega_i \Omega_j \Omega_R \sum_{m=1}^{N} \frac{b_{i,m} b_{j,m}}{\mu^2 - \nu_m^2}. \tag{6.4}$$

Since the energy required to flip any one spin depends on its interactions with every other spin, any given splitting is therefore sensitive to changes in any of the laser intensities, as well as changes to the motional mode structure.

We demonstrate the mapping of individual energy splittings in the weak-field regime $B(t)/J_0 \ll 1$ in Figures 6.2 and 6.1. Figure 6.1 sketches the concept, demonstrates the measurement of *individual* energy splittings, and shows that the measurement is insensitive to state preparation and measurement (SPAM) error: namely, transition frequencies can be identified in some cases despite loss of contrast from SPAM errors. Figure 6.2 shows measurements made starting from both ends of the energy spectrum, i.e. starting in either the ground or the highest excited state. In all cases, we cannot directly measure absorption of energy from (or stimulated emission into) the effective transverse field, so we must measure transitions by observing changes in the spin configurations.

The spins are prepared along the x direction in $|111\cdots\rangle$ or, for Figure 6.2(b) and (d), prepared in the antiferromagnetic ground states $|101010\rangle$ and $|010101\rangle$ using the adiabatic protocol described in Chapter 4 with an exponential ramp (chosen because of the simplicity in implementing this ramp experimentally). A transverse probe field corresponding to $B(t) = (100\text{ Hz})\sin(2\pi\nu_p t)$ is applied for 3 ms, which

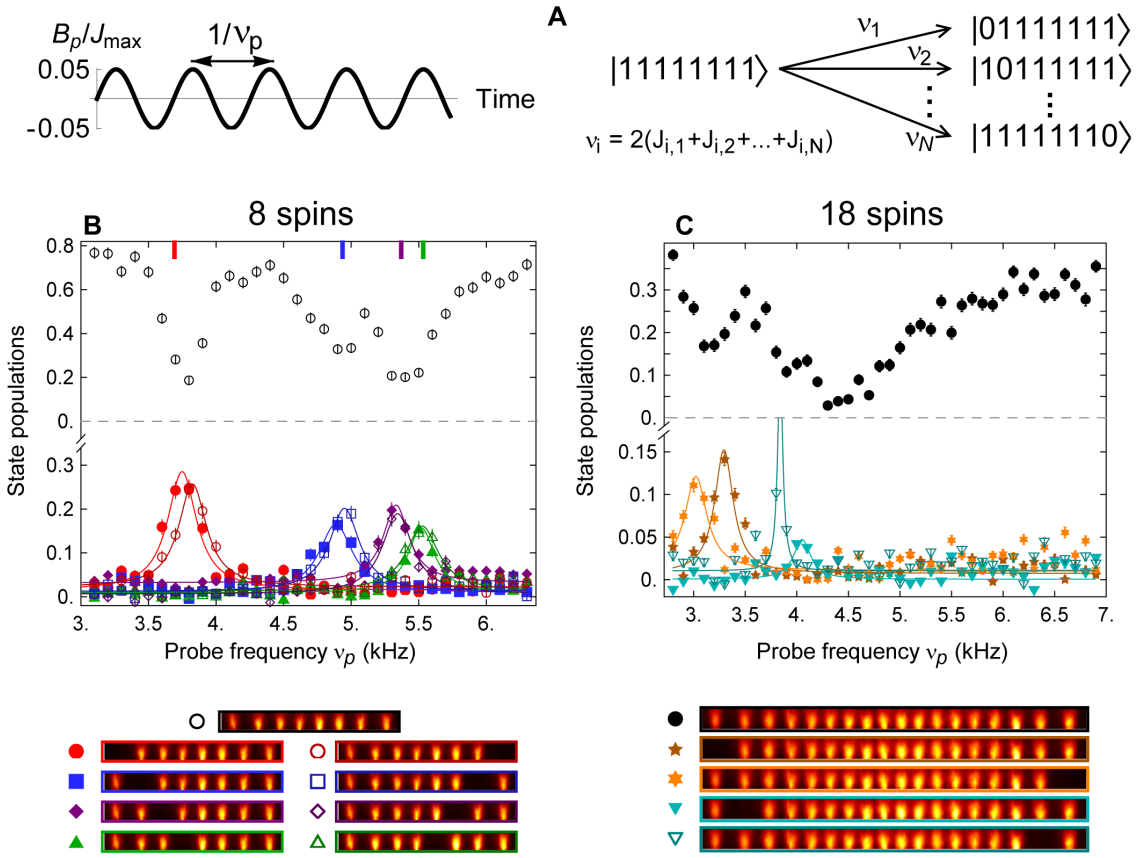

Figure 6.1: (A): The transverse field term B_p drives transitions between states when its modulation frequency matches an allowed energy splitting (such as between the state with all spins up along x and any single-defect state with a single spin down). (B): Measured populations in specific spin states (see legend, below, where a fluorescing (dark) ion represents $|\uparrow_x\rangle \equiv |1\rangle$ ($|\downarrow\rangle_x \equiv |0\rangle$)) vs. the frequency of the probe field for a system of 8 spins initialized in $|11111111\rangle$ before probing. Solid curves are Lorentzians fit to the data sets; the energy splittings predicted from Eq. 6.1 are indicated with colored bars at the top of the frame. Error bars represent statistical error from performing 1000 repetitions of each experiment. (C): Measured populations vs. the frequency of the probe field for a system of 18 spins. The left-right asymmetry is attributed to slight misalignment of the laser beams. Despite the low fidelity of the initial state (35% in the $|1111111111111111\rangle$ state), these energy splittings are still clearly visible.

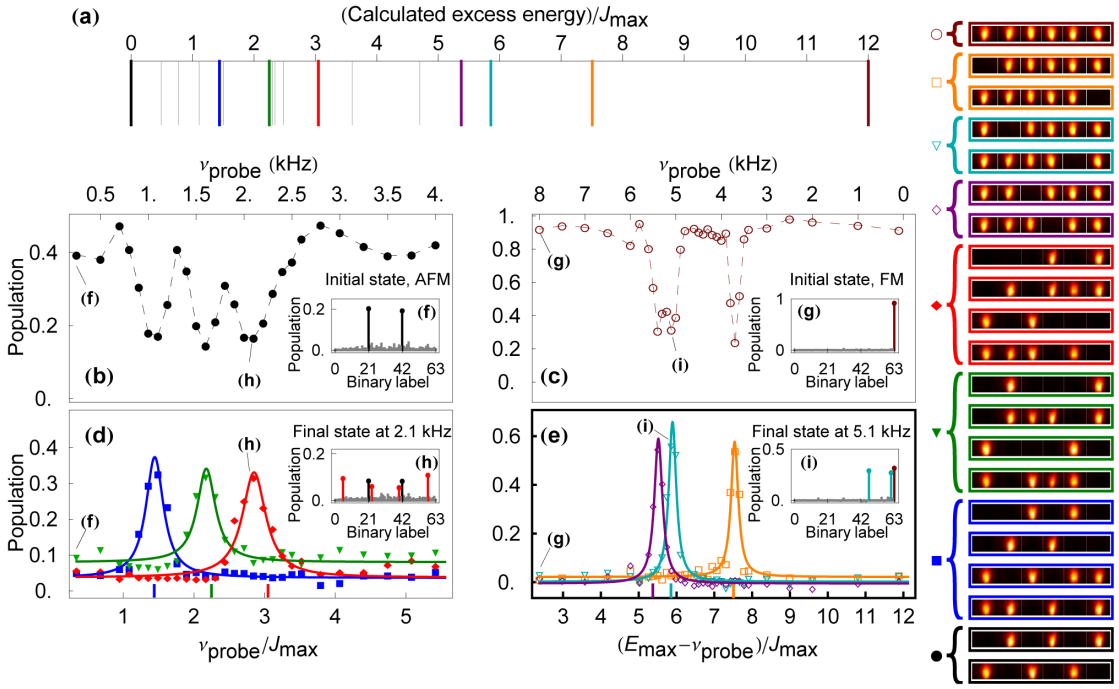

Figure 6.2: (a): Calculated energy spectrum of a long-range antiferromagnetic Ising Hamiltonian with 6 spins, scaled to the strength of the largest spin-spin coupling J_{max}. Bold colored lines indicate the energies of states probed experimentally. (b)-(e): Populations in spin states (indicated in the legend on right, where a fluorescing (dark) ion represents $|1\rangle$ ($|0\rangle$): e.g., solid black circles denote the sum of populations in $|010101\rangle$ and $|101010\rangle$) vs the frequency of a transverse probe field. Panels (b) and (d) show the results of probing a nominal Neél ordered state $|101010\rangle + |010101\rangle$. Dashed lines are to guide the eye. (c) shows the different sets of excited states that are coupled to the Neél states at 3 different energies. The resonance frequencies are identified by fitting Lorentzians to the data sets (solid lines). On the bottom axis the probe frequency is scaled to the calculated J_{max} to enable comparison with (a), while the top axis shows the actual probe frequency. Panels (c) and (e) show a similar experiment probing a polarized initial state $|111111\rangle$. In this case, since we start from the highest excited state, the bottom axis also subtracts the probe frequency from the calculated initial energy to enable comparison with (a). Insets (f) and (g) show the population distributions of the initial states; even in the nominal Neél state with 40% fidelity, there are no other highly populated states. The horizontal axis denotes the decimal form of the binary state, e.g. $|101010\rangle \equiv 42$. Insets (h) and (i) show the populations after applying a probe frequency at a resonance, demonstrating that the population is only transferred to the expected set of coupled states.

is sufficient to transfer more than 50% of the population between states, before measuring along x. These parameters allow resolution of the energy differences in a system of 6 to 8 spins while still accommodating the few ms decoherence timescale in our system.

Population transfer is clearly seen when ν_p is resonant with an energy splitting (e.g. Figure 6.2 (b)-(e); Figure 6.1, (b)-(d)). We quantify the energy of a particular state relative to the initial state by fitting Lorentzians to the spectra. (While a Rabi-type sinc function should be a more accurate representation of the lineshape, we find that the measured line centers are insensitive to whether the fit function chosen is a Lorentzian, sinc, Gaussian, etc. Thus, we avoid using a sinc simply because it would slow down the computational analysis of the data.) The reason that only a few energy peaks are shown for $N = 18$ is that the population driven into the other states, e.g., $|111111110111111111\rangle$ is on the order of the quantum projection noise or smaller, because of the close spacing of the energy levels in this region. Thus, another notable feature in Figure 6.1C is that even when we cannot resolve individual energy splittings, we can identify regions where energy levels reside from the depletion of the initial state (e.g., the pronounced dip centered around 4.5 kHz).

6.2 Multiple pulses to implement a scalable validation of the interactions

Measuring a certain number of energy splittings in the weak-field limit provides sufficient information to obtain the entire Ising coupling matrix $J_{i,j}$. The couplings

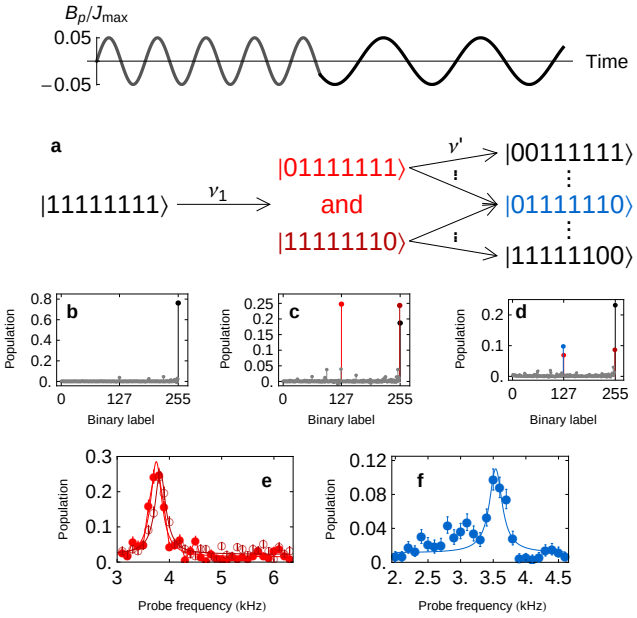

Figure 6.3: (a): Sketch of protocol for driving sequential excitations. (b)-(d): plots of the measured populations in each of the 2^N states in a system of $N = 8$ spins. We apply sequential pulses of the modulated transverse field to an initial polarized state, shown in (b). The first pulse drives transitions into states with single defects, $|01111111\rangle$ and $|11111110\rangle$ (c), and the second pulse can then create states with two defects (d). (e): Population in either of the states with a single defect on the end vs. the frequency of the first pulse. (f): Fixing the first pulse on resonance from (e), we show the population of a state with two defects, $|01111110\rangle$, vs. the frequency of the second pulse.

can be directly related to the energies as in Eq. 6.3, so measuring an appropriate set of $\binom{N}{2}$ energy splittings allows us to measure the $\binom{N}{2} = \frac{N^2}{2} - \frac{N}{2}$ couplings. For example, the state $|1111\cdots\rangle$ can be prepared and probed, yielding N energy measurements of the N single-defect states with a single spin in the $|0\rangle$ state; then, each single-defect state can be prepared with a pulse of the modulated transverse field at the measured frequency and probed with a second pulse of the modulated transverse field, as shown in Figure 6.3. In this manner, $N-1$ further energy splittings are measured for each single-defect state, yielding N^2 measurements (N from the first probe scan and $N(N-1)$ from the rest) with only $N+1$ scans. This protocol allows us to fully characterize the spin-spin couplings and directly demonstrate control over the interaction range; additionally, due to the parallel processing enabled by monitoring individual spin states, it scales favorably with the system size, as discussed below in Section 6.2.1.

We measure the interactions for two systems of 8 spins each, using different laser and trap parameters to generate interactions falling off with different power law exponent α. For each value of α, frequency scans are performed with initial states of $|11111111\rangle$ and all single-defect states thereof, i.e. $|01111111\rangle$, $\cdots$, $|11111110\rangle$, which are prepared with a pulse of the modulated transverse field. Because of the left-right symmetry in our system, pairs of the single-defect states (e.g. $|01111111\rangle$and $|11111110\rangle$) are degenerate in energy and are populated simultaneously, and we therefore require only $5{=}N/2+1$ scans to retrieve sufficient energy measurements to constrain the interaction profile. We thus have sufficient information to infer all of the spin-spin interactions, which are plotted in Figure 6.4. For

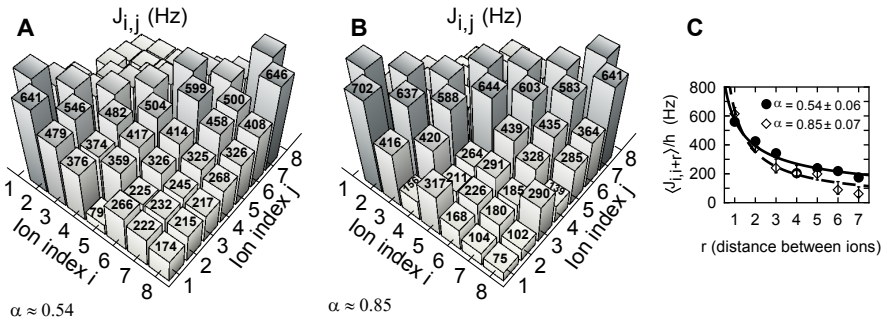

Figure 6.4: Experimentally determined spin-spin coupling profiles. The couplings were measured in a system of 8 spins for two sets of trap parameters, corresponding to a more long-range or more short-range interaction profile. (A) and (B) depict the individual elements of the measured coupling matrix. Larger deviations are present for certain interactions involving middle ions (see, e.g., $J_{5,1}$ in (A), which is lower than expected); this is likely due to the fact that the energies of flipping spins in the middle of the chain are more closely spaced, making them more difficult to resolve accurately. (C) plots measured average interactions against ion separation and shows fits to a power law J_0/r^α. The error in α is an estimate of the standard error in the fit parameter; this takes into account the errors in the $J_{i,j}$ estimates based on fit error and statistical error in population measurements.

each energy splitting, we know the initial and final spin ordering and use this to write the energy splitting in terms of the $J_{i,j}$'s, as in Eq. 6.3. We use these relations to build a design matrix $\mathbf{A}$ and a response vector $\vec{y}$ such that $\mathbf{A}.\vec{x} = \vec{y}$, where $\vec{y}$ is a vector consisting of the measured energy splittings, $\vec{x}$ is a vector consisting of the spin-spin couplings, and $\mathbf{A}$ is a matrix with rank equal to or greater than the number of independent couplings (i.e., $\mathbf{A}$ has $\binom{N}{2}$ columns corresponding to the $\binom{N}{2}$ couplings, and *at least* $\binom{N}{2}$ independent rows; in fact, since we can in principle measure N^2 energy splittings with this technique, $\mathbf{A}$ will in general have more than $\binom{N}{2}$ independent rows). In practice, we did not measure all N^2 of the energy splittings that could in principle be measured with this protocol, because certain spin configurations were never populated above the noise floor, as discussed above;

however, as long as an appropriate set of $\binom{N}{2}$ energy splittings can be measured, this is sufficient for our purposes. Mathematica's LinearModelFit routine is used to perform a linear least-squares analysis determining which vector $\vec{x}$ minimizes the sum of squares of residuals, $\min |\mathbf{A}\vec{x} - \vec{y}|^2$. In this analysis, the data points (i.e. energy splittings) are weighted according to $1/\sigma^2_{\nu_0}$, where $\sigma^2_{\nu_0}$ is the estimated variance in the fit center ν_0 that was used to determine each splitting. As a side note, we have taken advantage of the knowledge that our couplings are roughly of the form J_0/r^α (and in particular, all share the same sign), which means that single-defect states will always be lower energy than the polarized state in our system, and (for the systems presented here) two-defect states are lower in energy than single-defect states. Without this knowledge it would be necessary to determine not only the magnitude of the energy splittings, as we do here, but also the sign, in order to fully constrain the coupling matrix. This is however achievable by making a second set of measurements with a known longitudinal field $B_x \sum_{i=1}^{N} \sigma_i^x$, which will shift the energies in a known direction. Comparison between the two data sets to determine whether B_x shifts the levels closer together or further apart would yield the sign of the energy splitting.

6.2.1 Scaling for validation of a power law interaction profile

It is important to consider how well our technique will scale to larger systems. Characterizing all $N \times N$ interactions among N spins requires only $N+1$ scans using the method just described. However, the various energy splittings may become more

closely spaced for large systems, and hence the required interaction time per scan will also depend on the system size. Here we estimate the interaction time necessary to resolve the most closely spaced energy splittings in a system with homogeneous power-law interactions,

$$H = \sum_{i,j} J_{i,j} \sigma_i^x \sigma_j^x \tag{6.5}$$

$$J_{i,j} = \frac{J_0}{|i-j|^\alpha}, \tag{6.6}$$

assuming that the system starts in the $|1111\cdots\rangle$ state. In this case, the energy required to flip the ith spin from the end of an N spin chain is:

$$E_i = 2\left(\sum_{k=1}^{i-1} J_{i,k} + \sum_{k=i+1}^{N} J_{i,k}\right) = 2J_0\left(\sum_{k=1}^{i-1} \frac{1}{k^\alpha} + \sum_{k=1}^{N-i} \frac{1}{k^\alpha}\right). \tag{6.7}$$

The energy cost is lowest for flipping the spin on the end. In this case, the energy is simply 2×(nearest neighbor coupling + next nearest neighbor coupling + ...) = 2 $(1 + 1/2^\alpha + 1/3^\alpha + \cdots + 1/(N-1)^\alpha)$. For flipping the second spin, the contribution of the final coupling $J_{1,N} = 1/(N-1)^\alpha$ is replaced by another nearest neighbor contribution, as we now have $2(J_{1,2} + J_{2,3} + J_{2,4} + ... + J_{2,N}) = 2(1+1+1/2^\alpha + ... + 1/(N-2)^\alpha)$. Since $1 \geq 1/(N-1)^\alpha$ for finite, positive α (which includes our limitation of $0 < \alpha < 3$), it will always cost more energy to flip the second spin than the first. By induction, we can see that due to the monotonic falloff of the couplings, it will always cost more energy to flip a spin closer to the center than a spin closer to the edge.

The energy of flipping spin i monotonically increases with i ($1 \leq i \leq N/2$).

However, to estimate the interaction time necessary to resolve neighboring energy splittings, we must estimate the spacing between these energy splittings. From Eq. 6.7, this is:

$$E_i - E_{i-1} \equiv \Delta_i = 2J_0 \left(\frac{1}{(i-1)^\alpha} - \frac{1}{(N-i+1)^\alpha} \right). \tag{6.8}$$

One can show that $|\Delta_i| = 0$ at $i = N/2 + 1$, which intuitively makes sense for even N since the energy of flipping either of the middle two spins should be the same. Furthermore, the derivative is negative:

$$\frac{d\Delta_i}{di} = -2J_0\alpha \left(\frac{1}{(i-1)^{\alpha+1}} + \frac{1}{(N-i+1)^{\alpha+1}} \right), \tag{6.9}$$

so the two (nondegenerate) resonances which will be closest together are those with $i = N/2$ and $i = N/2 - 1$. In this case,

$$\Delta_{N/2} = 2J_0 \left(\frac{1}{(N/2-1)^\alpha} - \frac{1}{(N/2+1)^\alpha} \right), \tag{6.10}$$

which can be rearranged as

$$\Delta_{N/2} = 2J_0 \left(\frac{2}{N} \right)^\alpha \left(\frac{1}{(1-\frac{2}{N})^\alpha} - \frac{1}{(1+\frac{2}{N})^\alpha} \right), \tag{6.11}$$

or, for large N,

$$\Delta_{N/2} \approx 8J_0 \left(\frac{2}{N} \right)^\alpha \frac{\alpha}{N}. \tag{6.12}$$

We therefore see that the smallest energy splitting scales like $1/N^{\alpha+1}$, which

sets the scale for the frequency resolution necessary to excite individual resonances. (For purposes of preparing the single-defect states to be used for further scans, we do not wish to excite multiple resonances simultaneously. This is because populating many single-defect states simultaneously would prevent us from obtaining sufficient information to use the protocol described above: e.g., if both $|101\cdots1\rangle$ and $|110\cdots1\rangle$ are populated simultaneously, yet have slightly different energies, then when we excite this superposition to the $|100\cdots1\rangle$ we cannot tell which of the single-defect states is the initial state.)

This means that the necessary interaction time for resolving the energies scales like $1/\Delta_{N/2} \sim N^{\alpha+1}/J_0$. Thus, the total time necessary to perform N frequency scans will scale polynomially as $N^{\alpha+2}$. This is a conservative estimate; adaptive techniques that increase the interaction time only in regions of high energy state density could decrease the total time necessary to characterize the entire system.

For smaller systems, Eq. 6.11 can be used to estimate this characterization time more quantitatively – for example, comparing the 8 spin system characterized experimentally to a 30 spin system, which is sufficiently large that numerical simulation of its dynamics will be infeasible. A heavy disclaimer comes with this estimate, because here we are interested only in the fundamental speed limitation to the measurement, ignoring all technical difficulties. Typical values for the couplings might be $J_0 = 1$ kHz and $\alpha = 1$, for which the necessary probe time $1/\Delta_{N/2}$ to fully resolve neighboring eigenstates is roughly 4 ms in an 8 spin system or 50 ms in a 30 spin system. In the absence of factors such as background gas collisions that limit the experimental repetition rate, this means an 8 spin system could be fully

characterized in roughly an hour (assuming (A) only 5 frequency scans are required due to left-right symmetry considerations, (B) each scan probes 50 frequencies, and (C) 1000 repetitions of each experiment are performed). A similar calculation for a 30 spin system leads to an estimate of 22 hours, still less than a day. We note that the tactic of choosing interaction times that allow each energy level to be resolved allows us to hold the number of repetitions of each experiment constant, without the quantum projection noise affecting the signal-to-noise ratio for the technique (again, assuming that other technical limitations like initialization error can be dealt with). This is because in the ideal situation, the population driven into the state of interest should be the same regardless of the number of spins.

This estimate can be compared to alternative techniques, such as that demonstrated in [89], where each pair is addressed separately to directly measure its coupling strength. There, the idea is to initialize all ions other than the pair of interest into an auxiliary state that does not participate in the spin dynamics, then characterize the frequency of oscillation between e.g. $|{\downarrow\uparrow}\rangle$ and $|{\uparrow\downarrow}\rangle$. To accurately estimate a frequency J in this manner, the system must be allowed to evolve for a time of at least $1/J$, so the longest interaction time will be given by $1/J_{1,N} = (N-1)^{\alpha}/J_0$. To characterize $N(N-1)/2$ interactions will therefore take a total time of order $N(N-1)^{\alpha+1}/J_0$, leading to the same scaling behavior of $N^{\alpha+2}/J_0$. Thus, though our method shows similar scaling behavior in this analysis, it still compares favorably due to the lack of experimental overhead for individual addressing. Additionally, the method in [89] will need to probe each pair for varying lengths of time in order to reliably estimate the frequency of oscillation in the time evolution, so it will have

a larger constant prefactor associated with the scaling behavior.

6.3 Generation of defect states and entangled states with a global laser beam

In addition to enabling further energy measurements, the method described above to prepare single-defect states without individual addressing has the potential to be useful for further dynamics studies, e.g. [84]. With a sufficient coherence time, further pulses could be used to prepare any eigenstate of the $\sigma^x\sigma^x$ Hamiltonian with global laser beams in no more than $\lfloor N/2 \rfloor$ pulses, by initializing the system in either $|000\cdots\rangle$ or $|111\cdots\rangle$ (whichever is 'closer' to the target state), then applying multiple pulses of the modulated transverse field at carefully chosen frequencies. (However, the resulting states can be superpositions of multiple σ^x eigenstates, as with the left-right symmetric interaction profile. To overcome this limitation and populate a single spin configuration without requiring full individual addressing, some sort of gradient would be needed. As seen from the nondegeneracy of the σ^x eigenstates with their reflected partner in Figure 6.1C (e.g., the state $|1111111111111110\rangle$ having a different measured energy than $|0111111111111111\rangle$), this wouldn't necessarily be hard to accomplish.)

We have demonstrated this capability to transfer population into any configuration of 5 spins by starting in either the $|11111\rangle$ or $|00000\rangle$ and applying at most two pulses of the transverse field. This system is small enough to also measure the entire relative energy spectrum. We use the frequency measurements obtained by probing

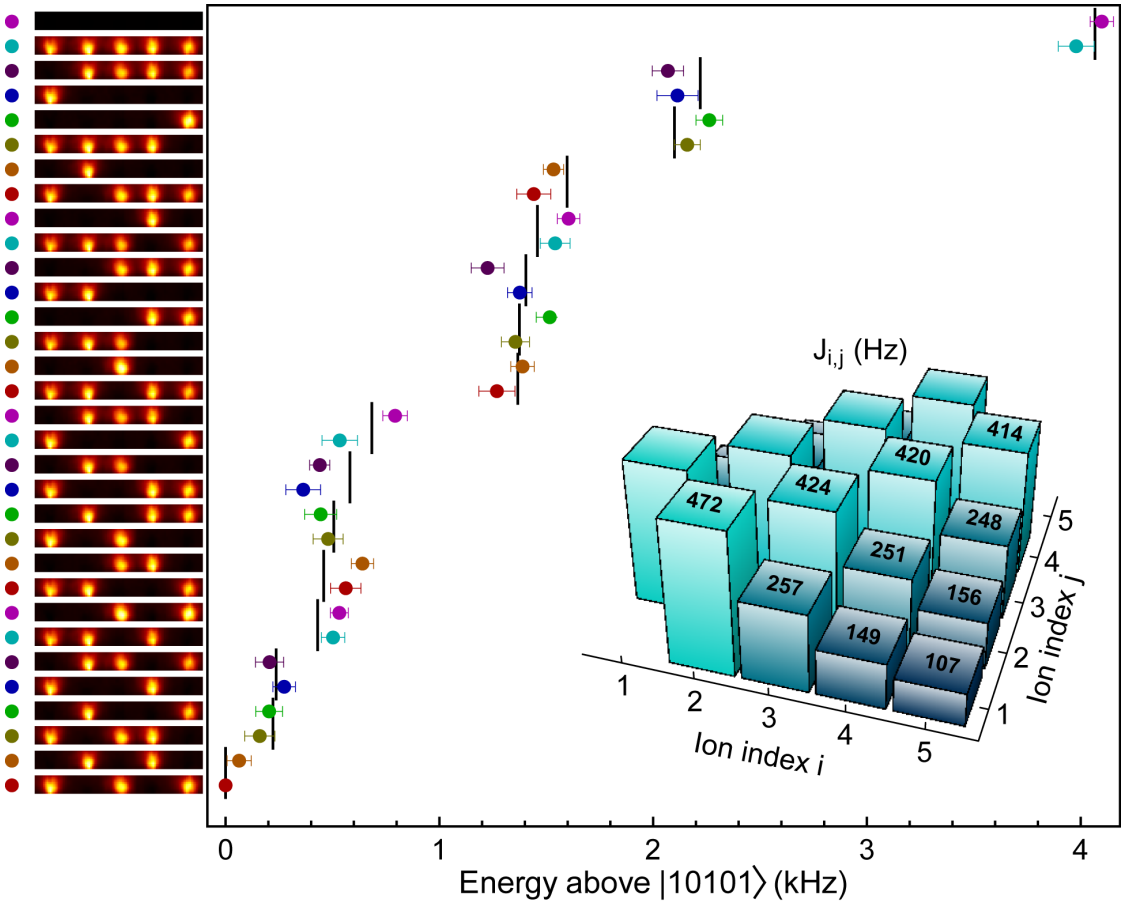

Figure 6.5: Reconstructed energy spectrum in a system of 5 spins with antiferromagnetic Ising couplings. The energy of each spin configuration above the $|10101\rangle$ ground state (colored points) is compared to the calculated energies (black lines). Calculations are based on the spin-spin couplings estimated from the same energy measurements (inset). Error bars include statistical errors and an estimate of systematic error due to experimental drifts.

the $|11111\rangle$ and $|00000\rangle$ states, and additionally perform spectroscopy on the states $|10101\rangle$ and $|01010\rangle$. To initialize these states, we adiabatically prepare the ground state of the antiferromagnetic couplings using the adiabatic protocol in Chapter 4; here the transverse field is ramped from $5J$ to $0.01J$ with an exponential profile with time constant 400 μs. Figure 6.5 shows the measured energy spectrum of this 5-spin system, obtained by direct addition of the measured energy splittings. The estimate of systematic error is based only on consistency checks when there are multiple ways to arrive at the same state: e.g., $E(|11111\rangle \leftrightarrow |11110\rangle) + E(|11110\rangle \leftrightarrow |01110\rangle)$ may not match $E(|11111\rangle \leftrightarrow |01111\rangle) + E(|01111\rangle \leftrightarrow |01110\rangle)$. The standard deviation of all estimates of a given energy is taken to be an estimate of the systematic error due to experimental drifts. As seen in the figure, this is not quite statistically consistent with the calculations, indicating that we underestimate the systematic error; this is not entirely surprising, because our estimate will not always be sensitive to (e.g.) the effective energies changing *between* frequency scans. Nevertheless, the spectrum matches reasonably well with that calculated for the coupling matrix estimated from the same measurements, which is within 10% of the predicted values. Such a detailed examination of the full spectrum of a many-body quantum system is generally difficult to achieve, and shows the versatility of this form of many-body spectroscopy.

In the absence of spatial gradients, driving the state $|111\cdots\rangle$ with a global modulated transverse field at any energy resonance will result in a symmetric superposition of σ^x eigenstates (e.g., $(|011\cdots11\rangle + |11\cdots110\rangle)/\sqrt{2}$), which should exhibit some degree of entanglement. However, the entanglement is difficult to de-

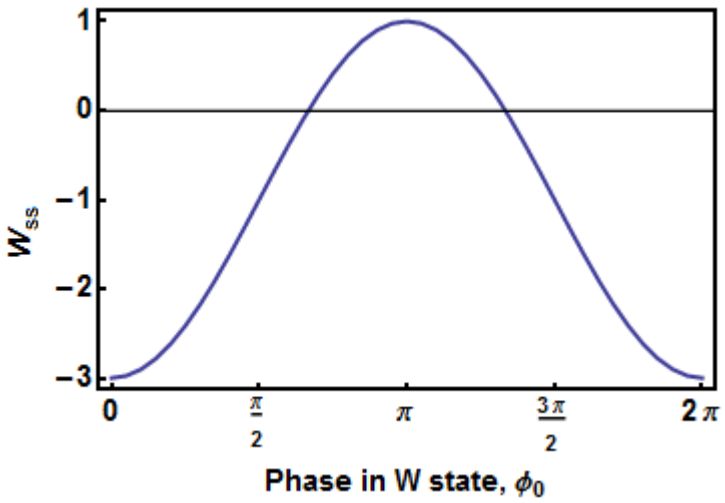

Figure 6.6: Result from applying the witness operator W_{ss} (Eq. 6.14) to the ideal $N = 4$ state $\frac{1}{2}(|0111\rangle + e^{i\phi_0}|1011\rangle + e^{i\phi_0}|1101\rangle + |1110\rangle)$. If the phases are set poorly, it may not be possible to certify entanglement using only global magnetization measurements.

tect without individual rotations for readout. To prepare a state with certifiable entanglement, we can instead subject an initial state $|111\cdots11\rangle$ to multiple frequencies simultaneously, such that all of the possible transitions are driven equally. After an appropriate time, the system will ideally be driven into a W-type state of the form

$$|\Psi_W\rangle = \frac{1}{\sqrt{N}}\left(e^{i\phi_0}|011\cdots11\rangle + e^{i\phi_1}|101\cdots11\rangle + \cdots + e^{i\phi_1}|111\cdots01\rangle + e^{i\phi_0}|111\cdots10\rangle\right). \tag{6.13}$$

The phases ϕ_i depend on the relative phase of the applied modulation frequencies. The entanglement present in such a state can be detected using global measurements of the magnetization along σ^x, σ^y, and σ^z [97].

Trace over 1?	Trace over 2?	Trace over 3?	Trace over 4?	$\langle W_{ss} \rangle$	Number ions involved, N	$\langle W_{ss} \rangle_{\min}$
No	No	No	No	-1.62(22)	4	-3
Yes	No	No	No	-0.382(121)	3	-2
No	Yes	No	No	-0.847(96)	3	-2
No	No	Yes	No	-0.735(101)	3	-2
No	No	No	Yes	-0.300(114)	3	-2
Yes	Yes	No	No	-0.115(40)	2	-1
Yes	No	Yes	No	-0.111(41)	2	-1
Yes	No	No	Yes	-0.001(44)	2	-1
No	Yes	Yes	No	-0.279(37)	2	-1
No	Yes	No	Yes	-0.081(38)	2	-1
No	No	Yes	Yes	-0.055(39)	2	-1

Table 6.1: Measured values of the spin-squeezing-type witness W_{ss} described in the text, compared to theoretical values for a perfect 4-spin state $|\Psi_W\rangle$ (rightmost column); a negative value certifies that the state is nonseparable and hence that at least two of the spins are entangled. By tracing over individual spins, we see that all pairs except ions 2 and 3 are at least 1σ below zero, showing that these pairs are entangled; entanglement between each possible pair is consistent with the multipartite entanglement that would be expected for a perfect W state.

We use a witness operator

$$W_{ss} = (N-1)(\langle J_x^2 \rangle - \langle J_x \rangle^2) + \frac{N}{2} - \langle J_y^2 \rangle - \langle J_z^2 \rangle , \tag{6.14}$$

where $J_\gamma \equiv \frac{1}{2} \sum_{i=1}^{N} \sigma_i^\gamma$ (with appropriate phases) and angle brackets denote ensemble averages. This spin-squeezing observable is provably nonnegative for all fully separable states, so measurement of a negative value certifies that at least two particles are entangled. Measuring a negative value is hence a sufficient but not necessary condition to show entanglement.

One caveat to note is that this witness operator relies on the relative phases of the state created. E.g., if the phases ϕ_i in the state 6.14 are nonzero, the witness

may be positive, as shown in Figure 6.6, although it is clear by inspection that there is still multipartite entanglement present.

We prepare an entangled state of 4 spins by applying two simultaneous frequencies of the modulated transverse field to the state $|1111\rangle$ with an appropriate relative phase for 1.8 ms and measure the resulting state along the Bloch sphere directions σ^x, σ^y, and σ^z to obtain a measurement of the witness shown above. The negative value thus obtained certifies that the full state is entangled. Moreover, individual spin state imaging allows us to trace over any given spin or pair of spins and apply the witness to this reduced density matrix. This data is shown in Table 6.1. Though this witness does not prove the existence of multipartite entanglement, the certification of bipartite entanglement between almost every pair of spins is suggestive of a high degree of entanglement. This demonstration that a highly entangled state can be created with the probe field shows the existence of quantum coherence in the population transfers.

6.4 Measurement of a critical gap

Finally, we probe energy levels at nonzero transverse field B_0, including near the critical region $B_0 \approx \langle J \rangle$. Determining the critical energy gap Δ, at which the energy difference between the ground and lowest coupled excited states is minimized, is useful because this parameter limits the ability to perform an adiabatic sweep of the transverse field, as discussed in Chapter 4. However, measuring the critical gap is difficult in general because of the inability to measure in or even know the

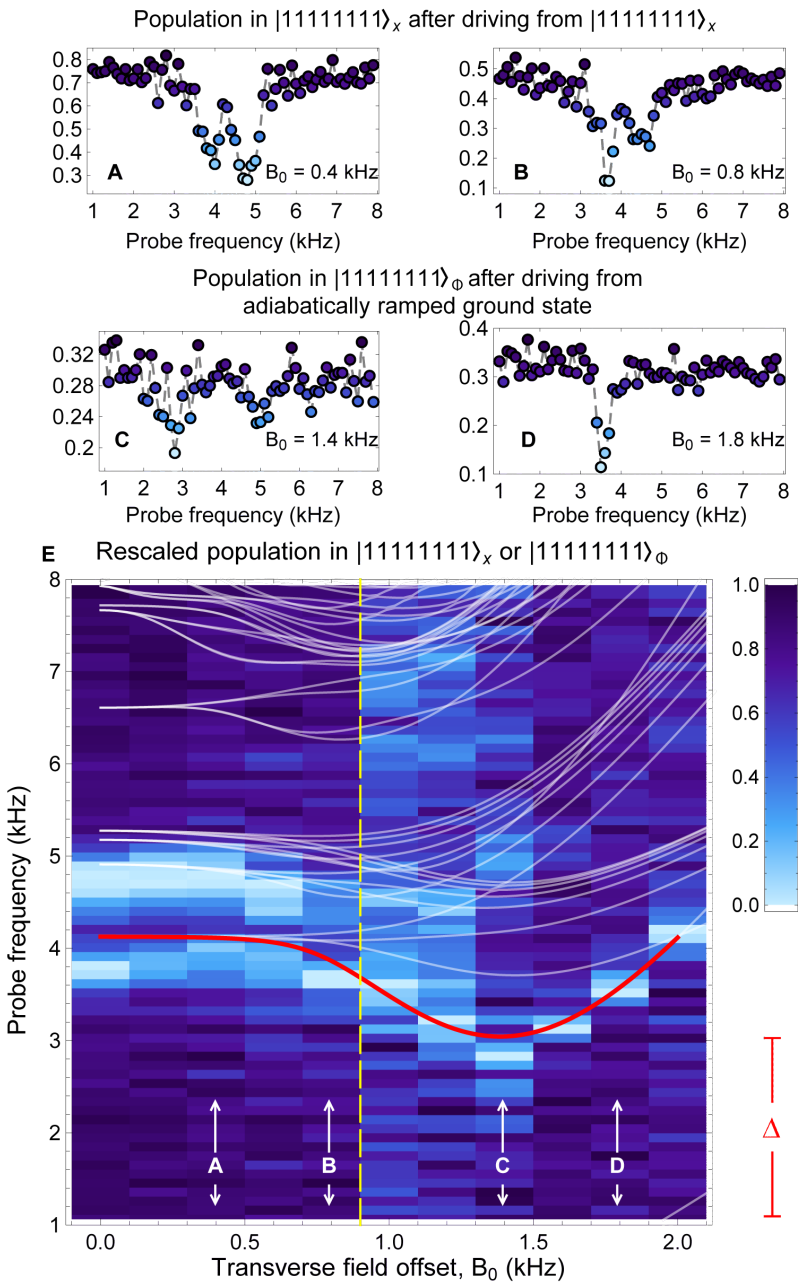

Figure 6.7: A-D: Populations in a polarized state vs modulation frequency of the transverse field at four different values of the offset field B_0. Coloring is according to the rescaling scheme used in E. In A and B, we subject the state $|11111111\rangle$ to the modulated field, then measure its population. In C and D, we prepare the ground state via an adiabatic ramp, subject it to the modulated field, and then measure the population in $|\uparrow\uparrow\uparrow\uparrow\uparrow\uparrow\uparrow\uparrow\rangle_\phi$ (see text). E: Rescaled populations in $|11111111\rangle$ (left of the dashed line) or $|\uparrow\uparrow\uparrow\uparrow\uparrow\uparrow\uparrow\uparrow\rangle_\phi$ (right of the dashed line) vs. static field offset B_0 and modulation frequency. The rescaling is a linear mapping of the population to the color scale, such that the largest (smallest) population in any vertical slice is mapped to the darkest (lightest) shade in the color bar on the right. Calculated energy levels, based on measurements of trap and laser parameters, are overlaid as thin white lines, and the lowest coupled excited state as a thick red line, showing the critical gap Δ at position C. The energy of the ground state is always taken to be zero.

instantaneous eigenbasis.

The protocol that was used to measure energy splittings in Figures 6.1 and 6.2 is effective even when there is a small DC transverse field B_0 (Figure 6.7A and 6.7B), but breaks down near the critical region. This is because $|111\cdots\rangle$ no longer approximates an eigenstate of the static Hamiltonian: For example, even in Figure 6.7A and 6.7B (where we can still identify the transitions), we see that the contrast is reduced because even when the modulated probe drives no transitions, the static field B_0 causes the state to evolve away from $|11111111\rangle$. However, for a finite-size ferromagnetic system, measurements along a different axis of the Bloch sphere (here, $\hat{x}+\hat{y}$) allow us to still observe transitions from the ground to the first coupled excited state near the critical gap (Figure 6.7C and 6.7D). This is because the ground state near the critical gap has a significant overlap with $|\uparrow\uparrow\uparrow\uparrow\uparrow\uparrow\uparrow\uparrow\rangle_\phi$, the state fully polarized along $\hat{x}+\hat{y}$. (E.g., for the parameters used in Figure 6.7, i.e. 8 spins with ferromagnetic Ising couplings with $J_0 \sim 560$ kHz and $\alpha \sim 0.63$, there is a 51% overlap of the ground state at the gap with $|\uparrow\uparrow\uparrow\uparrow\uparrow\uparrow\uparrow\uparrow\rangle_\phi$) Hence, measuring the population in $|\uparrow\uparrow\uparrow\uparrow\uparrow\uparrow\uparrow\uparrow\rangle_\phi$ allows us to monitor transitions away from the ground state, at least near the critical gap. As shown in Figure 6.7E, these experiments allow us to map the lowest coupled excited state from $B_0 = 0$ beyond the critical energy gap Δ. The downward drift in energies near $B_0 = 0$ can be attributed to drifts in laser and trap parameters as the experiments progressed from higher to lower fields; we have independent evidence that drifts have occurred from measuring the interaction between 2 ions, for nominally identical laser and trap parameters, to be different before and after the data collection. An alternative protocol, which

follows the time evolution after a quench, has recently been proposed for measuring the critical gap and may scale better for larger systems [98].

Chapter 7: Toolbox for simulating spin-1 particles

The final set of results in this thesis are a set of preliminary investigations into using our ion chain to study systems of interacting spin-1 particles, a pursuit that has several potential applications. Antiferromagnetic spin-1 chains support one of the simplest known examples of a topological phase of matter [99,100], known as the Haldane phase, a gapped phase that is not defined by a local order parameter but instead manifests as a special kind of nonlocal order [101]. Such topological phases are of interest not only from the perspective of many-body physics studies, but also for their potential connections to measurement-based quantum computation [102]. For example, ground states of the Haldane phase can in principle be used as a perfect quantum wire, as long as certain symmetries are respected, meaning that perturbing the ground state to the point where it is no longer useful as a quantum wire is equivalent to crossing a phase transition [103]. Developing an experimental platform to realize this phase would therefore be of interest both for fundamental studies of spin physics but also as a prototype to test ideas about using topologically ordered states to perform quantum computations.

The model we will study is a spin-1 chain subject to long-range flip-flop (XY)

interactions,

$$H = \sum_{i,j} J_{i,j} \left(S_+^i S_-^j + S_-^i S_+^j \right) + \sum_{i,m} \zeta_{i,m} \left(2 a_m^\dagger a_m + 1 \right) S_z^i \tag{7.1}$$

Here $S_\pm$ are the spin-1 raising and lowering operators satisfying the commutation relation $\left[S_z^i, S_\pm^j \right] = \pm S_\pm^i \delta_{ij}$ (δ_{ij} is the Kronecker delta); sums run from 1 to N, the number of spins present; a_m ($a_m^\dagger$) is the annihilation (creation) operator on the mth normal mode of motion; and $J_{i,j}$ is the interaction strength, which follows the same formula as in the spin-1/2 Ising model we have previously discussed. As before, we will operate in a regime where the interactions fall off with distance as roughly $J_{i,j} \sim J_0 / |i-j|^\alpha$ (α can be tuned between roughly 0.5 and 1.5 using trap and laser parameters.) In this work, it is the interaction term on the left that we want to study, and we will focus on the subspace of states with $\langle S_z \rangle = 0$, such that the phonon-dependent S_z term on the right can be neglected.

7.1 Experimental implementation

The switch from simulating spin-1/2 particles to spin-1 particles does not involve too much experimental overhead. Indeed, from the standpoint of the hardware required, the only change is to rotate a waveplate to polarize one of the Raman lasers in the magnetic field direction, such that the Raman lasers drive transitions between the $|F = 0, m_F = 0\rangle$ and $|F = 1, m_F = \pm 1\rangle$ states. This situation is depicted in Figure 7.1.

The Hamiltonian in Eq. 7.1 derives from the application of a pair of beat

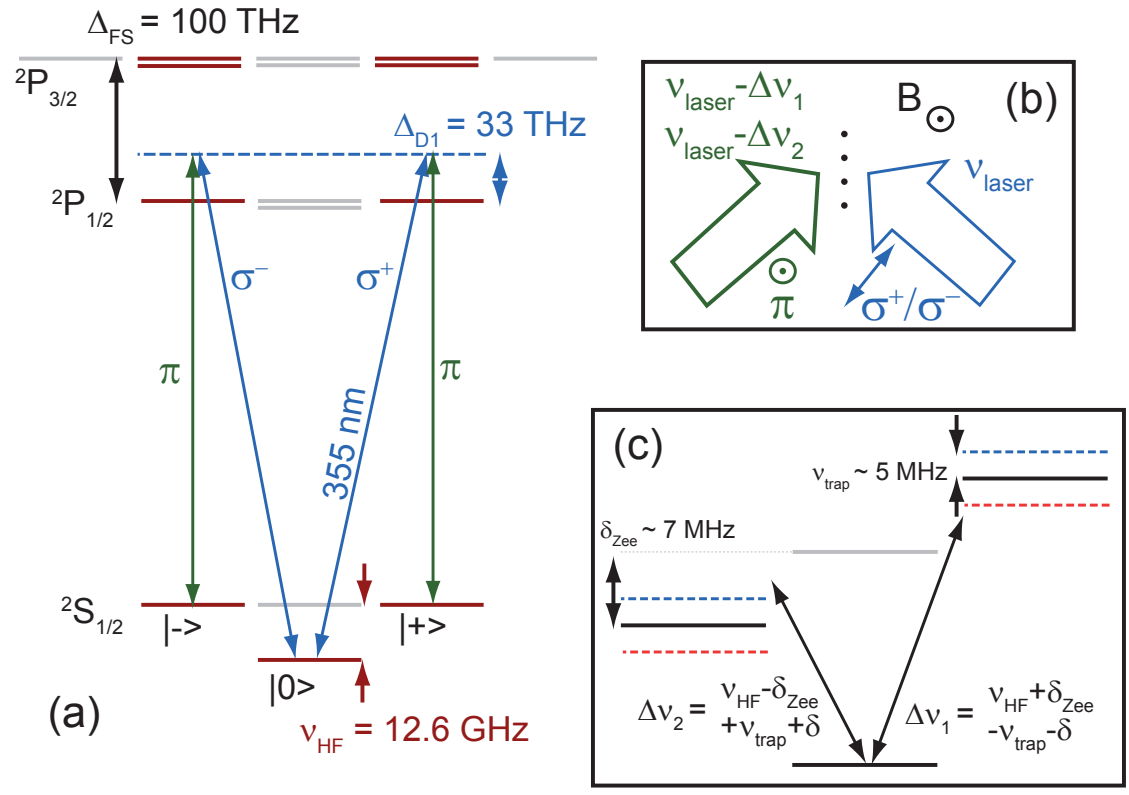

Figure 7.1: (a): Level diagram for $^{171}Yb^+$, highlighting relevant states. (b): Sketch of experimental geometry, showing the polarizations used to drive stimulated Raman transitions relative to laser wavevectors and the real magnetic field. (c): Detailed level diagram of the $^2S_{1/2}$ ground state, showing Raman beatnotes in relation to Zeeman splittings and motional sidebands. Level diagrams are not to scale.

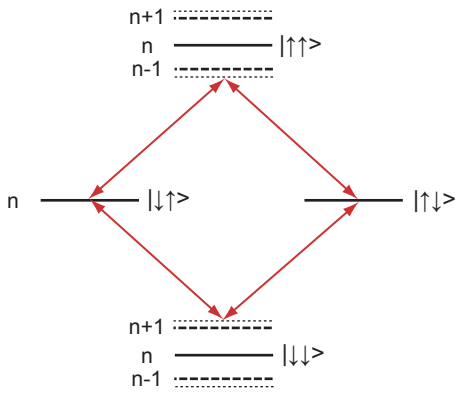

Figure 7.2: Two-body level diagram for single-sideband XY interaction in the spin-1/2 system. We can see that while there are resonant two-beatnote transitions from $|\uparrow\downarrow\rangle$ to $|\downarrow\uparrow\rangle$, the states $|\downarrow\downarrow\rangle$ and $|\uparrow\uparrow\rangle$ will not participate in the dynamics.

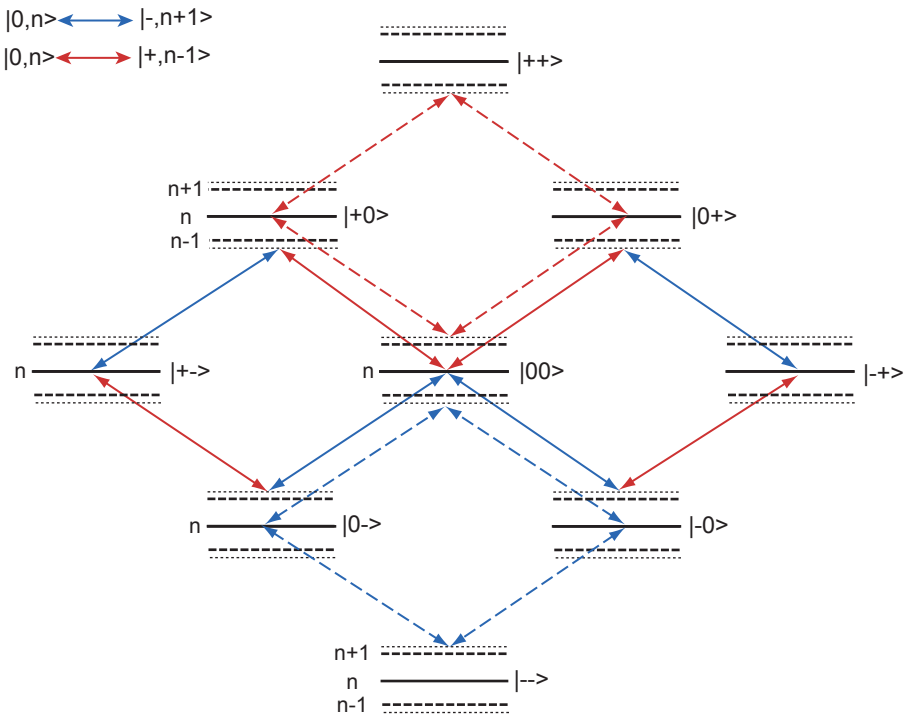

Figure 7.3: Many-body level diagram for XY interaction in the spin-1 system.

frequencies detuned near the '$|+\rangle$ red sideband' transition, corresponding to the Hamiltonian $|+\rangle\langle 0|\, a + h.c.$, and '$|-\rangle$ blue sideband', corresponding to $|-\rangle\langle 0|\, a^\dagger + h.c.$. A derivation of the spin-1 XY Hamiltonian in Eq. 7.1 is presented in Appendix D. While the frequencies required thus look rather similar to the frequencies for the spin-1/2 Ising model discussed previously, this is conceptually closer to the idea of applying a single detuned sideband to the spin-1/2 system, which similarly produces a flip-flop interaction and a phonon-dependent level shift, as can be seen by following the discussion of the Magnus expansion in Section D.2 with spin-1/2 operators. Figure 7.2 sketches a level diagram for this single-sideband XY operation, similar to the spin-1/2 Mølmer-Sørensen level diagram shown in Figure 2.5, and Figure 7.3 sketches the analogous level diagram for the spin-1 XY operation.

7.1.1 Dynamics of an XY spin-1 chain

The ions are initialized before each experiment by cooling the transverse modes of motion to their ground state and optically pumping the spins to the $|00\cdots\rangle$ state. This restricts the dynamics to the set of states with $\langle S_z\rangle = 0$, which allows the second term in Eq. 7.1 to be neglected. The subspace is also robust to fluctuations in the real magnetic field, which result in an unwanted noise term $\mu_B \Delta B \sum_i S_z^i$, so remaining in this decoherence-free subspace [104, 105] allows us to probe coherent dynamics for experimental durations longer than the T_2 coherence time of the $|0\rangle \leftrightarrow |\pm\rangle$ transitions. Remaining within this subspace does not substantially limit the size of the accessible Hilbert space: For $N = 4$ or more spins, the number of states in the $\langle S_z\rangle = 0$ subspace of N spin-1 particles is greater than the number of states in a system of N spin-1/2 particles. The number of states in this subspace can be quantified as

$$N_{\langle S_z\rangle=0} = 1 + \sum_{k=1}^{\lfloor N/2\rfloor} \binom{2k}{k}\binom{N}{k}. \tag{7.2}$$

These numbers are called central trinomial coefficients, because they give the largest coefficient in the expansion of $(1 + x + x^2)^N$.

After applying the Hamiltonian in Eq. 7.1 for some amount of time, we measure the probability of each individual spin remaining in state $|0\rangle$. Because both of the $|\pm\rangle$ states respond to the fluorescence laser, and are randomly scattered into all of the $|F = 1\rangle$ states during the detection process, our current setup does not allow discrimination among all three possible spin states in a single experiment. However,

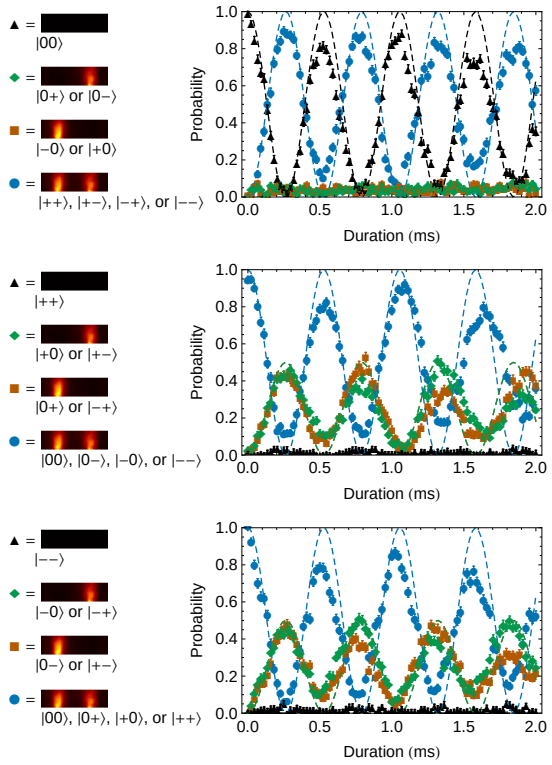

Figure 7.4: Dynamics of 2 spin-1 particles subjected to the XY Hamiltonian in Eq. 7.1, where the populations in state $|0\rangle$ (a), $|+\rangle$ (b), or $|-\rangle$ (c) are measured. The populations are consistent with Rabi flopping between the state $|00\rangle$ (appearing as black triangles in (a) or blue circles in (b) and (c)) and the symmetric superposition of $|+-\rangle$ (blue circles in (a), green diamonds in (b), orange squares in (c)) and $|-+\rangle$ (blue circles in (a), orange squares in (b), green diamonds in (c)). Dashed lines represent theoretical predictions, with no free parameters. Error bars: statistical uncertainty based on 500 repetitions of the experiment.

we can measure the population in either $|+\rangle$ or $|-\rangle$ by repeating the experiment and applying a π rotation to the appropriate transition before the fluorescence imaging. This is not a fundamental limitation, since future experiments could 'shelve' population(s) into long-lived states that do not participate in the cycling transition used for detection.

In the case of 2 spins, the dynamics of applying the Hamiltonian in Eq. 7.1 to $|00\rangle$ can be simply understood as Rabi flopping between the $|00\rangle$ and $(|+-\rangle + |-+\rangle)/\sqrt{2}$

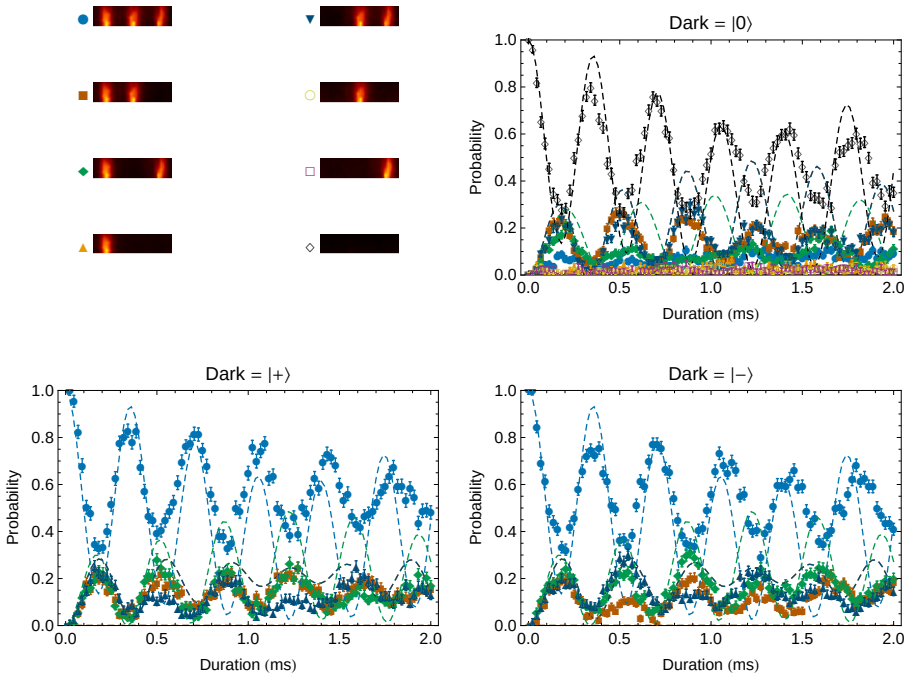

Figure 7.5: Dynamics of 3 spin-1 particles subjected to the XY Hamiltonian in Eq. 7.1, where the populations in state $|0\rangle$ (a), $|+\rangle$ (b), or $|-\rangle$ (c) are measured. In panel (a), all of the eight configurations of bright and dark ions are displayed, while in panels (b) and (c) only those populations consistent with the $\langle S_z \rangle = 0$ subspace are shown for clarity of presentation.

states. This behavior is shown in Figure 7.4. Though we do not extract the full spin correlations, there is sufficient information in this case to determine that the populations remain in the $\langle S_z \rangle = 0$ subspace as expected. Figure 7.4(b) and (c) show the absence of the $|{+}{+}\rangle$ and $|{-}{-}\rangle$ states, respectively, while Figure 7.4(a) shows the absence of the other $\langle S_z \rangle \neq 0$ states ($|0{+}\rangle$, $|0{-}\rangle$, $|{+}0\rangle$, and, $|{-}0\rangle$).

The dynamics in systems of more than 2 spins becomes complicated to analyze because of the many interaction frequencies involved. For 3 spins, the interactions are few enough to still qualitatively see oscillations at the interaction frequencies, as shown in Figure 7.5. Even with three spins restricted to the $\langle S_z \rangle = 0$ subspace, the many-body nature of the system prevents a simple analytical solution to the

dynamics: rather than simply flopping between $|000\rangle$ and the symmetric combinations, $(|0+-\rangle + |0-+\rangle)/\sqrt{2}$, $(|+0-\rangle + |-0+\rangle)/\sqrt{2}$, and $(|+-0\rangle + |-+0\rangle)/\sqrt{2}$, the flip-flop exchange term begins coupling (e.g.) $|0+-\rangle$ to $|+0-\rangle$ and $|-+0\rangle$.

One experimental challenge we have had to overcome in observing dynamics is what we interpret as a stray site-dependent S_z term. Specifically, the observation is as follows. One of the calibrations we perform is to load two ions, apply the XY interaction for some fixed amount of time, and scan the frequency of *one* of the sidebands generating the interaction. As with the similar calibration done with the spin-1/2 Ising model, this maps out the resonant frequency of the two-body transition from $|00\rangle$ to $|-+\rangle$ or $|+-\rangle$, and allows us to fine-tune the symmetric detunings so as to ensure the transition is not being driven off-resonance. However, we observe that under many conditions, this results in mapping more than one resonance: the transition to $|+-\rangle$ occurs at a different red-sideband frequency than the transition to $|-+\rangle$. Of course, the XY Hamiltonian we desire requires the transitions to $|+-\rangle$ and $|-+\rangle$ to have the same energy splitting. The solution to this problem has been to change the 'twist' DC voltages on the trap, which should rotate the longitudinal trap axis a small amount. The voltage change required to fix the nondegeneracy of $|+-\rangle$ and $|-+\rangle$ does not move the ions sufficiently to see the effect on the CCD, so we speculate that the unwanted effect is due to micromotion whose amplitude is position-dependent.

7.1.2 Measuring entanglement in spin-1 particles or qutrits

Some information about the relative phases of various components of the wavefunction can be extracted using techniques analogous to the parity oscillations that are used to demonstrate entanglement between two qubits [106].

7.1.2.1 Pedagogical discussion of the qubit case

The general flavor of these analysis sequences can be understood by analogy to the more usual parity measurement used to verify entanglement in a Bell pair of qubits, so we will first discuss the details of this measurement before describing the slightly more complicated measurement done on the spin-1 system. In the more common parity measurement, a state

$$|\psi_0\rangle = (|00\rangle + |11\rangle)/\sqrt{2} \tag{7.3}$$

is subjected to $\pi/2$ rotations of different phases $R(\pi/2, \phi)$. This maps the state to

$$\frac{i}{\sqrt{2}}\left[e^{-i\phi}\sin\phi\,|00\rangle - e^{i\phi}\sin\phi\,|11\rangle + \cos\phi\,|10\rangle + \cos\phi\,|01\rangle\right], \tag{7.4}$$

where the populations in $|00\rangle$ and $|11\rangle$ are each $\frac{1}{2}\sin^2\phi$, and the populations in $|01\rangle$ and $|10\rangle$ are each $\frac{1}{2}\cos^2\phi$. If we define the parity operator as the population in

states with even numbers of $|1\rangle$'s minus the population in states with odd numbers,

$$\Pi = \sum_{j=0}^{2} (-1)^j P_j, \tag{7.5}$$

where P_j is the probability of j spins up (in $|1\rangle$), then Π will vary with ϕ in the ideal case as $\Pi = -\cos 2\phi$. In a nonideal system, the parity oscillation will have an amplitude corresponding to the coherence (off-diagonal density matrix element) between $|00\rangle$ and $|11\rangle$,

$$\Pi = -2|\rho_{00\cdots,11\cdots}| \cos 2\phi. \tag{7.6}$$

This is easily shown, by appropriate application of the rotation matrix above. This is a simplification based on some assumptions about lack of populations in undesired states; for a fully general two-qubit density matrix,

$$\rho = \begin{pmatrix} p_0 & A_{01}e^{i\phi_{01}} & A_{02}e^{i\phi_{02}} & A_{03}e^{i\phi_{03}} \\ A_{01}e^{-i\phi_{01}} & p_1 & A_{12}e^{i\phi_{12}} & A_{13}e^{i\phi_{13}} \\ A_{02}e^{-i\phi_{02}} & A_{12}e^{-i\phi_{12}} & p_2 & A_{23}e^{i\phi_{23}} \\ A_{03}e^{-i\phi_{03}} & A_{13}e^{-i\phi_{13}} & A_{23}e^{-i\phi_{23}} & p_3 \end{pmatrix}, \tag{7.7}$$

the parity function is actually given by

$$\begin{aligned} \Pi = & \quad A_{12}\cos\phi_{12} - A_{03}\cos(2\phi + \phi_{03}) \\ & +2\left[A_{02}\sin(\phi+\phi_{02}) + A_{13}\sin(\phi+\phi_{13})\right]\left[A_{01}\sin(\phi+\phi_{01}) + A_{23}\sin(\phi+\phi_{23})\right]. \end{aligned} \tag{7.8}$$

However, in the context of attempting to make the state $(|00\rangle + |11\rangle)/\sqrt{2}$, the populations in states $|1\rangle$ and $|2\rangle$ (corresponding to $|01\rangle$ and $|10\rangle$) are generally small, and any coherences involving those states are hence also small ($|A_{02}| \ll 1$, $|A_{12}| \ll 1$, etc).

It is useful to distinguish among the parity measurement, the fidelity of the target state, and the criterion for verifying entanglement between the qubits. The parity measurement demonstrates only the amplitude of the coherence $\rho_{00,11}$. The fidelity of creating the state $|\psi_0\rangle$ given the actual density matrix ρ is given by

$$F = \langle\psi_0|\rho|\psi_0\rangle \tag{7.9}$$

$$= (P_0 + P_3 + 2|\rho_{03}|)/2. \tag{7.10}$$

Finally, it can be shown that for all separable states, the fidelity F defined here is limited by $F \leq 1/2$; hence, measuring $F > 1/2$ demonstrates entanglement in the system. Here I directly reproduce the argument in [106] leading to this conclusion. Suppose we have an arbitrary factorizable wavefunction of N particles,

$$|\psi_F\rangle = (a\,|0\cdots0\rangle_X + b\,|1\cdots1\rangle_X + \cdots) \otimes (c\,|0\cdots0\rangle_Y + d\,|1\cdots1\rangle_Y + \cdots)\,. \tag{7.11}$$

Here X and Y represent distinct subsystems of the N particles, and in our pedagogical case of two particles would refer simply to the left and right qubits. Because the factored wavefunctions must be normalized, we can infer the criteria $|a|^2 + |b|^2 \leq 1$

and $|c|^2 + |d|^2 \leq 1$, from which we obtain

$$|a|^2 + |b|^2 + |c|^2 + |d|^2 \leq 2. \tag{7.12}$$

We can rewrite the left hand side of this inequality as

$$(|a| - |c|)^2 + 2|ac| + (|b| - |d|)^2 + 2|bd| \leq 2. \tag{7.13}$$

Since the squared terms are positive, we can further write

$$|ac| + |bd| \leq 1 \tag{7.14}$$

or

$$(|ac| + |bd|)^2 \leq 1 \tag{7.15}$$

giving us

$$|ac|^2 + |bd|^2 + 2|abcd| = 2F \leq 1; \tag{7.16}$$

here we have used $F = P_0 + P_3 + |\rho_{03}|$ in the density matrix language above, $|ac|^2 = P_0$, $|bd|^2 = P_3$, and $|abcd| = |\rho_{03}|$. Hence, measuring a fidelity $F > 1/2$ directly shows entanglement between the subsystems, and the parity measurement of the coherence $|\rho_{03}|$ is what enables a measurement of $F > 1/2$.

7.1.2.2 The more complicated qutrit case

Once the analysis above is understood, it is simple to extend to the case of three-level systems. This time, we will write our factorizable wavefunction of two particles as

$$|\psi_F\rangle = (a\,|+\rangle_X + b\,|0\rangle_X + c\,|-\rangle_X) \otimes (d\,|+\rangle_Y + f\,|0\rangle_Y + g\,|-\rangle_Y)\,. \tag{7.17}$$

Again, we will have inequalities imposed by normalization, $|a|^2 + |b|^2 + |c|^2 \leq 1$ and $|d|^2 + |f|^2 + |g|^2 \leq 1$. This can be rewritten as

$$(|a| - |g|)^2 + 2|ag| + (|b| - |f|)^2 + 2|bf| + (|c| - |d|)^2 + 2|cd| \leq 2 \tag{7.18}$$

or

$$|ag| + |bf| + |cd| \leq 1 \tag{7.19}$$

Squaring, we get

$$|ag|^2 + |bf|^2 + |cd|^2 + 2|agcd| + 2|agbf| + 2|bfcd| \leq 1 \tag{7.20}$$

or

$$P_{+-} + P_{00} + P_{-+} + 2|\rho_{+-,-+}| + 2|\rho_{+-,00}| + 2|\rho_{-+,00}| \leq 1. \tag{7.21}$$

When we make the state $(|+-\rangle + |-+\rangle)/\sqrt{2}$ we can extract sufficient information to demonstrate a violation of this inequality by performing a slightly more

complex series of rotations on the $|0\rangle$ to $|\pm\rangle$ transitions,

$$R_{0\pm}(\theta,\phi) = \exp\left[i\frac{\theta}{2}\left(e^{\pm i\phi}\,|\pm\rangle\,\langle 0| \;\; + e^{\mp i\phi}\,|0\rangle\,\langle\pm|\right)\right]. \tag{7.22}$$

In this notation, we apply the sequence $R_{0+}(\pi/2,\phi).R_{0+}(\pi/2,0).R_{0-}(\pi,0)$. The intuition for this sequence is as follows. First, the π rotation $R_{0-}(\pi,0)$ maps the ideal state to $(|+0\rangle + |0+\rangle)/\sqrt{2}$. This step is important only because we do not have the ability either to directly perform rotations between $|+\rangle$ and $|-\rangle$, or to discriminate between them with a measurement, without first mapping one of them to the $|0\rangle$ state. Second, the rotation $R_{0+}(\pi/2,0)$ maps this state to $(|{+}{+}\rangle + |00\rangle)/\sqrt{2}$, which is directly analogous to the Bell state analyzed above. This step is important because even if the phase of the second rotation were varied as $R_{0+}(\pi/2,\phi')$, this would not affect any observables as it would create a state like $\left(|{+}{+}\rangle + e^{i\Phi(\phi')}\,|00\rangle\right)/\sqrt{2}$. Finally, the parity will oscillate with the phase of the third rotation, $R_{0+}(\pi/2,\phi)$. Here we again define the parity as

$$\Pi = \sum_{j=0}^{2}(-1)^j P_j, \tag{7.23}$$

where this time P_j is the probability of creating a state with j spins in the $|0\rangle$ state, which can be directly measured.

By doing lots of algebra with the help of Mathematica, we can show that the full dependence of the parity observable Π on the phase ϕ of the final rotation is

given by

$$\begin{aligned}\Pi(\phi) = \quad & \tfrac{1}{2}\left(P_{--} - P_{-+} + 2P_{00} - P_{+-} + P_{++} + 2|\rho_{+-,-+}|\right) \\ & + \cos\phi\left(P_{-0} + P_{0-} - P_{0+} - P_{+0}\right) \\ & -2\sin\phi\left(|\rho_{-0,+0}| + |\rho_{0-,0+}|\right) \\ & + \tfrac{1}{2}\cos 2\phi\left(P_{--} + P_{++} - P_{+-} - P_{-+} - 2|\rho_{+-,-+}| - 2|\rho_{--,++}|\right) \\ + \quad & \tfrac{1}{2}\sin 2\phi\left(2|\rho_{-+,++}| + 2|\rho_{+-,++}| - 2|\rho_{--,-+}| - 2|\rho_{-+,--}|\right). \end{aligned} \tag{7.24}$$

which, in the paper draft, is written as

$$\begin{aligned}\Pi(\phi) = \quad & C + \tfrac{1}{2}\cos 2\phi\left(P_{--} + P_{++} - P_{+-} - P_{-+} - 2|\rho_{+-,-+}| - 2|\rho_{--,++}|\right) \\ + \quad & \tfrac{1}{2}\sin 2\phi\left(2|\rho_{-+,++}| + 2|\rho_{+-,++}| - 2|\rho_{--,-+}| - 2|\rho_{-+,--}|\right). \end{aligned} \tag{7.25}$$

Here, C is dependent on various coherences but is independent of ϕ, and the various density matrix elements refer to those of the *input* state that is expected to look roughly like $\left(|+-\rangle + |-+\rangle\right)/\sqrt{2}$. In the case where the populations in $|++\rangle$ and $|--\rangle$ are negligible, this can be approximated as

$$\Pi(\phi) \approx C + \frac{1}{2}\cos 2\phi\left[-P_{+-} - P_{-+} - 2|\rho_{+-,-+}|\right] \equiv C - F\cos 2\phi. \tag{7.26}$$

Here, the amplitude of the $\cos 2\phi$ oscillation is written as F because it is essentially the fidelity of making the $\left(|+-\rangle + |-+\rangle\right)/\sqrt{2}$ state. Hence, by measuring this amplitude we directly get sufficient information to demonstrate violation of the in-

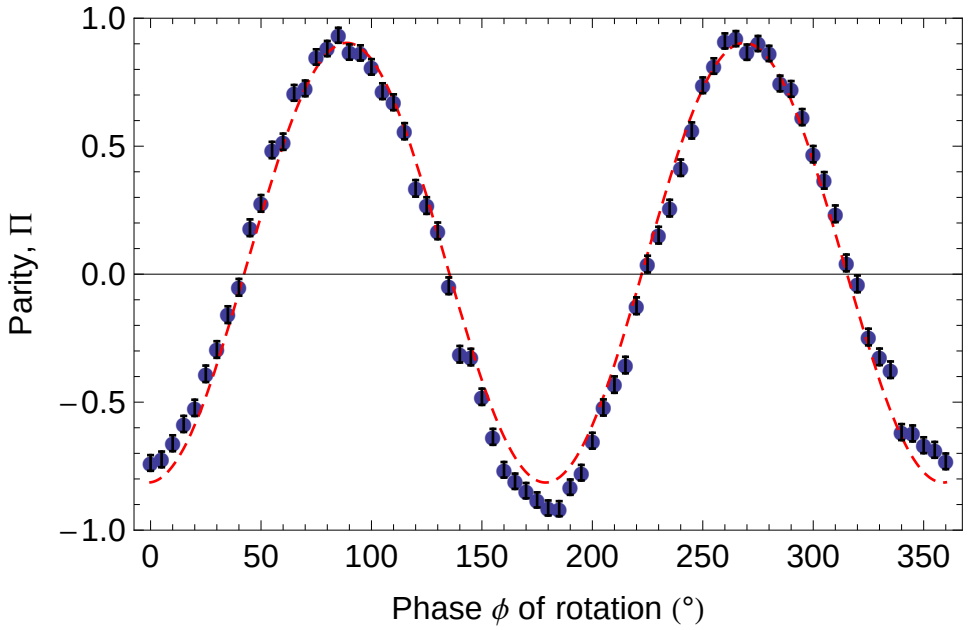

Figure 7.6: Measured parity versus phase of the final rotation in the protocol described in the text. The state being analyzed is the result of applying the XY Hamiltonian to the state $|00\rangle$ for a time $\pi/J_{1,2}$. The amplitude of the fitted curve (red dashed line) is 0.86, well above the threshold of 0.5 required to demonstrate entanglement.

equality 7.21 above, and a measurement of $F > 1/2$ certifies entanglement between the qutrits, or spin-1 systems.

Figure 7.6 displays the experimental measurements of the parity oscillation with the phase ϕ of the final rotation pulse, demonstrating entanglement at a time $t = \pi/J_{1,2}$. We can additionally measure the parity amplitude after different durations of exposure to the XY Hamiltonian: e.g., the fidelity should oscillate with time as the system Rabi flops between the states $|00\rangle$ and $(|+-\rangle + |-+\rangle)/\sqrt{2}$, as seen in Figure 7.7, and the state should again be fully in $(|+-\rangle + |-+\rangle)/\sqrt{2}$ at times $t = (2n+1)\pi/J_{1,2}$ (n integer). The fidelity of such states is plotted in Figure 7.8.

Incidentally, since the T_2 coherence time of the $|0\rangle \leftrightarrow |\pm\rangle$ transitions is measured to be 0.5 ms (limited by magnetic field noise), the coherence and entanglement

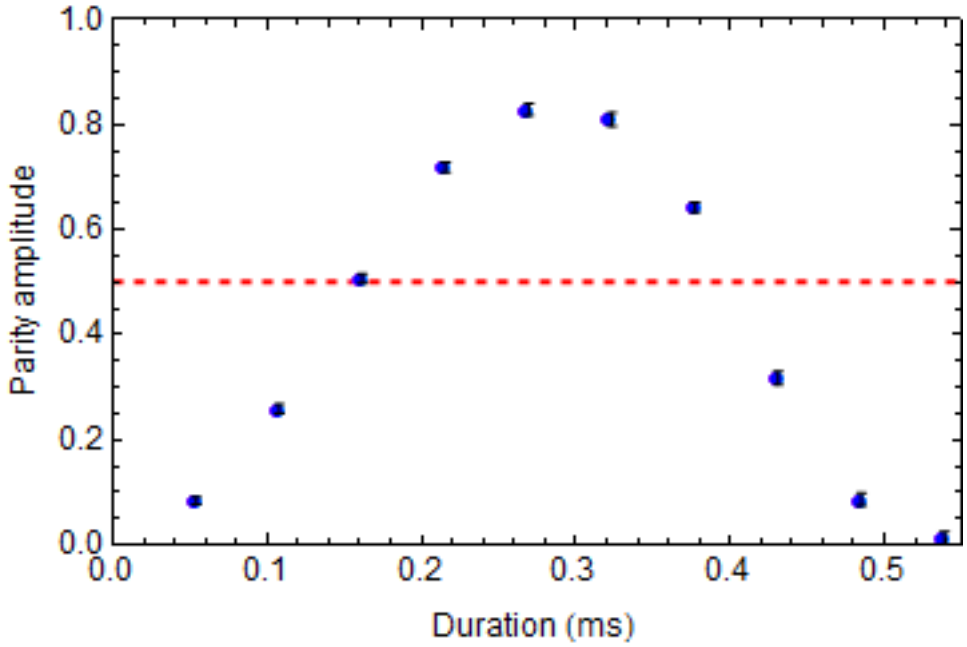

Figure 7.7: Contrast of parity curves like the one in Figure 7.6, versus duration of the XY interaction, showing that the entanglement criterion can still be met even when the state in superpositions of all three states $|+-\rangle$, $|-+\rangle$, and $|00\rangle$.

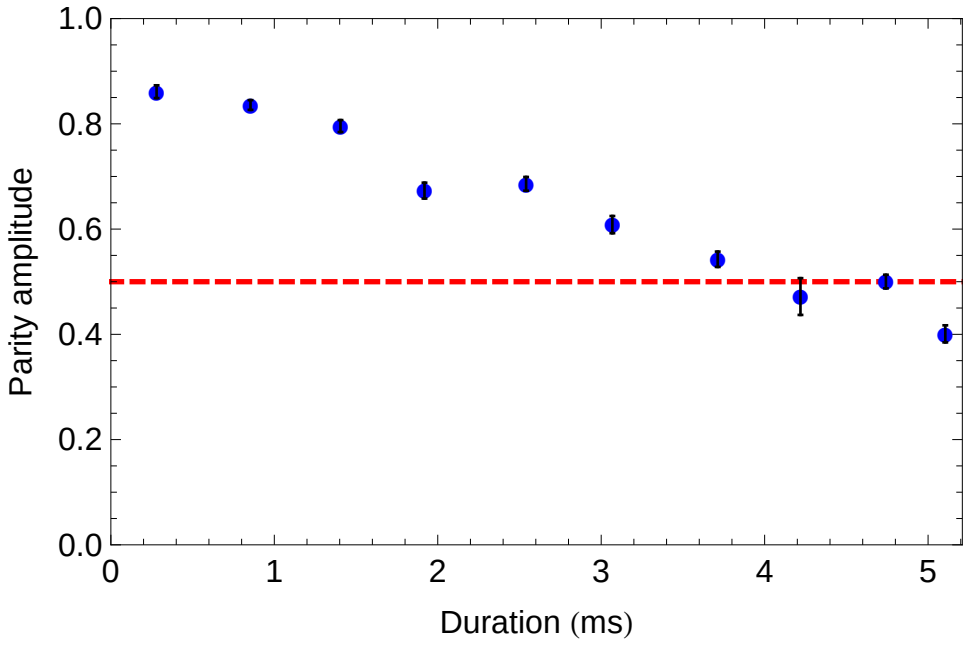

Figure 7.8: Contrast of parity curves like the one in Figure 7.6, versus duration of the XY interaction, where the durations are chosen to satisfy $t = (2n+1)\pi/J_{1,2}$ (n integer).

demonstrated in Figures 7.4 and 7.8 for two spin-1 ions show the robustness of the decoherence-free subspace against magnetic field noise.

7.2 Addition of a field term

In order to adiabatically prepare the ground state of the XY model in Eq. 7.1 we can add an effective S_z^2 field term, $D\sum_{i=1}^{N} S_z^i$, to the Hamiltonian by appropriately shifting the frequencies of the Raman beat frequencies used to generate the interactions. Namely, the beat frequencies are now set to

$$\Delta\nu_1 = \omega_+ - \mu - D, \tag{7.27}$$

$$\Delta\nu_2 = \omega_- + \mu - D, \tag{7.28}$$

where before the beatnotes were set to D=0 ($\omega_\pm \mp \mu$). This mimics the effect that a real S_z^2 term would have of shifting the $|-\rangle$ and $|+\rangle$ levels higher in energy, leaving us with the new Hamiltonian

$$H = \sum_{i,j} J_{i,j}\left(S_+^i S_-^j + S_-^i S_+^j\right) + \sum_{i,m,n}\left(2a_m^\dagger a_n + \delta_{mn}\right) S_z^i + D\sum_i (S_z^i)^2. \tag{7.29}$$

This term can be used to adiabatically prepare the ground state of the XY Hamiltonian in Eq. (7.1), with the same sorts of protocols discussed in Chapter 4.

There is a subtlety that is easy to miss (at least, we missed it at first) in implementing a dynamically changing D term. As discussed previously, the AWG

may be programmed to produce a waveform looking something like

$$V(t) = A_R \sin\left(2\pi(\omega_0 + \delta_{Zee} - \mu + D)t + \phi_R\right) + A_B \sin\left(2\pi(\omega_0 - \delta_{Zee} + \mu + D)t + \phi_B\right), \tag{7.30}$$

where ω_0 is the AOM frequency corresponding to driving a transition from $|F = 0, m_F = 0\rangle$ to $|F = 1, m_F = 0\rangle$. The mistake that we made was to plug a time-varying $D(t)$ directly into this equation, which produces weird effects because it isn't the right way to determine the instantaneous frequency. The apparently correct way to think about the changing frequency is to note that what we really have is a sine with a time-varying phase, $\sin(\Phi(t))$. Then the instantaneous frequency of the waveform is given by $d\Phi/dt$. So for example, if we want for the instantaneous frequency as a function of time to have an exponential profile (like for an adiabatic ramp),

$$2\pi f(t) = d\Phi/dt = 2\pi\left(f_0 + D_0 e^{-t\tau}\right), \tag{7.31}$$

then the time-varying argument of the sin is given by the integral of $f(t)$,

$$\Phi(t) = 2\pi\left(f_0 t - D_0 \tau e^{-t/\tau}\right). \tag{7.32}$$

Once we figured out this detail, the experiments worked well with the additional D term. For the adiabatic ground state preparation, the spins are again prepared in $|00\cdots\rangle$, which is the ground state in the presence of a large S_z^2 field, after which the field is ramped for 1 ms from a starting value of $D = 5$ kHz with an

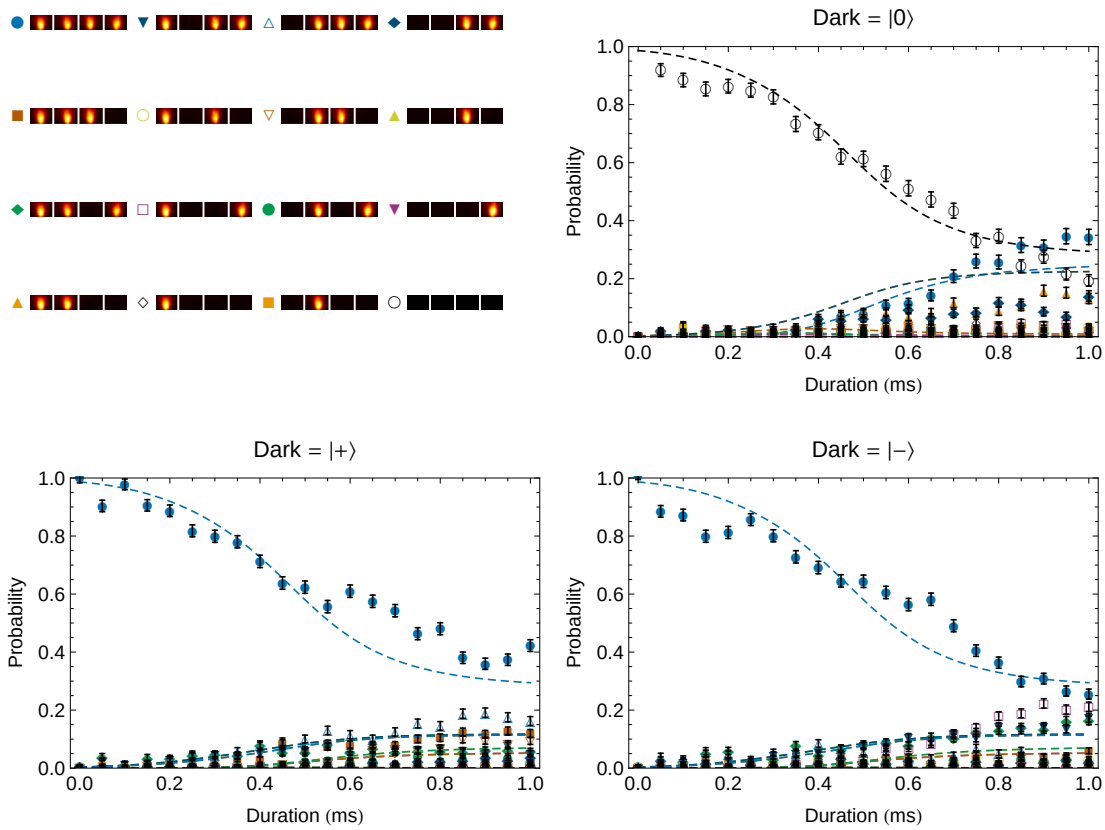

Figure 7.9: Populations at different points of the S_z^2 ramp, where the populations in state $|0\rangle$ (a), $|+\rangle$ (b), or $|-\rangle$ (c) are measured, along with theoretical predictions for the instantaneous ground state (dashed line).

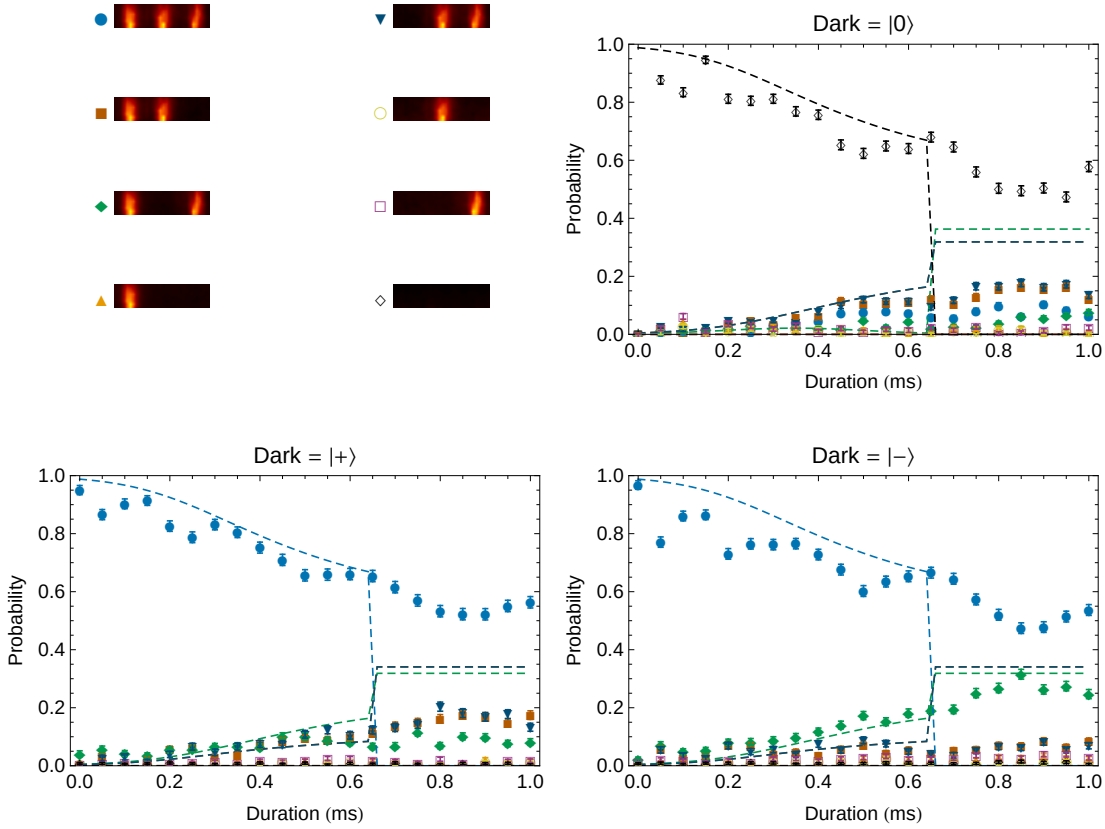

Figure 7.10: Populations at different points of the S_z^2 ramp, where the populations in state $|0\rangle$ (a), $|+\rangle$ (b), or $|-\rangle$ (c) are measured, along with theoretical predictions for the instantaneous ground state (dashed line). Note that the system crosses a first-order phase transition at roughly 0.65 ms, after which the spin populations follow the first excited state.

exponential profile with time constant 0.167 ms. Figure 7.9 shows the populations measured at varying points along the S_z^2 ramp, which match reasonably with the calculated instantaneous ground state.

Intriguingly, for odd numbers of spins (3 or 5), we find that a real (non-avoided) level crossing occurs during the S_z^2 ramp, and we hence prepare not the ground state but instead a nearby excited state, as seen in Figure 7.10. Ground states of the spin-1 XY model are known to belong to the Haldane phase in certain cases where next-nearest-neighbor interactions are present [107], and our calculations provide

evidence that power-law interactions can also support this phase.

The ground states for odd numbers bear a close qualitative resemblance to the AKLT states [108, 109], which are a canonical example of ground states in the Haldane phase. For example, one of the AKLT states can be written as [109]

$$|\psi\rangle_{AKLT} = \sqrt{\frac{1}{6}}\left(|0-+\rangle - |0+-\rangle + |-+0\rangle - |+-0\rangle + |+0-\rangle - |-0+\rangle\right), \tag{7.33}$$

while the exact ground state of the 3-spin XY Hamiltonian we implement is approximately

$$\begin{aligned} |\psi\rangle_{XY} = \quad & \sqrt{0.16}\,|0-+\rangle - \sqrt{0.16}\,|0+-\rangle + \sqrt{0.16}\,|-+0\rangle - \sqrt{0.16}\,|+-0\rangle \\ & + \sqrt{0.18}\,|+0-\rangle - \sqrt{0.18}\,|-0+\rangle\,. \end{aligned} \tag{7.34}$$

Clearly, the ground state is antisymmetric with respect to either left-right spatial inversion of the chain or a global rotation by π about S_x (which sends $|+\rangle$ to $|-\rangle$ and vice versa), and we cannot reach it with the operation performed here because the starting state $|000\rangle$ is symmetric with respect to either of these operations (and the D term does not break this symmetry). This is a manifestation of the symmetry protection afforded to the Haldane phase. Indeed, such symmetries are believed to be the most fundamental property governing the presence of these nontrivial topological phases [110, 111]. No such restriction prevents us from preparing the ground state for even numbers of spins (2 or 4), as our calculations reveal that these ground states are symmetric with respect to the operations mentioned above, and

hence can be smoothly connected to the initial state. It is as yet unclear whether the symmetric ground states for even numbers of spins also belong to the Haldane phase, or whether it even makes sense to discuss a Haldane phase in such a small system.

In the future, the toolset we have demonstrated for experimentally simulating spin-1 systems with tunable long-range interactions and effective fields could be used to explore a variety of questions that arise when considering particles of spin higher than 1/2. In particular, we have demonstrated the capability to create ground states of the spin-1 XY model, and that symmetry considerations prevent us from creating certain ground states that bear a close resemblance to AKLT states. Future work will address the question of how to deliberately break this symmetry in such a way as to allow preparation of a Haldane phase [112], which should allow us to create interesting edge states and study questions such as the dependence on interaction range of the presence of topologically nontrivial ground states.

Chapter A: Stimulated Raman transitions in a Λ system

We are solving for the dynamics in a three level system undergoing stimulated Raman transition-like behavior. We define three states $|A\rangle$, $|B\rangle$, $|e\rangle$ with energies 0, ω_{HF}, and ω_E, respectively. The states $|A\rangle$ and $|B\rangle$ are not directly coupled, but each is off-resonantly coupled to the excited state by a monochromatic laser beam. This situation is briefly sketched in Figure A.1. In this situation, the Hamiltonian for the atom is given by

$$H_0 = \omega_e \left|e\right\rangle\!\left\langle e\right| + \omega_{HF} \left|B\right\rangle\!\left\langle B\right| \tag{A.1}$$

The interaction caused by the light fields will be written as

$$H_{int} = g_A e^{i(k_A \cdot x - \omega_A t + \phi_A)} \left|e\right\rangle\!\left\langle A\right| + g_B e^{i(k_B \cdot x - \omega_B t + \phi_B)} \left|e\right\rangle\!\left\langle B\right| + h.c. \tag{A.2}$$

We have chosen the laser frequencies such that $\omega_A - \omega_B = \omega_{HF}$, and $\omega_A - E_e \equiv \Delta$ (such that $\Delta < 0$ for a red detuned beam). Now we define the state vector as

$$|\psi\rangle = c_A(t) \left|A\right\rangle + c_B(t) \left|B\right\rangle + c_e(t) \left|e\right\rangle . \tag{A.3}$$

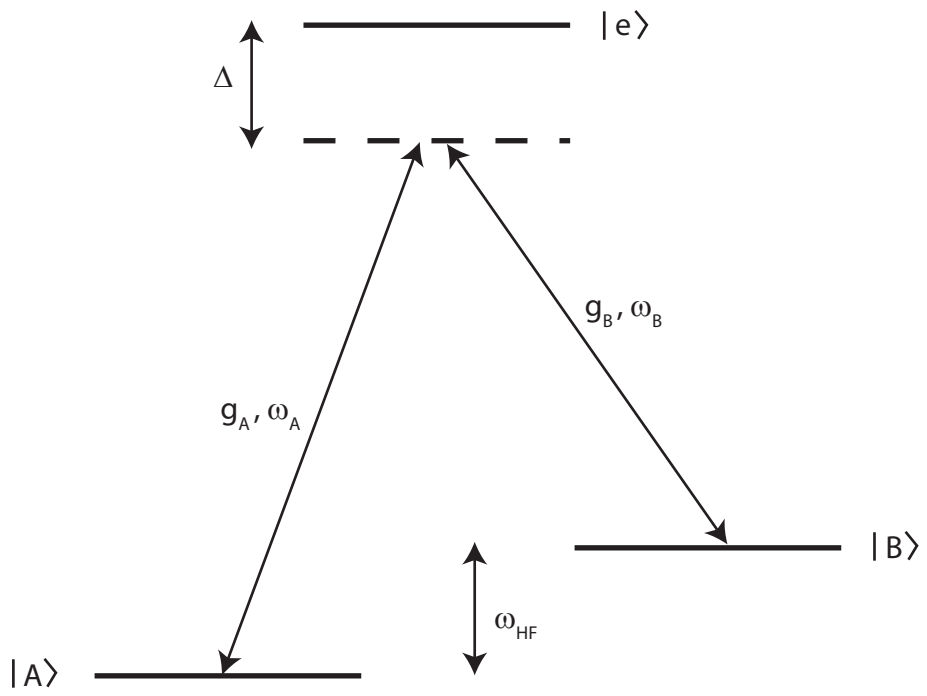

Figure A.1: Example three level system, for the case where the two laser beams have a beat frequency at exactly ω_{HF}, detuned by a large amount from the excited state $|e\rangle$.

Applying the Schrodinger equation to this state ket and equating coefficients of the (orthogonal) eigenstates $|A\rangle, |B\rangle, |e\rangle$, we wind up with three differential equations:

$$i\dot{c_A} = g_A^* e^{-i(k_A \cdot x - \omega_A t + \phi_A)} c_e \tag{A.4}$$

$$i\dot{c_B} = g_B^* e^{-i(k_B \cdot x - \omega_B t + \phi_B)} c_e + \omega_{HF} c_B \tag{A.5}$$

$$i\dot{c_e} = g_A e^{i(k_A \cdot x - \omega_A t + \phi_A)} c_A + g_B e^{i(k_B \cdot x - \omega_B t + \phi_B)} c_B + \omega_e c_e \tag{A.6}$$

We will now go to a different frame by making the following definitions:

$$a_A = c_A \tag{A.7}$$

$$a_B = e^{i\omega_{HF} t} c_B \tag{A.8}$$

$$a_e = e^{i\omega_A t} c_e \tag{A.9}$$

It is straightforward to find the new Schrodinger equations, as follows:

$$i\dot{a_A} = i\dot{c_A} \tag{A.10}$$

$$i\dot{a_A} = g_A^* e^{-i(k_A \cdot x - \omega_A t + \phi_A)} c_e \tag{A.11}$$

$$i\dot{a_A} = i\dot{a_A} = g_A^* e^{-i(k_A \cdot x - \omega_A t + \phi_A)} a_e e^{-i\omega_A t} \tag{A.12}$$

$$i\dot{a_A} = g_A^* e^{-i(k_A \cdot x + \phi_A)} a_e \tag{A.13}$$

For the second equation, we get

$$i\dot{a_B} = ie^{i\omega_{HF}t}\left(i\omega_{HF}c_B + \dot{c_B}\right) \tag{A.14}$$

$$i\dot{a_B} = e^{i\omega_{HF}t}\left(-\omega_{HF}c_B + g_B^* e^{-i(k_B\cdot x - \omega_B t + \phi_B)}c_e + \omega_{HF}c_B\right) \tag{A.15}$$

$$i\dot{a_B} = e^{i\omega_{HF}t} g_B^* e^{-i(k_B\cdot x - \omega_B t + \phi_B)}c_e \tag{A.16}$$

$$i\dot{a_B} = e^{i\omega_{HF}t} g_B^* e^{-i(k_B\cdot x - \omega_B t + \phi_B)}a_e e^{-i\omega_A t} \tag{A.17}$$

$$i\dot{a_B} = g_B^* e^{-i(k_B\cdot x + \phi_B)}a_e \tag{A.18}$$

And finally, we get

$$i\dot{a_e} = ie^{i\omega_A t}\left(i\omega_A c_e + \dot{c_e}\right) \tag{A.19}$$

$$i\dot{a_e} = e^{i\omega_A t}\left(-\omega_A c_e + g_A e^{i(k_A\cdot x - \omega_A t + \phi_A)}c_A + g_B e^{i(k_B\cdot x - \omega_B t + \phi_B)}c_B + \omega_e c_e\right) \tag{A.20}$$

$$i\dot{a_e} = e^{i\omega_A t}\left(g_A e^{i(k_A\cdot x - \omega_A t + \phi_A)}c_A + g_B e^{i(k_B\cdot x - \omega_B t + \phi_B)}c_B - \Delta c_e\right) \tag{A.21}$$

$$i\dot{a_e} = \left(g_A e^{i(k_A\cdot x + \phi_A)}a_A + g_B e^{i(k_B\cdot x + \phi_B)}a_B - \Delta a_e\right) \tag{A.22}$$

The resulting equations are:

$$i\dot{a_A} = g_A^* e^{-i(k_A\cdot x + \phi_A)}a_e \tag{A.23}$$

$$i\dot{a_B} = g_B^* e^{-i(k_B\cdot x + \phi_B)}a_e \tag{A.24}$$

$$i\dot{a_e} = \left(g_A e^{i(k_A \cdot x + \phi_A)} a_A + g_B e^{i(k_B \cdot x + \phi_B)} a_B - \Delta a_e\right) \tag{A.25}$$

and we have cleverly gotten rid of all the explicit time dependences to get here. Now we must do an approximation known as adiabatic elimination, wherein we assume $\dot{a_e} \ll \Delta a_e$ and make the approximation $\dot{a_e} \approx 0$. In particular, one also typically assumes that there is no population in the excited state to begin with, and a negligible amount of the population is ever driven there. This gives us an expression for a_e:

$$a_e = \frac{g_A e^{i(k_A \cdot x + \phi_0)} a_A + g_B e^{i(k_B \cdot x + \phi_B)} a_B}{\Delta} \tag{A.26}$$

This allows us to write the dynamics of a_A and a_B in a form that looks like a closed two-level system:

$$i\dot{a_A} = \frac{g_B g_A^*}{\Delta} e^{i[(k_B - k_A)x + (\phi_B - \phi_A)]} a_B + \frac{|g_A|^2}{\Delta} a_A \tag{A.27}$$

$$i\dot{a_B} = \frac{g_A g_B^*}{\Delta} e^{i[(k_A - k_B)x + (\phi_A - \phi_B)]} a_A + \frac{|g_B|^2}{\Delta} a_B \tag{A.28}$$

In particular, this is the set of equations one would get for an effective Hamiltonian looking like

$$\begin{aligned} H_{eff} = & \quad \tfrac{|g_A|^2}{\Delta} |A\rangle\langle A| + \tfrac{|g_B|^2}{\Delta} |B\rangle\langle B| \\ & + \left(\tfrac{g_A g_B^*}{\Delta} e^{i[(k_A - k_B)x + (\phi_A - \phi_B)]} |B\rangle\langle A| + \tfrac{g_B g_A^*}{\Delta} e^{i[(k_B - k_A)x + (\phi_B - \phi_A)]} |A\rangle\langle B|\right). \end{aligned} \tag{A.29}$$

Chapter B: Derivation of spin-dependent force from red and blue sidebands

In this appendix, we show the derivation of the Mølmer-Sørensen Hamiltonian from the application of symmetrically detuned red and blue sidebands to a single ion interacting with a single mode of motion, after which we use the this Hamiltonian (generalized to treat multiple ions and modes of motion) to derive the effective spin-1/2 Ising Hamiltonian we use in most of our experiments.

B.1 Single-atom spin-dependent force from two sidebands

We start from the atom-laser interaction Hamiltonian

$$H = \frac{\Omega}{2}\sigma^{+}e^{i(\Delta k\cdot r-\delta t+\phi)} + \frac{\Omega}{2}\sigma^{-}e^{-i(\Delta k\cdot r-\delta t+\phi)}. \tag{B.1}$$

Here Δk is the difference between the wavevectors of a pair of lasers at difference frequency ω, $\delta = \omega - \omega_0$ is the detuning from the hyperfine transition frequency ω_0, we have set Planck's constant $h = 1$, and we have gone into the interaction picture

with respect to the bare atomic and harmonic oscillator Hamiltonians,

$$H_{atom} = \frac{\omega_0}{2}\sigma^z, \tag{B.2}$$

$$H_{H.O.} = \omega_t a^\dagger a, \tag{B.3}$$

and made a rotating wave approximation. We can also write

$$\Delta k \cdot r = \eta \left(a e^{-i\omega_t t} + a^\dagger e^{i\omega_t t} \right), \tag{B.4}$$

where $\eta = \Delta k x_0$ is the Lamb-Dicke parameter and $x_0 = \sqrt{\frac{\hbar}{2M\omega_t}}$ is the ground-state wavefunction spread of the ion. In the case of multiple ions, we can instead write this as

$$\Delta k \cdot r = \eta_{i,m} \left(a_m e^{-i\omega_m t} + a_m^\dagger e^{i\omega_m t} \right), \tag{B.5}$$

where a_m is the creation operator for the mth normal mode with frequency ω_m, and $\eta_{i,m} = \sqrt{\hbar/(2M\omega_m)} b_{i,m}$ is dependent on the mode frequency m and the element of the matrix $\mathbf{b}$ gives the component of normal mode m at ion i. The remainder of the appendix will stick with the single-ion, single-mode case, but in Chapter 2 we will need to use this to generalize the result to multiple ions.

From this interaction Hamiltonian, we will further make the approximation that we are in the Lamb-Dicke limit, $\eta(2\bar{n}+1) \ll 1$, where the motional wavepacket is confined to a size much smaller than the inverse of the difference wavevector,

which lets us write

$$e^{i\Delta k\cdot r} \approx 1 + i\eta\left(ae^{-i\omega_t t} + a^\dagger e^{i\omega_t t}\right). \tag{B.6}$$

To generate the spin-dependent force we want, we apply a red sideband and blue sideband Hamiltonian simultaneously:

$$\begin{aligned} H_{rsb} &= \frac{\Omega}{2}\sigma^+\left(1 + i\eta\left[ae^{-i\omega_t t} + a^\dagger e^{i\omega_t t}\right]\right)e^{-i\delta_r t + i\phi_r} \\ &\quad + \frac{\Omega}{2}\sigma^-\left(1 - i\eta\left[ae^{-i\omega_t t} + a^\dagger e^{i\omega_t t}\right]\right)e^{i\delta_r t - i\phi_r}, \end{aligned} \tag{B.7}$$

$$\begin{aligned} H_{bsb} &= \frac{\Omega}{2}\sigma^+\left(1 + i\eta\left[ae^{-i\omega_t t} + a^\dagger e^{i\omega_t t}\right]\right)e^{-i\delta_b t + i\phi_b} \\ &\quad + \frac{\Omega}{2}\sigma^-\left(1 - i\eta\left[ae^{-i\omega_t t} + a^\dagger e^{i\omega_t t}\right]\right)e^{i\delta_b t - i\phi_b}. \end{aligned} \tag{B.8}$$

The Mølmer-Sørensen Hamiltonian is then the sum of the red and the blue sidebands, with Ω taken to be equal for each sideband, and the detunings taken to be equal and opposite, $\mu \equiv \delta_b = -\delta_r$:

$$\begin{aligned} H_{MS} &= \frac{\Omega}{2}\sigma^+\left(1 + i\eta\left[ae^{-i\omega_t t} + a^\dagger e^{i\omega_t t}\right]\right)\left(e^{i\mu t + i\phi_r} + e^{-i\mu t + i\phi_b}\right) \\ &\quad + \frac{\Omega}{2}\sigma^-\left(1 - i\eta\left[ae^{-i\omega_t t} + a^\dagger e^{i\omega_t t}\right]\right)\left(e^{-i\mu t - i\phi_r} + e^{i\mu t - i\phi_b}\right). \end{aligned} \tag{B.9}$$

What we want is for a σ^ϕ operator, where $\sigma^\phi = e^{i\phi}\sigma^+ + e^{-i\phi}\sigma^-$, to factor out from the phonon terms. To achieve this, let's start by rewriting H_{MS} into three

separate terms: a term without phonon operators,

$$H_{MS,NP} = \frac{\Omega}{2}\left(\sigma^+\left[e^{i\mu t+i\phi_r} + e^{-i\mu t+i\phi_b}\right] + \sigma^-\left[e^{-i\mu t-i\phi_r} + e^{i\mu t-i\phi_b}\right]\right); \tag{B.10}$$

a term with factors of $e^{i(\mu-\omega_t)t}$, which is the one we will keep if we want to do another rotating wave approximation,

$$\begin{aligned} H_{MS,RWA} = \; & i\eta\tfrac{\Omega}{2}\left(\sigma^+\left[ae^{i(\mu-\omega_t)t+i\phi_r} + a^\dagger e^{-i(\mu-\omega_t)t+i\phi_b}\right]\right. \\ & \left.-\sigma^-\left[ae^{i(\mu-\omega_t)t-i\phi_b} + a^\dagger e^{-i(\mu-\omega_t)t-i\phi_r}\right]\right), \end{aligned} \tag{B.11}$$

and a counter-rotating term with factors of $e^{i(\mu+\omega_t)t}$,

$$\begin{aligned} H_{MS,CR} = \; & i\eta\tfrac{\Omega}{2}\left(\sigma^+\left[ae^{-i(\mu+\omega_t)t+i\phi_b} + a^\dagger e^{i(\mu+\omega_t)t+i\phi_r}\right]\right. \\ & \left.-\sigma^-\left[ae^{-i(\mu+\omega_t)t-i\phi_r} + a^\dagger e^{i(\mu+\omega_t)t-i\phi_b}\right]\right). \end{aligned} \tag{B.12}$$

So what we want now is to rewrite the terms with phonons, e.g.

$$H_{MS,RWA} \equiv \frac{\eta\Omega}{2}\sigma_s^\phi\left(ae^{i(\mu-\omega_t)t+i\phi_m} + a^\dagger e^{-i(\mu-\omega_t)t-i\phi_m}\right). \tag{B.13}$$

If true, this means

$$\begin{aligned} H_{MS,RWA} = \; & \tfrac{\eta\Omega}{2}\left(e^{i\phi_s}\sigma^+ + e^{-i\phi_s}\sigma^-\right)\left(ae^{i(\mu-\omega_t)t+i\phi_m} + a^\dagger e^{-i(\mu-\omega_t)t-i\phi_m}\right) \\ = \; & \tfrac{\eta\Omega}{2}\left(\sigma^+ae^{i(\mu-\omega_t)t}e^{i(\phi_s+\phi_m)} + \sigma^+a^\dagger e^{-i(\mu-\omega_t)t}e^{i(\phi_s-\phi_m)}\right. \\ & \left.+\sigma^-ae^{i(\mu-\omega_t)t}e^{-i(\phi_s-\phi_m)} + \sigma^+a^\dagger e^{-i(\mu-\omega_t)t}e^{-i(\phi_s+\phi_m)}\right) \end{aligned} \tag{B.14}$$

but from before we had

$$\begin{aligned} H_{MS,RWA} = \quad & \eta\tfrac{\Omega}{2}\left(\sigma^{+}\left[ae^{i(\mu-\omega_t)t+i\phi_r+i\pi/2}+a^{\dagger}e^{-i(\mu-\omega_t)t+i\phi_b+i\pi/2}\right]\right. \\ & \left.+\sigma^{-}\left[ae^{i(\mu-\omega_t)t-i\phi_b-i\pi/2}+a^{\dagger}e^{-i(\mu-\omega_t)t-i\phi_r-i\pi/2}\right]\right). \end{aligned} \tag{B.15}$$

So clearly this holds iff the phase relationships $\phi_s+\phi_m = \phi_r+\pi/2$ and $\phi_s-\phi_m = \phi_b+\pi/2$ hold, or

$$\phi_s = \frac{\phi_r+\phi_b+\pi}{2}, \tag{B.16}$$

$$\phi_m = \frac{\phi_r-\phi_b}{2}. \tag{B.17}$$

With these definitions, we can rewrite the Hamiltonian as

$$\begin{aligned} H_{MS} = \quad & \tfrac{\Omega}{2}\left(\sigma^{+}\left[e^{i\mu t+i\phi_r}+e^{-i\mu t+i\phi_b}\right]+\sigma^{-}\left[e^{-i\mu t-i\phi_r}+e^{i\mu t-i\phi_b}\right]\right) \\ & +\tfrac{\eta\Omega}{2}\sigma_s^{\phi}\left(ae^{i(\mu-\omega_t)t+i\phi_m}+a^{\dagger}e^{-i(\mu-\omega_t)t-i\phi_m}\right) \\ & +\tfrac{\eta\Omega}{2}\sigma_s^{\phi}\left(ae^{-i(\mu+\omega_t)t-i\phi_m}+a^{\dagger}e^{i(\mu+\omega_t)t+i\phi_m}\right). \end{aligned} \tag{B.18}$$

Further, the off-resonant carrier term (i.e., the term with no phonon operators)

can be rewritten in terms of the spin phase ϕ_s and the motional phase ϕ_m:

$$\begin{aligned} H_{MS,NP} = \quad & \tfrac{\Omega}{2}\sigma^{+}\left[e^{i\mu t+i(\phi_s+\phi_m-\pi/2)}+e^{-i\mu t+i(\phi_s-\phi_m-\pi/2)}\right] \\ & +\tfrac{\Omega}{2}\sigma^{-}\left[e^{-i\mu t-i(\phi_s+\phi_m-\pi/2)}+e^{i\mu t-(\phi_s-\phi_m-\pi/2)}\right] \\ = \quad & \tfrac{\Omega}{2}\sigma^{+}e^{i(\phi_s-\pi/2)}\left[e^{i(\mu t+\phi_m)}+e^{-i(\mu t+\phi_m)}\right] \\ & +\tfrac{\Omega}{2}\sigma^{-}e^{-i(\phi_s-\pi/2)}\left[e^{-i(\mu t+\phi_m)}+e^{i(\mu t+\phi_m)}\right] \\ H_{MS,NP} = \quad & \Omega\cos(\mu t+\phi_m)\sigma^{\phi_s-\pi/2}. \end{aligned} \tag{B.19}$$

So we wind up with

$$\begin{aligned} H_{MS} = \quad & \Omega\cos(\mu t+\phi_m)\sigma^{\phi_s-\pi/2} \\ & +\tfrac{\eta\Omega}{2}\sigma^{\phi_s}\left(ae^{i(\mu-\omega_t)t+i\phi_m}+a^{\dagger}e^{-i(\mu-\omega_t)t-i\phi_m}\right) \\ & +\tfrac{\eta\Omega}{2}\sigma^{\phi_s}\left(ae^{-i(\mu+\omega_t)t-i\phi_m}+a^{\dagger}e^{i(\mu+\omega_t)t+i\phi_m}\right). \end{aligned} \tag{B.20}$$

Finally, the phonon terms can be rewritten as

$$\begin{aligned} H_{MS} = \quad & \Omega\cos(\mu t+\phi_m)\sigma^{\phi_s-\pi/2} \\ & +\eta\Omega\sigma^{\phi_s}\cos\left(\mu t+\phi_m\right)\left(ae^{-i\omega_t t}+a^{\dagger}e^{i\omega_t t}\right), \end{aligned} \tag{B.21}$$

or

$$H_{MS} = \Omega \cos(\mu t + \phi_m) \left[\sigma^{\phi_s - \pi/2} + \eta \sigma^{\phi_s} \left(a e^{-i\omega_t t} + a^\dagger e^{i\omega_t t}\right)\right]. \tag{B.22}$$

B.2 Ising Hamiltonian from spin-dependent force

The above Mølmer-Sørensen Hamiltonian is written for a single ion interacting with a single mode of motion, but in general we have multiple ions interacting with multiple modes. The generalization to multiple ions is simply

$$H_{MS} = -\sum_{i,m} \eta_{i,m} \Omega_i \sin(\mu t) \sigma_i^x \left(a_m e^{-i\omega_m t} + a_m^\dagger e^{i\omega_m t}\right), \tag{B.23}$$

as discussed in Appendix B.

To show that the evolution under this Hamiltonian is roughly equivalent to that of a pure spin-spin interaction under certain conditions, we use the Magnus expansion for the evolution operator,

$$U(t) = T\left[e^{-i\int_0^t dt_1 H(t_1)}\right] = e^{\bar{\Omega}_1 + \bar{\Omega}_2 + \bar{\Omega}_3 + \cdots}, \tag{B.24}$$

where T is the time-ordering operator and the first few orders of the expansion are given by

$$\bar{\Omega}_1 = -i \int_0^t dt_1 H(t_1), \tag{B.25}$$

$$\bar{\Omega}_2 = -\frac{1}{2}\int_0^t dt_1 \int_0^{t_1} dt_2 \left[H(t_1), H(t_2)\right], \tag{B.26}$$

$$\bar{\Omega}_3 = \frac{i}{6}\int_0^t dt_1 \int_0^{t_1} dt_2 \int_0^{t_2} dt_3 \left([H(t_1), [H(t_2), H(t_3)]] + [H(t_3), [H(t_2), H(t_1)]]\right). \tag{B.27}$$

Plugging in the Hamiltonian above, we can see that $\bar{\Omega}_1$ will involve integrals like

$$\int_0^t dt_1 \sin\mu t_1 e^{ift_1} = \frac{e^{ift}\left(\mu\cos\mu t - if\sin\mu t\right) - \mu}{f^2 - \mu^2}, \tag{B.28}$$

which lets us obtain

$$\bar{\Omega}_1 = \sigma_i^x \left(\alpha_{i,m}(t) a_m^\dagger - \alpha_{i,m}^*(t) a_m\right), \tag{B.29}$$

$$\alpha_{i,m}(t) = \frac{i\eta_{i,m}\Omega_i}{\mu^2 - \omega_m^2}\left(\mu - e^{i\omega_m t}\left[\mu\cos\mu t - i\omega_m \sin\mu t\right]\right). \tag{B.30}$$

For the second term we need to compute the commutator

$$\begin{aligned}[H(t_1), H(t_2)] = \; & [\textstyle\sum_{i,m} \eta_{i,m}\Omega_i \sin(\mu t)\sigma_i^x \left(a_m e^{-i\omega_m t} + a_m^\dagger e^{i\omega_m t}\right), \\ & \textstyle\sum_{j,n} \eta_{j,n}\Omega_j \sin(\mu t)\sigma_j^x \left(a_n e^{-i\omega_n t} + a_n^\dagger e^{i\omega_n t}\right)].\end{aligned} \tag{B.31}$$

We can see that the only noncommuting operators in this expression are the phonon operators, which obey

$$\left[a_n, a_m^\dagger\right] = \delta_{mn}, \tag{B.32}$$

where δ_{mn} is the Kronecker delta. From this we can see that

$$\left[\sigma_i^x a_m e^{-i\omega_m t_1}, \sigma_j^x a_n^\dagger e^{i\omega_n t_2}\right] = \sigma_i^x \sigma_j^x e^{i\omega_m(t_2-t_1)}\delta_{mn}, \tag{B.33}$$

$$\left[\sigma_i^x a_m^\dagger e^{-i\omega_m t_1}, \sigma_j^x a_n e^{i\omega_n t_2}\right] = -\sigma_i^x \sigma_j^x e^{-i\omega_m(t_2-t_1)}\delta_{mn}, \tag{B.34}$$

and from this finally get the commutator,

$$[H(t_1), H(t_2)] = \sum_{i,j,m} \eta_{i,m}\eta_{j,m}\Omega_i\Omega_j\sigma_i^x\sigma_j^x \sin\mu t_1 \sin\mu t_2 \left(e^{-i\omega_m(t_1-t_2)} - e^{i\omega_m(t_1-t_2)}\right). \tag{B.35}$$

To obtain the term $\bar{\Omega}_2$, we perform some nasty integration and finally wind up with

$$\bar{\Omega}_2 = \sum_{i,j,m} \frac{i\eta_{i,m}\eta_{j,m}\Omega_i\Omega_j}{2(\mu^2-\omega_m^2)}\sigma_i^x\sigma_j^x \left(\frac{\omega_m \sin 2\mu t}{2\mu} + \frac{\mu\sin(\mu-\omega_m)t}{\mu-\omega_m} - \frac{\mu\sin(\mu+\omega_m)t}{\mu+\omega_m} - \omega_m t\right). \tag{B.36}$$

Note that with this Hamiltonian, there are no further orders to the Magnus expansion, because the commutator of $\sigma_i^x a_m$ with $\sigma_j^x\sigma_k^x$ is always zero, and so the following form for the evolution operator is exact:

$$U = \exp\left(\sum_{i,j,m} \sigma_i^x \left(\alpha_{i,m}(t)a_m^\dagger - \alpha_{i,m}^*(t)a_m\right) + \chi_{ij}(t)\sigma_i^x\sigma_j^x\right), \tag{B.37}$$

$$\alpha_{i,m}(t) = \frac{i\eta_{i,m}\Omega_i}{\mu^2-\omega_m^2}\left(\mu - e^{i\omega_m t}\left[\mu\cos\mu t - i\omega_m \sin\mu t\right]\right), \tag{B.38}$$

$$\chi_{ij}(t) = \sum_m \frac{i\eta_{i,m}\eta_{j,m}\Omega_i\Omega_j}{2(\mu^2-\omega_m^2)}\left(\frac{\omega_m \sin 2\mu t}{2\mu} + \frac{\mu\sin(\mu-\omega_m)t}{\mu-\omega_m} - \frac{\mu\sin(\mu+\omega_m)t}{\mu+\omega_m} - \omega_m t\right). \tag{B.39}$$

Here we have a number of terms that we would like not to have to deal with, in particular the terms coupling spin to motion ($\sigma_i^x a_m$, etc). We therefore operate in a regime where we can 'adiabatically eliminate' the phonons, imposing the condition that the laser beatnotes be far detuned from the motional modes:

$$\mu - \omega_m \gg \eta_{i,m}\Omega_i. \tag{B.40}$$

In this case the displacement is only virtual, $\alpha_{i,m} \ll 1$. When this condition holds, the term in the evolution operator corresponding to spin-phonon coupling, Ω_1, can be neglected entirely. Furthermore, we take the long time limit, noting that for large t,

$$\chi_{ij}(t) \approx -\sum_m \frac{i\eta_{i,m}\eta_{j,m}\Omega_i\Omega_j}{2(\mu^2-\omega_m^2)}\omega_m t. \tag{B.41}$$

By making these approximations, we have reduced the evolution operator to

$$U \approx \exp\left(-\sum_{i,j,m}\sigma_i^x\sigma_j^x\frac{i\eta_{i,m}\eta_{j,m}\Omega_i\Omega_j}{2(\mu^2-\omega_m^2)}\omega_m t\right), \tag{B.42}$$

which is exactly the evolution operator of a set of static spin-spin interactions,

$$H_{eff} = \sum_{i,j} J_{i,j}\sigma_i^x\sigma_j^x, \tag{B.43}$$

whose interaction strengths are given by

$$J_{i,j} = \sum_m \frac{b_{i,m} b_{j,m} \Omega_i \Omega_j \Omega_R}{2(\mu^2 - \omega_m^2)}, \tag{B.44}$$

where we have used $\eta_{i,m} = \Delta k \sqrt{\hbar/(2M\omega_m)} b_{i,m}$ to rewrite the effective couplings in terms of the recoil frequency $\Omega_R = \frac{\hbar(\Delta k)^2}{2M}$ and the normal mode matrix b.

Chapter C: The big bad MBR

The MBR has been well documented both by its supplier, Coherent, and in Rajibul Islam's thesis. Here, I describe some of the same information present in these sources so as to provide context for the additional information I want to document - a partial analysis of the locking circuitry, for example. Some of the parameters I document here are different from those recommended in the manual, and may only be relevant to the MBR that is currently on our table.

C.1 Optics

Figure C.1 sketches the main components of the laser. The MBR is pumped by a 532 nm source (for the majority of my time on the experiment, a Verdi V-18 from Coherent was run at 18.5 W to pump the MBR; that laser died, and at the time I am writing we are limping along with an old V-10 running at 7.5 W that we expect to soon replace with a new Sprout-G-18W). The pump beam is passed through a telescope (consisting of a $\sim 1\ddot{}$ diameter, f=88 mm positive lens and a $\sim 1/2\ddot{}$ diameter, f=-200 mm negative lens) before being coupled into a bowtie-configuration ring cavity via mirror M1. The curvature of M1 serves to further focus the 532 nm light into the Ti:sapph crystal.

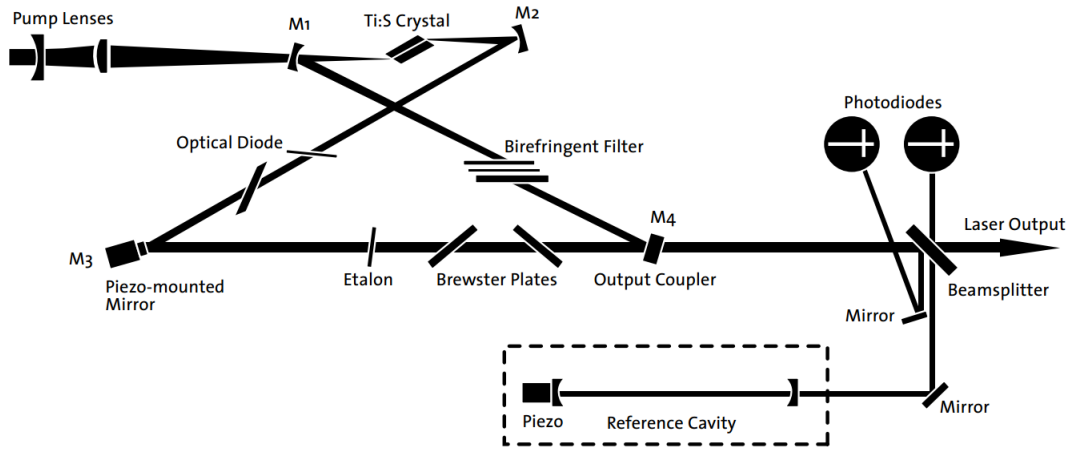

Figure C.1: Sketch of the optics in the MBR laser, borrowed from the manual by the Coherent Lasers company.

Because the pump beam is focused so tightly inside the Ti:sapph, the alignment of the telescope is quite important. For a couple of years, the centers of the lenses did not form a straight line with the center of M1, and the Verdi beam appeared to clip on the negative lens mount. Upon installing the old V-10, we had insufficient 739 nm power to begin with, but realigning the telescope such that the pump beam can come straight through the centers of the lenses and M1 increased the 739 nm power by roughly 50%.

The Ti:sapph crystal is Brewster cut, allowing the cavity to support horizontally polarized light, so the cavity is sensitive to the angle of this element. We once replaced the Ti:sapph and found that the angle that minimizes reflection of the 532 nm pump light is not the optimum for 739 nm, and in fact was far enough off that we had difficulty achieving lasing at all. This angle thus has to be tuned to optimize

the output power rather than reflection of the 532 nm light.

Mirrors M1 and M2 have a nominal radius of curvature of 10 cm, allowing the cavity mode to be tightly focused within the gain medium. We have seen that once it was necessary to back out both M1 and M2 away from the Ti:sapph by a full turn on each mirror knob to achieve lasing. This was speculated to have something to do with the cavity stability, but could also have had something to do with the mode waist inside the gain medium.

The cavity beam passes through an optical diode to prevent bidirectional lasing. This element consists of a waveplate that rotates the polarization a small amount and a Faraday rotator that reverses this rotation only for light propagating in the 'correct' direction; due to the various Brewster-cut elements in the cavity, light propagating in the wrong direction (whose polarization gets rotated further at every round trip) sees very high losses. We have seen that the output power is maximized when the Faraday rotator is rotated almost as far clockwise (as looking down on the cavity) as possible within the throw of the screws. We have tried to set the Faraday mount to the angle we believe it was designed for and optimize the cavity from there, but it was not even possible to get the cavity lasing at this angle, and less drastic changes to the angle still decrease the output power.

The mount for M3, also called the 'tweeter' mirror, has a piezoelectric drive, such that fine adjustments of the cavity length can be made electronically. Feedback from the 'servo' lock described below is used to stabilize against small fluctuations in cavity length on fast timescales, as well as to noise eat the $\sim$ 80 kHz modulation that is imprinted on the light by the etalon (next paragraph). The mount for the

tweeter mirror sets it at a slight angle, so it is possible for rotation of this mount to make a difference in the cavity alignment.

The etalon is a thin piece of glass which acts to suppress unwanted longitudinal cavity modes (frequencies). It is mounted against two piezos that are driven 90° out of phase in such a way as to set up a standing wave in the etalon. This is in turn mounted to a galvanometer (aka galvo), which can rotate the etalon; this can be used to lock the etalon position to a single cavity mode.

Next, two more glass plates are mounted on galvanometers at the Brewster angle (hence their name 'Brewster plates'). By using the galvos to rotate both Brewster plates in tandem, the cavity length can be changed with a larger range of motion than the tweeter mirror can provide, without significantly displacing the transverse cavity mode in doing so. The final mirror, M4, is also the output coupler. Finally, the birefringent filter is used as a coarse frequency selection element.

C.2 Electronics

We find that, day to day, the lock circuits tend to be the most finicky part of the MBR system to deal with. When the locks are unusually troublesome, I often wind up going back nearly to the beginning of the procedure for getting the locks online after a major cavity realignment, so I will describe this procedure here. (Also, it is usually straightforward to achieve a good output power when the etalon is removed from the cavity, so when we are struggling for power we often need to redo this procedure anyway.)

The etalon lock is the first to be optimized, as it is generally counterproductive to mess with the servo lock if the etalon lock isn't working. The etalon lock stabilizes the angle of the etalon to the point of highest transmission of a single frequency mode from the cavity. The error signal derives from the reflection off the etalon, which is directed onto a photodiode. The etalon mount contains two piezoelectric actuators which are driven 90° out of phase with each other at ∼80 kHz, which sets up a standing wave in the etalon itself. If the light travels through an appropriate part of this standing wave, this will modulate the angle that the light 'sees' and hence the reflection.

The photodiode signal thus carries an 80 kHz modulation, which is demodulated with the driving signal to result in a phase-sensitive DC signal. As the etalon is slowly rotated, this signal will linearly increase (or decrease), until the angle is changed sufficiently to select a different cavity mode, resulting in our friend the sawtooth error signal.

Usually the main trick to getting the etalon lock working properly is to tweak its alignment. When affixing the etalon mount to its galvo, the angle is set so that with the etalon knob on the control box rotated fully counterclockwise (or rather, epsilon away from fully counterclockwise, since the scan offset can cause a large jump at that knob position), the etalon is roughly at normal incidence to the cavity beam. This can be checked by monitoring the frequency on the wavemeter. As the etalon is rotated clockwise on the galvo rod (as seen from the M1/M2 side of the laser), the frequency will decrease until normal incidence is reached, and then increase again. Setting the angle to be very slightly clockwise of normal incidence

allows for the largest frequency range to be reached with the electronic etalon knob. Next, the etalon potentiometer in the laser head should be tweaked such that the magnitude of the signal at the etalon test point (also in the head) is roughly 8 V with the etalon knob fully clockwise, and 1.5-2 V with the etalon knob (almost) fully counterclockwise. The etalon is then translated through the beam with the galvo's mount, until we find a spot with both good transmission (i.e. output laser power) and a good sawtooth error signal ($>$ 100 mV peak-to-peak), which is of course much more easily said than done. Tweaking the drive frequency of the etalon piezos, as described in the manual, sometimes also helps in achieving a good error signal.

The servo lock drives both the tweeter mirror and the Brewster plate galvos in order to stabilize the MBR frequency to the reference cavity. Two low-power reflections are picked off the light coming out of the cavity, one of which is sent directly to a photodiode (PD B) and one of which is sent to the reference cavity, and its reflection is sent to another photodiode (PD A). As described in the manual, the laser cavity and reference cavity should be sufficiently well aligned to achieve a finesse of 25 or better in order for the servo lock to function well.

The PD A signal is from the beam that is reflected only if the cavity is on resonance. This signal is used for a side-of-fringe locking technique. In order to eliminate dependence of the lock signal on the output power, the zero point of the fringes is determined by an offset proportional to the PD B signal. In principle, as long as the cavity fringes look fine, all that needs to be done to get the servo lock working is to set the fringe potentiometer in the laser head such that the peaks from the fringe test point are roughly 6 V peak-to-peak, then set the 'normalize'

potentiometer such that the servo error signal from the back of the control box is centered around 0 V.

In practice, the gains and time constants in the servo circuit often also need to be tweaked, and it is sometimes difficult to attain a balance between a sufficiently high gain for the lock to capture and a sufficiently slow galvo response to prevent the circuit from scanning too quickly over the fringes (the signature of this is that when pressing the servo lock button, the frequency quickly scans up several GHz before capturing a fringe, or railing at the end of its range). Before opening the control box, though, it is worth checking the stability of the etalon lock, e.g. by rotating the etalon knob small amounts and checking that the laser does not mode hop. On occasion the etalon lock can appear to be working fine when it is actually does not have a sufficiently high gain to follow as the servo lock changes the cavity length; in this case, it may incorrectly appear that the servo lock is the problem, because the etalon lock button seemingly works as desired, and its instability is only seen once the servo lock is engaged.

The circuit that servos the galvos and tweeter based on the fringes from the reference cavity is difficult to decode at first glance for those (like me) who are mostly only familiar with single-op-amp circuits like inverting amplifiers, integrators, and the like, but it turns out to be a PI-type controller with proportional and integral gain as well as a double-integrator gain. The full schematic of the 'Analogue' board of which this circuit is a part is far too detailed to fit into a single figure, so I have sketched a simplified circuit showing the key parts of this P/I/double-integrator, in Figure C.2. (Note that while there are several analog, as in not digital, circuit

boards in the MBR controller, 'Analogue' is Coherent's name for a particular circuit board that is accessible by opening the top of the control box.)

As this figure shows, there are two branches to this circuit: both are essentially integrators, but the output of the first integrator is fed into the second integrator, which compares this output to the original signal. We will analyze this circuit using the simplified rules for op amps:

(1) Neither op amp input draws any current;

(2) The output (when it is part of a feedback loop to one of the inputs) pushes whatever current/voltage necessary to ensure the two inputs are held at the same voltage.

We first consider the lower branch, shown in Figure C.2(b). The positive input is grounded, so the negative input is also forced to ground, so the current across R_1 is

$$I_1 = V_{in}/R_1. \tag{C.1}$$

The negative input draws no current, so I_1 is also the current across C_1. For a capacitor, $Q = CV$ or $I = dQ/dt = C\,dV/dt$, from which we get

$$I_1 = -C_1 \frac{dV_1}{dt}. \tag{C.2}$$

Equating these expressions, we find V_1 in terms of V_{in}:

$$V_1(t) = -\int_0^t dt' \frac{V_{in}(t')}{R_1 C_1}. \tag{C.3}$$

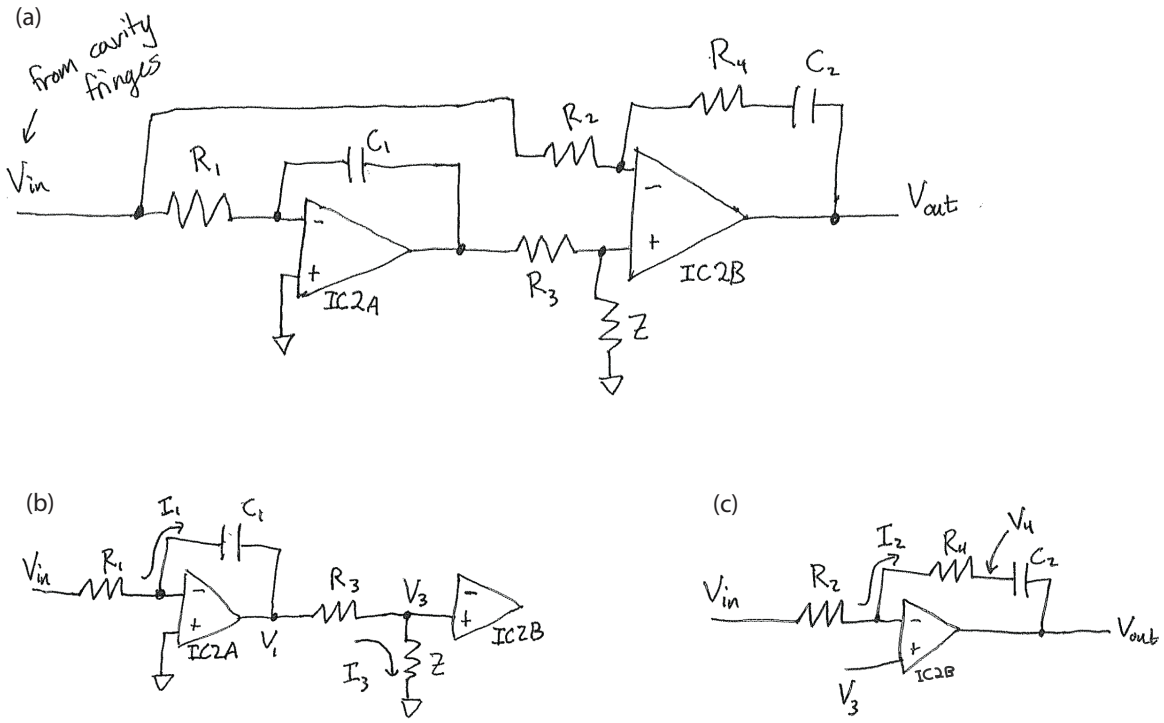

Figure C.2: (a): a simplified schematic of some key elements in the servo circuit. (b) and (c): portions of the schematic in (a), with currents and intermediate voltages labeled as in the derivation (see text). Note that the subscripts on the resistances relate to the potentiometer labels, e.g. R_1 is the sum of a constant resistance with the resistance of potentiometer PR1 on the control board.

The output voltage V_1 of the first op-amp is passed through a voltage divider to produce the voltage V_3 at the positive input of the second op-amp,

$$V_3 = \frac{Z}{R_3 + Z} V_1(t) \tag{C.4}$$

or

$$V_3 = -\frac{Z}{R_3 + Z} \int_0^t dt' \frac{V_{in}(t')}{R_1 C_1}. \tag{C.5}$$

To analyze the second branch of the circuit, shown in Figure C.2(b), we will find V_{out} in terms of V_{in} and V_3 before using the above expression to write V_{out} in terms of V_{in}. Because both inputs of the second op-amp are held at V_3, we see that

$$I_2 = \frac{V_{in} - V_3}{R_2} \tag{C.6}$$

and

$$V_4 = V_3 - I_2 R_4 = V_3 - \frac{R_4}{R_2} \left(V_{in} - V_3 \right), \tag{C.7}$$

$$V_4 = V_3 \left(1 + \frac{R_4}{R_2} \right) - \frac{R_4}{R_2} V_{in}. \tag{C.8}$$

The voltage across C_2 is $V_4 - V_{out}$, so

$$I_2 = C_2 \frac{d}{dt} \left(V_4 - V_{out} \right) = \frac{V_{in} - V_3}{R_2}. \tag{C.9}$$

Rearranging, we get

$$\frac{dV_{out}}{dt} = \frac{dV_4}{dt} + \frac{V_{in} - V_3}{R_2 C_2} \tag{C.10}$$

Along with Eq. C.8 above, this gives us

$$\frac{dV_{out}}{dt} = \left(1 + \frac{R_4}{R_2}\right)\frac{dV_3}{dt} - \frac{R_4}{R_2}\frac{dV_{in}}{dt} + \frac{V_3}{R_2C_2} - \frac{V_{in}}{R_2C_2}. \tag{C.11}$$

Using

$$V_3 = -\frac{Z}{R_3 + Z}\int_0^t dt' \frac{V_{in}(t')}{R_1C_1}; \tag{C.12}$$

$$\frac{dV_3}{dt} = \frac{-Z}{R_3 + Z}\frac{V_{in}}{R_1C_1}, \tag{C.13}$$

we finally get an equation directly relating V_{out} to V_{in}:

$$\frac{dV_{out}}{dt} = \frac{-Z}{R_3 + Z}\left(1 + \frac{R_4}{R_2}\right)\frac{V_{in}}{R_1C_1} - \frac{R_4}{R_2}\frac{dV_{in}}{dt} - \frac{V_{in}}{R_2C_2} - \left(\frac{1}{R_2C_2}\right)\frac{Z}{R_3 + Z}\int_0^t dt' \frac{V_{in}(t')}{R_1C_1}. \tag{C.14}$$

Integrating and rearranging slightly, we finally find

$$\begin{aligned} V_{out}(T) &= -\frac{R_4}{R_2}V_{in}(t) - \left[\frac{1}{R_2C_2} + \frac{Z}{R_3 + Z}\left(\frac{1}{R_1C_1}\right)\left(1 + \frac{R_4}{R_2}\right)\right]\int_0^T dt V_{in}(t) \\ &\quad - \frac{Z}{R_3 + Z}\left(\frac{1}{R_2C_2}\right)\left(\frac{1}{R_1C_1}\right)\int_0^T dt \int_0^t dt' V_{in}(t'). \end{aligned} \tag{C.15}$$

The only use of this expression as far as my experience goes is the following: we often find ourselves tweaking the potentiometers PR1 through PR4 in an attempt to stabilize the servo lock performance, so gaining even a slight amount of intuition as to which of these pots does what is somewhat useful. For example, we see from

this that the absolute value of PR4 plays no role, only its ratio with PR2.

The simplified impedances above are in actuality given by the following quantitative values, according to the schematic provided by Coherent:

$$R_1 = 2k\Omega + \text{PR1}; \quad 0 < \text{PR1} < 100k\Omega \tag{C.16}$$

$$R_2 = \text{PR2}; \quad 0 < \text{PR2} < 100k\Omega \tag{C.17}$$

$$R_3 = \text{PR3}; \quad 0 < \text{PR3} < 20k\Omega \tag{C.18}$$

$$R_4 = \text{PR4}; \quad 0 < \text{PR4} < 1k\Omega \tag{C.19}$$

$$C_1 = 18\text{nF} \tag{C.20}$$

$$C_2 = 10\text{nF} \tag{C.21}$$

and Z consists of a 1kΩ resistor and 330nF capacitor in parallel, so the impedance Z is dependent on frequency:

$$\frac{Z}{R_3 + Z} = \frac{1k\Omega}{1k\Omega + R_3\,(1 + i\omega/(3.03\,\text{kHz}))}, \tag{C.22}$$

so basically, its effect is to keep frequencies significantly higher than 3.03 kHz from getting into the first integration stage; at low frequencies, $\frac{Z}{R_3+Z} \approx \frac{1k\Omega}{1k\Omega+R_3}$.

From these numbers, we can see that $\left(\frac{1}{R_2C_2}\right)$ is 1 kHz or higher; $\left(\frac{1}{R_1C_1}\right)$ is 545 Hz or higher; R_4/R_2 is typically less than 1; and $0.05 \lesssim \frac{Z}{R_3+Z} \lesssim 1$. Qualitatively, increasing PR2 decreases all of the gains; increasing PR1 or PR3 decreases the

integral and double-integral gains; and increasing PR4 increases the proportional and integral gains.

Chapter D: Derivation of the effective spin-1 XY Hamiltonian from first principles

D.1 Deriving the single-particle Hamiltonian

In order to see how the XY model is generated, we go through essentially the same steps that were done in the Mølmer-Sørensen case that gave us the spin-1/2 Ising model used in all of the other experiments in this thesis.

The first thing we will do is to derive the single-particle Hamiltonian that is analogous to the Mølmer-Sørensen spin-dependent force. In this step, we want to show that with an appropriate set of sidebands (e.g., the '$|+\rangle$ red sideband' transition, $|+\rangle\langle 0|\, a + h.c.$, and '$|-\rangle$ blue sideband', $|-\rangle\langle 0|\, a^\dagger + h.c.$), we obtain a Hamiltonian of the form $(S_+ a + S_- a^\dagger)$, analogous to a single red sideband in a spin-1/2 system.

We begin with the result of the standard adiabatic elimination problem with a three-level Λ-type system, as derived in Appendix A:

$$\begin{aligned} H_{Raman} = \; & E_A \left|A\right\rangle\!\left\langle A\right| + E_B \left|B\right\rangle\!\left\langle B\right| + \tfrac{g_A g_B^*}{4\Delta} e^{i[(k_A - k_B)\cdot x - (\omega_A - \omega_B)t + \phi_A - \phi_B]} \left|B\right\rangle\!\left\langle A\right| \\ & + \tfrac{g_A^* g_B}{4\Delta} e^{-i[(k_A - k_B)\cdot x - (\omega_A - \omega_B)t + \phi_A - \phi_B]} \left|A\right\rangle\!\left\langle B\right| . \end{aligned} \tag{D.1}$$

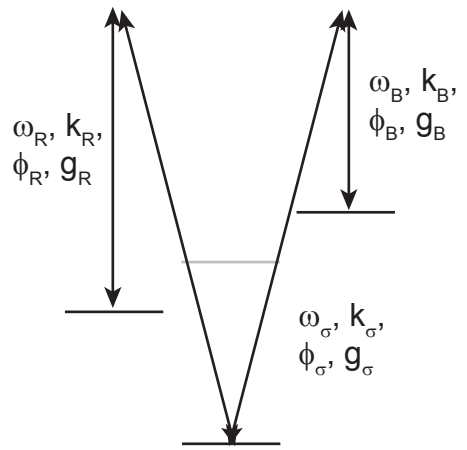

Figure D.1: Laser fields considered in deriving the Hamiltonian. It is assumed that there is a σ polarized beam of a single frequency, which has equal amounts of σ_+ and σ_- polarization, and a π polarized beam carrying two frequencies, one corresponding to a redder beatnote (R) and the other to a bluer beatnote (B).

Here, $|A\rangle$ and $|B\rangle$ are the two coupled ground states, and the corresponding laser field coupling to each state has some characteristic single-photon Rabi frequency g_i, wavevector k_i, frequency ω_i, and phase ϕ_i. Note that we are NOT in a rotating frame here, and we are eliding Stark shifts into the energies E_A and E_B. It should be fine to start from the rotating frame, but here I will take into account the multiple Raman transitions we will be driving before transforming to the rotating frame.

We will assume a single σ-polarized beam that has equal amounts of σ_+ and σ_- polarization, and whose parameters will be labeled with a σ (i.e., ω_σ, k_σ, ϕ_σ, g_σ). A noncopropagating π polarized beam will carry two frequencies (subscripts R and B). This situation is depicted in Figure D.1. The polarizations are chosen in this manner so as to couple to different excited states for the different Raman transitions, eliminating any possibility of the pathways interfering through a shared excited state, although in retrospect this was probably an overcautious choice, since

none of our spin-1/2 experiments have suffered from driving multiple transitions through the same shared excited states. We thus obtain the following Hamiltonian for the two Λ-type systems:

$$\begin{aligned} H = & \omega_- |-\rangle\langle -| + \omega_+ |+\rangle\langle +| + \tfrac{g_\sigma g_B^*}{4\Delta} e^{i\left[(k_\sigma - k_B)\cdot x - (\omega_\sigma - \omega_B)t + \phi_\sigma - \phi'_B\right]} |+\rangle\langle 0| \\ & + \tfrac{g_\sigma^* g_B}{4\Delta} e^{-i\left[(k_\sigma - k_B)\cdot x - (\omega_\sigma - \omega_B)t + \phi_\sigma - \phi'_B\right]} |0\rangle\langle +| + \tfrac{g_\sigma g_R^*}{4\Delta} e^{i\left[(k_\sigma - k_R)\cdot x - (\omega_\sigma - \omega_R)t + \phi_\sigma - \phi'_R\right]} |-\rangle\langle 0| \\ & + \tfrac{g_\sigma^* g_R}{4\Delta} e^{-i\left[(k_\sigma - k_R)\cdot x - (\omega_\sigma - \omega_R)t + \phi_\sigma - \phi'_R\right]} |0\rangle\langle -| . \end{aligned} \tag{D.2}$$

Here, $\omega_\pm \equiv \omega_{HF} \pm \delta_Z$ are the energy of the $|\pm\rangle$ states above the $|0\rangle$ state. This can be rewritten in terms of two-photon Rabi frequencies $\Omega_i \equiv \frac{g_\sigma g_i^*}{2\Delta}$, beat frequencies $\Delta\omega_i \equiv \omega_\sigma - \omega_i$, and phases $\phi_i = \phi_\sigma - \phi'_i$, and Lamb-Dicke parameters given by $(k_\sigma - k_i)\cdot x \equiv \Delta k_i \cdot x \equiv \eta_i \left(a e^{-i\omega_{tr} t} + a^\dagger e^{i\omega_{tr} t}\right)$ (where we have already gone to the interaction picture with respect to the harmonic oscillator Hamiltonian $H_{HO} = \omega_{tr} a^\dagger a$):

$$\begin{aligned} H = & \omega_- |-\rangle \langle -| + \omega_+ |+\rangle\langle +| + \tfrac{\Omega_B}{2} e^{i\left[\eta_B\left(a e^{-i\omega_{tr} t} + a^\dagger e^{i\omega_{tr} t}\right) - \Delta\omega_B t + \phi_B\right]} |+\rangle\langle 0| \\ & + \tfrac{\Omega_B^*}{2} e^{-i\left[\eta_B\left(a e^{-i\omega_{tr} t} + a^\dagger e^{i\omega_{tr} t}\right) - \Delta\omega_B t + \phi_B\right]} |0\rangle \langle +| + \tfrac{\Omega_R}{2} e^{i\left[\eta_R\left(a e^{-i\omega_{tr} t} + a^\dagger e^{i\omega_{tr} t}\right) - \Delta\omega_R t + \phi_R\right]} |-\rangle\langle 0| \\ & + \tfrac{\Omega_R^*}{2} e^{-i\left[\eta_R\left(a e^{-i\omega_{tr} t} + a^\dagger e^{i\omega_{tr} t}\right) - \Delta\omega_R t + \phi_R\right]} |0\rangle\langle -| . \end{aligned} \tag{D.3}$$

From this, we will make the Lamb-Dicke approximation and go into the rotat-

ing frame with respect to $H_{atom} = \omega_- |-\rangle\langle -| + \omega_+ |+\rangle\langle +|$:

$$\begin{aligned} H = \quad & \tfrac{\Omega_B}{2}\left(1 + i\eta_B\left[ae^{-i\omega_{tr}t} + a^\dagger e^{i\omega_{tr}t}\right]\right) e^{i[(\omega_+ - \Delta\omega_B)t + \phi_B]} |+\rangle\langle 0| \\ & + \tfrac{\Omega_B^*}{2}\left(1 - i\eta_B\left[ae^{-i\omega_{tr}t} + a^\dagger e^{i\omega_{tr}t}\right]\right) e^{-i[(\omega_+ - \Delta\omega_B)t + \phi_B]} |0\rangle\langle +| \\ & + \tfrac{\Omega_R}{2}\left(1 + i\eta_R\left[ae^{-i\omega_{tr}t} + a^\dagger e^{i\omega_{tr}t}\right]\right) e^{i[(\omega_- - \Delta\omega_R)t + \phi_R]} |-\rangle\langle 0| \\ & + \tfrac{\Omega_R^*}{2}\left(1 - i\eta_R\left[ae^{-i\omega_{tr}t} + a^\dagger e^{i\omega_{tr}t}\right]\right) e^{-i[(\omega_- - \Delta\omega_R)t + \phi_R]} |0\rangle\langle -| \,. \end{aligned} \tag{D.4}$$

(Note: by going into the rotating frame I mean that $H = e^{iH_{atom}t} V e^{-iH_{atom}t}$, where V comprises the interaction terms and $e^{iH_{atom}t} = e^{i\omega_- t} |-\rangle\langle -| + e^{i\omega_+ t} |+\rangle\langle +|$.)

We will choose our frequencies $\Delta\omega_R$ and $\Delta\omega_B$ so as to pick out the terms that allow us to make $S_+ a$ and $S_- a^\dagger$. Namely, for e.g. the $S_+ a$ term we want the $|+\rangle\langle 0|\, a$ and $|0\rangle\langle -|\, a$ terms near resonance, so we can impose the conditions $\Delta\omega_B \approx \omega_+ - \omega_{tr}$ and $\Delta\omega_R \approx \omega_- + \omega_{tr}$. Explicitly, let us set the frequencies to be symmetrically detuned blue of the $|-\rangle$ blue sideband and red of the $|+\rangle$ red sideband, such that when we add more ions the beat frequencies will still be detuned from all modes with the same sign:

$$\Delta\omega_B = \omega_+ - \omega_{tr} - \delta, \tag{D.5}$$

$$\Delta\omega_R = \omega_- + \omega_{tr} + \delta. \tag{D.6}$$

When we do this, we can make a rotating wave approximation to drop the far-off-

resonant terms and get

$$H = \frac{i\eta_B\Omega_B}{2}e^{i[\delta t+\phi_B]}\left|+\right\rangle\left\langle 0\right| a - \frac{i\eta_B\Omega_B^*}{2}e^{-i[\delta t+\phi_B]}\left|0\right\rangle\left\langle +\right| a^\dagger + \frac{i\eta_R\Omega_R}{2}e^{i[-\delta t+\phi_R]}\left|-\right\rangle\left\langle 0\right| a^\dagger - \frac{i\eta_R\Omega_R^*}{2}e^{-i[-\delta t+\phi_R]}\left|0\right\rangle\left\langle -\right| a. \tag{D.7}$$

There are yet further assumptions we must make in order to write this in terms of a familiar S_+ or S_- operator: let us take the phase-sensitive geometry where $\Delta k_R = \Delta k_B$ and write $\eta \equiv \eta_R = \eta_B$, and require that the Rabi frequencies of each beatnote are identical (and real), $\Omega \equiv \Omega_R = \Omega_B$, and rearrange terms to get

$$H = \frac{i\eta\Omega}{2}\left[ae^{i\delta t}\left(e^{i\phi_B}\left|+\right\rangle\left\langle 0\right| - e^{-i\phi_R}\left|0\right\rangle\left\langle -\right|\right) + a^\dagger e^{-i\delta t}\left(e^{i\phi_R}\left|-\right\rangle\left\langle 0\right| - e^{-i\phi_B}\left|0\right\rangle\left\langle +\right|\right)\right] \tag{D.8}$$

And finally, we see that to have operators like $S_+ = \sqrt{2}\left(\left|+\right\rangle\left\langle 0\right| + \left|0\right\rangle\left\langle -\right|\right)$ we will require

$$e^{i\phi_B} = -e^{-i\phi_R} \tag{D.9}$$

or

$$\phi_R + \phi_B = \pi. \tag{D.10}$$

So we can use our usual convention of $\phi_R = 0$ and $\phi_B = \pi$ to reach the Hamiltonian

$$H = \frac{i\eta\Omega}{2\sqrt{2}}\left[-S_+ae^{i\delta t} + S_-a^\dagger e^{-i\delta t}\right]. \tag{D.11}$$

As a side note, we saw in the case of the spin-1/2 Ising model that a change in the

sideband phases corresponded to a change in the Pauli spin operator σ_ϕ. However, if the sideband phases are changed in this spin-1 Hamiltonian, it seemingly is not possible to write the altered spin operators in such a clean way.

D.2 Magnus expansion

Now we will take the Hamiltonian we just derived (suitably modified to take into account multiple ions) and calculate the first few terms in the corresponding evolution operator with a Magnus expansion, in the same approach used to derive the spin-1/2 Ising interactions.

$$H = \sum_{i,m} \frac{i\eta_{i,m}\Omega_i}{2\sqrt{2}} \left[-S_+^i a_m e^{i(\mu-\omega_m)t} + S_-^i a_m^\dagger e^{-i(\mu-\omega_m)t} \right]. \tag{D.12}$$

Here the sums on ion i and mode m run from 1 to N.

Recall that the evolution operator is given by

$$U(t) = e^{\bar{\Omega}_1 + \bar{\Omega}_2 + \bar{\Omega}_3 + \cdots}, \tag{D.13}$$

$$\bar{\Omega}_1 = -i \int_0^t dt_1 H(t_1), \tag{D.14}$$

$$\bar{\Omega}_2 = -\frac{1}{2!} \int_0^t dt_1 \int_0^{t_1} dt_2 \left[H(t_1), H(t_2) \right], \tag{D.15}$$

$$\bar{\Omega}_3 = \frac{i}{3!} \int_0^t dt_1 \int_0^{t_1} dt_2 \int_0^{t_2} dt_3 \left([H(t_1), [H(t_2), H(t_3)]] + [H(t_3), [H(t_2), H(t_1)]] \right). \tag{D.16}$$

The direct integration is straightforward for the first term, giving us

$$\bar{\Omega_1} = \sum_{i,m} i\frac{\eta_{i,m}\Omega_i}{2\sqrt{2}(\mu-\omega_m)}\left[S^i_+ a_m(e^{i(\mu-\omega_m)t}-1) + S^i_- a^\dagger_m(e^{-i(\mu-\omega_m)t}-1)\right]. \quad \text{(D.17)}$$

As with the spin-1/2 Ising model, we will be able to neglect this entire term if $\eta_{i,m}\Omega_i \ll (\mu-\omega_m)$.

The second term requires us to calculate a commutator:

$$[H(t_1), H(t_2)] = \quad \text{(D.18)}$$
$$\left[\sum_{i,m}\frac{i\eta_{i,m}\Omega_i}{2\sqrt{2}}\left(-S^i_+ a_m e^{i(\mu-\omega_m)t_1} + S^i_- a^\dagger_m e^{-i(\mu-\omega_m)t_1}\right),\right.$$
$$\left.\sum_{j,n}\frac{i\eta_{j,n}\Omega_j}{2\sqrt{2}}\left(-S^j_+ a_n e^{i(\mu-\omega_n)t_2} + S^j_- a^\dagger_n e^{-i(\mu-\omega_n)t_2}\right)\right]$$

From this, the nonzero terms will be the cross terms $\left[S^i_+ a_m, S^j_- a^\dagger_n\right]$ and $\left[S^i_- a^\dagger_m, S^j_+ a_n\right]$. With the usual definitions of $S_\pm$, the commutator of the spin operators is $\left[S^i_+, S^j_-\right] = 2S_z \equiv 2\left|+\right\rangle\left\langle+\right| - 2\left|-\right\rangle\left\langle-\right|$. So we can work out that

$$\left[S^i_+ a_m, S^j_- a^\dagger_n\right] = S^i_+ S^j_- \delta_{mn} + 2a^\dagger_n a_m S^i_z \delta_{ij} \quad \text{(D.19)}$$

$$\left[S^i_- a^\dagger_m, S^j_+ a_n\right] = -S^i_- S^j_+ \delta_{mn} - 2a_n a^\dagger_m S^i_z \delta_{ij} \quad \text{(D.20)}$$

And after some accounting for signs, we can write

$$[H(t_1), H(t_2)] = \sum_{i,j,m,n}\frac{\eta_{i,m}\eta_{j,n}\Omega_i\Omega_j}{8}\left(\left[S^i_+ a_m e^{i(\mu-\omega_m)t_1}, S^j_- a^\dagger_n e^{-i(\mu-\omega_n)t_2}\right]\right.$$
$$\left. + \left[S^i_- a^\dagger_m e^{-i(\mu-\omega_m)t_1}, S^j_+ a_n e^{i(\mu-\omega_n)t_2}\right]\right) \quad \text{(D.21)}$$

or, using the commutators from above,

$$[H(t_1), H(t_2)] = \sum_{i,j,m,n} \frac{\eta_{i,m}\eta_{j,n}\Omega_i\Omega_j}{8} \left(e^{i(\mu(t_1-t_2)+\omega_n t_2-\omega_m t_1)} \left(S_+^i S_-^j \delta_{mn} + 2a_n^\dagger a_m S_z^i \delta_{ij} \right) \right.$$
$$\left. - e^{i(\mu(t_2-t_1)+\omega_m t_1-\omega_n t_2)} \left(S_-^i S_+^j \delta_{mn} + 2a_n a_m^\dagger S_z^i \delta_{ij} \right) \right) \qquad \text{(D.22)}$$

which can be regrouped into

$$[\quad H(t_1), H(t_2)] = \sum_{i,j,m} \frac{\eta_{i,m}\eta_{j,m}\Omega_i\Omega_j}{8} \left(e^{i(\mu-\omega_m)(t_1-t_2)} S_+^i S_-^j - e^{i(\mu-\omega_m)(t_2-t_1)} S_-^i S_+^j \right)$$
$$+ \sum_{i,m,n} \frac{\eta_{i,m}\eta_{i,n}\Omega_i^2}{4} \left(e^{i(\mu(t_1-t_2)+\omega_n t_2-\omega_m t_1)} a_n^\dagger a_m - e^{i(\mu(t_2-t_1)+\omega_m t_1-\omega_n t_2)} a_n a_m^\dagger \right) S_z^i.$$

Now we must integrate this twice to obtain $\int_0^t dt_1 \int_0^{t_1} dt_2 \, [H(t_1), H(t_2)]$. The non-phonon terms are of the form

$$\int_0^t dt_1 \int_0^{t_1} dt_2 e^{\pm i\delta(t_1-t_2)} = \frac{1 \pm i\delta t - e^{i\delta t}}{\delta^2}. \qquad \text{(D.23)}$$

For the phonon terms, the result depends on whether $m = n$. When $m \neq n$ we get

$$\int_0^t dt_1 \int_0^{t_1} dt_2 e^{i(\mu(t_1-t_2)+\omega_n t_2-\omega_m t_1)} = \frac{1 - e^{i(\mu-\omega_m)t}}{(\mu-\omega_m)(\mu-\omega_n)} + \frac{1 - e^{-i(\omega_m-\omega_n)t}}{(\omega_m-\omega_n)(\mu-\omega_n)}, \qquad \text{(D.24)}$$

but when $m = n$ we get the same integral as for the non-phonon terms. Hence, we

get the following expression for the integrated commutator:

$$\int_0^t dt_1 \int_0^{t_1} dt_2 \qquad [H(t_1), H(t_2)] = \tag{D.25}$$

$$\sum_{i,j,m} \frac{\eta_{i,m}\eta_{j,m}\Omega_i\Omega_j}{8(\mu-\omega_m)^2} \left[S_+^i S_-^j (1 + i(\mu-\omega_m)t - e^{i(\mu-\omega_m)t}) \right.$$

$$\left. + S_-^i S_+^j (-1 + i(\mu-\omega_m)t + e^{i(\mu-\omega_m)t})\right]$$

$$+ \sum_{i,m\neq n} \frac{\eta_{i,m}\eta_{i,n}\Omega_i^2}{4} \left[a_n^\dagger a_m \left(\frac{1-e^{i(\mu-\omega_m)t}}{(\mu-\omega_m)(\mu-\omega_n)} + \frac{1-e^{i(\omega_m-\omega_n)t}}{(\omega_m-\omega_n)(\mu-\omega_n)}\right)\right.$$

$$\left. + a_n a_m^\dagger \left(\frac{1-e^{-i(\mu-\omega_m)t}}{(\mu-\omega_m)(\mu-\omega_n)} + \frac{1-e^{i(\omega_m-\omega_n)t}}{(\omega_m-\omega_n)(\mu-\omega_n)}\right)\right] S_z^i$$

$$+ \sum_{i,m} \frac{\eta_{i,m}^2\Omega_i^2}{4(\mu-\omega_m)^2} \left(a_m^\dagger a_m (1 + i(\mu-\omega_m)t - e^{i(\mu-\omega_m)t}) \right.$$

$$\left. + a_m a_m^\dagger (-1 + i(\mu-\omega_m)t + e^{i(\mu-\omega_m)t})\right) S_z^i.$$

We see that the terms with a 1 or an $e^{i(\mu-\omega_m)t}$ are bounded and, under the condition $\eta_{i,m}\Omega_i \ll 1$ from before, we will consider them to be negligible, so the second term in the evolution operator can be simplified drastically to be written as

$$\bar{\Omega_2} \approx -i \sum_{i,j} J_{i,j} \left(S_+^i S_-^j + S_-^i S_+^j\right) t - i \sum_{i,m} V_{i,m} \left[2a_m^\dagger a_m + 1\right] S_z^i t, \tag{D.26}$$

where we have used $a_m a_m^\dagger = a_m^\dagger a_m + 1$, allowing us to write the effective Hamiltonian as

$$H_{XY} = \sum_{i,j} \frac{J_{i,j}}{4} \left(S_+^i S_-^j + S_-^i S_+^j\right) + \sum_{i,m} V_{i,m} \left[2a_m^\dagger a_m + 1\right] S_z^i \tag{D.27}$$

where

$$J_{i,j} = \Omega_i \Omega_j \sum_m \frac{\eta_{i,m}\eta_{j,m}}{4(\mu-\omega_m)}, \tag{D.28}$$

$$V_{i,m} = \frac{(\eta_{i,m}\Omega_i)^2}{2(\mu - \omega_m)}. \tag{D.29}$$

Here, we have made our definitions such that $J_{i,j}$ is identical to what it would be in the case of a spin-1/2 Ising model. The formula differs slightly from that given in (e.g.) Appendix B, which was

$$J_{i,j} = \sum_m \frac{i\eta_{i,m}\eta_{j,m}\Omega_i\Omega_j}{2(\mu^2 - \omega_m^2)}\omega_m. \tag{D.30}$$

However, if the spin-1/2 Ising Hamiltonian is calculated without including the counter-rotating terms previously pointed out as unnecessary, the formulae are identical. We can also see this by noting that usually $\mu \approx \omega_m$, such that $\omega_m/(\mu^2 - \omega_m^2) \approx 1/2(\mu - \omega_m)$.

D.2.1 Addition of an S_z^2 term

We next want to show that shifting the applied sideband frequencies appropriately is equivalent to adding a term $D(S_z)^2 = D\,|+\rangle\langle+| + D\,|-\rangle\langle-|$. We will start from a slightly different place, having made the Lamb-Dicke approximation as in

Eq. D.4, but without yet entering a rotating frame:

$$\begin{aligned} H = & \quad \omega_- \left|-\right\rangle\!\left\langle-\right| + \omega_+ \left|+\right\rangle\!\left\langle+\right| \\ & + \Omega_B \left(1 + i\eta_B \left[a e^{-i\omega_{tr}t} + a^\dagger e^{i\omega_{tr}t}\right]\right) e^{i[-\Delta\omega_B t + \phi_B]} \left|+\right\rangle\!\left\langle 0\right| \\ & + \Omega_B^* \left(1 - i\eta_B \left[a e^{-i\omega_{tr}t} + a^\dagger e^{i\omega_{tr}t}\right]\right) e^{-i[-\Delta\omega_B t + \phi_B]} \left|0\right\rangle\!\left\langle+\right| \\ & + \Omega_R \left(1 + i\eta_R \left[a e^{-i\omega_{tr}t} + a^\dagger e^{i\omega_{tr}t}\right]\right) e^{i[-\Delta\omega_R t + \phi_R]} \left|-\right\rangle\!\left\langle 0\right| \\ & + \Omega_R^* \left(1 - i\eta_R \left[a e^{-i\omega_{tr}t} + a^\dagger e^{i\omega_{tr}t}\right]\right) e^{-i[-\Delta\omega_R t + \phi_R]} \left|0\right\rangle\!\left\langle-\right|. \end{aligned} \tag{D.31}$$

This time we will shift both beatnotes *down* in frequency, which should have essentially the same effect as shifting both the $|+\rangle$ and $|-\rangle$ states up in energy. So we will have

$$\Delta\omega_B = \omega_+ - \omega_{tr} - \delta - D, \tag{D.32}$$

$$\Delta\omega_R = \omega_- + \omega_{tr} + \delta - D. \tag{D.33}$$

If we substitute these in and keep only terms where ω_{tr} drops out (i.e., this is the rotating wave approximation step), we get

$$\begin{aligned} H = & \quad \omega_- \left|-\right\rangle \left\langle-\right| + \omega_+ \left|+\right\rangle \left\langle+\right| \\ & + i\eta_B \Omega_B a e^{i[(D-\delta-\omega_+)t + \phi_B]} \left|+\right\rangle\!\left\langle 0\right| - i\eta_B \Omega_B^* a^\dagger e^{i[(\omega_+ + \delta - D)t - \phi_B]} \left|0\right\rangle\!\left\langle+\right| \\ & + i\eta_R \Omega_R a^\dagger e^{i[(D-\delta-\omega_-)t + \phi_R]} \left|-\right\rangle\!\left\langle 0\right| - i\eta_R \Omega_R^* a e^{i[(\omega_- + \delta - D)t - \phi_R]} \left|0\right\rangle\!\left\langle-\right|. \end{aligned} \tag{D.34}$$

To simplify things, I will go ahead and set $\eta = \eta_R = \eta_B$ and $\Omega = \Omega_R = \Omega_B$ as

before, so that we have just

$$\begin{aligned} H = & \quad \omega_- \left|-\right\rangle\!\left\langle-\right| + \omega_+ \left|+\right\rangle\!\left\langle+\right| \\ & + i\eta\Omega a e^{i[(D-\delta-\omega_+)t+\phi_B]} \left|+\right\rangle\!\left\langle 0\right| - i\eta\Omega a^\dagger e^{i[(\omega_+ +\delta-D)t-\phi_B]} \left|0\right\rangle\!\left\langle+\right| \\ & + i\eta\Omega a^\dagger e^{i[(D-\delta-\omega_-)t+\phi_R]} \left|-\right\rangle\!\left\langle 0\right| - i\eta\Omega a e^{i[(\omega_- +\delta-D)t-\phi_R]} \left|0\right\rangle\!\left\langle-\right|. \end{aligned} \tag{D.35}$$

We again want to be able to factorize this into terms that look like $ae^{i\theta}(|+\rangle\langle 0| + |0\rangle\langle -|)$, and are prevented from doing so by the different time dependences. Before, this was overcome by going into a rotating frame where $H \to e^{iH_0 t} V e^{-iH_0 t}$, where we had $H_0 = \omega_- |-\rangle\langle -| + \omega_+ |+\rangle\langle +|$ and $H = H_0 + V$. By the same token, in order to get our time dependences to play nicely, we now want our transformation to be given by

$$H_0 = (\omega_- - D) \left|-\right\rangle\!\left\langle-\right| + (\omega_+ - D) \left|+\right\rangle\!\left\langle+\right|. \tag{D.36}$$

However, now our $V = H - H_0$ will have an extra term $D(|-\rangle\langle -| + |+\rangle\langle +|)$, so we will wind up with

$$\begin{aligned} H = & \quad D \left|-\right\rangle\!\left\langle-\right| + D \left|+\right\rangle\!\left\langle+\right| \\ & + i\eta\Omega a e^{i[-\delta t+\phi_B]} \left|+\right\rangle\!\left\langle 0\right| - i\eta\Omega a^\dagger e^{i[\delta t-\phi_B]} \left|0\right\rangle\!\left\langle+\right| \\ & + i\eta\Omega a^\dagger e^{i[-\delta t+\phi_R]} \left|-\right\rangle\!\left\langle 0\right| - i\eta\Omega a e^{i[\delta t-\phi_R]} \left|0\right\rangle\!\left\langle-\right|. \end{aligned} \tag{D.37}$$

So now, treating the raising and lowering terms in the same way as before (setting $\phi_R = 0$ and $\phi_B = \pi$, etc), and writing $|-\rangle\langle -| + |+\rangle\langle +| = (S_z)^2$, we wind up with a

single-particle Hamiltonian

$$H = D(S_z)^2 + i\eta\Omega\left[-S_+ a e^{i\delta t} + S_- a^\dagger e^{-i\delta t}\right]. \tag{D.38}$$

As with the transverse-field Ising model, it is not quite correct to write the effective Hamiltonian as the interaction term derived above plus the non-interacting field term $D(S_z)^2$, since the field term will enter into the commutators of the Magnus expansion [113]; however, for our purposes this seems to be a close enough approximation to the effective dynamics.

Bibliography

[1] I. Bloch, J. Dalibard, and S. Nascimbene, "Quantum simulations with ultracold gases," *Nature Physics*, vol. 8, p. 267, 2012.

[2] R. Blatt and C. F. Roos, "Quantum simulations with trapped ions," *Nature Physics*, vol. 8, p. 277, 2012.

[3] A. Aspuru-Guzik and P. Walther, "Photonic quantum simulators," *Nature Physics*, vol. 8, p. 285, 2012.

[4] J. J. Garcia-Ripoll, E. Solano, and M. A. Martin-Delgado, "Quantum simulation of anderson and kondo lattices with superconducting qubits," *Phys. Rev. B*, vol. 77, p. 024522, 2008.

[5] J. Simon, W. S. Bakr, R. Ma, M. E. Tai, P. M. Preiss, and M. Greiner, "Quantum simulation of antiferromagnetic spin chains in an optical lattice," *Nature*, vol. 472, p. 307, 2011.

[6] M. Cheneau, P. Barmettler, D. Poletti, M. Endres, P. Schauss, T. Fukuhara, C. Gross, I. Bloch, C. Kollath, and S. Kuhr, "Light-cone-like spreading of correlations in a quantum many-body system," *Nature*, vol. 481, p. 484, 2012.

[7] W. S. Bakr, A. Peng, M. E. Tai, R. Ma, J. Simon, J. I. Gillen, S. Flling, L. Pollet, and M. Greiner, "Probing the superfluidtomott insulator transition at the single-atom level," *Science*, vol. 329, no. 5991, pp. 547–550, 2010.

[8] T. Uehlinger, G. Jotzu, M. Messer, D. Greif, W. Hofstetter, U. Bissbort, and T. Esslinger, "Artificial graphene with tunable interactions," *Phys. Rev. Lett.*, vol. 111, p. 185307, Oct 2013.

[9] G.-D. Lin, S.-L. Zhu, R. Islam, K. Kim, M.-S. Chang, S. Korenblit, C. Monroe, and L.-M. Duan, "Large-scale quantum computation in an anharmonic linear ion trap," *Europhysics Letters*, vol. 86, p. 60004, 2009.

[10] Y.-J. Lin, R. L. Compton, K. Jimenez-Garcia, W. D. Phillips., J. V. Porto, and I. B. Spielman, "A synthetic electric force acting on neutral atoms," *Nature Physics*, vol. 7, p. 531, 2011.

[11] K. M. O'Hara, S. L. Hemmer, M. E. Gehm, S. R. Granade, and J. E. Thomas, "Observation of a strongly interacting degenerate fermi gas of atoms," *Science*, vol. 298, no. 5601, pp. 2179–2182, 2002.

[12] T. Bourdel, J. Cubizolles, L. Khaykovich, K. M. F. Magalhaes, S. J. J. M. F. Kokkelmans, G. V. Shlyapnikov, and C. Salomon, "Measurement of the interaction energy near a feshbach resonance in a ^{6}Li fermi gas," *Phys. Rev. Lett.*, vol. 91, p. 020402, Jul 2003.

[13] C. A. Regal, M. Greiner, and D. S. Jin, "Observation of resonance condensation of fermionic atom pairs," *Phys. Rev. Lett.*, vol. 92, p. 040403, Jan 2004.

[14] M. W. Zwierlein, C. A. Stan, C. H. Schunck, S. M. F. Raupach, A. J. Kerman, and W. Ketterle, "Condensation of pairs of fermionic atoms near a feshbach resonance," *Phys. Rev. Lett.*, vol. 92, p. 120403, Mar 2004.

[15] B. Yan, S. A. Moses, B. Gadway, J. P. Covey, K. R. A. Hazzard, A. M. Rey, D. S. Jin, and J. Ye, "Observation of dipolar spin-exchange interactions with lattice-confined polar molecules," *Nature*, vol. 501, p. 521, 2013.

[16] R. Loew, H. Weimer, J. Nipper, J. B. Balewski, B. Butscher, H. P. Buechler, and T. Pfau, "An experimental and theoretical guide to strongly interacting rydberg gases," *Journal of Physics B: Atomic, Molecular and Optical Physics*, vol. 45, no. 11, p. 113001, 2012.

[17] O. Firstenberg, T. Peyronel, Q.-Y. Liang, A. V. Gorshkov, M. D. Lukin, and V. Vuletic, "Attractive photons in a quantum nonlinear medium," *Nature*, vol. 502, p. 71, 2013.

[18] K. Kim, M.-S. Chang, R. Islam, S. Korenblit, L.-M. Duan, and C. Monroe, "Entanglement and tunable spin-spin couplings between trapped ions using multiple transverse modes," *Phys. Rev. Lett.*, vol. 103, p. 120502, 2009.

[19] K. Kim, M.-S. Chang, S. Korenblit, R. Islam, E. E. Edwards, J. K. Freericks, G.-D. Lin, L.-M. Duan, and C. Monroe, "Quantum simulation of frustrated ising spins with trapped ions," *Nature*, vol. 465, p. 590, 2010.

[20] E. E. Edwards, S. Korenblit, K. Kim, R. Islam, M.-S. Chang, J. K. Freericks, G.-D. Lin, L.-M. Duan, and C. Monroe, "Quantum simulation and phase diagram of the transverse-field ising model with three atomic spins," *Phys. Rev. B*, vol. 82, p. 060412, 2010.

[21] R. Islam, E. E. Edwards, K. Kim, S. Korenblit, C. Noh, H. Carmichael, G.-D. Lin, L.-M. Duan, C.-C. J. Wang, J. K. Freericks, and C. Monroe, "Onset of

a quantum phase transition with a trapped ion quantum simulator," *Nature Communications*, vol. 2, p. 377, 2011.

[22] R. Islam, C. Senko, W. C. Campbell, S. Korenblit, J. Smith, A. Lee, E. E. Edwards, C.-C. J. Wang, J. K. Freericks, and C. Monroe, "Emergence and frustration of magnetic order with variable-range interactions in a trapped ion quantum simulator," *Science*, vol. 340, p. 583, 2013.

[23] P. Richerme, C. Senko, J. Smith, A. Lee, S. Korenblit, and C. Monroe, "Experimental performance of a quantum simulator: Optimizing adiabatic evolution and identifying many-body ground states," *Phys. Rev. A*, vol. 88, p. 012334, 2013.

[24] P. Richerme, C. Senko, S. Korenblit, J. Smith, A. Lee, R. Islam, W. C. Campbell, and C. Monroe, "Quantum catalysis of magnetic phase transitions in a quantum simulator," *Phys. Rev. Lett.*, vol. 111, p. 100506, 2013.

[25] P. Richerme, Z.-X. Gong, A. Lee, C. Senko, J. Smith, M. Foss-Feig, S. Michalakis, A. V. Gorshkov, and C. Monroe, "Non-local propagation of correlations in quantum systems with long-range interactions," *Nature*, vol. 511, p. 198, 2014.

[26] C. Senko, J. Smith, P. Richerme, A. Lee, W. C. Campbell, and C. Monroe, "Coherent imaging spectroscopy of a quantum many-body spin system," *Science*, vol. 345, p. 430, 2014.

[27] K. Toyoda, Y. Matsuno, A. Noguchi, S. Haze, and S. Urabe, "Experimental realization of a quantum phase transition of polaritonic excitations," *Phys. Rev. Lett.*, vol. 111, p. 160501, Oct 2013.

[28] R. Gerritsma, G. Kirchmair, F. Zaehringer, E. Solano, R. Blatt, and C. F. Roos, "Quantum simulation of the dirac equation," *Nature*, vol. 462, p. 68, 2010.

[29] R. Gerritsma, B. P. Lanyon, G. Kirchmair, F. Zaehringer, C. Hempel, J. Casanova, J. J. Garcia-Ripoll, E. Solano, R. Blatt, and C. F. Roos, "Quantum simulation of the klein paradox," *Phys. Rev. Lett.*, vol. 106, p. 060503, 2011.

[30] D. Porras, F. Marquardt, J. von Delft, and J. I. Cirac, "Mesoscopic spin-boson models of trapped ions," *Phys. Rev. A*, vol. 78, p. 010101, Jul 2008.

[31] A. Benassi, A. Vanossi, and E. Tosatti, "Nanofriction in cold ion traps," *Nature Communications*, vol. 2, p. 236, 2010.

[32] J. Casanova, L. Lamata, I. L. Egusquiza, R. Gerritsma, C. F. Roos, J. J. Garcia-Ripoll, and E. Solano, "Quantum simulation of quantum field theories in trapped ions," *Phys. Rev. Lett.*, vol. 107, p. 260501, Dec 2011.

[33] K. R. Islam, *Quantum Simulation of Interacting Spin Models with Trapped Ions*. PhD thesis, University of Maryland, College Park, 2012.

[34] S. Korenblit, *Quantum Simulations of the Ising Model: Devil's Staircase and Arbitrary Lattice Proposal*. PhD thesis, University of Maryland, College Park, 2013.

[35] E. T. Jaynes and F. W. Cummings, "Comparison of quantum and semiclassical radiation theories with application to the beam maser," *Proc. IEEE*, vol. 51, p. 89, 1963.

[36] B. W. Shore and P. L. Knight, "The jaynes-cummings model," *Journal of Modern Optics*, vol. 40, p. 1195, 1993.

[37] S. Haroche, "Nobel lecture: Controlling photons in a box and exploring the quantum to classical boundary," *Rev. Mod. Phys.*, vol. 85, pp. 1083–1102, Jul 2013.

[38] A. A. Houck, D. I. Schuster, J. M. Gambetta, J. A. Schreier, B. R. Johnson, J. M. Chow, L. Frunzio, J. Majer, M. H. Devoret, S. M. Girvin, and R. J. Schoelkopf, "Generating single microwave photons in a circuit," *Nature*, vol. 449, p. 328, 2007.

[39] T. J. Kippenberg and K. J. Vahala, "Cavity optomechanics: Back-action at the mesoscale," *Science*, vol. 321, no. 5893, pp. 1172–1176, 2008.

[40] S. Kolkowitz, A. C. Bleszynski Jayich, Q. P. Unterreithmeier, S. D. Bennett, P. Rabl, J. G. E. Harris, and M. D. Lukin, "Coherent sensing of a mechanical resonator with a single-spin qubit," *Science*, vol. 335, no. 6076, pp. 1603–1606, 2012.

[41] V. Galitski and I. B. Spielman, "Spin-orbit coupling in quantum gases," *Nature*, vol. 494, p. 49, 2013.

[42] L. J. LeBlanc, M. C. Beeler, K. Jimnez-Garca, A. R. Perry, S. Sugawa, R. A. Williams, and I. B. Spielman, "Direct observation of zitterbewegung in a boseeinstein condensate," *New Journal of Physics*, vol. 15, no. 7, p. 073011, 2013.

[43] D. Porras and J. I. Cirac, "Effective quantum spin systems with trapped ions," *Phys. Rev. Lett.*, vol. 92, p. 207901, 2004.

[44] A. Friedenauer, H. Schmitz, J. T. Glueckert, D. Porras, and T. Schaetz, "Simulating a quantum magnet with trapped ions," *Nature Physics*, vol. 4, p. 757, 2008.

[45] Y. L. Zhou, M. Ortner, and P. Rabl, "Long-range and frustrated spin-spin interactions in crystals of cold polar molecules," *Phys. Rev. A*, vol. 84, p. 052332, Nov 2011.

[46] S. Olmschenk, K. C. Younge, D. L. Moehring, D. N. Matsukevich, P. Maunz, and C. Monroe, "Manipulation and detection of a trapped yb$^+$ hyperfine qubit," *Phys. Rev. A*, vol. 76, p. 052314, 2007.

[47] S. M. Olmschenk, *Quantum Teleportation Between Distant Matter Qubits*. PhD thesis, University of Michigan, Ann Arbor, 2009.

[48] S. Olmschenk, D. Hayes, D. N. Matsukevich, P. Maunz, D. L. Moehring, K. C. Younge, and C. Monroe, "Measurement of the lifetime of the $6p\ ^2P^o_{1/2}$ level of yb$^+$," *Phys. Rev. A*, vol. 80, p. 022502, Aug 2009.

[49] W. C. Campbell, J. Mizrahi, Q. Quraishi, C. Senko, D. Hayes, D. Hucul, D. N. Matsukevich, P. Maunz, and C. Monroe, "Ultrafast gates for single atomic qubits," *Phys. Rev. Lett.*, vol. 105, p. 090502, 2010.

[50] P. Taylor, M. Roberts, S. V. Gateva-Kostova, R. B. M. Clarke, G. P. Barwood, W. R. C. Rowley, and P. Gill, "Investigation of the $^2S_{1/2}$–$^2D_{5/2}$ clock transition in a single ytterbium ion," *Phys. Rev. A*, vol. 56, pp. 2699–2704, Oct 1997.

[51] D. J. Wineland, C. Monroe, W. M. Itano, D. Leibfried, B. E. King, and D. M. Meekhof, "Experimental issues in coherent quantum-state manipulation of trapped atomic ions," *Journal of Research of the National Institute of Standards and Technology*, vol. 103, p. 259, 1998.

[52] A. Sorensen and K. Molmer, "Entanglement and quantum computation with ions in thermal motion," *Phys. Rev. A*, vol. 62, p. 022311, 2000.

[53] I. V. Inlek, G. Vittorini, D. Hucul, C. Crocker, and C. Monroe, "Quantum gates with phase stability over space and time." arxiv:1405.5207.

[54] D. Hayes, D. N. Matsukevich, P. Maunz, D. Hucul, Q. Quraishi, S. Olmschenk, W. Campbell, J. Mizrahi, C. Senko, and C. Monroe, "Entanglement of atomic qubits using an optical frequency comb," *Phys. Rev. Lett.*, vol. 104, p. 140501, 2010.

[55] J. Mizrahi, B. Neyenhuis, K. G. Johnson, W. C. Campbell, C. Senko, D. Hayes, and C. Monroe, "Quantum control of qubits and atomic motion using ultrafast laser pulses." Applied Physics B, 2013.

[56] W. Paul, "Electromagnetic traps for charged and neutral particles," *Rev. Mod. Phys.*, vol. 62, p. 531, 1990.

[57] A. Chew, "Doppler-free spectroscopy of iodine at 739 nm," Master's thesis, University of Michigan, Ann Arbor, 2008.

[58] R. Islam, W. C. Campbell, T. Choi, S. M. Clark, S. Debnath, E. E. Edwards, B. Fields, D. Hayes, D. Hucul, I. V. Inlek, K. G. Johnson, S. Korenblit, A. Lee,

K. W. Lee, T. A. Manning, D. N. Matsukevich, J. Mizrahi, Q. Quraishi, C. Senko, J. Smith, and C. Monroe, "Beat note stabilization of mode-locked lasers for quantum information processing," *Optics Letters*, vol. 39, p. 3238, 2014.

[59] A. C. Lee, "Ytterbium ion qubit state detection on an iccd camera," b.sc. thesis, University of Maryland, College Park, 2012.

[60] C. Shen and L.-M. Duan, "Correcting detection errors in quantum state engineering through data processing," *New Journal of Physics*, vol. 14, p. 053053, 2012.

[61] C. Monroe, D. M. Meekhof, B. E. King, S. R. Jefferts, W. M. Itano, and D. J. Wineland, "Resolved-sideband raman cooling of a bound atom to the 3d zero-point energy," *Phys. Rev. Lett.*, vol. 75, p. 4011, 1995.

[62] S. Sachdev, *Quantum Phase Transitions*. Cambridge University Press, 1999.

[63] A. Messiah, *Quantum Mechanics*. Amsterdam: North-Holland, 1962.

[64] J. Roland and N. J. Cerf, "Quantum search by local adiabatic evolution," *Phys. Rev. A*, vol. 65, p. 042308, 2002.

[65] H. T. Quan and W. H. Zurek, "Testing quantum adiabaticity with quench echo," *New J. Phys.*, vol. 12, p. 093025, 2010.

[66] C. Lanczos, "An iteration method for the solution of the eigenvalue problem of linear differential and integral operators," *Journal of Research of the National Bureau of Standards*, vol. 45, p. 255, 1950.

[67] E. Farhi, J. Goldstone, S. Gutmann, and M. Sipser, "Quantum computation by adiabatic evolution," *e-print quant-ph/0001106*, 2000.

[68] C. Zener, "Non-adiabatic crossing of energy levels," *Proc. R. Soc. A*, vol. 137, p. 696, 1932.

[69] B. Damski and W. H. Zurek, "Adiabatic-impulse approximation for avoided level crossings: From phase-transition dynamics to landau-zener evolutions and back again," *Phys. Rev. A*, vol. 73, p. 063405, 2006.

[70] W. M. Itano, J. C. Bergquist, J. J. Bollinger, J. M. Gilligan, D. J. Heinzen, F. L. Moore, M. G. Raizen, and D. J. Wineland, "Quantum projection noise: Population fluctuations in two-level systems," *Phys. Rev. A*, vol. 47, p. 3554, 1993.

[71] B. Nachtergaele, Y. Ogata, and R. Sims, "Propagation of correlations in quantum lattice systems," *J. Stat. Phys.*, vol. 124, p. 1, 2006.

[72] J. Schachenmayer, B. P. Lanyon, C. F. Roos, and A. J. Daley, "Entanglement growth in quench dynamics with variable range interactions," *Phys. Rev. X*, vol. 3, p. 031015, 2013.

[73] P. Hauke and L. Tagliacozzo, "Spread of correlations in long-range interacting quantum systems," *Phys. Rev. Lett.*, vol. 111, p. 207202, Nov 2013.

[74] K. R. A. Hazzard, S. R. Manmana, M. Foss-Feig, and A. M. Rey, "Far-from-equilibrium quantum magnetism with ultracold polar molecules," *Phys. Rev. Lett.*, vol. 110, p. 075301, 2013.

[75] J. Eisert, M. Cramer, and M. Plenio, "Colloquium: Area laws for the entanglement entropy," *Rev. Mod. Phys.*, vol. 82, p. 277, 2010.

[76] E. Lieb and D. Robinson, "The finite group velocity of quantum spin systems," *Commun. Math. Phys.*, vol. 28, p. 251, 1972.

[77] S. Bravyi, M. B. Hastings, and F. Verstraete, "Lieb-robinson bbound and the generation of correlations and topological quantum order," *Phys. Rev. Lett.*, vol. 97, p. 050401, 2006.

[78] M. Hastings and T. Koma, "Spectral gap and exponential decay of correlations," *Commun. Math. Phys.*, vol. 265, p. 781, 2006.

[79] B. Nachtergaele and R. Sims, "Lieb-robinson bound and the exponential clustering theorem," *Commun. Math. Phys.*, vol. 265, p. 119, 2006.

[80] M. Hastings, "An area law for one-dimensional quantum systems," *J. Stat. Mech*, p. (2007) P08024, 2007.

[81] S. Michalakis, "Stability of the area law for the entropy of entanglement," *e-print 1206.6900*, 2012.

[82] M. Rigol, V. Dunjko, V. Yurovsky, and M. Olshanii, "Relaxation in a completely integrable many-body quantum system: An ab initio study of the dynamics of the highly excited states of 1d lattice hard-core bosons," *Phys. Rev. Lett.*, vol. 98, p. 050405, 2007.

[83] P. Calabrese and J. Cardy, "Time dependence of correlation functions following a quantum quench," *Phys. Rev. Lett.*, vol. 96, p. 136801, 2006.

[84] Z.-X. Gong and L.-M. Duan, "Prethermalization and dynamic phase transitions in an isolated trapped ion spin chain," *New J. Phys.*, vol. 15, p. 113051, 2013.

[85] S. Bose, "Quantum communication through spin chain dynamics: an introductory overview," *Contemp. Phys.*, vol. 48, p. 13, 2007.

[86] J. Eisert, M. van den Worm, S. Manmana, and M. Kastner, "Breakdown of quasi-locality in long-range quantum lattice models," *e-print*, p. 1309.2308, 2013.

[87] M. van den Worm, B. Sawyer, J. Bollinger, and M. Kastner, "Relaxation timescales and decay of correlations in a long-range interacting quantum simulator," *New J. Phys.*, vol. 15, p. 083007, 2013.

[88] Z.-X. Gong, M. Foss-Feig, S. Michalakis, and A. V. Gorshkov, "Persistence of locality in systems with power-law interactions," *Phys. Rev. Lett.*, vol. 113, p. 030602, Jul 2014.

[89] P. Jurcevic, B. P. Lanyon, P. Hauke, C. Hempel, P. Zoller, R. Blatt, and C. F. Roos, "Quasiparticle engineering and entanglement propagation in a quantum many-body system," *Nature*, vol. 511, p. 202, 2014.

[90] M. Foss-Feig, K. R. A. Hazzard, J. J. Bollinger, and A. M. Rey, "Nonequilibrium dynamics of arbitrary-range ising models with decoherence: An exact analytic solution," *Phys. Rev. A*, vol. 87, p. 042101, 2013.

[91] F. Casas, A. Murua, and M. Nadinic, "Efficient computation of the zassenhaus formula," *Computer Physics Communications*, vol. 183, no. 11, pp. 2386 – 2391, 2012.

[92] J. W. Britton, B. C. Sawyer, A. C. Keith, C.-C. J. Wang, J. K. Freericks, H. Uys, M. J. Biercuk, and J. J. Bollinger, "Engineered two-dimensional ising interactions in a trapped-ion quantum simulator with hundreds of spins," *Nature*, vol. 484, p. 489, 2012.

[93] M. van den Worm, B. C. Sawyer, J. J. Bollinger, and M. Kastner, "Relaxation timescales and decay of correlations in a long-range interacting quantum simulator," *New J. Phys.*, vol. 15, no. 8, p. 083007, 2013.

[94] M. Knap, A. Kantian, T. Giamarchi, I. Bloch, M. D. Lukin, and E. Demler, "Probing real-space and time resolved correlation functions with many-body ramsey interferometry," *Phys. Rev. Lett.*, vol. 111, p. 147205, 2013.

[95] A. Khromova, C. Piltz, B. Scharfenberger, T. F. Gloger, M. Johanning, A. F. Varon, and C. Wunderlich, "Designer spin pseudomolecule implemented with trapped ions in a magnetic gradient," *Phys. Rev. Lett.*, vol. 108, p. 220502, 2012.

[96] J. J. Sakurai, *Modern Quantum Mechanics*. Addison Wesley, 1993.

[97] G. Tóth, C. Knapp, O. Gühne, and H. J. Briegel, "Optimal spin squeezing inequalities detect bound entanglement in spin models," *Phys. Rev. Lett.*, vol. 99, p. 250405, Dec 2007.

[98] B. Yoshimura, W. C. Campbell, and J. K. Freericks, "Diabatic ramping spectroscopy of many-body excited states for trapped-ion quantum simulators." arXiv:1402.7357.

[99] F. D. M. Haldane, "Continuum dynamics of the 1-d heisenberg antiferromagnet: Identification with the o(3) nonlinear sigma model," *Physics Letters A*, vol. 93, p. 464, 1983.

[100] F. D. M. Haldane, "Nonlinear field theory of large-spin heisenberg antiferromagnets: Semiclassically quantized solitons of the one-dimensional easy-axis néel state," *Phys. Rev. Lett.*, vol. 50, pp. 1153–1156, Apr 1983.

[101] M. den Nijs and K. Rommelse, "Preroughening transitions in crystal surfaces and valence-bond phases in quantum spin chains," *Phys. Rev. B*, vol. 40, pp. 4709–4734, Sep 1989.

[102] D. V. Else, S. D. Bartlett, and A. C. Doherty, "Symmetry protection of measurement-based quantum computation in ground states," *New Journal of Physics*, vol. 14, no. 11, p. 113016, 2012.

[103] D. V. Else, I. Schwarz, S. D. Bartlett, and A. C. Doherty, "Symmetry-protected phases for measurement-based quantum computation," *Phys. Rev. Lett.*, vol. 108, p. 240505, Jun 2012.

[104] D. A. Lidar, I. L. Chuang, and K. B. Whaley, "Decoherence-free subspaces for quantum computation," *Phys. Rev. Lett.*, vol. 81, p. 2594, 1998.

[105] D. Kielpinski, V. Meyer, M. A. Rowe, C. A. Sackett, W. M. Itano, C. Monroe, and D. J. Wineland, "A decoherence-free quantum memory using trapped ions," *Science*, vol. 291, p. 1013, 2001.

[106] C. A. Sackett, D. Kielpinski, B. E. King, C. Langer, V. Meyer, C. J. Myatt, M. Rowe, Q. A. Turchette, W. M. Itano, D. J. Wineland, and C. Monroe, "Experimental entanglement of four particles," *Nature*, vol. 404, p. 256, 2000.

[107] T. Murashima, K. Hijii, K. Nomura, and T. Tonegawa, "Phase diagram of s=1 xxz chain with next-nearest-neighbor interaction," *Journal of the Physical Society of Japan*, vol. 74, no. 5, pp. 1544–1551, 2005.

[108] I. Affleck, T. Kennedy, E. H. Lieb, and H. Tasaki, "Rigorous results on valence-bond ground states in antiferromagnets," *Phys. Rev. Lett.*, vol. 59, pp. 799–802, Aug 1987.

[109] I. Affleck, T. Kennedy, E. Lieb, and H. Tasaki, "Valence bond ground states in isotropic quantum antiferromagnets," *Communications in Mathematical Physics*, vol. 115, no. 3, pp. 477–528, 1988.

[110] F. Pollmann, A. M. Turner, E. Berg, and M. Oshikawa, "Entanglement spectrum of a topological phase in one dimension," *Phys. Rev. B*, vol. 81, p. 064439, Feb 2010.

[111] F. Pollmann, E. Berg, A. M. Turner, and M. Oshikawa, "Symmetry protection of topological phases in one-dimensional quantum spin systems," *Phys. Rev. B*, vol. 85, p. 075125, Feb 2012.

[112] I. Cohen and A. Retzker, "Proposal for verification of the haldane phase using trapped ions," *Phys. Rev. Lett.*, vol. 112, p. 040503, Jan 2014.

[113] C.-C. J. Wang and J. K. Freericks, "Intrinsic phonon effects on analog quantum simulators with ultracold trapped ions," *Phys. Rev. A*, vol. 86, p. 032329, 2012. quantum simulation trapped ions phonons.